The vascular smooth muscle T-type Ca^{2+} channel: An anti-proliferative target for heme oxygenase-1

Hayley Duckles

Submitted in accordance with the requirements for the degree of Doctor of Philosophy.

The University of Leeds, Faculty of Medicine and Health, Leeds Institute of Genetics, Health, and Therapeutics, Division of Cardiovascular and Diabetes Research.

April 2013

Acknowledgements

First and foremost I would like to thank my supervisors for their excellent guidance and words of encouragement throughout my PhD. Thank you Professor Chris Peers for giving me the opportunity to pursue an interesting and challenging project within a friendly and accommodating research group, and for always having an open door. Thank you Dr Karen Porter for your support in both academic and non-academic matters. And Dr Jason Scragg, thank you for always being approachable and for offering advice whenever I doubted myself.

Many thanks to Dr John Boyle for imparting knowledge and for teaching me numerous skills. Additionally, thank you for spending countless hours at the microscope with me. I very much appreciate all your advice and help over the past three years. Also, thank you to David Myers, Phillip Warburton and Dr Nadira Yuldasheva for technical assistance.

To Tania, Kirsty, Jacob, and Emily, thank you for your friendship and advice, and for keeping my spirits up.

And to my family and friends, thank you for your continued love and support throughout this challenging period. Thank you for listening to many presentation rehearsals, for your encouragement, and for always being there. I would like to convey a special thank you to my wonderful sister Karen, this would not have been possible without you.

Finally, thank you to the British Heart Foundation for providing the funding for this project.

Abstract

Pathological proliferation of vascular smooth muscle cells (VSMC) is a central feature of vascular disorders such as atherosclerosis and restenosis. During such proliferative conditions the expression of the T-type Ca^{2+} channel is increased, providing an important route for Ca^{2+} entry. The inducible stress-response protein, heme oxygenase-1 (HO-1), is also up-regulated during vascular disorders. This enzyme confers cytoprotective effects via the breakdown of free heme to produce iron, biliverdin, and carbon monoxide (CO). CO has been shown to be anti-inflammatory, anti-apoptotic, and anti-proliferative at low concentrations. Furthermore, CO is emerging as a modulator of various ion channels, and our research group has recently found that CO inhibits the T-type Ca^{2+} current via whole-cell patch clamp recordings. Therefore, the aim of this thesis was to investigate whether the VSMC T-type Ca^{2+} channel could act as an anti-proliferative target for HO-1-derived CO.

HEK293 cells over-expressing the $Ca_v3.2$ T-type Ca^{2+} channel produced higher basal $[Ca^{2+}]_i$ and displayed an augmented proliferative response. $[Ca^{2+}]_i$ and proliferation were both reduced by T-type Ca^{2+} channel inhibition, CO exposure, and HO-1 induction. T-type Ca^{2+} channel inhibition and HO-1 induction reduced $[Ca^{2+}]_i$ and proliferation in the rat aortic VSMC line, A7r5. Exogenous CO exposure decreased $[Ca^{2+}]_i$ in A7r5 cells, but conferred insignificant anti-proliferative effects, which correlated to a relatively low expression of the T-type Ca^{2+} channel. T-type Ca^{2+} channel inhibition, CO exposure, and HO-1 induction all have anti-proliferative effects in human VSMCs, yet simultaneous HO-1 induction and T-type Ca^{2+} channel inhibition do not cause additive inhibitory effects on proliferation.

These data provide evidence that CO is anti-proliferative, and that CO potentially acts via the T-type Ca^{2+} channel. This pathway could be a novel therapeutic target for vascular disorders involving excessive smooth muscle cell proliferation.

Table of Contents

Tables

Figures

Chapter 1

Chapter 2

Chapter 3

Chapter 6

Abbreviations

A7r5	Rat aortic smooth muscle cell line
AM	Acetoxymethyl
β2M	β2-Microglobulin
BSA	Bovine Serum Albumin
CABG	Coronary Artery Bypass Graft
CAD	Coronary Artery Disease
CaMKII	Ca^{2+}/Calmodulin Protein Kinase II
COHb	Carboxyhemoglobin
CCE	Capacitative Ca^{2+} Entry
CICR	Ca^{2+}-Induced Ca^{2+}-Release
CO	Carbon Monoxide
CORM	Carbon Monoxide Releasing Molecule
I_{CRAC}	Ca^{2+} release activated Ca^{2+} current
DMEM	Dulbecco's Minimum Essential Medium
DTT	Dithiothreitol
EC	Endothelial Cells
ECL	Enhanced Chemiluminescence
eNOS	Endothelial Nitric Oxide Synthase
ERK1/2	Extracellular Signal-Regulated Kinase 1/2
FBS	Foetal Bovine Serum
FCS	Foetal Calf Serum
GAPDH	Glyceraldehyde Phosphate Dehydrogenase
GPCR	G Protein-Coupled Receptor

HCASMC	Human Coronary Artery Smooth Muscle Cells
HEK	Human Embryonic Kidney Cells
HIF	Hypoxia Inducible Factor
HMOX1	Heme Oxygenase 1 gene
HO-1/HO-2	Heme Oxygenase 1/2
HPRT1	Hypoxanthine Phosphoribosyltransferase 1
HRP	Horseradish Peroxidise
HSVSMC	Human Saphenous Vein Smooth Muscle Cells
iCORM-3	Inactivated CORM-3
IP_3R	Inositol Trisphosphate
iNOS	Inducible Nitric Oxide Synthase
LDL	Low Density Lipoprotein
MAPK	Mitogen Activated Protein Kinase
MEM	Minimum Essential Medium
MMP	Matrix Metalloproteinase
mPER	Mammalian Protein Extraction Reagent
mTOR	Mammalian Target of Rapamycin
NADPH	Nicotinamide Adenine Dinucleotide Phosphate
NFAT	Nuclear factor of activated T-cells
NGS	Normal goat serum
NO	Nitric Oxide
NOS	Nitric Oxide Synthase
oxLDL	oxidised-Low Density Lipoprotein
PDGF	Platelet Derived Growth Factor

PBS	Phosphate Buffered Saline
PIP_2	Phosphatidylinositol 4,5-bisphosphate
PKA	Protein Kinase A
PKC	Protein Kinase C
PLC	Phospholipase C
PMCA	Plasma Membrane Ca^{2+} ATPase
PPAR	Peroxisome Proliferator-Activated Receptor
RMP	Resting Membrane Potential
ROC	Receptor-Operated Channel
ROS	Reactive Oxygen Species
RT	Room Temperature
RTK	Receptor Tyrosine Kinase
RT-PCR	Real Time Polymerase Chain Reaction
r.u.	ratio units
RyR	Ryanodine Receptor
SERCA	Sarco/Endoplasmic Reticulum ATPase
sGC	Soluble Guanylyl Cyclase
SHR	Spontaneously Hypertensive Rat
shRNA	short hairpin RNA
SnPP	Tin Protoporphyrin
SOC	Store Operated Channel
SR	Sarcoplasmic Reticulum
TBS	Tris Buffered Saline
TBST	TBS Tween

TGF-β	Transforming Growth Factor-β
TRPC	Transient Receptor Potential Canonical channel
VSMC	Vascular Smooth Muscle Cells
WKY	Wistar Kyoto rat
WT	Wildtype
ZnPP	Zinc Protoporphyrin

CHAPTER 1

Introduction

This thesis reports the results of a series of studies designed to investigate whether the vascular smooth muscle T-type Ca^{2+} channel is an anti-proliferative target for heme oxygenase-1 (HO-1). The prominent features of cardiovascular disorders will be reviewed, including the roles of both vascular smooth muscle cells (VSMCs) and endothelial cells (ECs), in addition to the changes that occur in cellular proteins and Ca^{2+} homeostasis. The relationship of the T-type Ca^{2+} channel to cardiovascular disorders will also be reviewed in detail, as will the stress response protein HO-1, and the associated by-product, carbon monoxide (CO).

1.1 Disorders of Vascular Remodelling

Cardiovascular disease accounts for 47% of all European deaths, equating to over 4 million deaths each year (British Heart Foundation, 2012, resource code HS2012EC, http://www.bhf.org.uk/publications/view-publication.aspx?ps=1002098). Coronary heart disease and stroke are the main forms of cardiovascular disease and the most common cause of death in western societies (Lusis, 2000). Vascular smooth muscle cell (VSMC) proliferation is a central feature of cardiovascular disorders, therefore the elucidation of therapeutic targets to limit this pathological proliferation is imperative. The major cardiovascular diseases in which VSMC proliferation is an important factor are considered further.

Atherosclerosis

Atherosclerosis is a progressive, chronic inflammatory disease of large arteries (Lusis, 2000). Lipid-rich sub-endothelial lesions consist of necrotic debris and VSMCs covered by a fibrotic cap (Lusis, 2000). This complex disease involves numerous cell types, the accumulation of extracellular matrix, and the action of proteases and inflammatory mediators (Owens *et al.*, 2004). High circulating low density lipoprotein (LDL) levels are a primary factor in lesion formation, as they migrate into the sub-endothelial space where they are oxidised, forming oxidised LDL (oxLDL), and an inflammatory cascade ensues. Endothelial injury, in response to disturbed blood flow, for example, also

influences lesion formation and stimulates VSMC migration and proliferation (Lusis, 2000). Monocytes enter the sub-endothelial space where they differentiate into macrophages, and subsequently into foam cells as they imbibe lipids (Lusis, 2000). Activated macrophages release inflammatory mediators and growth factors that stimulate VSMC migration and proliferation. VSMCs secrete extracellular matrix which contributes to vessel occlusion (Rzucidlo *et al.*, 2007). In response to oxLDL, synthetic VSMCs form a fibrous cap which overlays the atherosclerotic plaque. Matrix metalloproteinases (MMPs) are endopeptidases produced by VSMCs and macrophages. MMPs are involved in extracellular matrix degradation and remodelling, which can lead to plaque instability (Galis *et al.*, 1994). Extracellular matrix proteins are degraded prior to VSMC migration (Galis *et al.*, 1994), and elevated MMP levels have been linked to neointimal hyperplasia (Porter *et al.*, 1999). Simvastatin has been shown to reduce neointimal hyperplasia in organ-cultured human VSMCs, in addition to limiting MMP activity and VSMC proliferation (Porter *et al.*, 2002). Plaque rupture and subsequent thrombosis can lead to stroke or myocardial infarction (Lusis, 2000), therefore the inhibition of excessive VSMC proliferation may have beneficial effects on vessel morbidity by limiting the progression of atherosclerosis.

Hypertension

Hypertension results from increased vascular resistance and causes structural changes within the vessel wall. This process is termed eutrophic remodelling and involves narrowing of the vessel lumen via increased vessel wall thickness (Sonoyama *et al.*, 2007). Hypertrophic remodelling can ensue upon increased wall stress, which also modulates collagen distribution, producing a less compliant vessel wall. This adaptive response to increased vessel wall stress involves the growth of VSMCs (Owens, 1989;Mulvany, 1993). Hypertension causes increased contractility, increased VSMC proliferation and vascular remodelling. Both systemic and pulmonary hypertension are linked to VSMC proliferation and altered Ca^{2+} handling (Firth *et al.*, 2007). Up-regulation of Transient Receptor Potential Canonical (TRPC) channels has been associated with increased Ca^{2+} influx and the development of hypertension (Firth *et al.*, 2007). Using cerebral arterial smooth muscle from a rat model of salt-sensitive hypertension, higher basal $[Ca^{2+}]_i$ was found in addition to a more depolarised resting membrane potential (Wellman *et al.*, 2001). Reduced function of K_v channels together with an increase in $[Ca^{2+}]_i$ via voltage-dependent Ca^{2+} channel activity stimulated activation of the cAMP response element binding protein transcription factor and the immediate early gene c-fos, thereby linking altered Ca^{2+} handling to gene expression in

hypertension (Wellman *et al.*, 2001). Furthermore, the transcription factor c-fos has been identified as an important signalling component in pathological VSMC proliferation (Sylvester *et al.*, 1998), which is linked to cyclin A transcription and cell cycle progression (Wei *et al.*, 1997).

T-type Ca^{2+} channels have been linked to hypertension. The inhibition of both L- and T-type Ca^{2+} channels was shown to confer anti-hypertensive effects in systemic and renal circulation (Nakamura *et al.*, 1999). Indeed, both L-type and T-type Ca^{2+} channels are expressed in afferent vessels, whereas efferent vessels appear to express T-type Ca^{2+} channels only, as reviewed by Cribbs (2006). Blockade of T-type Ca^{2+} channels was demonstrated to cause vasodilation of both afferent and efferent arterioles of Sprague-Dawley rats via *in vitro* perfusion (Feng *et al.*, 2004). Furthermore, T-type Ca^{2+} channel inhibition has been linked to positive effects on the renin-angiotensin-aldosterone system, VSMC proliferation, and extracellular matrix deposition (Buhler, 1997). Given that adequate $[Ca^{2+}]_i$ levels are required for the progression of the cell cycle (Ciapa *et al.*, 1994), the increased Ca^{2+} influx via voltage-dependent Ca^{2+} channels may facilitate the enhanced gene expression, VSMC replication, and extracellular matrix remodelling of proliferative disorders such as hypertension.

Restenosis

Intimal hyperplasia occurs in response to vessel wall injury and endothelial damage as a result of stenting (Rzucidlo *et al.*, 2007). Excessive amounts of extracellular matrix are produced by proliferating VSMCs, which causes hyperplastic lesions and restenosis (Rzucidlo *et al.*, 2007). VSMC proliferation in response to stenting appears as an early event immediately post-stent insertion to repair the damaged endothelium, but this process can also continue and subsequently cause restenosis in order to shield the stent from thrombogenic blood constituents (Curcio *et al.*, 2011). By blocking the mitogen-activated protein kinase (MAPK) and cAMP- protein kinase A (PKA) cell signalling pathways involved in VSMCs, studies have shown that the inhibition of VSMC proliferation in order to limit restenosis is a promising therapeutic strategy, as reviewed by Curcio *et al.* (2011). Indeed, the exposure of the compromised vessel to anti-proliferative compounds via drug-eluting stents initially demonstrated advantageous effects on intimal hyperplasia (Curcio *et al.*, 2011). Rapamycin inhibits mTOR (mammalian target of rapamycin) which mediates environmental cues and, in-turn, regulates cell proliferation (Sarbassov *et al.*, 2005). This immunosuppressant has

been shown to inhibit VSMC migration and proliferation *in vitro* and *in vivo* (Marx et al., 1995;Poon et al., 1996), and promote VSMC differentiation (Martin *et al.*, 2004). Additionally, rapamycin drug-eluting stents have been shown to limit restenosis (Eisenberg & Konnyu, 2006). However, follow-up studies demonstrated the need for both anti-proliferative and anti-inflammatory drug-eluting stents.

Evidently numerous factors or interventions can cause vessel injury. The disruption of vascular integrity begins with damage to the endothelium, vascular remodelling then follows which involves VSMC proliferation, apoptosis, and the production of extracellular matrix proteins such as collagen, elastin and fibronectin (McCarthy & Bennett, 2000). Apoptosis of VSMCs can play a dual role in vascular remodelling by limiting intimal hyperplasia and reducing vessel occlusion, yet conversely VSMC apoptosis can contribute to atherosclerotic plaque rupture and thrombosis (McCarthy & Bennett, 2000). Vascular remodelling has been described as both the cause and consequence of ensuing pathology, as the inherent plasticity of VSMCs is a pre-disposing factor for proliferative disorders (Owens *et al.*, 2004). The roles of the endothelium and the plasticity of VSMC in vascular remodelling are discussed further below.

1.2 The response to vascular injury

1.2.1 The role of the endothelium

Endothelial cells (ECs) form a continuous non-thrombogenic layer that mediates metabolic exchange through the arterial wall. A healthy endothelium co-ordinates vascular tone by the secretion of vasoactive agents, and plays a role in coagulation and inflammation (Widlansky *et al.*, 2003). However, endothelial injury increases the risk of a cardiovascular event, as reviewed by Widlansky *et al.* (2003). Injury can occur as a result of denudation, inflammation, oxidative stress, hyperglycaemia or elevated levels of free fatty acids (Atochin & Huang, 2010).

ECs are an important source of nitric oxide (NO) which acts as a positive regulator of vascular function (Atochin & Huang, 2010). NO is principally a vasodilator of VSMC, although this signalling molecule also limits VSMC proliferation and inhibits platelet aggregation. A reduction in the bioavailability of NO can induce endothelial dysfunction

(Higashi *et al.*, 2009). Oxidative stress is a prominent feature in the pathogenesis of cardiovascular diseases such as hypertension, dyslipidemia, diabetes mellitus, atherosclerosis, and myocardial infarction. Reactive oxygen species (ROS) arise from numerous sources including nicotinamide adenine dinucleotide phosphate (NADPH) oxidase, xanthine oxidase, uncoupled endothelial nitric oxide synthase (eNOS), cyclooxygenase, and the mitochondrial electron transport chain (Higashi *et al.*, 2009). ROS can inactivate NO by forming toxic peroxynitrite, thereby inducing endothelial dysfunction (Higashi *et al.*, 2009). ROS can be produced in VSMCs, ECs, and mononuclear cells, and the associated effects include lipid and protein oxidation, increased $[Ca^{2+}]_i$ load, and DNA fragmentation (Higashi *et al.*, 2009). Upon injury to the endothelium, EC located at the periphery of a wound are able to migrate and proliferate, whilst also remaining attached to neighbouring ECs. However, ECs located at sites distal to the wound are unable to participate in injury repair (Ross, 1981), and so the reparative capacity of the endothelium is limited. ECs are able to influence VSMC growth and migration by the secretion of growth factors, and it is this response by VSMCs that is central, not only to repair after injury, but to proliferative disorders of the vasculature.

1.2.2 Vascular smooth muscle cells and phenotypic switching

VSMCs are situated in the medial layer of the blood vessel wall, and are responsible for maintaining basal vascular tone. They respond to chemical, mechanical, and electrical signals, and thereby regulate systemic blood pressure (Cribbs, 2006). VSMCs are highly proliferative during vasculogenesis and development, before differentiating into contractile VSMCs in mature vessels (Owens *et al.*, 2004). In healthy blood vessels VSMCs contain cytoskeletal proteins and ion channels specific to their contractile function, and exhibit low proliferative activity (Rzucidlo *et al.*, 2007). Mature, contractile VSMCs retain the ability to de-differentiate in response to environmental cues in order to adapt to cellular stresses (Owens, 1995). This response to vessel injury is central to the repair and restoration of vascular function, yet excessive proliferation is associated with cardiovascular disorders such as restenosis, atherosclerosis and hypertension (House *et al.*, 2008).

During the early stages of primary culture, VSMCs can be maintained in the contractile state by seeding at a high cell density, or by supplying endothelial growth factors (Ross, 1981). As VSMCs lose myosin and the ability to contract, they are able to

respond to mitogens and subsequently switch to a synthetic state (Ross, 1981). Synthetic VSMCs play a prominent role in the response to injury, according to the hypothesis proposed by Ross (1981); injury to the endothelial lining of blood vessels as a result of mechanical, chemical or immunological insult leads to the activation of platelets and monocytes. The subsequent release of growth factors and chemoattractant molecules, such as platelet derived growth factor (PDGF), stimulate medial VSMCs to migrate into the intima where they proliferate. Indeed, endothelial injury is the underlying factor that recruits VSMCs to neointima formation (Schwartz *et al.*, 1986). Upon repair of the endothelium, VSMCs of the neointima switch back to a contractile state and exhibit prominent myofilaments, with a concurrent loss of synthetic organelles (Clowes *et al.*, 1983). Differentiated VSMCs of the adult aorta predominantly express smooth muscle α-actin, which, in addition to smooth muscle myosin heavy chain, is a marker of contractile VSMCs (Kocher *et al.*, 1985). The expression of these proteins decreases upon de-differentiation along with a simultaneous increase in abundance of the Golgi network and the endoplasmic reticulum, demonstrating two distinct phenotypes (Chamley-Campbell *et al.*, 1981). *In vitro* studies have shown that VSMCs plated at a high density can revert back to a contractile state upon confluence, although VSMCs plated at a low density remain in a synthetic state (Chamley-Campbell *et al.*, 1981). Using a rabbit model of aortic balloon injury, Louis *et al.* (2006) demonstrated that contractile VSMC markers declined and de-differentiation markers appeared at 2 days post injury. These changes appeared in all medial VSMCs, whereas inflammatory markers were isolated to VSMCs near to the site of injury (Louis *et al.*, 2006). This implies that VSMCs are activated and de-differentiate in a timely manner in response to endothelial injury.

The phenotype of VSMC is also modulated by growth factors. ECs have been demonstrated to maintain VSMCs in a differentiated state *in vitro,* and co-culture of VSMCs with ECs limited activation of transforming growth factor-β1 (TGF-β1), thereby preventing VSMC growth (Powell *et al.*, 1996). TGF-β was shown to mediate VSMC differentiation in culture conditions by increasing smooth muscle α-actin and smooth muscle myosin heavy chain (Owens *et al.*, 1988). Conversely, in balloon injury models, TGF-β has been shown to increase neointima formation, matrix deposition and VSMC proliferation (Schulick *et al.*, 1998). PDGF release from platelets was also demonstrated to be a requirement for VSMC proliferation after balloon injury (Ross, 1981). PDGF appears to mediate the down-regulation of contractile VSMC markers *in vitro* (Blank & Owens, 1990), and mediate VSMC migration and proliferation *in vivo*

(Ferns *et al.*, 1991). The down-regulation of VSMC markers reported by Blank and Owens (1990) in response to PDGF treatment was associated with only a temporary increase in VSMC growth, and the VSMC markers remained down-regulated during PDGF stimulation, leading the authors to conclude that the effects on VSMC markers are not secondary to proliferation. Consistent with this finding, a previous study also demonstrated that cell cycle withdrawal is not a pre-requisite for the up-regulation of contractile proteins in confluent VSMCs (Blank *et al.*, 1988). The transition between the contractile and synthetic states of VSMCs appears complex, and the resulting changes occur in response to both environmental stimuli and active control (Owens *et al.*, 2004). Another key feature of the phenotypic switch of VSMCs, which is central to the studies reported in this thesis, is the modulation of calcium signalling.

1.2.3 Modulation of Ca^{2+} signalling during the phenotypic switch

Ca^{2+} is an important second messenger that mediates VSMC contraction, migration, proliferation and gene expression. VSMC contraction is slow and sustained, and occurs in response to membrane depolarisation, or by the binding of contractile agonists, which produces an increase in cytoplasmic Ca^{2+} (House *et al.*, 2008). Cytoplasmic Ca^{2+} activates Ca^{2+}/calmodulin-dependent myosin light chain kinase; myosin light chain is subsequently phosphorylated and interacts with actin myofilaments (Webb, 2003). Cytoplasmic Ca^{2+} is increased further by Ca^{2+}-induced Ca^{2+}-release (CICR) via ryanodine receptor (RyR) activation leading to Ca^{2+} release from the sarcoplasmic reticulum (SR), and receptor-operated channel (ROC) activation at the plasma membrane leading to further Ca^{2+} influx (Webb, 2003). VSMC relaxation occurs via Ca^{2+} extrusion from the cytoplasm and an increase in myosin light chain phosphatase activity. Cytoplasmic Ca^{2+} is decreased via Ca^{2+} extrusion by both the plasma membrane Ca^{2+} ATP-ase (PMCA) and the Na^{+}/Ca^{2+} exchanger, and reuptake by the sarco/endoplasmic reticulum ATPase (SERCA). In addition, L-type Ca^{2+} channels and ROC are inactivated (Webb, 2003). Cell proliferation depends on a sustained and adequate $[Ca^{2+}]_i$ level which is sourced from intracellular stores and extracellular milieu (Kao *et al.*, 1990;Sheng *et al.*, 1990;Chao *et al.*, 1992;Negulescu *et al.*, 1994;Pratt *et al.*, 2002). Numerous Ca^{2+} signalling pathways are modulated during the phenotypic switch of VSMCs in order to provide adequate $[Ca^{2+}]_i$ levels, and these are outlined below.

Voltage-dependent L-type Ca^{2+} channels are characterised by their high voltage-activated currents, large single channel conductance, and slow voltage dependent inactivation (Catterall, 2000). L-type Ca^{2+} channels provide the dominant route of Ca^{2+} entry in muscle cells, and are highly expressed in contractile VSMCs (Catterall, 2000). These channels are essential for controlling blood pressure, and L-type antagonists are commonly used anti-hypertensive agents (Cribbs, 2006). Using rat aortic VSMCs, L-type Ca^{2+} channel expression was shown to decrease during de-differentiation, which correlated with a lower expression of the contractile VSMC markers, α-actin and myosin heavy chain, in addition to smaller L-type Ca^{2+} currents (Gollasch *et al.*, 1998). The mechanisms underlying L-type Ca^{2+} channel suppression involve mitogenic transcriptional down-regulation, and MAPK-mediated post-transcriptional down-regulation (Ihara *et al.*, 2002). This study used primary rat aortic VSMCs and demonstrated that L-type Ca^{2+} channels were re-expressed by contact inhibition of the cells. Conversely, voltage-dependent T-type Ca^{2+} channels have been shown to be up-regulated during VSMC de-differentiation, and therefore may have a role in augmenting a proliferative response (Kuga *et al.*, 1996;Vallot *et al.*, 2000). T-type Ca^{2+} channels convey small single channel conductance, are inactivated rapidly, and are characterised by activation at more negative membrane potentials than L-type Ca^{2+} channels (Cribbs, 2006). Consequently there is a strong case for the role of T-type Ca^{2+} channels in VSMC proliferation given that de-differentiated VSMCs have a more negative resting membrane potential (RMP), (McDonald *et al.*, 1994;Gollasch *et al.*, 1998). The role of the T-type Ca^{2+} channel, which is a major focus of this thesis, will be discussed in section 1.3.

TRPC channels have also been shown to be up-regulated in proliferative VSMCs. TRPC channels are non-selective cation channels, inactivated by membrane depolarisation, and are often active at RMP allowing Ca^{2+} influx at negative membrane potentials (Nilius *et al.*, 2007). Furthermore, TRPC channels have been demonstrated to constitute store operated channels (SOCs) and ROCs, and therefore mediate capacitative Ca^{2+} entry (CCE) (Golovina, 1999;Nilius *et al.*, 2007;House *et al.*, 2008). SOCs are activated by Ca^{2+} store depletion and function to sustain Ca^{2+} influx. Therefore, SOCs have been indicated to play a role in proliferation and gene expression (Albert & Large, 2003). ROCs mediate Ca^{2+} influx in response to agonist activation, although both SOCs and ROCs function downstream of phospholipase C (PLC) (Gonzalez-Cobos & Trebak, 2010). TRPC1 and TRPC6 appear to have

important roles in VSMCs as they are expressed throughout the vasculature (Firth *et al.*, 2007);

TRPC1

This TRPC channel has been correlated with SOC activity in both human and rat pulmonary artery VSMCs (Remillard & Yuan, 2006). TRPC1 is involved in VSMC contraction and proliferation in numerous vascular beds and species by mediating store-operated Ca^{2+} entry (Gonzalez-Cobos & Trebak, 2010). The Ca^{2+} release activated Ca^{2+} current (I_{CRAC}) provided by SOCs has been linked to the migratory and proliferative capacity of VSMCs, and TRPC channels appear to have a significant role in the phenotypic switch (Golovina, 1999;Bergdahl *et al.*, 2005;Potier *et al.*, 2009). De-differentiated human pulmonary artery VSMCs were shown to have higher basal $[Ca^{2+}]_i$ and increased TRPC1 mRNA, suggesting that TRPC channels are involved in sustaining adequate $[Ca^{2+}]_i$ for cell proliferation (Golovina, 1999;Golovina *et al.*, 2001). Store-operated Ca^{2+} entry via TRPC1 also contributes to the maintenance of $[Ca^{2+}]_i$ for neointimal hyperplasia in human organ culture (Kumar *et al.*, 2006), and in hypertension (Firth *et al.*, 2007).

TRPC3/6/7

This subfamily are activated by diacylglycerol in a protein kinase C (PKC)-dependent manner and are therefore considered to form ROCs (Gonzalez-Cobos & Trebak, 2010). Up-regulation of TRPC6 expression correlates with greater Ca^{2+} entry upon store depletion, and CCE via TRPC6 is enhanced during proliferative phases of VSMCs, as reviewed by Gonzalez-Cobos and Trebak (2010). TRPC6 expression was shown to be higher in mesenteric arterioles of salt-hypertensive rats, and high levels of TRPC6 were demonstrated in rat pulmonary artery VSMCs in a model of hypoxic pulmonary hypertension, implying this channel plays a role in vascular remodelling of hypertension, as reviewed by Gonzalez-Cobos and Trebak (2010).

K_{Ca} channels are K^+ channels activated in response to increases in $[Ca^{2+}]_i$ which occur as a result of cell depolarisation, and serve to induce hyperpolarisation (House *et al.*, 2008). $K_{Ca}1.1$ expression is characteristic of differentiated VSMCs, and limits Ca^{2+} influx via L-type Ca^{2+} channels by cell hyperpolarisation. This channel displays voltage-dependent activation, which also occurs in response to high $[Ca^{2+}]_i$ (Neylon *et al.*, 1999;Wei *et al.*, 2005). $K_{Ca}3.1$ channels are expressed in de-differentiated VSMCs, are voltage insensitive, and are activated in response to low levels of $[Ca^{2+}]_i$ (Wei *et al.*, 2005). Down-regulation of $K_{Ca}1.1$, along with the concomitant increase in $K_{Ca}3.1$

channel expression is apparent in cultured VSMCs, and in VSMCs *in vivo* post balloon injury (Neylon *et al.*, 1999;Kohler *et al.*, 2003;Ledoux *et al.*, 2006). These altered expression levels increase the driving force for Ca^{2+} influx, therefore maintaining $[Ca^{2+}]_i$ for proliferation. The major Ca^{2+} entry pathways in de-differentiated VSMCs are illustrated in Figure 1.1.

Ca^{2+}-release channels and re-uptake pumps are also modulated during the phenotypic switch. The ryanodine receptor, RyR3, on the SR is down-regulated in de-differentiated VSMCs, which hampers CICR that is important for VSMC contraction (House *et al.*, 2008). More recently, RyR agonists were shown to induce Ca^{2+} release in freshly dissociated rat aortic VSMCs, whereas Ca^{2+} release was not stimulated in cultured cells (Kim *et al.*, 2011a). Inositol trisphosphate receptor (IP_3R) down-regulation is another feature of the phenotypic switch, and is apparent in VSMCs exposed to oxLDL, and in VSMCs of animal models of diabetes (Narayanan *et al.*, 2012). SERCA2a is down-regulated in de-differentiated VSMCs, but re-expressed when cells reach confluence, indicating the importance of sustaining $[Ca^{2+}]_i$ in proliferating cells (Lipskaia *et al.*, 2009). Indeed, gene transfer of SERCA2a limited neointima formation in the injured rat carotid artery, and VSMCs demonstrated cell cycle arrest at G_1 (Lipskaia *et al.*, 2005). The inhibition of VSMC proliferation in response to SERCA2a up-regulation was mediated by inactivation of calcineurin and nuclear factor of activated T-cells (NFAT). This study also demonstrated a marked decrease in the amplitude and the propagation of IP_3 stimulated Ca^{2+} signals. However, contrasting data have been generated regarding the effects of PMCA modulation on cell proliferation, indicating that spatial Ca^{2+} arrangements and microdomains may play a role in the physiological response of the VSMC, as reviewed by (House *et al.*, 2008).

NFAT is a Ca^{2+} dependent transcription factor involved in the proliferative response of VSMCs (Hill-Eubanks *et al.*, 2003). Sustained increases of $[Ca^{2+}]_i$ activate calcineurin which dephosphorylates NFAT, promoting activation and nuclear translocation (Hill-Eubanks *et al.*, 2003). The calcineurin/NFAT pathway is implicated as the major VSMC transcription pathway, and sustained rises in $[Ca^{2+}]_i$ have been associated with NFAT stimulation and subsequent VSMC proliferation and remodelling (Lipskaia *et al.*, 2009). Balloon injury of the carotid artery stimulated NFAT expression, and pharmacological inhibition of NFAT limited neointimal hyperplasia (Liu *et al.*, 2005). The vasoactive agonists, angiotensin II (Gomez *et al.*, 2002), PDGF (Liu *et al.*, 2004), and LDL

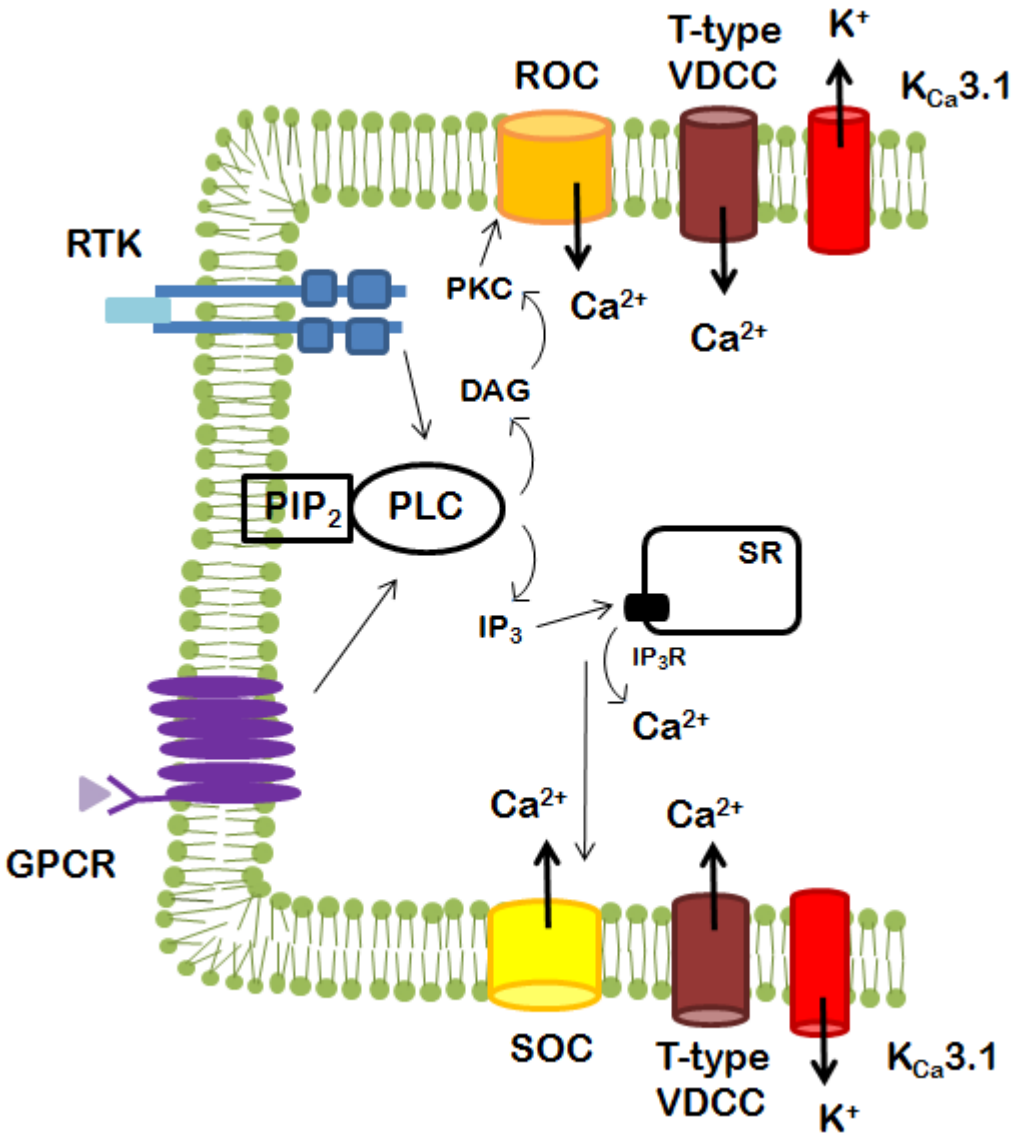

Figure 1.1 Ca^{2+} entry pathways in de-differentiated VSMCs

$[Ca^{2+}]_i$ is sustained in de-differentiated VSMCs for gene expression and proliferation by modulation of numerous ion channels. TRPC channels in the form of both SOC and ROC channels are up-regulated. These channels are active at RMP and can be stimulated by G protein-coupled receptor (GPCR) or Receptor Tyrosine Kinase (RTK)-mediated production of PLC. T-type Ca^{2+} channels are also up-regulated, which are active at negative membrane potentials, and allow Ca^{2+} influx via their window current at RMP. Increased K^+ efflux via $K_{Ca}3.1$ channels leads to hyperpolarisation and a greater driving force for Ca^{2+} entry. PIP_2 = phosphatidylinositol 4,5-bisphosphate. Image adapted from Remillard & Yuan (2006).

(Lipskaia *et al.*, 2003), all stimulate NFAT activation and subsequent VSMC proliferation. Different splice variants of Ca^{2+}/calmodulin protein kinase II (CaMKII) mediate Ca^{2+} signalling in the differentiated and de-differentiated VSMC phenotypes; CaMKIIγ is prominently expressed in differentiated VSMCs, whereas CaMKIIδ_2 is prominently expressed in de-differentiated VSMCs (House *et al.*, 2007). The altered expression of the splice variant occurred within 30 hours of rat aortic VSMC culture, and CaMKIIδ_2 suppression halted cell cycle progression. Comparable results were seen *in vivo* after balloon angioplasty; CaMKIIγ was the dominant variant in medial VSMCs, and CaMKIIδ_2 was expressed in neointimal VSMCs (House & Singer, 2008).

Evidently a wide variety of modulations in Ca^{2+} handling occur during the phenotypic switch of VSMCs. Modulation of voltage-dependent Ca^{2+} channels, $K_{Ca}3.1$, and SOCs mediate an increase in $[Ca^{2+}]_i$, which is required for cell proliferation and cell cycle checkpoints (Golovina, 1999;House *et al.*, 2008). The processes mediating the phenotypic switch appear highly complex and involve numerous pathways. It is likely that the duration and amplitude of the Ca^{2+} signals determines the physiological response of the VSMCs (Munaron *et al.*, 2004). Moreover, a recent report implies that nanojunctions between the plasma membrane and the SR are responsible for deciphering local Ca^{2+} signals to produce specific functional responses such as contraction, relaxation, or proliferation (van *et al.*, 2013). Therapeutic targeting of the pathways involved in maintaining $[Ca^{2+}]_i$ for proliferation and gene expression may assist the treatment of disorders involving vascular remodelling. This thesis focuses on one particular Ca^{2+} entry pathway, the T-type Ca^{2+} channel. As described previously, the up-regulation of T-type Ca^{2+} channels appears to be a prominent feature in the phenotypic switch of VSMCs. Therefore, this channel may provide a potential therapeutic target within cardiovascular disease.

1.3 T-type Ca^{2+} channels

1.3.1 Properties of T-type Ca^{2+} channels

T-type Ca^{2+} channels are activated upon membrane depolarisation and provide a route for Ca^{2+} influx, which is fundamentally linked to numerous cellular physiological effects (Catterall *et al.*, 2005). There are three T-type Ca^{2+} channel subtypes; $Ca_v3.1$, $Ca_v3.2$, and $Ca_v3.3$, and they are expressed in a range of cell types. All three subtypes are found in neuronal cell bodies and dendrites, and $Ca_v3.1$ and $Ca_v3.2$ are also found in

cardiac and smooth muscle, with $Ca_v3.2$ displaying the widest expression level (Catterall *et al.*, 2005). T-type Ca^{2+} channels are termed low-voltage activated as they open in response to weak depolarisations at low voltages. They play a role in intracellular Ca^{2+} oscillations, repetitive firing and pacemaker potentials (Perez-Reyes, 2003). T-type Ca^{2+} currents have the following characteristics:

- Transient currents due to fast inactivation at strong depolarisations
- Tiny single channel conductance (in comparison to L-types Ca^{2+} channels)
- Slow channel deactivation (closing), producing tail currents
- Voltage dependence of steady state inactivation overlaps significantly with voltage dependence of activation, giving rise to a window current

T-type Ca^{2+} channel activity has been studied in numerous cell types including neurons, cardiomyocytes and fibroblasts, which has subsequently allowed the transitions between open and closed states to be defined, as reviewed by Perez-Reyes (2003). Upon depolarisation, T-type Ca^{2+} channels exhibit burst firing by opening and closing rapidly, then they begin to inactivate as membrane depolarisation continues. The channels may be inactive for some time before recovering to a deactivated state. This model contains further complexity as T-type Ca^{2+} channels are also capable of deactivating immediately from their open state, without inactivation, and different sub-types display different kinetics. An important feature of T-type Ca^{2+} channels is the associated window current that is active at physiologically relevant membrane potentials. This window current is produced under basal conditions and is due to the overlap of activation and inactivation curves (Perez-Reyes, 2003), as illustrated in Figure 1.2. Consequently, Ca^{2+} is constantly able to enter the cell via a proportion of T-type Ca^{2+} channels that are active and not fully inactivated, therefore influencing $[Ca^{2+}]_i$ levels at RMP (Capiod, 2011). Indeed, the over-expression of T-type Ca^{2+} channels was shown to increase basal $[Ca^{2+}]_{i,}$ which could be reduced by the T-type antagonists, mibefradil and Ni^{2+} (Chemin *et al.*, 2000). In numerous cell types the window current is active at -65 to -40mV, which acts as a driving force for Ca^{2+} entry (Lory *et al.*, 2006), and has been demonstrated to be an important contributor to vascular tone in mesenteric and renal arterioles (Bijlenga *et al.*, 2000). L-type Ca^{2+} channels also display a window current, although it is not active at RMP (Capiod, 2011).

Voltage-dependent Ca^{2+} channels are composed of up to five subunits. The auxiliary β-subunit is essential for L-type Ca^{2+} channel expression at the cell membrane, in

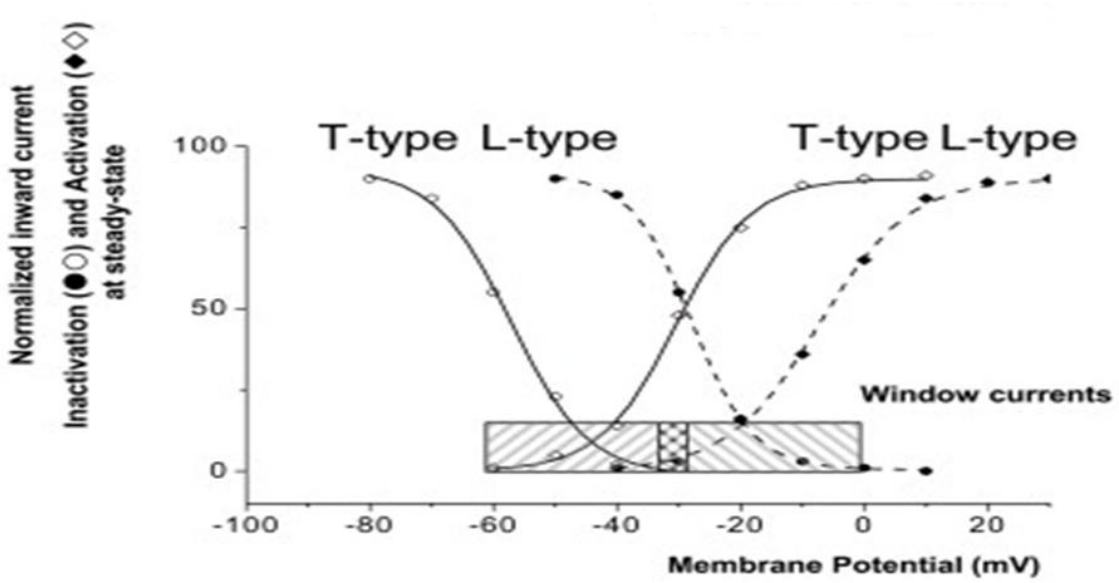

Figure 1.2 Window currents of T-type and L-type Ca^{2+} channels

The window currents of voltage-gated Ca^{2+} channels are a result of the overlap between the activation and inactivation curves at steady state. The window current of T-type Ca^{2+} channels has an important role in Ca^{2+} homeostasis. Ca^{2+} is able to flow continuously into the cell via T-type Ca^{2+} channels that are partially active, thereby contributing to sustained $[Ca^{2+}]_i$ at RMP. The L-type Ca^{2+} channel window current is active at more depolarised membrane potentials, and therefore, does not contribute to Ca^{2+} homeostasis at RMP. Image taken from Capiod (2011).

addition to the voltage dependence of the channel (Perez-Reyes, 2003). However, it appears T-type Ca^{2+} channels are capable of functioning without auxiliary subunits, as recombinant channels have comparable electrophysiological properties to native T-type currents (Perez-Reyes, 2003). Despite this, co-expression with the α2-δ auxiliary subunit was shown to increase membrane expression of the channel (Dolphin *et al.*, 1999). The α_1 subunit acts as the conduction pore and has four domains, each with six transmembrane segments, and confers voltage sensitivity, in addition to gating apparatus (Catterall *et al.*, 2005). Figure 1.3 illustrates the structure of the T-type Ca^{2+} channel α_1 subunit. The cloning of rat and human isoforms of the T-type Ca^{2+} channels by the Perez-Reyes group (Perez-Reyes *et al.*, 1998), has allowed for the over-expression of recombinant channels in various cell models in order to assess further the properties of these currents (Perez-Reyes, 1998). Indeed, the stable over-expression of $Ca_v3.1$ or $Ca_v3.2$ in HEK293 cells was shown to augment a proliferative response, with more cells in the S phase of the cell cycle (Wang *et al.*, 2002a;Wang *et al.*, 2002b;Gray *et al.*, 2004). Indeed, Gray *et al.* (2004) demonstrated that a direct, non-linear relationship existed between Ca^{2+} entry and HEK293/$Ca_v3.2$ cell proliferation.

1.3.2 Modulation of T-type Ca^{2+} channels

Mibefradil was introduced as an anti-hypertensive agent in 1997, but withdrawn the following year due to adverse interactions with β-blockers (Mullins *et al.*, 1998). However, the drug has subsequently been used as an experimental tool to inhibit T-type Ca^{2+} channels. First described as Ro 40-5967; a selective T-type Ca^{2+} channel antagonist found to inhibit T-type Ca^{2+} currents after dihyropyridine abolition of L-type Ca^{2+} currents in rat VSMCs (Mishra & Hermsmeyer, 1994). Subsequent investigations have described the actions of mibefradil to be less specific. Mibefradil can inhibit Ca^{2+} activated Cl^- channels with a K_i of 4.7μM (Nilius *et al.*, 1997), voltage gated Na^+ channels with an IC_{50} of 0.98μM (Strege *et al.*, 2005), and L-type Ca^{2+} channels with an IC_{50} of 13μM (Martin *et al.*, 2000). Although, the concentration required to inhibit L-Type Ca^{2+} channels has been stated to be at least 10-fold higher than that for T-type Ca^{2+} channels (Bezprozvanny & Tsien, 1995;Martin *et al.*, 2000). Ni^{2+} has also been demonstrated as a selective T-type channel inhibitor, with varying affinities for the different channel subtypes, and the $Ca_v3.2$ subtype exhibiting the highest sensitivity (Lee *et al.*, 1999).

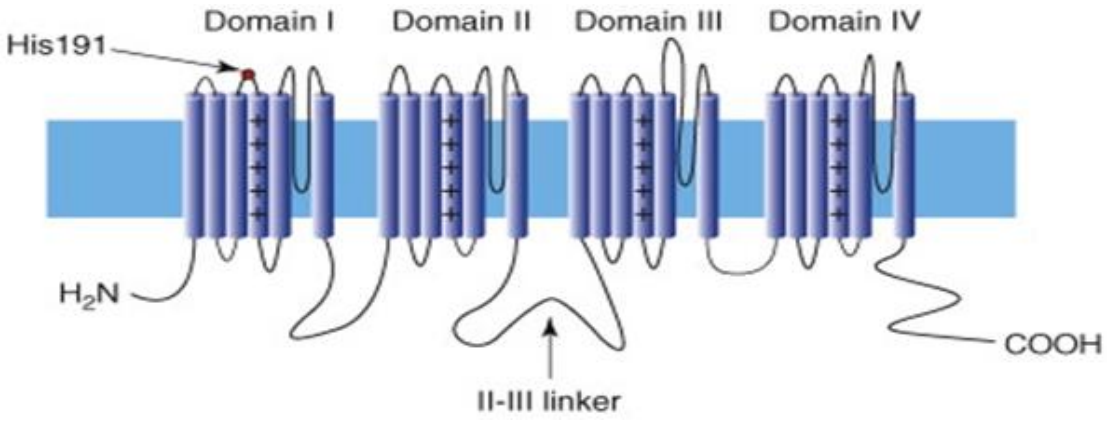

Figure 1.3 Transmembrane structure of the T-type Ca^{2+} channel α_1 subunit

The α_1 subunits of voltage-gated Ca^{2+} channels comprise of four homologous domains (I to IV), each with six transmembrane spanning helices (S1 to S6). The S4 helix of each domain contains positive amino acids, which constitutes the voltage sensor of the channel. The II-III linker is the site of action by numerous pathways, including PKA, PKC, Rho kinase, and CaMKII. The extracellular His191 residue is the site of redox modulation by Zn^{2+}, ascorbate, and L-cysteine. Image taken from Iftinca and Zamponi (2009).

T-type Ca^{2+} channels contain numerous phosphorylation consensus sites for modulation by protein kinases (Iftinca & Zamponi, 2009). Serine/threonine kinases (PKA and PKC), calmodulin dependent kinases and RTKs have all been shown to modulate T-type Ca^{2+} channel activity, and the II-III loop of Ca_v3 channels appears to be an important site of regulation, as reviewed by Iftinca and Zamponi (2009). Numerous hormones have been demonstrated to inhibit or stimulate T-type Ca^{2+} currents in neurons (Perez-Reyes, 2003). Endothelin has been shown to stimulate smooth muscle and cardiac muscle T-type Ca^{2+} currents (Perez-Reyes, 2003). Lysophosphatidic acid inhibits T-types Ca^{2+} channels via Rho kinase activation, and Rho kinase inhibitors have been shown to limit seizures, suggesting a role for this pathway in epilepsy (Iftinca & Zamponi, 2009). The reducing agent L-cysteine can increase T-type Ca^{2+} currents in nociceptive and thalamic neurons, and the oxidising agent ascorbate inhibited $Ca_v3.2$ Ca^{2+} channels (Huc *et al.*, 2009). This redox modulation of $Ca_v3.2$ Ca^{2+} channels was mediated via the extracellular His191 residue. Zn^{2+} selectively blocks $Ca_v3.2$ channels, but in contrast can slow the deactivation kinetics of $Ca_v3.3$ (Huc *et al.*, 2009). Considering the wide range of endogenous and exogenous modulators of Type Ca^{2+} channels, there is scope for therapeutic intervention of the numerous functions that these channels are involved in, and these functions are discussed in detail below.

1.3.3 Physiological Functions of T-type Ca^{2+} channels

T-type Ca^{2+} channels are prevalent throughout the body including VSMCs, the heart, nerves, sperm, and endocrine organs. In these tissues the channels are involved in proliferation, gene expression, VSMC contraction, vascular tone, fertilisation, hormone secretion, neuronal firing, nociception, cancer growth, and epilepsy (Perez-Reyes, 2003). These channels enhance membrane depolarisation in excitable cells and mediate Ca^{2+} influx in non-excitable cells (Nilius *et al.*, 2006).

Oxygen sensing

Hypoxia has been shown to enhance T-type Ca^{2+} channel gene expression via a hypoxia inducible factor (HIF) -dependent signalling pathway (del Toro *et al.*, 2003). T-type Ca^{2+} channel mRNA, in addition to Ca^{2+} currents, were increased in response to hypoxia in rat pheochromocytoma (PC12) cells (del Toro *et al.*, 2003). This enhanced T-type activity occurred via HIF, which is reinforced by the presence of hypoxia responsive elements in the $Ca_v3.2$ gene, and demonstrates the importance of the T-

type Ca^{2+} channel as regulator of the hypoxic response (del Toro *et al.*, 2003). Exposure of human VSMCs to hypoxia attenuated depolarisation-stimulated Ca^{2+} entry via voltage-gated Ca^{2+} channels, although T-type Ca^{2+} channels appeared to play a more prominent role than L-type Ca^{2+} channels (Aley *et al.*, 2008). This response was apparent in VSMCs from internal mammary artery, but not saphenous vein, implying that hypoxic remodelling is dependent on the vascular bed. T-type Ca^{2+} channels have also been shown to be re-expressed in the heart in response to hypoxia (Pluteanu & Cribbs, 2009). Ventricular myocytes demonstrated a reduction in T-type current density, and $Ca_v3.1$, but not $Ca_v3.2$, mRNA was reduced via HIF-1α during a hypoxic insult. These data show that T-type Ca^{2+} channels selectively undergo redox modulation (Pluteanu & Cribbs, 2009).

Cardiac pacemaker potential

In health, T-type Ca^{2+} channels are prominent in the conduction system of the heart where they contribute to pacemaker potential (Perez-Reyes, 2003). T-type Ca^{2+} channels are expressed in embryonic hearts; this expression decreases after birth, but can increase again under pathological conditions (Perez-Reyes, 2003). One example is cardiac hypertrophy, as this condition involves reversion to the foetal gene program. Pressure overload-induced hypertrophy was attenuated in $Ca_v3.2^{-/-}$ mice, but not $Ca_v3.1^{-/-}$ mice, implying that Ca^{2+} entry via the $Ca_v3.2$ T-type Ca^{2+} channel plays a role in this condition (Chiang *et al.*, 2009).

Smooth muscle cell contraction and relaxation

T-type Ca^{2+} channels were reported to play a role in arterial vasoconstriction, as mibefradil treatment produced vasodilatory effects (Cribbs, 2006). These channels have been attributed to vasoconstrictor responses of renal microcirculation, more specifically efferent arteriole resistance, as reviewed by Cribbs (2006). Indeed, a role for T-type Ca^{2+} channels in microvascular tone has been demonstrated in both rats and humans (Ball *et al.*, 2009). The $Ca_v3.1$ T-type Ca^{2+} channel has been shown to play a role in vasoconstriction of rat mesenteric arterioles (Braunstein *et al.*, 2009). $Ca_v3.1$ was also found to be the most prominent subtype in A7r5 cells, a rat aortic VSMC line, and mibefradil abrogated arginine-vasopressin induced Ca^{2+} oscillations (Brueggemann *et al.*, 2005). This group concluded that T-type Ca^{2+} channels are important for VSMC Ca^{2+} oscillations, but are not the sole contributors, as $Ca_v3.2$ over-expression did not increase oscillation frequency. Ca^{2+} oscillations mediate pacemaker

activity, which manifests as vasomotion (Cribbs, 2006). Pacemaker potential as a result of T-type Ca^{2+} channel activity has been documented in pulmonary veins as reviewed by Cribbs (2006). Unexpectedly, the $Ca_v3.2$ T-type Ca^{2+} channel was demonstrated to be responsible for coronary artery relaxation, as $Ca_v3.2^{-/-}$ mice demonstrated constricted vessels (Chen *et al.*, 2003). This group hypothesised that the $Ca_v3.2$ T-type Ca^{2+} channel could be functionally coupled to BK_{Ca} channels in coronary artery VSMC. The presence of T-type Ca^{2+} channels in the endothelium still remains controversial, as reviewed by Kuo *et al.* (2011). The presence of these channels has not been documented in cultured ECs, yet their expression in small vessels has been suggested, where they may play a role in vasodilation (Kuo *et al.*, 2011). From these data it appears that T-type Ca^{2+} channels play a prominent role in vasoconstriction of peripheral arterioles.

Proliferation and the cell cycle

VSMCs

T-type Ca^{2+} channels are often expressed alongside L-type Ca^{2+} channels, which in addition to their small conductance, makes for challenging current detection (Cribbs, 2006). It is likely that T-type Ca^{2+} channels contribute to $[Ca^{2+}]_i$ in VSMCs via the associated window current, which lies in the range of -65 to -40mV, as determined in numerous cell types (Janssen, 1997;Blanks *et al.*, 2007;Lory *et al.*, 2006;Capiod, 2011). The RMP of de-differentiated VSMCs is initiated at -60mV, implying that T-type Ca^{2+} channels can influence $[Ca^{2+}]_i$ via their window current (Perez-Reyes, 2003). $Ca_v3.1$ and $Ca_v3.2$ are the most prominent cardiovascular subtypes (Cribbs, 2006), and $Ca_v3.2$ is involved in VSMC contraction and proliferation (Catterall *et al.*, 2005). T-type Ca^{2+} currents have been characterised in numerous smooth muscle cell tissues from a variety of species, including VSMCs, as reviewed by Perez-Reyes (2003).

The profile of T-type Ca^{2+} channel activity has been demonstrated to change across the period of culture of rat aortic VSMCs. At day 5 and 6 of culture, T-type Ca^{2+} channel currents were prominent. However, at day 15 of culture when the cells were confluent, T-type Ca^{2+} currents were reduced, and L-type Ca^{2+} currents were more prominent (Akaike *et al.*, 1989). These findings were corroborated by Neveu *et al.* (1994). Rat aortic VSMCs displayed a progressive increase in T-type Ca^{2+} channel currents throughout culture, which decreased as the cells reached confluence. In contrast, L-

type Ca^{2+} currents decreased during the first few days of culture, remaining constant until the cells reached confluence. Furthermore, L-type Ca^{2+} currents increased upon growth arrest by serum-starvation, with the concomitant decrease of T-type Ca^{2+} currents (Neveu *et al.*, 1994). Similarly, L-type Ca^{2+} channels were predominantly associated with freshly isolated VSMCs and confluent cultures, and T-type Ca^{2+} currents were apparent throughout proliferative phases (Richard *et al.*, 1992). Furthermore, T-type Ca^{2+} currents were not detected in freshly isolated human coronary artery VSMCs, but they were found after 4 days in culture (Quignard *et al.*, 1997). The U8A4 VSMC line can be maintained in the differentiated state, or stimulated to de-differentiate. Mibefradil was able to cause a dose-dependent inhibition of proliferation of de-differentiated U8A4 cells, with no effect of differentiated U8A4 cells (Louis *et al.*, 2006). These data strongly link T-type Ca^{2+} channel up-regulation to the de-differentiated VSMC phenotype.

Consistent with a role for T-type Ca^{2+} channels in VSMC proliferation, mibefradil was shown to limit neointima formation after balloon injury in rat carotid arteries, and also inhibit rat VSMC proliferation *in vitro* (Schmitt *et al.*, 1995). The role of the T-type Ca^{2+} channel was confirmed by the lack of effect of L-type Ca^{2+} channel blockers. A study of rat aortic VSMCs in primary culture demonstrated cell cycle dependent expression of T- and L-type Ca^{2+} channels (Kuga *et al.*, 1996). T-type current density was shown to be greater in cells of the G_1 and S phases, therefore linking DNA replication and proliferation to T-type Ca^{2+} currents. $Ca_v3.1$ was found to be the most prominent T-type Ca^{2+} channel subtype in human pulmonary artery VSMCs, and $Ca_v3.1$-targeting siRNA limited cell proliferation (Rodman *et al.*, 2005). Mibefradil also inhibited proliferation of these cells, which correlated with a higher proportion of cells in the G_0/G_1 phase of the cell cycle, implying T-type Ca^{2+} channels play a central role in the proliferative response. Insulin-like growth factor-1 has a role in pathological VSMC proliferation. This growth factor increased $Ca_v3.1$ mRNA in rat pulmonary artery VSMCs, and consequently enhanced cyclin D signalling (Pluteanu & Cribbs, 2011). Furthermore, the $Ca_v3.1$, but not the $Ca_v3.2$, T-type Ca^{2+} channel mediated VSMC proliferation and neointima formation in mice (Tzeng *et al.*, 2012). Injury of carotid arteries produced neointima in $Ca_v3.2^{-/-}$ but not in $Ca_v3.1^{-/-}$ mice, and the proliferative response of VSMCs from $Ca_v3.1^{-/-}$ mice was suppressed. This group also demonstrated that $Ca_v3.1$ knockdown hampered the progression of the S phase of the cell cycle, and indicated that the $Ca_v3.1$ channel regulates VSMC proliferation by a calmodulin dependent pathway. Moreover, inhibition of $Ca_v3.1$ by the more selective T-type Ca^{2+} channel

blocker, NNC55-0396, limited $[Ca^{2+}]_i$ in addition to cell proliferation, implying that this channel is essential to VSMC proliferation, and is a potential therapeutic target for vascular disorders.

Cancer

A sustained level of $[Ca^{2+}]_i$ is required for activation of calmodulin and downstream signals that stimulate cell cycle progression (Means, 1994). The G_1/S and the G_2/M cell cycle checkpoints are dependent on adequate $[Ca^{2+}]_i$ and calmodulin activity (Means, 1994). Highly proliferative cells, such as cancer cells, have increased Ca^{2+} requirements, and T-type Ca^{2+} channels have been shown to be up-regulated in many forms of cancer (Taylor *et al.*, 2008). The window current associated with T-type Ca^{2+} channel expression is important for the maintenance of $[Ca^{2+}]_i$ in non-excitable cancer cells (Taylor *et al.*, 2008). T-type Ca^{2+} channels are expressed in many types of cancer including, but not limited to neuroblastoma, glioblastoma, and breast, prostate, and colorectal carcinoma. The T-type inhibitors mibefradil and NNC55-0396 have been shown to limit breast cancer growth, as reviewed by Taylor *et al.* (2008). Proliferation of both U87MG glioma cells and N1E-115 neuroblastoma cells was reduced in response to T-type Ca^{2+} channel inhibition by mibefradil, or via serum starvation (Panner *et al.*, 2005). This study also demonstrated that over-expression of $Ca_v3.2$ enhanced cell proliferation. The blockade of T-type Ca^{2+} channels by the endogenous angiogenesis inhibitor, endostatin, was demonstrated to have limiting effects on U87MG cell migration and proliferation (Zhang *et al.*, 2012). These data establish a role for T-type Ca^{2+} channels in cancer progression. T-type Ca^{2+} channels have been linked to a CCE in non-excitable cancer cells (Gray *et al.*, 2004). This study demonstrated that prostate cancer, breast cancer, T cell leukemia, and neuroblastoma cell lines expressed $Ca_v3.2$ T-type Ca^{2+} channels or the splice variant α25B. These cell lines were sensitive to the novel compound, TH-1177, which blocked Ca^{2+} entry through T-type Ca^{2+} channels, as demonstrated in HEK/$Ca_v3.2$ cells, but not in cells lacking T-type Ca^{2+} channel expression. This inhibition of Ca^{2+} entry led to a decrease in cell proliferation, implicating a role for T-type Ca^{2+} channels in CCE. However, a role for T-type Ca^{2+} channels in CCE was excluded in a range of prostate cancer cell lines (Gackiere *et al.*, 2006). Mibefradil was able to decrease CCE in prostate cancer cells over-expressing the $Ca_v3.2$ T-type Ca^{2+} channel, yet this inhibition could not be reproduced with other T-type Ca^{2+} channel blockers, such as Ni^{2+}. This group proposed that mibefradil is therefore able to inhibit SOC channels, which is another group of channels proposed to be essential for sustaining $[Ca^{2+}]_i$ in proliferating cells.

Mechanisms linking Ca^{2+} channels and Ca^{2+} influx to proliferation are complex and cell dependent. NFAT was shown to be highly sensitive to Ca^{2+} and can be activated by low Ca^{2+} levels accordingly (Dolmetsch *et al.*, 1997). Furthermore, NFAT requires sustained $[Ca^{2+}]_i$ to remain in the nucleus. The amplitude and duration of Ca^{2+} signals contribute to differing Ca^{2+} sensitivities, and therefore, the specificity of Ca^{2+} waves or oscillations can selectively activate gene expression and proliferation (Dolmetsch *et al.*, 1997). Nevertheless, T-type Ca^{2+} channels are evidently involved in the pathological proliferative response, and appear to play an important role in sustaining $[Ca^{2+}]_i$ levels required for cell cycle progression.

In addition to excess VSMC proliferation, cardiovascular disorders often feature hypoxia, oxLDL, ROS and inflammatory mediators, and all of which are capable of inducing the stress-response protein, HO-1. This enzyme is also studied in depth in this thesis, and is discussed in detail below.

1.4 Heme oxygenase 1

Heme oxygenase was discovered over 40 years ago as a microsomal enzyme responsible for the oxidative breakdown of heme (Tenhunen *et al.*, 1969). Free heme has pro-oxidant properties, therefore the action of heme oxygenase provides cellular defence (Abraham & Kappas, 2008). HO-1 is a highly inducible form of the enzyme and up-regulation occurs in response to numerous cell stresses (Kim *et al.*, 2011b). Found at basal levels in select tissues including the spleen and reticuloendothelial cells of the liver and bone marrow, HO-1 can be induced in all other cell types (Kim *et al.*, 2011b). Figure 1.4 shows the crystal structure of human HO-1. Heme oxygenase 2 (HO-2) is a constitutively expressed form of the enzyme found mainly in the testes, the brain, and the vasculature (Kim *et al.*, 2011b). The functions of HO-2 appear to include heme sequestration to maintain an intracellular heme pool, oxygen sensing, and basal levels of cytoprotection, as reviewed by Kim *et al.* (2011b). A third isoform of HO was detected, although this form is sparsely distributed, has low enzyme activity, and is a pseudogene of HO-2 which is not expressed in humans (Kim *et al.*, 2011b). HO-1 is a membrane bound protein, principally localised to the endoplasmic reticulum, although studies have identified HO-1 in mitochondria, in the nucleus and within caveolae, as reviewed by Abraham and Kappas (2008). Plasma membrane caveolae localisation correlated with reduced HO-1 activity, yet these lipid rafts may provide a scaffold for

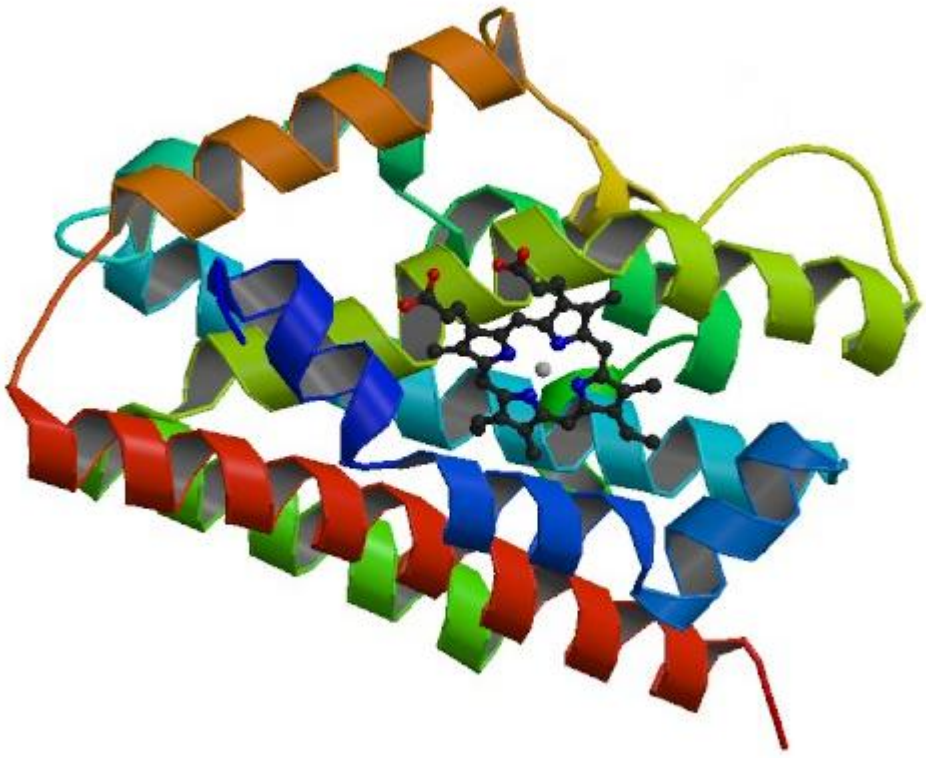

Figure 1.4 Crystal Structure of human HO-1

This image shows the secondary structure of the human HO-1 protein, together with a depiction of the heme substrate within the active site. Image taken from http://nist.rcsb.org/pdb/explore/images.do?structureId=1N45

the cytoprotective actions of this enzyme (Kim *et al.*, 2004). One study outlined that translocation of HO-1 into the nucleus upon cleavage of the C-terminus augmented oxidant-responsive transcription factor activation, suggesting that the effects of HO-1 can be produced in various cell locales (Lin *et al.*, 2007). HO-1 is highly conserved and expressed in many species (Ryter *et al.*, 2006). The natural substrate of this enzyme, heme, can induce HO-1 expression and activity, and heme also acts a cofactor (Ryter *et al.*, 2006). Upon induction, HO-1 degrades free heme oxidatively in a NADPH-dependent reaction to produce iron, biliverdin, and carbon monoxide (CO), and these by-products mediate the numerous cytoprotective effects of this enzyme (Ryter *et al.*, 2006). Figure 1.5 illustrates the HO-1 pathway. Free iron has pro-oxidant properties, although increased production stimulates ferritin synthesis, which rapidly sequesters free iron, thereby promoting anti-oxidant effects. Indeed, ferritin confers protection against oxLDL in ECs, as reviewed by Abraham and Kappas (2008). Biliverdin is rapidly converted to bilirubin by biliverdin reductase, and both compounds are able to scavenge reactive oxygen species (ROS) (Durante, 2002). Endogenous bilirubin has anti-apoptotic effects in ECs, exogenous bilirubin limits oxidative stress-induced injury in vascular cells, and this compound has positive effects on leukocyte infiltration, as reviewed by Durante (2002). HO-1 derived bilirubin can inhibit NADPH oxidase, and was shown to limit ROS generation and proliferation of human airway smooth muscle cells via extracellular signal-regulated kinase 1/2 (ERK1/2) MAPK (Taille *et al.*, 2003). Furthermore, serum bilirubin has been described as an independent, inverse risk factor for coronary artery disease (Ryter *et al.*, 2006). Low serum bilirubin levels correlate with an increased incidence of peripheral vascular disease, whereas mild elevations have protective cardiovascular effects (Ryter *et al.*, 2006). HO-1 activity is the major source of endogenous CO, and this signalling molecule is associated with a vast array of protective effects, which are discussed in detail later.

1.4.1 Inducers of HO-1

The majority of HO-1 inducers regulate the transcription of the HO-1 gene (HMOX1) in a cell specific manner (Gozzelino *et al.*, 2010). Oxidative stress is an important regulator of HO-1 expression, and the promoter regions of the HMOX1 gene contain stress response elements (Gozzelino *et al.*, 2010). HO-1 induction occurs in response to heme and protoporphyrins, heavy metals, ROS, hypoxia, hyperoxia, UVA radiation, NO gas and NO donors, resveratrol, curcumin, aspirin, statins, growth factors such as PDGF and TGF-β, inflammatory cytokines such as TNF-α and IL-1, anti-inflammatory cytokines, angiotensin II, oxLDL and endotoxin (Abraham & Kappas, 2008). The

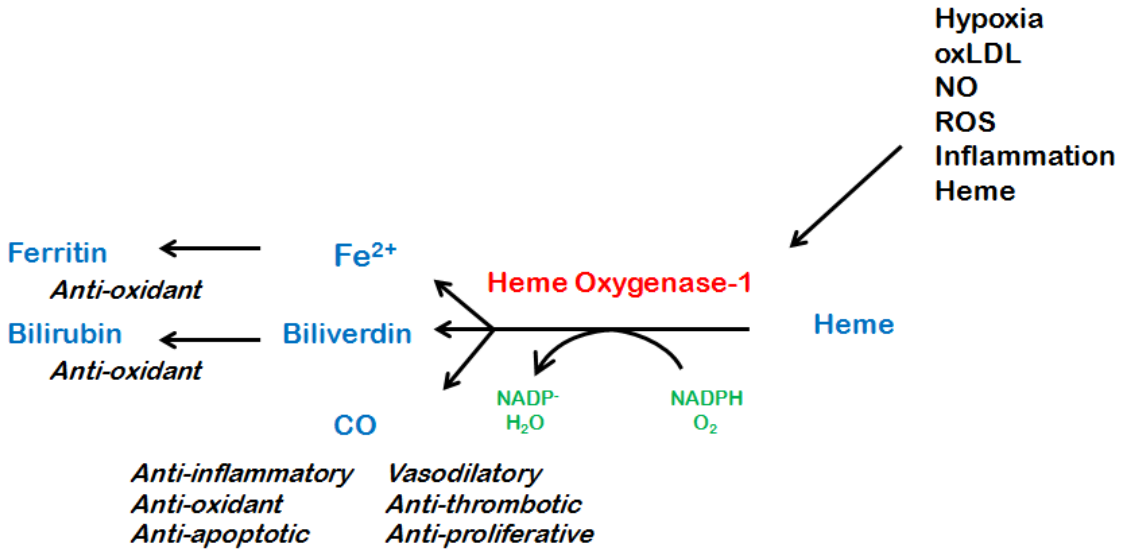

Figure 1.5 The HO-1 Pathway

HO-1 is induced in response to numerous cell stressors including, but not limited to, hypoxia, oxLDL, NO, ROS, inflammation and heme. HO-1 breaks down free heme oxidatively to produce iron, biliverdin, and CO. It is the by-product CO that mediates the majority of the cytoprotective effects associated with HO-1 activity.

recruitment of signalling pathways and subsequent transcription factors by this vast array of inducers appears to be cell type and species specific (Ryter *et al.*, 2006). The MAPK signal transduction pathways are involved in HO-1 induction along with numerous transcription factors (Ryter *et al.*, 2006). Nrf2 is involved in HO-1 induction, along with redox sensitive transcription factors NF-κβ and AP-1 (Ryter *et al.*, 2006).

A vast amount of data regarding the protective effects of HO-1 has relied on the use of metalloporphyrins such as cobalt protoporphyrin IX (CoPPIX), which consists of a cobalt ion chelated by protoporphyrin IX (Kappas & Drummond, 1986). Administration of CoPPIX or cobalt chloride in rats caused an induction of hepatic HO-1 which lasted 48-72h (Maines & Kappas, 1975). Cobalt chloride and tin chloride are also HO-1 inducers, however tin protoporphyrin (SnPP) is a competitive HO-1 inhibitor (Kappas & Drummond, 1986). The heme pocket within the HO-1 molecule where heme binds is also the site at which the synthetic metalloporphyrins bind, thereby acting as competitive inhibitors (Maines, 1997). Zinc protoporphyrin (ZnPP) is a competitive inhibitor of HO-1 activity, but ZnPP is conversely able to induce HO-1 mRNA and protein levels (Maines & Trakshel, 1992;Yang *et al.*, 2001). It appears that a region of DNA upstream of the murine HO-1 gene is the convergence point for the different signalling pathways from numerous HO-1 inducers, including hemin and CoPPIX (Alam *et al.*, 1995). It has also been demonstrated in chick embryonic liver cells that the response element for HO-1 induction by heme and CoPPIX differs from that of stress inducers such as heavy metals (Shan *et al.*, 2000;Shan *et al.*, 2002). The signalling pathway in human liver cells involves down-regulation of Bach1 and up-regulation of Nrf2 transcription factors (Shan *et al.*, 2006). Hypoxia has been demonstrated to induce HO-1 in rat tissues and in culture via the action of HIF-1α (Lee et al., 1997). Peroxisome Proliferator-Activated Receptors (PPAR) are also capable of up-regulating HO-1 expression. Upon ligand activation, PPARα and PPARγ have been shown to induce HO-1 expression in VSMCs and ECs (Kronke *et al.*, 2007). Therefore, PPAR ligands, such as lipid-lowering fibrates, may also enhance cardiovascular integrity (Kronke *et al.*, 2007). The cytoprotective effects of HO-1 have been examined in a wide range of tissues and diseases, but for the purpose of this project only those effects relating to disorders of the vasculature will be examined.

1.4.2 Effects of HO-1 induction

Proliferation and Apoptosis

PDGF was demonstrated to induce HO-1 mRNA and protein levels in rat aortic VSMCs, with a concomitant increase in CO and ROS production (Durante *et al.*, 1999). A later study by this group once again demonstrated mitogen-induced HO-1 induction, yet they concluded that CO was able to inhibit VSMC proliferation via modulation of the cell cycle (Peyton *et al.*, 2002). Exogenously applied gaseous CO was able to limit cell cycle progression by increasing the number of cells in the G_0/G_1 phase. Additionally, cyclin A expression was reduced, as was cyclin A-associated kinase activity and cyclin-dependent kinase 2 activity. Concerning cell cycle progression, differential effects of HO-1 induction have been demonstrated in VSMCs and ECs. In VSMCs HO-1 induction increased the proportion of cells in the G_0/G_1 phase, and decreased the proportion of cells in the S and G_2/M phases. The opposite effect was observed with HO-1 inhibition. In ECs HO-1 induction produced reciprocal effects, mediating a pro-proliferative response (Li *et al.*, 2002). HO-1 induction and subsequent CO production occurred in response to balloon injury in rat carotid arteries, and CO limited neointimal hyperplasia via a cGMP dependent pathway (Togane *et al.*, 2000). HO-1 expression within VSMCs of the intima correlated with the timely migration of medial VSMCs, further demonstrating a role for HO-1 in the repair of cardiovascular injury.

An extensive study involving numerous *in vitro* and *in vivo* methods demonstrated the pleiotropic and protective effects of HO-1 within the vasculature. Transfection of HO-1 in primary VSMCs reduced cell proliferation in a soluble guanylyl cyclase (sGC) and cGMP dependent pathway, which was associated with cell cycle arrest in the G_0/G_1 phase and up-regulation of the cyclin-dependent kinase inhibitor, p21 (Duckers *et al.*, 2001). HO-1 gene transfer in pig arteries limited the development of intimal hyperplasia after angioplasty, and this correlated with the expression of cyclin-dependent kinase inhibitors p21 and p27, leading the authors to conclude that HO-1 functions upstream of these inhibitors to limit cell cycle progression (Duckers *et al.*, 2001). Enhanced relaxation of these arteries was also apparent, and was mediated via a cGMP mechanism. The beneficial effects of HO-1 were also evidenced by experimentation with HO-1 gene knockout mice ($HMOX1^{-/-}$). Wire injury of the femoral artery produced significant hyperplastic lesions, and VSMCs cultured from these mice proliferated to a greater extent than control VSMCs (Duckers *et al.*, 2001). Consistent with the effects of proliferation, p21 was down-regulated and G_1/S phase progression occurred in

HMOX1$^{-/-}$ VSMCs. These data established the vasodilatory and anti-proliferative effects of HO-1 in VSMCs.

Metalloporphyrins also demonstrate how the cytoprotective effects of HO-1 are involved in numerous cardiovascular disorders. Hemin pre-treatment of rats subject to balloon injury of the carotid artery induced HO-1 in both the endothelial and medial vessel layers, and limited neointima formation (Tulis *et al.*, 2001). Furthermore, neointimal hyperplasia was not affected by pre-treatment with the HO-1 inhibitor, SnPP, demonstrating that HO-1 protects against vascular remodelling (Tulis *et al.*, 2001). The contrasting effects of hemin and SnPP were also demonstrated *in vitro* using rat aortic VSMCs. An increase in HO-1 expression and activity decreased the proliferative response, arresting cells in the G_0/G_1 phase of the cell cycle and increasing p21 expression (Chang *et al.*, 2008). SnPP and HO-1 siRNA attenuated such effects. The levels of ROS were also reduced by HO-1 induction, demonstrating a role for HO-1 in proliferative and oxidative disorders of the vasculature (Chang *et al.*, 2008). Zhang *et al.* (2002) also provided evidence that HO-1 is likely to confer anti-oxidant effects. Rat aortic VSMCs transfected with HO-1 exhibited increased HO-1 activity, decreased proliferation, and resistance to oxidative stress in the form of H_2O_2. ZnPP abolished these effects, implying that HO-1 could protect against cardiovascular disorders such as atherosclerosis (Zhang *et al.*, 2002).

Restenosis is another proliferative disorder that could benefit from enhanced HO-1 activity. Hemin treatment of stented rabbit aorta and iliac arteries limited neointima formation without causing adverse effects on re-endothelialisation (Hyvelin *et al.*, 2010). HO-1 induction reduced early adverse inflammatory, proliferative, and apoptotic events, thereby enhancing the integrity of a stented vessel (Hyvelin *et al.*, 2010). HO-1 inhibition attenuated the associated protective responses, and the anti-proliferative effects appeared to be mediated via activation of cyclin-dependent kinase inhibitors and a reduction in RhoA expression (Hyvelin *et al.*, 2010). Furthermore, the application of a CO donor, CORM-2, also limited intimal hyperplasia, implying that the beneficial effects associated with HO-1 induction are in fact mediated by the product CO (Hyvelin *et al.*, 2010). HO-1 may play a role in limiting vascular damage during hypertension. It was found that basal HO-1 was higher in spontaneously hypertensive rats (SHR) than in wistar Kyoto rats (WKY) (Jeon *et al.*, 2009). HO-1 gene transfer or induction by hemin inhibited VSMC proliferation to a greater extent in SHR, and this correlated to a

higher proportion of cells in the G_1 phase of the cell cycle, lower cyclin D expression, and higher p21 expression (Jeon *et al.*, 2009).

Morita *et al.* have provided extensive data regarding the effects of HO-1 induction by hypoxia. HO-1 mRNA and activity were up-regulated in response to hypoxia in rat aortic and pulmonary VSMCs, producing CO which was shown to regulate cGMP (Morita *et al.*, 1995). Hypoxia was not able to induce HO-1 in ECs, although the induction of HO-1 and CO in VSMCs limited proliferation of these cells, and exerted paracrine effects on ECs (Morita & Kourembanas, 1995). CO production increased levels of cGMP and inhibited the expression of growth factors. A later study corroborated these findings and proved that the reduction in rat aortic VSMC proliferation in response to hypoxia is due to CO (Morita *et al.*, 1997). CO reduced E2F-1 and c-myc expression in a cGMP-dependent manner.

In contrast to the well documented anti-proliferative effects in VSMCs, HO-1 functions in a pro-proliferative manner in ECs and some tumours. Transfection of HO-1 into rabbit ECs resulted in an increase in HO-1 activity, cell proliferation, and angiogenesis (Deramaudt *et al.*, 1998). Inhibition of HO-1 activity in a B-cell leukaemia/lymphoma 1 tumour down-regulated cyclin D1 expression and tumorigenesis (La *et al.*, 2009). The pro-proliferative effects of HO-1 on tumorigenesis are tissue specific, as are the anti-apoptotic effects (Jozkowicz *et al.*, 2007). However, HO-1 activity appears to enhance tumour viability by promoting angiogenesis and metastasis, in addition to limiting apoptosis, as reviewed by Jozkowicz *et al.* (2007). The DAOY medulloblastoma cell line was documented to have constitutive HO-1 expression, which was potentiated by hypoxia or metalloporphyrins, and augmented anti-apoptotic effects via a p38/MAPK-dependent pathway (Al-Owais *et al.*, 2012). Exogenous application of the CO donor, CO releasing molecule-2 (CORM-2), reproduced these effects, implying that CO is the HO-1 by-product responsible for promoting cancer cell survival. Interestingly, the abolition of HO-1 expression improves the response to chemotherapy in pancreatic cancer cells, as reviewed by Abraham and Kappas (2008).

There are conflicting data regarding the effects of HO-1 and CO on apoptosis in vascular cells. Adenovirus-mediated HO-1 over-expression limited VSMC proliferation

and caused apoptosis (Liu *et al.*, 2002b). Furthermore, these effects were mimicked by exogenous bilirubin and biliverdin, implying that the anti-oxidant properties of these by-products can stimulate apoptosis (Liu *et al.*, 2002b). In contrast, HO-1 over-expression or exogenous CO confer anti-apoptotic effects in rat aortic VSMCs, which was dependent on the sGC/cGMP pathway (Liu *et al.*, 2002a). However, HO-1 and CO appear to protect ECs from apoptosis, which may play an essential role in maintaining endothelial integrity. (Liu *et al.*, 2002b;Liu *et al.*, 2002a).

Inflammation and oxidation

HO-1 activity has been associated with anti-inflammatory effects in numerous *in vivo* and *in vitro* studies. The expression of this enzyme has been documented in VSMCs, ECs, and macrophages involved in an inflammatory response. However, expression is visibly lacking in adjoining, unaffected cells, as reviewed by Kim *et al.* (2011). A study involving aortic balloon injury of rabbits fed an atherogenic diet demonstrated a prominent inflammatory response together with thin fibrous caps of lesions (Li *et al.*, 2011). Metalloporphyrin induction of HO-1 limited the development of atherosclerosis and plaque disruption by preventing lipid deposition and attenuating an inflammatory response. Plaque stability was maintained by a reduced level of apoptosis, a decreased expression of pro-inflammatory mediators such as MMP-9, IL-6 and TNF-α, and an increased expression of the anti-inflammatory cytokine IL-10 (Li *et al.*, 2011). An increase in eNOS activity also appeared to play a protective role. HO-$1^{-/-}$ apoE$^{-/-}$ mice demonstrated advanced atherosclerotic lesions containing higher levels of lipids, macrophages and VSMCs (Yet *et al.*, 2003). HO-$1^{-/-}$ mice underwent vein grafting which promoted neointimal hyperplasia, followed by neointimal cell death (Yet *et al.*, 2003). The pleiotropic effects of HO-1 are evidently important in the progression of atherosclerosis.

HO-1 is induced by oxidative stress and alterations in the redox state of proteins such as glutathione, as reviewed by Ryter *et al.* (2006). Human pulmonary artery VSMCs were shown to express HO-1 upon an oxidative insult. The application of the CO donor, CORM-2, reduced cell proliferation, suggesting a protective role for the by-products of this enzyme in airway remodelling and pulmonary hypertension (Stanford *et al.*, 2003). HO-1 induction in human airway VSMCs also limited oxidative stress and apoptosis via an Akt-dependent pathway leading to Nrf2 activation of the HO-1 promoter (Brunt *et al.*, 2006).

Vasodilation

High flow laminar shear stress can induce HO-1 expression (Wagner *et al.*, 1997). Indeed, this shear stress also leads to NO production and mitochondrial derived H_2O_2, which play a role in resistance artery remodelling (Freidja *et al.*, 2011). HO-1 derived CO activates sGC with subsequent cGMP production and vasodilation, therefore contributing to adaptive vascular remodelling (Freidja *et al.*, 2011). Moreover, NO is capable of inducing HO-1 in numerous vascular cells and the associated compensatory mechanisms are discussed below.

1.4.3 HO-1 and NO

Both NO and CO can promote vasodilation via the sGC/cGMP pathway. NO is an inducer of HO-1, and the HO-1/CO system can regulate NOS activity. High CO levels inhibit NOS and NO generation which leads to vasoconstriction, whereas low CO levels stimulate eNOS activity leading to vasodilation, as reviewed by Kim *et al.* (2011). NO bioavailability is critical to endothelial function and vascular homeostasis. Shear stress can up-regulate eNOS via NF-κβ leading to NO production in vascular cells (Pae *et al.*, 2010). In addition to conferring vasodilatory effects, the generation of NO via eNOS has been shown to inhibit VSMC proliferation and platelet aggregation (Pae *et al.*, 2010). Oxidative stress can cause eNOS uncoupling and subsequent HO-1 induction, which can compensate for a reduction in NO bioavailability, as reviewed by Pae *et al.* (2010). The interplay between the HO-1/CO and eNOS/NO systems serves to protect cells from physiological stress. In a rat model of carotid artery balloon injury the exposure to gaseous CO (250ppm) or to the CO donor, CORM-2, enhanced the proliferation of ECs *in vivo* and *in vitro* (Wegiel *et al.*, 2010). The increased cell growth was associated with a higher proportion of cells in the S phase of the cell cycle and was mediated via RhoA with subsequent downstream phosphorylation of Akt and eNOS (Wegiel *et al.*, 2010). These effects associated with CO appeared to be dependent on NO, as re-endothelialisation did not occur in $eNOS^{-/-}$ mice. In human ECs, HO-1 was induced in response to a NO donor, which limited NADPH oxidase activity, thereby promoting anti-oxidant effects (Jiang *et al.*, 2006). Bilirubin also inhibited NADPH oxidase, therefore NO is able to regulate ROS production via HO-1 activity (Jiang *et al.*, 2006).

Inducible NOS (iNOS) expression occurs in response to inflammatory cytokines and produces abundant amounts of NO over extended time periods, whereas eNOS

production of NO is transient (Durante, 2002). Furthermore, NO production via iNOS has the potential to produce both beneficial and adverse effects (Singh & Evans, 1997). iNOS plays an adverse role in oxidative stress, whereas a beneficial role has been documented in hypertension, as summarised by (Lee & Yen, 2009) However, iNOS expression has been demonstrated in intimal VSMCs after injury, and this expression was linked to increased VSMC proliferation (Chyu *et al.*, 1999). The interaction between HO-1/CO and NO is complex and cell specific. There are feedback mechanisms that allow CO to compensate for a reduction in NO bioavailability, which is essential to vascular integrity.

1.4.4 Therapeutic potential of HO-1

Evidently from the data described above, HO-1 holds great potential as a therapeutic target for cardiovascular disorders. However, metalloporphyrins are unsuitable for clinical use due to associated side effects and structural similarity to heme, which can cause cytotoxicity, as reviewed by (Kinobe *et al.*, 2008). However, there are numerous naturally occurring compounds that have the ability to induce HO-1, and therefore could confer cardiovascular benefits. Resveratrol is a polyphenolic component of red grapes that is associated with anti-oxidant properties, and has been shown to induce HO-1 in rat aortic VSMCs (Huang *et al.*, 2005). Indeed, moderate consumption of red wine correlates with a reduced incidence of cardiovascular disease (Huang *et al.*, 2005). Numerous studies have detailed the effects of the spice curcumin on HO-1 expression. Curcumin increased HO-1 mRNA and provided protection against oxidative stress when applied to bovine ECs (Motterlini *et al.*, 2000). Proliferation of primary rat VSMCs and human airway VSMCs was inhibited by curcumin-induced HO-1 via up-regulation of p21 (Pae *et al.*, 2007). This study demonstrated that curcumin induced HO-1 via Nrf2 translocation and anti-oxidant response element activation within the HO-1 promoter.

A range of drugs currently used to treat disorders of the vasculature have also been demonstrated to induce HO-1, including rapamycin and probucol. Aspirin can induce HO-1 in human ECs, the effects of which were associated with anti-inflammatory and anti-oxidative benefits, as reviewed by Abraham and Kappas (2008). The pleiotropic effects of statins also extend to HO-1 induction, as increased protein and mRNA levels have been produced in human ECs *in vitro* and *in vivo* in response to simvastatin and lovastatin, as reviewed by Abraham and Kappas (2008). The associated anti-

inflammatory and anti-oxidative effects were shown to be mediated by the p38/MAPK and the ERK1/2 MAPK pathways, implying that the MAPK pathways act co-operatively, as reviewed by Kim *et al.* (2011).

As HO-1 can be induced in all cells, targeting a HO-1 inducer to the correct tissue poses difficulties. To try and overcome this issue, HO-1 gene transfer has been investigated. Trials in animals have been successful, yet the major risks include an immune response and the development of cancer, as reviewed by Abraham and Kappas (2008). Delivery of the human HO-1 gene into rats generated protective effects within the vasculature, and the use of adenovirus-mediated gene transfer of HO-1 into liver cells of mice did not elicit immune or inflammatory responses (McCarter *et al.*, 2003). These effects have been corroborated within a cardiac allograft of rats (Braudeau *et al.*, 2004).

HMOX1 is an extremely sensitive gene which can be up-regulated by numerous factors that are associated with the cellular redox state. HO-1 activity has pleiotropic actions within the vasculature, and all three of the by-products confer cytoprotective effects. However, the majority of these effects appear to be mediated by CO.

1.5 Carbon Monoxide

CO is a renowned environmental toxin that causes tissue hypoxia at high levels by producing carboxyhemoglobin (COHb), (Wu & Wang, 2005). Chronic exposure modulates mitochondrial function promoting superoxide production and ensuing adverse effects including oxidative damage and apoptotic cell death (Ryter *et al.*, 2006). Contrastingly, this gas is also a vital cell signalling molecule produced endogenously via HO-1 activity (Ryter *et al.*, 2006). CO is a stable signalling molecule in comparison to NO, and the cellular targets of CO are hemoproteins such as hemoglobin, myoglobin, guanyl cyclase, cyclooxygenase, cytochrome P450, cytochrome c oxidase, iNOS, and NADPH oxidase (Otterbein *et al.*, 2003a). Oxidative stress is an underlying factor of numerous cardiovascular disorders, and CO plays an important role in regulating ROS availability. CO can rapidly increase ROS production in the mitochondria by modulation of cytochrome c oxidase, as reviewed by Peers and Steele (2012). ROS production may subsequently regulate physiological functions by

interacting with ion channels, as discussed in section 1.5.2. Additionally, CO has been proposed to initiate an adaptive response which subsequently leads to a reduction in ROS and the restoration of cellular homeostasis via the inhibition of NADPH oxidase and HO-1 induction (Ruiz & Ameredes, 2012). This may involve the conditioning of cells via transcriptional up-regulation of genes to combat a subsequent oxidant mediated insult (Bilban *et al.*, 2008). Moreover, CO induced ROS can confer cell-specific anti-inflammatory, anti-proliferative and anti-apoptotic effects, as reviewed by Bilban *et al.* (2008). The plethora of cytoprotective effects associated with CO in vascular cells appear to be mediated by the sGC/cGMP and p38/MAPK pathways, either in concert or independently, with additional effects on PI3K-Akt, PPARγ, and HIF-1α (Kim *et al.*, 2006).

1.5.1 Cytoprotective effects of CO

Vasorelaxation

CO stimulates vasorelaxation in numerous vascular beds across numerous species via direct binding to sGC and increased levels of cGMP, or via stimulation of BK_{Ca} channels, which leads to K^+ efflux, membrane hyperpolarisation and subsequent closure of voltage-dependent Ca^{2+} channels, as reviewed by Bilban *et al.* (2008). CO has been proposed to bind to histidine residues within the channel, to the heme moiety associated with the channel, or to histidine/aspartate residues in the conductance regulator domain to augment this channel (Wilkinson & Kemp, 2011). Gaseous CO has been shown to dilate VSMCs of rat aortas (Lin & McGrath, 1988), and the CO donor, CORM-3, relaxed pre-contracted rat aortae (Foresti *et al.*, 2008). The vasodilatory effects of the latter were associated with an increase in cGMP and were mediated in part by BK_{Ca} channels. CO may be a viable therapeutic agent for pulmonary arterial hypertension, as gaseous CO restored pulmonary arterial pressures in a rodent model (Zuckerbraun *et al.*, 2006). Acute exposure of low dose CO (250ppm) stimulated VSMC apoptosis and limited VSMC proliferation in hypertrophied vessels. These protective effects required eNOS, implying that a functional endothelium is critical to limiting vessel remodelling (Zuckerbraun *et al.*, 2006). The vasodilatory responses to hypoxia appear to be tissue specific; systemic vessels dilate, but pulmonary vessels constrict, as reviewed by Wu and Wang (2005). Ventilation with CO abolishes this constriction of pulmonary vessels (Wu & Wang, 2005).

Proliferation

In airway VSMCs 250ppm CO conferred anti-proliferative effects by halting the cell cycle in the G_0/G_1 phase via an ERK1/2 MAPK-dependent pathway (Song *et al.*, 2002). These effects also correlated with increased levels of p21 and a reduction of cyclin D1. The same pathway was proposed to be responsible for limiting proliferation of airway smooth muscle cells in response the CO donor, CORM-2 (Taille *et al.*, 2005). In this study, CO played a role in redox signalling by inhibiting NADPH oxidase cytochrome b activity, leading to mitochondrial ROS production and subsequent anti-proliferative effects. The idea that the mitochondrial electron transport chain could act as a CO sensor may underlie the mechanism of airway remodelling (Taille *et al.*, 2005).

Transplant-associated atherosclerosis was limited in a rat model by exogenous CO (250ppm), which also inhibited leukocyte infiltration (Otterbein *et al.*, 2003b). Additionally, intimal hyperplasia was limited by exogenous CO (250ppm) after balloon injury of the carotid artery (Otterbein *et al.*, 2003b). This level of exogenous CO also increased the expression of p21, and the anti-proliferative effects of CO appeared to be mediated by a pathway involving both cGMP and p38/MAPK (Otterbein *et al.*, 2003b). Caveolae may play a role in the anti-proliferative effects of exogenous CO, as up-regulation of the p38β/MAPK signalling pathway by CO increased the expression of caveolin-1 in fibroblasts and VSMCs (Kim *et al.*, 2005). This cell cycle arrest was promoted by the up-regulation of p21 and the down-regulation of cyclin A, and also appeared to involve cGMP (Kim *et al.*, 2005).

In a porcine model of balloon injury, pre-operatively and intra-operatively inhaled CO (250ppm) limited neointima formation (Raman *et al.*, 2006). Interestingly, inhaled CO and iNOS gene transfer together conferred non-additive but enhanced effects on intimal hyperplasia. This evidences the co-operative effects of CO and NO, and it is possible that NO induced HO-1, which would further produce CO. The protective effects of 250ppm inhaled CO on intimal hyperplasia were also demonstrated within a porcine model of femoral artery grafting (Ramlawi *et al.*, 2007). Levels of COHb did not reach toxicity in either of these studies, suggesting that gaseous CO could be a potential therapeutic agent. The anti-proliferative effects of CO were also reproduced with porcine VSMCs *in vivo* (Ramlawi et al., 2007).

Inflammation

Exogenous CO has demonstrated anti-inflammatory properties both *in vitro* and *in vivo*, the effects of which appear to be mediated by the p38/MAPK pathway (Otterbein *et al.*, 2000). Pro-inflammatory cytokines were down-regulated and anti-inflammatory cytokines were up-regulated in murine macrophages and MKK3$^{-/-}$ mice by gaseous CO (Otterbein *et al.*, 2000). The application of CORM-3, a CO donor, to human umbilical vein ECs suppressed the expression of the adhesion molecules, E-selectin and I-CAM (Song *et al.*, 2009). These data suggest that CO is able to promote an anti-inflammatory environment that could protect the vasculature and limit remodelling. However, when gaseous CO (500ppm) was inhaled by human volunteers for 1 hour prior to an endotoxin challenge, anti-inflammatory effects were absent (Mayr *et al.*, 2005a). These data contrast the beneficial anti-inflammatory and anti-proliferative effects demonstrated in rodent and murine models in response to 250ppm CO (Otterbein *et al.*, 2000;Otterbein *et al.*, 2003b). Species differences obviously factor into the response, as CO tissue levels will depend on the respiration rate of the subject (Mayr *et al.*, 2005b). However, the exposure of chronic obstructive pulmonary disease patients to 125ppm CO for 2 hours a day, for a period of 4 days, conferred moderate anti-inflammatory benefits (Bathoorn *et al.*, 2007). CO may therefore be a potential therapy for disorders involving remodelling of the airways and the vasculature.

Thrombosis

The inhibition of platelet aggregation by CO was demonstrated over 20 years ago, and is dependent on the cGMP pathway (Brune & Ullrich, 1987). These anti-thrombotic effects were also demonstrated by endogenous CO in rat aortic VSMCs (Wagner *et al.*, 1997). Induction of HO-1 by shear stress limited platelet aggregation via a cGMP-dependent mechanism, as HO-1 and not iNOS inhibitors abrogated the effects (Wagner *et al.*, 1997). The CO donor, CORM-3, inhibited platelet aggregation *in vitro*, *ex vivo*, and *in vivo*, although these effects were attributed to actions of both NO and CO, in a sGC/cGMP-dependent mechanism (Soni *et al.*, 2011). These anti-thrombotic effects of CO are likely to play a protective role after endothelial injury, during late stage atherosclerosis, and during organ grafting. Delivering the optimal concentration of CO in a timely and tissue specific manner may lead to beneficial effects, yet the cellular targets of CO are still being uncovered.

1.5.2 Ion channels as targets of CO

Our research group has demonstrated that CO can inhibit numerous ion channels. Both CO and CORM-2 inhibited L-type Ca^{2+} channel currents, and given these channels provide an important route for Ca^{2+} entry in VSMCs, this has important implications during situations of vascular stress, when CO production is enhanced via HO-1 induction (Scragg *et al.*, 2008). CO was shown to increase mitochondrial ROS, which caused redox modulation of cysteine residues within the L-type Ca^{2+} channel in cardiac myocytes and HEK293 cells expressing the human $Ca_v1.2$ subunit. Both gaseous CO and CORM-2, were shown to inhibit $K_v2.1$ channels. CO inhibited native neuronal $K_v2.1$ and HEK293 cells expressing recombinant $K_v2.1$ by a protein kinase G dependent mechanism (Dallas *et al.*, 2011). More recently, our group demonstrated that CO was able to block $K_v2.1$ channels in a medulloblastoma cell line, which consequently plays a role in limiting apoptosis (Al-Owais *et al.*, 2012). Subsequently, our group has made a novel discovery in the form of $Ca_v3.2$ T-type Ca^{2+} current inhibition by CORM-2, and these currently unpublished findings opened avenues of investigation which led to this PhD project. Recent reviews discuss the findings that CO is also able to inhibit epithelial Na^+ channels, whilst conversely augmenting BK_{Ca} channels, tandem P domain K^+ channels, interstitial smooth muscle L-type Ca^{2+} channels, and the ATP gated P2X receptor (Peers, 2011;Wilkinson & Kemp, 2011;Peers & Steele, 2012). These ion channels may provide novel therapeutic targets for a wide range of disorders. Figure 1.6 illustrates the pathways involved in mediating the cytoprotective effects of CO in VSMCs, and given the various signalling pathways that are sensitive to CO, it seems likely that other ion channels will also be found to be regulated by CO.

1.5.3 Therapeutic potential of CO

The wide ranging cytoprotective effects attributed to CO allow this gasotransmitter to be regarded as an essential signalling molecule and a potential therapeutic agent. Concerning gaseous CO, the data thus far is equivocal, with the beneficial effects dependent on dose, length of exposure and the species under examination. However, the general consensus is that acute CO exposure confers positive effects, whereas chronic exposure is associated with adverse outcomes, as reviewed by Bilban *et al.* (2008). Indeed, the first Phase I clinical trial assessing the safety of inhaled CO in humans using the Covox DS CO delivery device has been completed (Motterlini & Otterbein, 2010). This study assessed acute CO exposure, 3mg/kg/hour for 1 hour a day for 10 days, and reported no cytotoxic COHb levels, as reviewed by Motterlini and

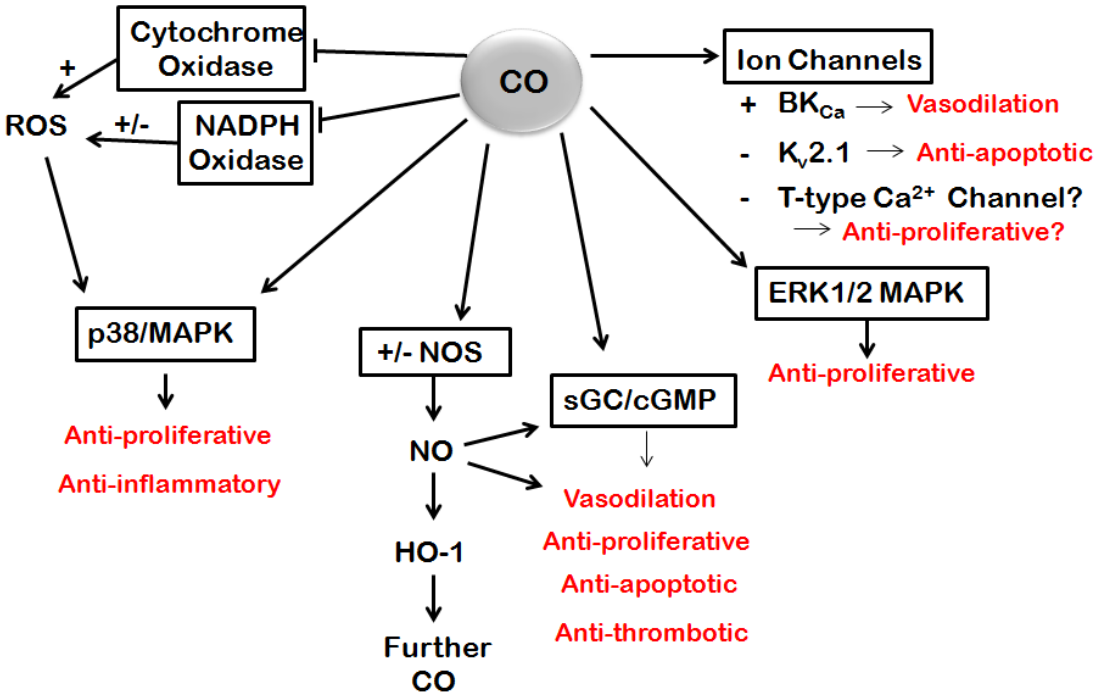

Figure 1.6 Pathways mediating the cytoprotective effects of CO in VSMC

CO acts at numerous cellular targets, shown in boxes in the diagram, to mediate cytoprotective effects. CO modulates numerous ion channels; BK_{Ca} channels are augmented, $K_v2.1$ channels are inhibited, and T-type Ca^{2+} channels have also been shown to be inhibited. CO interacts with cytochrome oxidase in the mitochondria and with NADPH oxidase to inhibit their activity, thereby modulating ROS production. NOS is either inhibited or up-regulated depending on the level of CO available, with subsequent effects on NO production, sGC activity and HO-1 induction. CO binds sGC and directly activates this second messenger leading to increased levels of cGMP. The p38/MAPK pathway also mediates a variety of cytoprotective effects associated with CO, potentially via interaction with the MAPK-mediated protein phosphatase 2C (Boczkowski *et al.*, 2006). The ensuing physiological effects are displayed in red.

Otterbein (2010). Issues associated with the targeting of this gas to the correct tissue, such as respiration rates, levels of CO exhalation, and COHb conversion, may restrict the use as therapeutic agent to disorders involving pulmonary remodelling (Mayr *et al.*, 2005b;Ruiz & Ameredes, 2012). However, the advent of CORMs may allow targeted CO delivery for specific disorders with a view to providing distinct physiological benefits. CORMs are transition metal carbonyls that release CO either in the presence of light (in the case of CORM-1), by a pH change (in the case of CORM-A1), or by ligand substitution (in the case of CORM-2 and CORM-3), and allow controlled delivery of low doses of CO (Foresti *et al.*, 2008). CORM-1 and -2 were the first to be produced and are soluble in inorganic solvents. The treatment of VSMCs with CORM-2 did not affect cell viability, and had favourable vasodilatory and anti-hypertensive effects on isolated aortic tissue and on *in vivo* models respectively (Motterlini *et al.*, 2002). Indeed, CORM-2 has been associated with numerous beneficial effects including reduced proliferation and inflammation, as described in the previous section. CORM-3 has a biological ligand incorporated into the molecular structure, resulting in a less toxic compound that is water soluble, and therefore more compatible with experiments involving live cells, (Motterlini *et al.*, 2003). CORM-3 has demonstrated cardioprotective effects on cardiac cells and isolated hearts (Clark *et al.*, 2003), and has been shown to dilate pre-contracted rat aortic rings (Foresti *et al.*, 2004). The experimental use of CORMs has further validated the understanding that CO is a cytoprotective molecule at the correct concentration (Motterlini *et al.*, 2003), and application of micromolar concentrations of CORM-3 are deemed to be comparable to the effects of endogenous CO (Foresti *et al.*, 2004). CORMs are currently undergoing assessment in Phase III clinical trials (Motterlini & Otterbein, 2010), therefore it is possible that these molecules will provide safe and effective targeting of therapeutic levels of CO, as reviewed by Foresti *et al.* (2008), although tissue selectivity remains an issue to be resolved.

1.6 Aims of the present study

Numerous cardiovascular disorders involve excess proliferation of VSMCs, therefore limiting this adverse response may confer beneficial effects. HO-1 is up-regulated during disorders of vascular remodelling and is associated with cytoprotective effects. HO-1 induction is the major pathway of endogenous CO production, and this vital gasotransmitter is gaining a reputation as a possible therapeutic agent. Moreover, CO has anti-proliferative effects on VSMCs and pro-proliferative effects on ECs, indicating that this signalling molecule could promote the optimal conditions to limit vascular remodelling. The phenotypic switch of VSMCs involves extensive modulation of Ca^{2+}

signalling, which in turn involves the maintenance of $[Ca^{2+}]_i$ appropriate for cell proliferation and gene expression. Both the T-type Ca^{2+} channel and TRPC channels appear to have prominent roles in proliferative VSMCs, as their expression is heavily linked to the cell cycle, and they allow Ca^{2+} influx at RMP. Our research group has recently discovered that CO can inhibit the T-type Ca^{2+} channel, with no effect on TRPC channels. Therefore, the aim of this study was to investigate whether the VSMC T-type Ca^{2+} channel could act as an anti-proliferative target for HO-1.

CHAPTER 2

Methods and Materials

2.1 Cell Isolation and Culture

2.1.1 WT HEK293 and HEK293/Ca_v3.2 Cells

Wild-type (WT) HEK293 cells (European Collection of Cell Cultures (ECACC), Health Protection Agency Culture Collection (HPACC), Salisbury UK) were grown in minimum essential medium (MEM; Gibco, Cambridge UK), containing 10% foetal bovine serum (FBS; Biosera, Ringmer UK), 1% non-essential amino acids (Gibco, Cambridge UK), 1% antibiotic/antimycotic (Gibco, Cambridge UK), and 0.1% gentamicin (Gibco, Cambridge UK). HEK293/Ca_v3.2 cells, engineered to over-express the human Ca_v3.2 subunit of the T-type Ca^{2+} channel (gift from Prof. E. Perez-Reyes; University of Virginia Virginia, USA), were cultured in WT HEK293 media as above, yet additionally supplemented with 1mg/ml G-418 (Gibco, Cambridge UK) to maintain selection for the transfected cells. HEK293 cells were passaged on a weekly basis from 75cm^2 flasks as follows: culture media was aspirated from the flask and replaced by 10ml of Dulbecco's phosphate buffered saline (PBS; Gibco, Cambridge UK), to wash the cells. The PBS was removed and replaced with 2ml of 0.05% trypsin-EDTA (Gibco, Cambridge UK) to promote cell detachment. After 2-3 minutes in a humidified incubator (37ºC; 95% air, 5% CO_2), the cells had detached from the flask. This cell suspension was transferred to a 50ml falcon tube along with 10ml of complete growth media (outlined above, Ca_v3.2 or WT as required) to neutralise the trypsin, and then centrifuged (600*g* for 6 minutes). The supernatant was removed leaving the cell pellet in the tube. If cells were to be propagated into new 75cm^2 flasks, 20ml of complete growth media (Ca_v3.2 or WT as required) was added to the cell pellet and the cells resuspended. Dilutions of this cell suspension were then performed at 1:20 and 1:40 for HEK293/Ca_v3.2 cells, and at 1:10 and 1:20 for WT HEK293 cells. Conversely, if cells were to be seeded at a specific density in 6- or 24-well plates, 1ml of complete media (Ca_v3.2 or WT as required) was added to the cell pellet, and the cells resuspended and counted to enable the required aliquot of cell suspension to be calculated. Subsequent sections outline the protocols for seeding cells for specific experiments. HEK293/Ca_v3.2 cells were used at passages between P1 and P8, and WT HEK293 cells were used at passages between P1 and P12.

2.1.2 A7r5 Cells

A7r5 cells (ECACC, HPACC, Salisbury UK) are smooth muscle cells derived from rat thoracic aorta (Kimes & Brandt, 1976). A7r5 cells were grown in Dulbecco's minimum essential medium (DMEM; Gibco, Cambridge UK), containing 10% FBS and 1% glutamax (Gibco, Cambridge UK), (Hall *et al.*, 2006), and kept in a humidified incubator (37ºC; 95% air, 5% CO_2). A7r5 cells were passaged weekly from 75cm^2 flasks following the same procedure as described above for HEK293 cells. The cell dilutions seeded into 75cm^2 flasks varied depending on when the cells were required to be confluent, a range of 1:5 to 1:40 was often seeded on a weekly basis. A 1:20 dilution became 80-90% confluent within a week. To maintain optimum cell viability, half the media in the flasks was changed twice weekly. A7r5 cells were used at passages between P1 and P6.

2.1.3 Human Coronary Artery Smooth Muscle Cells (HCASMC)

HCASMCs (ECACC, HPACC, Salisbury UK) were grown in complete smooth muscle cell growth medium (470ml of basal medium plus 30ml of growth supplement) as supplied by HPACC and maintained in a humidified incubator (37ºC; 95% air, 5% CO_2). HCASMCs were passaged weekly from 75cm^2 flasks following the same procedure as described above for HEK293 cells, with dilutions of 1:10 and 1:20 seeded into 75cm^2 flasks. To maintain optimum cell viability, half the media in the flasks was changed twice weekly. HCASMCs were used at passages between P1 and P6.

2.1.4 Human Saphenous Vein Smooth Muscle Cells (HSVSMC)

Smooth muscle cells were isolated from the saphenous vein of patients undergoing coronary bypass graft surgery at Leeds General Infirmary following ethical approval and informed patient consent. Ethical approval received from Leeds West Research Ethics Committee; reference number CA/01/040. Smooth muscle cell isolation was carried out using the medial pad of the vessel, after endothelial cells had been removed for culture. Segments of saphenous vein, around 1cm in length were cut open longitudinally, lumen facing upwards. The segment was then divided into two pieces. 2ml of complete medium (DMEM containing 10% foetal calf serum (FCS; Biosera, Ringmer UK), 1% L-glutamine (Gibco, Cambridge UK), and 1% penicillin/streptomycin (Gibco, Cambridge UK)), was transferred into a clean petri dish. A segment of vein was placed in the media. This was then cut up with a razorblade into fragments around 0.5cm^2 in size. This tissue and media mixture was then transferred to a 25cm^2 tissue

culture flask. Cells were kept in a humidified incubator at (37ºC; 95% air, 5% CO_2). Cells migrated out from these tissue fragments within 7-10 days and when 80-90% confluent, the cells were passaged using 1ml of 0.05% trypsin-EDTA into a 75cm^2 flask, and thereafter passaged at a ratio of 1:3. Half the media in the flasks was changed twice weekly and passaged when 80-90% confluent. The flask was washed with 10ml of PBS and then 2ml of 0.05% trypsin-EDTA was added to the cells. The flask was incubated in a humidified incubator (37ºC; 95% air, 5% CO_2) for 4-5 minutes until the cells detached. If propagation of more cells was required from this cell suspension, 30ml of complete medium was added to neutralise the trypsin then the suspension divided between three 75cm^2 flasks. Alternatively, if the cell suspension was required for seeding a specific density of cells, 10ml of complete medium was added to neutralise the trypsin then centrifuged (600*g* for 6 minutes). The supernatant was aspirated and the cell pellet re-suspended in 1ml of complete medium, then the cells were counted to enable the required aliquot of cell suspension to be calculated. Subsequent sections outline the protocols for seeding cells for specific experiments. HSVSMCs were used at passages between P1 and P6.

2.2 Proliferation Assay

2.2.1 Proliferation Assay Protocol

The techniques used for proliferation assays and cell counting were based on longstanding protocols from our research group (Porter *et al.*, 2002). Cells were plated in complete media at 1x10^4 cells per well in 24-well plates. HSVSMCs and HCASMCs were allowed to adhere overnight and subjected to serum free or 0.5% serum containing media for 2.5 days respectively. This produced a quiescent state and cell cycle synchronisation of the whole cell population. As the growth medium for HCASMCs was purchased commercially, no details were given regarding the composition of the medium, except that it contained 5% serum and various growth factors. To quiesce the cells without inducing proliferation, a 1:10 dilution of the complete growth medium with basal medium was prepared to give a final serum concentration of 0.5%. This decision was also based on a preliminary experiment involving HSVSMCs, which is presented in results section 6.2.1. A7r5 cells, along with WT HEK293 and HEK293/Ca_v3.2 cells, were allowed to adhere for 6 hours and then subjected to serum free media overnight. On day 0 of the assay, serum free media was removed and 1ml of the relevant complete media added to each well, in addition to the required drug or compound being investigated. To count cells the media was removed

from the well, cells were washed with 1ml of PBS, and 200µl 0.05% trypsin-EDTA was added (pre-warmed to 37ºC). Post-incubation 800µl of complete media was added and the cell suspension centrifuged (600*g* for 6 minutes). Following removal of 950µl of media, 50µl of supernatant remained with the cell pellet, which was then re-suspended with 50µl of 0.4% Trypan Blue (Thermo Scientific, Rockford USA) to exclude unviable cells. Media was retained from one well of each treatment, processed in the same manner as the cell samples, and any cells present were counted as a quantification of non-viable, floating cells. Day zero counts and media counts were performed using a hemocytometer. All other counts were performed using a hemocytometer initially, until a TC10 Automated Cell Counter (Bio-Rad, Hemel Hempstead UK) was acquired. Data produced using the TC10 was validated by counting samples on both the hemocytometer and the TC10 over a period of 3 weeks with HSVSMCs, and WT HEK293 and HEK293/Ca_v3.2 cells. All data was comparable with the exception of day 0 counts as fewer cells were present in these samples, and it was therefore decided that the hemocytometer would give more accurate day 0 data.

2.2.2 Determination of Proliferation Assay Length

Optimal assay length for HEK293 cells had been previously determined in the laboratory. A 3 day proliferation assay was adopted as this was adequate to demonstrate significant changes in the growth curves of HEK293/Ca_v3.2 cells and WT HEK293 cells. A 3 day proliferation assay was also adopted for A7r5 cells based on the growth characteristics observed between passages in 75mm^2 flasks, and preliminary proliferation assays. The optimal assay length for HSVSMCs and HCASMCs was determined via the proliferative response to 0.4% and 10% serum, as described in results section 6.2.1.

2.3 Sodium-Dodecyl Sulphate Polyacrylamide Gel Electrophoresis

2.3.1 Cell Lysis and Protein Extraction of samples

HSVSMCs, A7r5 and HEK293 cells used for western blotting were plated at 3x10^4 cells/ml in 6-well plates. The cells were allowed to establish and become 80-90% confluent, then the wells were replenished with 0.4% serum media and the required treatment added. Post-treatment, the cells were washed once with PBS and lysed via incubation for 30 minutes with 200µl Mammalian Protein Extraction Reagent (M-PER^{TM}), (Thermo Scientific, Rockford USA) containing Complete Mini protease inhibitor

(Roche Diagnostics Ltd, Lewes UK; 1x Complete Mini protease inhibitor tablet per 10ml Mammalian Protein Extraction Reagent). The cell lysates were retrieved in a 1.5ml microcentrifuge tube using a cell scraper, centrifuged on a short spin for 10 seconds, and frozen at -20ºC until required.

2.3.2 Membrane Enrichment of HSVSMC samples

To detect the $Ca_v3.2$ and $Ca_v3.1$ T-type Ca^{2+} channels via western blotting in A7r5 cells and HSVSMCs the cell lysates required membrane enrichment. The following protocol was used for lysates from a 6-well plate. Subsequently the harvested lysates were kept on ice at all times.

Cells were washed in ice-cold PBS and incubated with 1ml of 0.05% trypsin-EDTA for 3-4 minutes. To neutralise the trypsin 3ml of ice-cold PBS was added to the wells and all the cell suspension removed into a 50ml falcon tube. A further 10ml of ice-cold PBS was added then the suspension centrifuged (600*g* for 2 minutes at 4^0C). The supernatant was discarded and cell pellets homogenized (passed x12) using a teflon homogeniser (Wheaton, Millville, USA) in 1ml ice-cold membrane enrichment buffer (50mM Tris HCl, 140mM KCl, 1mM EGTA, 1mM $MgCl_2$, 1x Complete Mini protease inhibitor tablet, pH 7.4). This suspension was then centrifuged (600*g* for 2 minutes at 4^0C) to pull down any remaining intact cells. The supernatants were then removed and centrifuged (1600*g* for 40 minutes at 4^0C). The cell pellets were then solubilised in 100µl M-PER™ containing Complete Mini protease inhibitor via ultrasonic agitation. Lysates were frozen at -20ºC until required, and kept on ice when defrosted until used.

2.3.3 Immunoprecipitation

Immunoprecipitation was also employed to improve detection of the $Ca_v3.2$ and $Ca_v3.1$ channels via western blotting in A7r5 cells and HSVSMCs. The following protocol was used for lysates from a 6 well plate. The harvested lysates were kept on ice at all times. Cell lysates were solubilised in 500µl ice-cold M-PER™ containing Complete Mini protease inhibitor and centrifuged at 10,000g for 5 minutes. Following retrieval of the supernatant, 15µl protein A sepharose beads (Sigma, Gillingham UK), 15µl protein G sepharose beads (Sigma, Gillingham UK) and 5µg of $Ca_v3.2$ or $Ca_v3.1$ antibody was added, then the sample placed on a GyroMini™ nutating mixer overnight at 4ºC. The following day the sample was centrifuged (5000g for 5 minutes), the supernatant discarded, and the beads were then washed to remove any unbound proteins with 1ml

of sterile PBS. The sample was then placed on a GyroMini™ nutating mixer at 4ºC for 20 minutes. This step was repeated for a total of 3 washes. The sample was then centrifuged (20,000g for 5 minutes), the supernatant was discarded, and 20µl of 4x sample buffer (detailed in table 2.1) was added to the beads. This was allowed to incubate for 20 minutes to maximise protein elution, followed by centrifugation (20,000g for 5 minutes), and the sample then transferred to the gel for electrophoresis.

2.4 Bicinchoninic acid protein assay

This assay (Thermo Scientific, Rockford USA) allows quantification of total protein levels in samples, which enables normalisation of protein loading onto gels for electrophoresis. Under alkaline conditions, proteins in the sample reduce Cu^{2+}, which is then chelated by bicinchoninic acid, producing a colour change from green to purple. The total protein level in each sample is proportional to the intensity of the purple colour formed, which is determined by colorimetry (Smith *et al.*, 1985). The amount of protein in each sample can then be determined from a standard curve. Bovine serum albumin (BSA) protein standards were used with a range of 0-2000µg/ml. 10µl of standards and 2.5µl of samples with unknown protein levels were pipetted into separate wells of a 96-well plate and 200µl of working reagent added to each well. After a 30 minute incubation period at 37ºC, the plate was allowed to cool to room temperature (RT) and absorbance read at 570nm. The appropriate ratio of sample to sample buffer, (detailed in table 2.1), was determined using Graphpad Prism 6. These sample solutions were allowed to stand for 15 minutes at RT to maximise protein denaturisation prior to loading onto the gel for electrophoresis.

2.5 Gel Electrophoresis

Gel electrophoresis was performed to separate the proteins in the cell lysate samples to allow subsequent isolation and visualisation of the protein band of interest. Separating gels were prepared using the reagents shown in table 2.2. The size of the protein of interest dictated the percentage of acrylamide in the gel. For example the HO-1 protein is approximately 32kDa, so a 10% or 12% gel is sufficient. However, the $Ca_v3.2$ and $Ca_v3.1$ T-type Ca^{2+} channels are much larger proteins of approximately 250kDa, therefore a gel with a larger pore size is required to allow the larger proteins to move through the gel, which dictates the use of a 7.5% acrylamide gel.

Reagent	1x Sample buffer
Tris HCl	125mM
SDS (w/v)	2%
EDTA	2mM
EGTA	2mM
Glycerol (w/v)	20%
β-mercaptoethanol (v/v)	10%
Bromophenol blue (v/v)	1%

Table 2.1 Composition of sample buffers used for gel electrophoresis
(All compunds from Sigma, Gillingham UK)

Reagent	Resolving Gel			Stacking Gel
Acrylamide %	12%	10%	7.5%	4%
Acrylamide (30%)	6.25ml	5ml	3.75ml	1ml
Ammonium persulphate	1.5ml	1.5ml	1.5ml	0.5ml
Distilled Water	3.5ml	4.75ml	6ml	2.35ml
Separating Gel Buffer (1.5M Tris Base pH8.8, 0.4% w/v SDS)	3.75ml	3.75ml	3.75ml	-
TEMED	15µl	15µl	15µl	2.5µl
Stacking Gel Buffer Buffer (0.5M Tris Base pH6.8, 0.4% w/v SDS)	-	-	-	1.25ml

Table 2.2 Composition of electrophoretic gels

Gels were cast and a layer of isobutan-2-ol was pipetted on top of the separating gel to ensure a flat, even surface. Once the separating gel had polymerised, the isobutan-2-ol was poured off. A few grains of phenol red (Acros Organics, Geel Belgium) were added to the 4% stacking gel solution to allow visualisation of the wells, and this stacking gel solution was pipetted on top of the separating gel. 0.75mm combs were inserted at an angle to force out any air bubbles. Once polymerisation of the stacking gel had occurred, the gels were run on vertical mini gel (11 x 11cm) apparatus (Mini Protean III electrophoresis cell, Bio-Rad, Hemel Hempstead UK). The gel cassette sandwich was placed in the electrode assembly and running buffer added (25mM Tris, 192mM glycine, 0.1% w/v SDS, Bio-Rad, Hemel Hempstead UK). Combs were removed and

the samples and molecular weight markers pipetted slowly into the wells to prevent overflow. Running time was approximately 1 hour at 35mA, or until the markers of interest were in the correct position.

2.6 Western Blotting

2.6.1 Electrophoretic Transfer

After separation, proteins were transferred onto 0.45µm Immobilon-P polyvinylidine difluoride membrane (Millipore Corporation, Massachusetts USA). The membrane, along with x2 Mini Trans Blot filter paper (Bio-Rad, Hemel Hempstead UK) and x2 sponges, were soaked in methanol (Fisher Scientific, Rockford USA) and then in transfer buffer (600ml ddH_20, 70ml Tris-Glycine transfer buffer (Invitrogen, Cambridge UK), and 30ml methanol). The blotting sandwich was assembled in cassettes as follows: Anode(+), sponge, filter paper, membrane, gel, filter paper, sponge, Cathode(-). The cassettes were placed in a Mini Trans-Blot electrophoretic transfer cell (Bio-Rad, Hemel Hempstead UK) and subjected to 30V overnight.

2.6.2 Immunodetection

Post transfer, the membranes were removed from the cassettes and soaked in methanol, followed by blocking in 5% (w/v) Marvel non-fat dried milk powder in TBST (tris-buffered saline (TBS) containing 0.05% (v/v) Tween-20) for 1 hour. The membranes were then incubated with primary antibody for 3 hours at RT in 5% Marvel in TBST (see table 2.3 for dilutions of the anitbodies used). For loading control, β-actin (Sigma, Gillingham UK) was used at 1:4000. The membranes were then washed in TBST for 30 minutes, with the TBST changed every 5 minutes. Following this wash protocol, the membranes were then incubated with the corresponding anti-rabbit or anti-mouse peroxidase conjugated secondary antibody (GE Healthcare, Amersham UK) at 1:2000 dilution in 5% Marvel in TBST for 1 hour at RT. The wash protocol was then followed again. Protein bands were detected using the enhanced chemi-luminescent (ECL) method (GE Healthcare, Amersham UK). The secondary antibodies used (see table 2.3), are conjugated to horseradish peroxidase (HRP) which catalyses a substrate in the ECL detection reagent, producing chemiluminescence that was detected on hyperfilm (GE Healthcare, 2012). The hyperfilm was scanned using Canon 5600F scanner and densitometric analysis performed using Image J (NIH UK). The expression of HO-1 was normalised to β-actin in each instance.

	Anti-HO-1 (Santa Cruz, SC-10789)	**Anti-Cav3.1 (Santa Cruz, SC-16259)**	**Anti-Cav3.2 (Santa Cruz, SC-16263)**	**Anti-Cav3.1 (Alomone, ACC-021)**	**Anti-Cav3.2 (Alomone, ACC-025)**
Polyclonal/ Monoclonal	Rabbit Polyclonal	Goat Polyclonal	Goat Polyclonal	Rabbit Polyclonal	Rabbit Polyclonal
Western Blotting Dilution	1:200	1:200	1:200	1:200	1:200
Western blotting Secondary Antibody	Anti-Rabbit ECL HRP Linked (GE Healthcare) 1:2000	Anti-Goat ECL HRP Linked (GE Healthcare) 1:2000	Anti-Goat ECL HRP Linked (GE Healthcare) 1:2000	Anti-Rabbit ECL HRP Linked (GE Healthcare) 1:2000	Anti-Rabbit ECL HRP Linked (GE Healthcare) 1:2000
Immunocytochemistry Dilution	1:50	1:50	1:50	1:50	1:50
Immunocytochemistry Secondary Antibody	Goat Anti-Rabbit Alexa Fluor^{488} (Invitrogen, Cambridge UK)	Donkey Anti-Goat Alexa Fluor^{488} (Invitrogen, Cambridge UK)	Goat Anti-Goat Alexa Fluor^{488} (Invitrogen, Cambridge UK)	Goat Anti-Rabbit Alexa Fluor^{488} (Invitrogen, Cambridge UK)	Goat Anti-Rabbit Alexa Fluor^{488} (Invitrogen, Cambridge UK)

Table 2.3 Primary and secondary antibodies used in western blotting and immunocytochemistry
(Santa Cruz Biotechnology Santa Cruz USA, Alomone Jerusalem Israel)

2.7 Immunocytochemistry

Cells used for immunocytochemistry were plated on sterile glass coverslips (22x22mm, thickness 0) in 6-well plates at $1x10^4$ cells/ml for A7r5 cells and HSVSMCs, and at $2x10^4$cells/ml for HEK293 cells. To enhance the adherence of HEK293 cells, 1.5ml polylysine (Sigma, Gillingham UK) was added to each well containing the coverslip and removed after 30 seconds. Once the wells were completely dry, the cells were then plated. This was not required for A7r5 or SVSMCs. If HO-1 induction was required, cells were allowed to adhere to the coverslips for 24 hours and then the correct protoporphyrin added for 48 hours. Post-treatment, the media was removed and the coverslips were washed with PBS (3x5 minutes). The cells were then fixed with 4% paraformaldehyde in PBS for 20 minutes. This was followed by incubation for 20 minutes at RT in PBS containing 0.2% Triton X100 and 10% normal goat serum (NGS; Sigma, Gillingham UK), or BSA (Sigma, Gillingham UK) if the primary antibody was raised in goat. The coverslips were then washed again with PBS (3x5minutes), followed by a wash with PBS containing 1% NGS/BSA for 2 minutes. The primary antibody was diluted in PBS containing 1% NGS/BSA. See tables 2.3 and 2.4 for details of the antibodies used. The coverslips were incubated with primary antibody overnight at 4ºC in an air-tight box lined with wet tissue paper.

The following day the coverslips were washed with PBS (3x5 minutes). The secondary antibody was used at 1:1000 in PBS containing 1% NGS/BSA. 1ml/well was incubated for 1 hour in the dark at RT. The coverslips were again washed with PBS (3x5 minutes). Coverslips were mounted on glass slides using 20µl Vectasheild containing DAPI (Vector Laboratories, Burlingame USA) and the edges sealed with nail varnish. The slides were allowed to dry in the dark, then visualised using a Zeiss laser scanning confocal microscope (LSM510), (Oberkochen, Germany), and Zeiss AIM software. LSM Image Browser software was used to produce images. Settings were identical for each condition.

2.7.1 HO-1

Immunocytochemistry was performed in HSVSMCs, A7r5, HEK293/Ca_v3.2, and WT HEK293 cells to visualise HO-1 after induction with Cobalt Protoporphyrin IX (CoPPIX; Sigma, Gillingham UK) or Hemin Chloride (Calbiochem, Darmstadt Germany). The cells were allowed to adhere for 24 hours then treated for the required time period. The details of the antibodies used are listed in table 2.3.

	Dilution	Polyclonal/Monoclonal	Secondary Antibodies
Anti α-SM Actin (Clone 1A4) (A2547, Sigma, Gillingham UK)	1:300	Mouse Monoclonal	Donkey Anti-Mouse Alexa Fluor^{555} (Life Technologies, Cambridge UK)
Anti-Vimentin (V9) (Santa Cruz Biotechnology sc-6260, Santa Cruz USA)	1:50	Mouse Monoclonal	Donkey Anti-Mouse Alexa Fluor^{555} (Life Technologies, Cambridge UK)
Anti-SM Myosin Heavy Chain (H-44) (Santa Cruz Biotechnology sc-98705, Santa Cruz USA)	1:50	Rabbit Polyclonal	Goat Anti-Rabbit Alexa Fluor^{488} (Life Technologies, Cambridge UK)

Table 2.4 Primary and secondary antibodies used in immunocytochemistry for cell characterisation

2.7.2 Cav3.2 and Ca_v3.1 T-type Ca^{2+} channels

Immunocytochemistry was performed in HSVSMCs, A7r5 cells, HEK293/Ca_v3.2, and WT HEK293 cells to demonstrate the presence or absence of the Ca_v3.2 T-type Ca^{2+} channel. The above protocol was followed using two different Ca_v3.2 primary antibodies as listed in table 2.3.

2.7.3 Cell Characterisation

HSVSMCs and A7r5 cells were subject to immunocytochemistry using the antibodies listed in table 2.4 to characterise them as smooth muscle cells.

2.8 Detection of Caspase-3/7 Activation via CellEvent™

Activation of caspases 3 and 7 were monitored fluorogenically via CellEvent™ Caspase-3/7 detection reagent (Molecular Probes, Cambridge UK). The reagent consists of a nucleic acid binding dye conjugated to a four amino acid peptide. Upon activation of caspases 3 and 7, the four amino acid peptide is removed allowing the dye to bind to DNA and fluoresce. Maximal absorbance is measured at 530nm.

This experiment was employed as an alternative to trypan blue exclusion and media counts, to determine conclusively whether the drugs used in proliferation assays cause an inhibition of proliferation as opposed to apoptosis. A7r5 cells were plated at $2x10^4$ cells/ml on sterile square glass coverslips (22x22mm, thickness 0) in a 6-well plate. Cells were allowed to adhere overnight then the following morning the media in the wells was replenished and treated the with the appropriate compound. As a positive control, one well was treated with 2µM staurosporine (Sigma, Gillingham UK), an established inducer of apoptosis (Bertrand *et al.*, 1994), for 3 hours on day 3 of the assay. All wells were then washed briefly with PBS, then 8µM CellEvent™ added to each well. Cells were incubated for 30 minutes at RT in the dark. All wells were washed again with PBS and two drops of NucBlue™ Live Cell Stain (Hoechst 33342), (Molecular Probes, Cambridge UK), added per ml of PBS. Cells were again incubated for 20 minutes at RT in the dark. Cells were then washed for 5 minutes with PBS, fixed with 4% paraformaldehyde for 20 minutes, mounted using 20µl Vectasheild without DAPI (Vector Laboratories, Burlingame USA), and sealed with nail varnish. Cells were imaged with a Nikon E600 light microscope (Nikon, Kingston upon Thames UK), x40 lens, and Q Imaging Micropublisher ACQuis (Syncroscopy) software.

2.9 Measurement and analysis of $[Ca^{2+}]_i$

2.9.1 Measurement of $[Ca^{2+}]_i$ by microfluorimetry

Microfluorimetry was performed to monitor $[Ca^{2+}]_i$ of A7r5, HEK293/Ca_v3.2 and WT HEK293 cells. Fura 2-AM (Invitrogen, Cambridge UK) was used as the $[Ca^{2+}]_i$ indicator for the microfluorimetry experiments. Fura 2-AM is an acetoxymethyl (AM) ester and it is this AM group which confers hydrophobicity to the otherwise hydrophilic dye, allowing passage through the cell membrane (Paredes *et al.*, 2008). The action of intracellular esterases ensures the dye remains inside the cell by hydrolysing the AM group. This high affinity fluorescent dye is ratiometric. On Ca^{2+} binding the peak excitation wavelength shifts from 380nm to 340nm (Paredes *et al.*, 2008), which is

illustrated in figure 2.1. Higher $[Ca^{2+}]_i$ produces an increase in emission intensity at 510nm when Fura 2 is excited at 340nm, whereas lower $[Ca^{2+}]_i$ produces an increase in emission intensity at 510nm when Fura 2 is excited at 380nm. The ratiometric property of Fura 2 allows for any differences in dye loading, cell size, and cell volume in the recording field to be overcome, therefore allowing data from different experiments to be compared (Paredes *et al.*, 2008), and for the shift in excitation wavelength to correlate directly to $[Ca^{2+}]_i$ (Duchen, 1992).

$[Ca^{2+}]_i$ can be determined from the Fura 2 ratio using the following equation (Grynkiewicz *et al.*, 1985):

$$[Ca^{2+}] = K_d S_{f2} / S_{b2} (R – R_{min} / R_{max} – R)$$

Where:

K_d is the dissociation constant for Fura 2, which is the $[Ca^{2+}]_i$ when the concentration of Ca^{2+} bound and free Fura 2 are equal.

R is the fluorescence ratio defined as the fluorescence intensity induced by λ_1 (F_1 340nm) divided by the fluorescence intensity induced by λ_2 (F_2 380nm), (I_{340}/I_{380}).

R_{min} is the R recorded when the $[Ca^{2+}]$ is 0.

R_{max} is the R recorded when the $[Ca^{2+}]$ is a maximum or much higher than K_d.

S_{f2} is F_2 when Ca^{2+} is not bound to Fura 2 and S_{b2} is F_2 when Fura 2 is fully bound to Ca^{2+}.

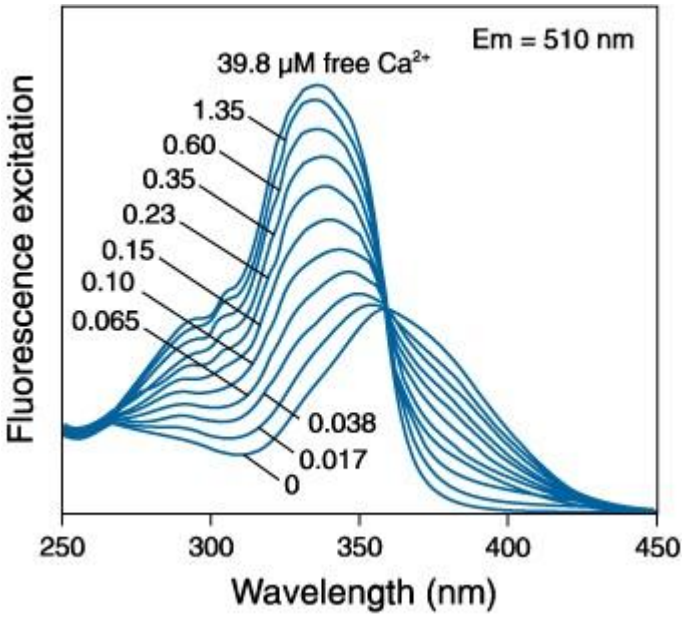

Figure 2.1 Fluorescence excitation spectra of Fura 2-AM in solutions containing 0-39.8µM free Ca^{2+} (Diagram taken from www.invitrogen.com)

The determination of $[Ca^{2+}]_i$, however, is not without limitations. To calculate $[Ca^{2+}]_i$ precisely, K_d must be determined for each cell type and fluorescent indicator (Neher, 2000), which varies with temperature, pH, and Mg^{2+} levels (Paredes *et al.*, 2008). Additional issues associated with the indicator can also contribute to inaccuracies, such as compartmentalisation of the indicator, and sub maximal hydrolysis which produces fluorescence without Ca^{2+} sensitivity (Duchen, 1992;Neher, 2000) For these reasons, changes in $[Ca^{2+}]_i$ were expressed as changes in Fura 2 ratio in this thesis.

For all Ca^{2+} microfluorimetry experiments A7r5 and HEK293 cells were plated on circular glass coverslips (10mm, thickness 0) in 24 well plates at a 1:3 dilution for A7r5 cells, and at a 1:5 dilution for HEK293 cells. Previous to cell plating, 1ml polylysine was added to each well containing the coverslip and removed after 30 seconds. Once the wells were completely dry the cells were then plated and kept in a humidified incubator (37ºC; 95% air, 5% CO_2), until the cell monolayer was confluent. The coverslip was transferred to a 35mm petri dish and cells were loaded with 4µM Fura 2-AM (dissolved in Ca^{2+} containing buffer) for 40 minutes. The cells were then washed with 1ml of Ca^{2+} containing buffer and then incubated in Ca^{2+} containing buffer for 15 minutes to allow de-esterification of the loaded dye. During both incubations the petri dish was wrapped in foil and kept in a dark drawer at RT. Table 2.5 lists the buffer compositions.

	Normal (Ca^{2+}-containing)	**Ca^{2+}-Free**	**20mM K^+**	**80mM K^+**	**80mM K^+/ Ca^{2+} Free**
NaCl	135mM	135mM	120mM	60mM	60mM
KCl	5mM	5mM	20mM	80mM	80mM
$MgCl_2$	1.2mM	1.2mM	1.2mM	1.2mM	1.2mM
HEPES	5mM	5mM	5mM	5mM	5mM
D-Glucose	10mM	10mM	10mM	10mM	10mM
Sucrose	300mOsm	300mOsm	300mOsm	300mOsm	300mOsm
$CaCl_2$	2.5mM	-	2.5mM	2.5mM	-
EGTA	-	1mM	-	-	1mM

Table 2.5 Composition of 1L buffers used in Ca^{2+} microfluorimetry
(All compunds from Sigma, Gillingham UK)

Composition of Ca^{2+}-containing buffer (in mM): NaCl 135, KCl 5, $MgSO_4$ 1.2, $CaCl_2$ 2.5, HEPES 5, glucose 10, osmolarity adjusted to 300 mOsm with sucrose, pH 7.4. Ca^{2+}-free buffere as above minus $CaCl_2$ 2.5, plus 1mM EGTA.

Coverslip segments were loaded into a perfusion chamber (volume approximately 80µl) on an inverted epi-fluorescence microscope with the required buffer perfused via gravity at 2-3ml/min. The perfusion system consisted of four 60ml disposable syringes which acted as reservoirs (Merck, Feltham UK), connected to a 6 way tap (Hamilton GB Ltd., Birmingham UK) via Tygon tubing (2.5mm outside diameter, 0.83mm inside diameter; Merck, Feltham UK). Buffer was delivered from the tap to the perfusion chamber by Tygon tubing. Various compounds and drugs were used to alter the activity of the T-type Ca^{2+} channels, L-type Ca^{2+} channels and HO-1 (see section 2.14 and specific results chapters for details), and these were applied to the perfusion chamber from the appropriate reservoir via the Hamilton tap as and when required. A suction tube connected to a peristaltic pump (Gilson, Minipulse 3, Anachem, Luton UK) was used to continuously remove the perfusate from the chamber.

The cellular Ca^{2+} responses were recorded using a Cairn Research ME-SE Photometry system (Cairn Research, Faversham UK). Acquisition Engine 1.6.1 software was used to visualise the wavelength traces. Plotting and analysis of the data was done using Graphing (in house program) and GraphPad Prism version 6 (GraphPad Software, Inc., La Jolla USA).

2.9.2 Analysis of microfluorimetry traces from A7r5 cells

It was noted that the response of A7r5 cells to 20mM K^+ buffer declined over time with each subsequent exposure. This can be seen in Figure 2.2 (A), the response to each exposure numbered from 1 to 3. These three consecutive responses on the control traces were analysed to determine the standard to which to compare the effects of any drugs or compounds. Two sets of data were retrieved for each exposure to 20mM K^+ buffer; these were the change in Fura 2 ratio, and spikes per second (spikes/s). The change in Fura 2 ratio is illustrated in Figure 2.2 (B), and calculated by subtracting the basal Fura 2 level (F_1) from the Fura 2 level in response to K^+ buffer (F_2). These Fura 2 ratio values were taken as the response reached plateau. Spikes/s were achieved by dividing the time period (in seconds) of each exposure to 20mM K^+ buffer, by the number of spikes for the response during this exposure. This is illustrated in Figure 2.2 (C). The same analyses were performed on the traces from A7r5 cells in response various compounds or drugs.

The Graphing program was also used to calculate the integral of the response of A7r5 cells to 80mM K^+ buffer. Exposure to 80mM K^+ buffer was timed, and the integral of the curve for the initial 200 seconds was determined. This is illustrated in Figure 2.3; the integral of the curve bound by the red lines was calculated for all traces. This time-point was chosen to demonstrate the different responses to the various compounds used as some responses were extremely brief with a rapid return to baseline, whereas the control traces would continue to decline slowly, possibly not returning to baseline within an ideal timeframe in which to monitor the cells. Therefore, a snapshot of the initial response was assessed for all traces.

2.9.3 Analysis of microfluorimetry traces from HEK293 cells

An example of how traces from HEK293/$Ca_v3.2$ and WT HEK293 cells were analysed is shown in Figure 2.4. The response to normal buffer (F_1) was compared to the response to Ca^{2+} free buffer, or normal buffer plus specified compound (F_2) on each trace. The Fura 2 ratio of each response was recorded from a plateau level.

2.10 Real-Time Polymerase Chain Reaction (RT-PCR)

The basal expression of $Ca_v3.2$ and $Ca_v3.1$ mRNA in A7r5 cells and HSVSMCs was quantified via RT-PCR. This technique was then used to monitor changes in mRNA expression post-siRNA knockdown of the $Ca_v3.1$ gene (CACNA1G) in A7r5 cells.

2.10.1 RNA generation

To determine the expression levels of $Ca_v3.2$ and $Ca_v3.1$ channels, T25 flasks of 70-80% confluency were washed with PBS and cells dissociated using 0.5ml 0.05% trypsin-EDTA for 3 minutes (37ºC; 95% air, 5% CO_2). Enzyme activity was halted by adding 0.5ml ice-cold PBS, the cell suspension was then centrifuged (600*g* for 6 minutes). If RNA was not to be generated immediately, the supernatant was discarded and the cell pellets dispersed in 100µl of RNA*later*® (Ambion, Cambridge UK) and frozen at -20ºC until required.

RNA was generated from whole cell lysates using the Aurum Total RNA Mini Kit (Bio-Rad, Hemel Hempstead UK). The RNA*later*® solution containing the cells was centrifuged (600*g* for 6 minutes) then the supernatant discarded. 350µl of lysis solution was added to each cell pellet, and the cells were dispersed by pipetting up and down

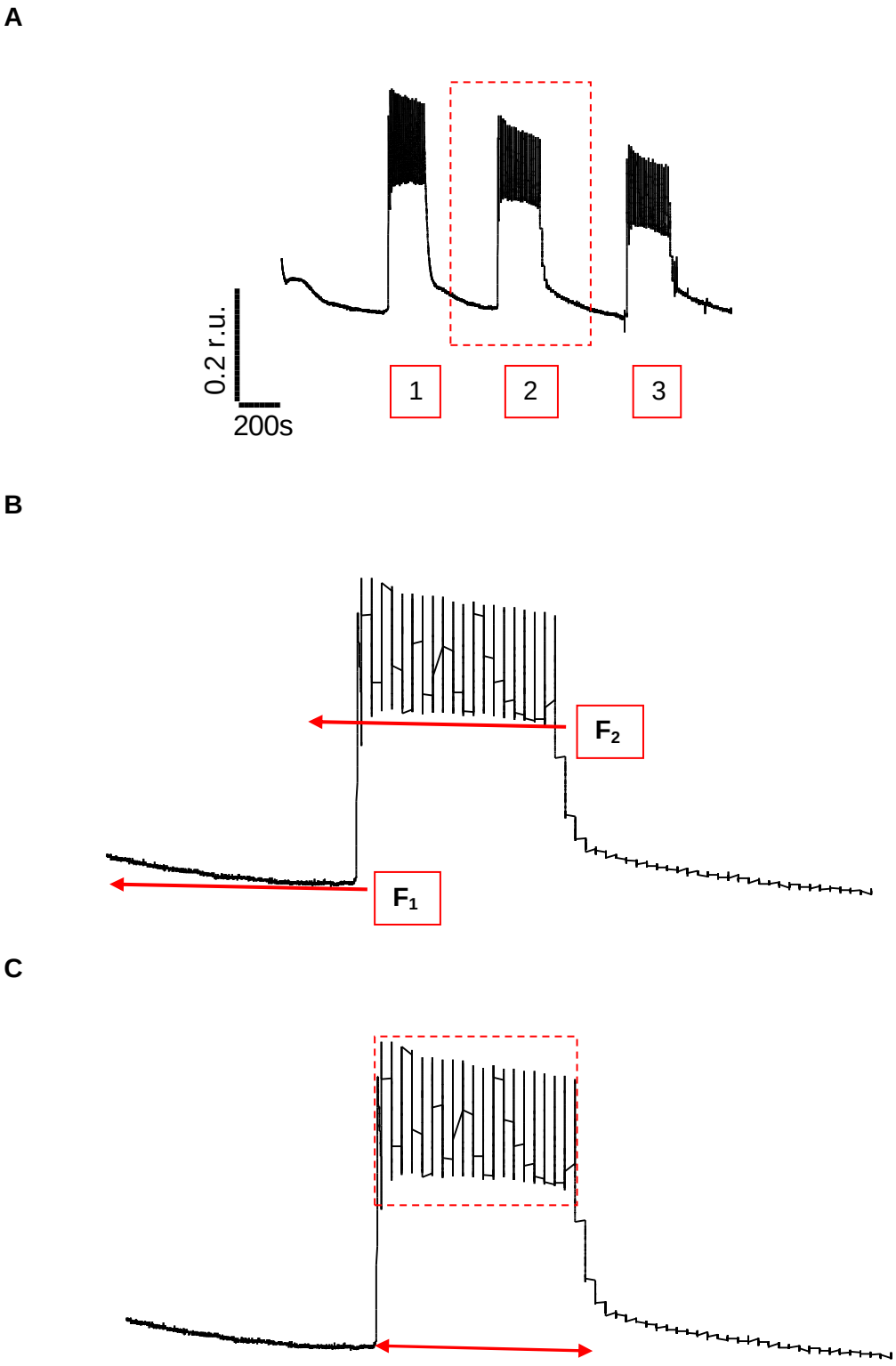

Figure 2.2 Details of how A7r5 traces were analysed

(A) Representative A7r5 control trace. (B) Enlarged view of the highlighted centre section demonstrating how the change in Fura 2 ratio was determined. (C) Demonstration of how spikes per second were calculated.

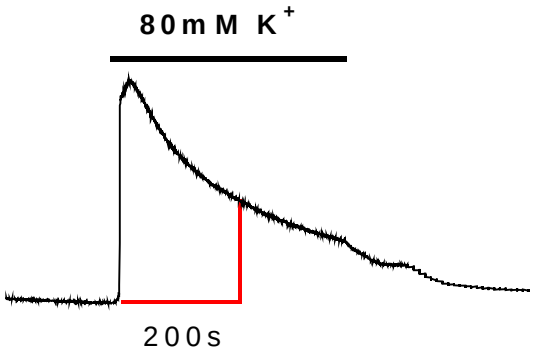

Figure 2.3 Illustration of the 200s integral calculated for all A7r5 cell traces in response to 80mM K^+ buffer

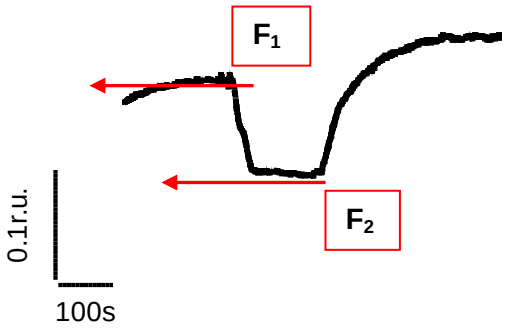

Figure 2.4 Details of how HEK293 traces were analysed

approximately 15 times. Then 350µl of 70% ethanol (molecular biology grade, Sigma, Gillingham UK) was added, and the solution mixed by pipetting up and down approximately 15 times. Each lysate was transferred to a spin column inserted in a 2ml collection tube and centrifuged (13000*g* for 30 seconds). Flowthrough was discarded and 700µl of low stringency wash was added, the columns then centrifuged (13000*g* for 30 seconds). Again flowthrough was discarded and 75µl DNase Incubation Mix (5µl DNase I: 75µl DNase Dilution Solution) added to each column. This was incubated at RT for 15 minutes then centrifuged at 13000*g* for 30 seconds. Flowthrough was discarded, 700µl of high stringency wash solution was added, then the columns centrifuged (13000 *g* for 30 seconds). Flowthrough was again discarded, 700µl low stringency wash added and the columns centrifuged (13000*g* for 1 minute). Again, flowthrough was discarded and the columns centrifuged (13000*g* for a further 2 minutes). Each spin column was then placed in a new elution tube, 80µl of elution solution (pre-warmed to 70ºC) was added and incubated for 1 minute at RT. RNA was eluted by centrifugation (13000*g* for 2 minutes). RNA samples were frozen at -70ºC if cDNA was not generated immediately.

2.10.2 cDNA generation

A cDNA template was generated from RNA samples using the iScript cDNA Synthesis Kit (Bio-Rad, Hemel Hempstead UK). Firstly, 20µl of the reaction solution, as shown in table 2.6, was transferred into a dome-capped 0.2ml PCR tube, and placed in a bench top thermocycler (Applied Biosystems). The reaction samples were subjected to 5 minutes at 25^0C, followed by 30 minutes at 42^0C, 5 minutes at 85^0C, and then held at 4^0C.

Component	Volume per Reaction
5x iScript reaction mix	4µl
Reverse Transcriptase	1µl
Nuclease-free water	12.5µl
RNA template	2.5µl

Table 2.6 Composition of iScript reaction solution

2.10.3 RT-PCR

The reaction mix for each primer was prepared as outlined in table 2.7. The details of the primers used are outlined in table 2.8; rat primers employed for A7r5 cells, and human primers employed for HSVSMCs. Firstly, 18µl of RT-PCR reaction mix was added to the required wells of a 96 well PCR plate (Applied Biosystems, Cambridge UK), followed by 2µl of sample cDNA in the same pattern. The plate was then sealed with an optical adhesive cover, centrifuged briefly, and then placed in an RT-PCR machine (Applied Biosystems, Cambridge UK). The RT-PCR reaction was as follows: 2 minutes at 50ºC, 10 minutes at 95ºC,15 seconds at 95ºC for 60 cycles, then 1 minute at 60ºC.

Component	Volume per Reaction
Taqman Universal PCR Master Mix (Roche Diagnostics Ltd, Lewes UK)	10µl
Taqman Primer	0.5µl
RNase/DNase-free water (Gibco Cambridge UK)	7.5µl

Table 2.7 Composition of RT-PCR reaction mix

Primer	Species	Function
HPRT1 (hypoxanthine phosphoribosyltransferase 1)	Rat/Human	Endogenous House Keeper
B_2M ($\beta_2$microglobulin)	Rat/Human	Endogenous House Keeper
CACNA1G	Rat/Human	Target
CACNA1H	Rat/Human	Target

Table 2.8 RT-PCR Primer details (all from Applied Biosystems, Cambridge UK)

2.11 Stable Transfection of A7r5 cells with pcDNAhHO-1

To generate a cell line stably expressing human (hH-O1) HO-1, referred to hereafter as A7r5/hHO-1, cells were initially transfected with the pcDNA3.1/Neo (hHO-1) construct using the Genejammer transfection reagent (Agilent Technologies, Stockport UK) according to manufacturer's instructions. Stable A7r5/hHO-1 cell lines were achieved by antibiotic selection with 1mg/ml G-418, added to the medium 3 days after transfection. Selection was applied for 3-4 weeks (media changed every 4-5 days),

after which time individual colonies were isolated. To isolate individual clones, first the cells were washed with PBS, the top of the T75 flask broken and removed, and individual colonies enclosed with a greased cloning ring. Specifically, 200µl 0.05% trypsin-EDTA was added to each ring for 2 minutes then neutralised with an equal volume of FCS, gently triturated and subsequently transferred to an upright T25 and allowed to reach confluence. Next, cells were harvested by trypsinization and then transferred to T75 flasks for further culture and examination of hHO-1 expression. Generation of the pcDNA3.1/Neo (hHO-1) construct and A7r5/hHO-1 cell line was performed by Dr Jason L. Scragg.

Four clones were screened via western blotting for the HO-1 protein, and a clone which demonstrated a high level of HO-1 overexpression was chosen for further experiments. A7r5/hHO-1 cells were compared to control A7r5 cells via proliferation assays and monitoring of $[Ca^{2+}]_i$ responses by microfluorimetry, (as described previously), with or without HO-1 induction with 10µM CoPPIX.

2.12 Cell Transfection with HO-1-targeting siRNA

HSVSMCs were transfected using hHO-1-targeting siRNA (sc-35554; Santa Cruz Biotechnology, Santa Cruz USA). Numerous parameters needed to be confirmed in order to optimise the cell transfection protocol including which concentration of HO-1 siRNA produced the optimal mRNA knock-down, how long the mRNA knock-down would last, and as the HMOX1 gene is inducible, at what time-point the CoPPIX should be added to the cells.

2.12.1 Transfection Protocol for a 6 well plate

HSVSMCs were plated in four wells of a 6-well plate at $1x10^5$ cells/well (as determined by previous experiments) in complete growth medium without penicillin/streptomycin, and allowed to attach overnight. Mock and transfected cell groups were utilised. Mock groups were subjected to all transfection reagents with the exception of siRNA. On the day of transfection, Optimem (Invitrogen, Cambridge UK) and 0.4% FCS-containing media without penicillin/streptomycin were pre-warmed to 37ºC. Lipofectamine 2000® (Invitrogen, Cambridge UK) was used as the transfection reagent. The transfection solutions for a 6-well plate format are shown in tables 2.9-2.11. Tubes 1 and 2 were prepared separately, mixed gently, and left to stand for 5 minutes at RT. Tubes 1 and 2 were then combined and left to stand for 20 minutes at RT. Tube 3 was then added to

the solution and mixed gently. Media was removed from the cells, followed by a PBS wash, and 1.5ml of the appropriate solution (Mock or Transfected) was then added to each well. After 6 hours in a humidified incubator (37ºC; 95% air, 5% CO_2), the transfection media was removed and replaced with complete growth medium and the cells were then incubated for 2 days. Cell lysates were removed at the end of the incubation period using 200µl M-PER™ plus Complete Mini protease inhibitor per well. The plate was rocked for 30 minutes at RT. The wells were then scraped using a cell scraper, the lysates collected and centrifuged on a short spin for 10 seconds, and then frozen at -20ºC until required for western blotting.

Cell Group	**Tube 1**		**Tube 2**		**Tube 3**
	10µM siRNA	Optimem	Lipofectamine	Optimem	0.4%fcsw/opsf
Mock	-	375µl	5µl	370µl	750µl
Transfected	15µl	360µl	5µl	370µl	750µl

Table 2.9 Transfection volumes per well of each experimental group using 100nM siRNA

Cell Group	**Tube 1**		**Tube 2**		**Tube 3**
	10µM siRNA	Optimem	Lipofectamine	Optimem	0.4%fcs w/o psf
Mock	-	375µl	5µl	370µl	750µl
Transfected	7.5µl	367.5µl	5µl	370µl	750µl

Table 2.10 Transfection volumes per well of each experimental group using 50nM siRNA

Cell Group	**Tube 1**		**Tube 2**		**Tube 3**
	10µM siRNA	Optimem	Lipofectamine	Optimem	0.4%fcs w/o psf
Mock	-	375µl	5µl	370µl	750µl
Transfected	3.75µl	371.25µl	5µl	370µl	750µl

Table 2.11 Transfection volumes per well of each experimental group using 25nM siRNA

2.12.2 First transfection – determination of optimal HO-1-targeting siRNA

Transfection was performed in 6-well plates to evaluate the efficiency of mRNA knock-down using 25nM, 50nM, and 100nM siRNA following the protocol stated above, and protein knockdown verified by western blotting of protein lysates at 48 hours post transfection.

2.12.3 Second transfection – determination of the period of gene knock-down

Once the optimal concentration of siRNA had been determined, the experiment was performed once again, but over 4 days to determine the maximal time frame of mRNA knockdown. At day 2, the media and CoPPIX were replenished. Protein lysates were prepared sequentially each day for 4 days.

2.12.4 Proliferation assay post-transfection

Once the time period of gene knockdown and optimal siRNA concentration had been established, the transfection was performed in 24-well plates. Initially cells were plated at $1x10^4$ cells/well, prior to a 4 day proliferation assay in which cells were counted daily. Cells were plated in parallel at $1x10^5$ in 6 well plates to retrieve protein lysates for western blotting at days 2 and 4. The transfection protocol was performed as stated in 2.12.1, but with a smaller volume of 300µl transfection media per well for the 24 well plate format. The transfection solutions for a 24-well plate are stated in table 2.12.

Cell Group	**Tube 1**		**Tube 2**		**Tube 3**
	10µM siRNA	Optimem	Lipofectamine	Optimem	0.4%fcsw/opsf
Mock	-	75µl	1µl	74µl	150µl
Transfected	1.5µl	73.5µl	1µl	74µl	150µl

Table 2.12 Transfection volumes per well of each experimental group using 100nM siRNA

2.13 Cell Transfection with $Ca_v3.1$-targeting siRNA

Preliminary RT-PCR was performed on cDNA from A7r5 cells to determine the expression level of $Ca_v3.2$ and $Ca_v3.1$ T-type Ca^{2+} channels, and to screen $\beta_2$microglobulin (β2M) and hypoxanthine phosphoribosyltransferase 1 (HPRT1) as possible housekeeper genes. Once expression levels were known, and the appropriate

housekeeper gene chosen, cells were transfected using ON-TARGETplus SMARTpool rat CACNA1G siRNA (Dharmacon, Waltham USA). The protocol described in section 2.12.1 was followed, with the exception of the final step as cells were retrieved using trypsin, the activity of which was halted with ice-cold PBS, and the cells stored in 100µl RNA*later*® until RNA generation.

2.13.1 First transfection – determination of optimal Ca_v3.1-targeting siRNA concentration

Three concentrations of Ca_v3.1-targeting siRNA were employed; 25nM, 50nM and 100nM, and all cells retrieved at 48 hours post-transfection. The transfection volumes for a 6-well plate format are shown in tables 2.13-2.15. Dharmafect 2 (Dharmacon, Waltham USA) was utilised as the transfection reagent, as gene knock-down proved unsuccessful when Lipofectamine 2000® was utilised.

Cell Group	**Tube 1**		**Tube 2**		**Tube 3**
	5µM siRNA	Optimem	Dharmafect 2	Optimem	0.4%fcsw/o psf
Mock	-	200µl	3.5µl	196.5µl	1600µl
Transfected	20µl	180µl	3.5µl	196.5µl	1600µl

Table 2.13 Volumes for 50nM siRNA transfection for 1 well of each experimental group.

Cell Group	**Tube 1**		**Tube 2**		**Tube 3**
	5µM siRNA	Optimem	Dharmafect 2	Optimem	0.4%fcs w/o psf
Mock	-	200µl	3.5µl	196.5µl	1600µl
Transfected	10µl	190µl	3.5µl	196.5µl	1600µl

Table 2.14 Volumes for 25nM siRNA transfection for 1 well of each experimental group.

Cell Group	Tube 1		Tube 2		Tube 3
	5µM siRNA	Optimem	Dharmafect 2	Optimem	0.4%fcs w/o psf
Mock	-	200µl	3.5µl	196.5µl	1600µl
Transfected	4µl	196µl	3.5µl	196.5µl	1600µl

Table 2.15 Volumes for 10nM siRNA transfection for 1 well of each experimental group.

2.13.2 Second transfection – determination of the period of gene knock-down

A 3 day time-course was then performed with 50nM $Ca_v3.1$-targeting siRNA. This concentration was chosen on the basis of adequate knock-down, as demonstrated by RT-PCR. The cell transfection process was performed as described above, in 6-well plates and 24-well plates. Post-transfection, cells were counted daily from a 24-well plate, and retrieved daily for RT-PCR from both 6-well and 24-well plates, for a total of three days. The volumes for a 24-well plate are given in table 2.16. An untransfected cell group, which contained 0.4% FCS medium only, was also included in this experiment to determine whether any minor fluctuations seen with the housekeeper were due to the transfection process or a natural occurrence for this cell line.

Cell Group	Tube 1		Tube 2		Tube 3
	5uM siRNA	Optimem	Dharmafect 2	Optimem	0.4%fcs w/o psf
Mock	-	50µl	1µl	49µl	400µl
Transfected	5µl	45µl	1µl	49µl	400µl
Untransfected	-	-	-	-	500µl

Table 2.16 Volumes for 50nM siRNA transfection for 1 well of each experimental group.

2.14 Drugs

Table 2.17 outlines all the drugs used in experiments. Figure legends in results chapters provide more specific details.

Reagent	Solvent	Storage	Concentration used
CoPPIX	100mM NaOH	Freezer -20ºC, dark	0.1 - 30 µM
Hemin	100mM NaOH	Freezer -20ºC, dark	1 - 100 µM
QC-15	Distilled water	Freezer -20ºC	10 µM
Mibefradil	Distilled water	Freezer -20ºC	0.3 - 30 µM
NNC55-0396	Distilled water	Freezer -20ºC	3 µM
Nickel	Distilled water	Made fresh	1 - 250 µM
Nifedipine	100% Ethanol/DMSO	Freezer -20ºC, dark	0.5 - 4 µM
CORM-3	Distilled water	Freezer -20ºC	1 - 60 µM
iCORM-3	Distilled water	Freezer -20ºC	1 - 60 µM

Table 2.17 Drugs used in experiments

2.15 Statistical Analysis

Statistical analysis was performed using GraphPad Prism 6. Data are presented as mean ± standard error of the mean (s.e.m.). With regards to proliferation assay data, in some cases there was large variation in Day 0 counts, which impacted on the Day 3 or Day 4 comparisons. A higher Day 0 count inevitably resulted in a much higher end of assay count due to the exponential growth of the cells. In order to compare equivalent proliferative responses, the cell counts were normalised to Day 0 counts. This data was then transformed using the Y=log(Y) function, and the statistical analysis performed on this transformed data. Statistical significance is displayed on graphs showing the original, untransformed data. Ratio repeated measures one-way ANOVA was performed on concentration response curve data, with Dunnett's or Bonferroni's multiple comparison test as appropriate. With regards to time-course proliferation data, each proliferation curve was normalised, transformed, and then analysed by a two-way repeated measures ANOVA, with sample matching by time point. This was followed by Sidak's multiple comparison test between control and treated groups for each time point.

Samples from individual western blotting experiments were processed on the same gel, and run on duplicate gels within the same electrophoresis tank. The amount of protein loaded was maximised in every instance, but varied between experiments. The time

spent developing the films was also another source of variation, as this was dependent on how fresh the developer was, and also how much protein was loaded. Therefore, the use of repeated measures ANOVA is not appropriate for this data. HO-1 and β-actin levels of each gel lane were expressed as percentage area of the total blot, then HO-1 normalised to the corresponding β-actin. Densitometry data from western blots was analysed via one-way ANOVA, with Dunnett's or Bonferroni's multiple comparison test as appropriate.

All microfluorimetry data was analysed by two-tailed, paired t-test, excluding data in Figures 4.15, 4.16, 4.17, 5.2, 5.7, and 5.11, which was analysed via one-way ANOVA followed by Tukey's multiple comparison test. The 200s integrals from 80mM K^+ experiments on A7r5 cells were analysed by one-way ANOVA with Bonferroni's multiple comparison test. The corresponding sections of the bar graph were then shown in separate figures, as the data are presented systematically based on the drug used. RT-PCR data was analysed by one-way ANOVA, or two-way ANOVA, as appropriate, with Bonferroni's multiple comparison test.

CHAPTER 3

The role of T-type Ca^{2+} channels in cell proliferation and the inhibitory effects of CO and HO-1

3.1 Introduction

HO-1 is an inducible, stress-response protein that has cytoprotective effects within the vasculature, as discussed in detail in Chapter 1. HO-1 induction has been linked with many favourable effects on cardiovascular pathology; it is anti-oxidative, anti-apoptotic, anti-inflammatory, anti-proliferative, and it promotes vasodilation (Kim *et al.*, 2011b). Each of the by-products of HO-1 induction have positive attributes, yet CO is able to mediate the vast majority of these protective effects (Wu & Wang, 2005). Heme proteins are cellular targets of CO, one of which is sGC. Activation of sGC by CO is one pathway through which CO mediates its cytoprotective effects, another is via p38/MAPK activation (Kim *et al.*, 2006). The emerging topic of gasotransmitter regulation of ion channels links CO to alternative cellular targets. CO has been shown to be a modulator of numerous ion channels producing variable physiological effects (Peers, 2011;Wilkinson & Kemp, 2011;Peers & Steele, 2012). Our research group has made a novel discovery, that of $Ca_v3.2$ T-type Ca^{2+} current inhibition by CORM-2, and these currently unpublished findings led to this PhD project. The experimental use of CORMs has further validated our understanding that CO is a cytoprotective molecule at low doses (Motterlini *et al.*, 2003). T-type Ca^{2+} channels have proven to be central to cell proliferation in cancer (Taylor *et al.*, 2008), to be involved in de-differentiation of mouse embryonic stem cells (Rodriguez-Gomez *et al.*, 2012), and in disorders involving VSMCs (Rodman *et al.*, 2005;Cribbs, 2006;Pluteanu & Cribbs, 2011).

HEK293 cells have been used as a model system to over-express T-type Ca^{2+} channel subtypes. This cell line offers a simple system in which to investigate the physiological effects of T-type Ca^{2+} channel expression and their modulation. HEK293 cells engineered to over-express the $Ca_v3.2$ T-type Ca^{2+} channel (HEK293/$Ca_v3.2$ cells) were used in this project, as the $Ca_v3.2$ channel sub-type has been described as the most prominent cardiovascular sub-type (Cribbs, 2006). HEK293/$Ca_v3.2$ cells are an ideal cell line in which to explore the role of the $Ca_v3.2$ T-type Ca^{2+} channel in proliferation as the WT HEK293 cells act as an adequate control cell line. Experiments

were carried out on HEK293/Ca_v3.2 and WT HEK293 cells to examine the effects of T-type Ca^{2+} channel inhibition, CO availability, and HO-1 induction on cell proliferation and $[Ca^{2+}]_i$. Three compounds were used to inhibit T-type Ca^{2+} channels. Mibefradil, first described as Ro 40-5967, is a T-type Ca^{2+} channel antagonist, and was found to inhibit T-type Ca^{2+} currents after dihyropyridine abolition of L-type Ca^{2+} currents in rat smooth muscle cells (Mishra & Hermsmeyer, 1994). The structure of mibefradil has been modified to produce a compound named NNC55-0396, which has higher selectivity for T-type Ca^{2+} channels over L-Type Ca^{2+} channels, given that no detectable inhibition of L-type Ca^{2+} currents was detected using 100µM NNC55-0396 (Huang *et al.*, 2004). NNC55-0396 has also been employed here, in addition to Ni^{2+}. Ni^{2+} has been demonstrated as a selective T-type Ca^{2+} channel inhibitor, with varying affinities for the different channel subtypes, and the Ca_v3.2 subtype exhibiting the highest sensitivity (Lee *et al.*, 1999). The effect of CO was examined using CORM-3. CORMs are transition metal carbonyls that release CO by various mechanisms; CORM-3 releases CO by ligand substitution (Foresti *et al.*, 2008). CORM-3 has a biological ligand incorporated into the molecular structure, resulting in a less toxic compound that is water soluble, and therefore more compatible with experiments involving live cells, (Motterlini *et al.*, 2003), which is the reason for using CORM-3 in these experiments. The metalloporphyrin cobalt protoporphyrin IX (CoPPIX) was used to induce HO-1 as it does not act as a substrate for the enzyme, unlike hemin (Shan *et al.*, 2000).

It is evident that HO-1 is important in cardiovascular health, the product CO can exert anti-proliferative effects, and also appears to be capable of modulating T-type Ca^{2+} channel function. T-type Ca^{2+} channels themselves have a role in the maintenance of $[Ca^{2+}]_i$ and cell proliferation (Gray *et al.*, 2004). Therefore, in disorders of the vasculature, where excess VSMC proliferation is a shaping feature of vessel integrity, could T-type Ca^{2+} channels be a target of stress-induced HO-1?

3.2 Results

3.2.1 Characterisation of HEK293/Ca_v3.2 cells

Immunocytochemistry was performed on the two cell lines to provide evidence of the difference in expression of Ca_v3.2 T-type Ca^{2+} channels. Figure 3.1 demonstrates the

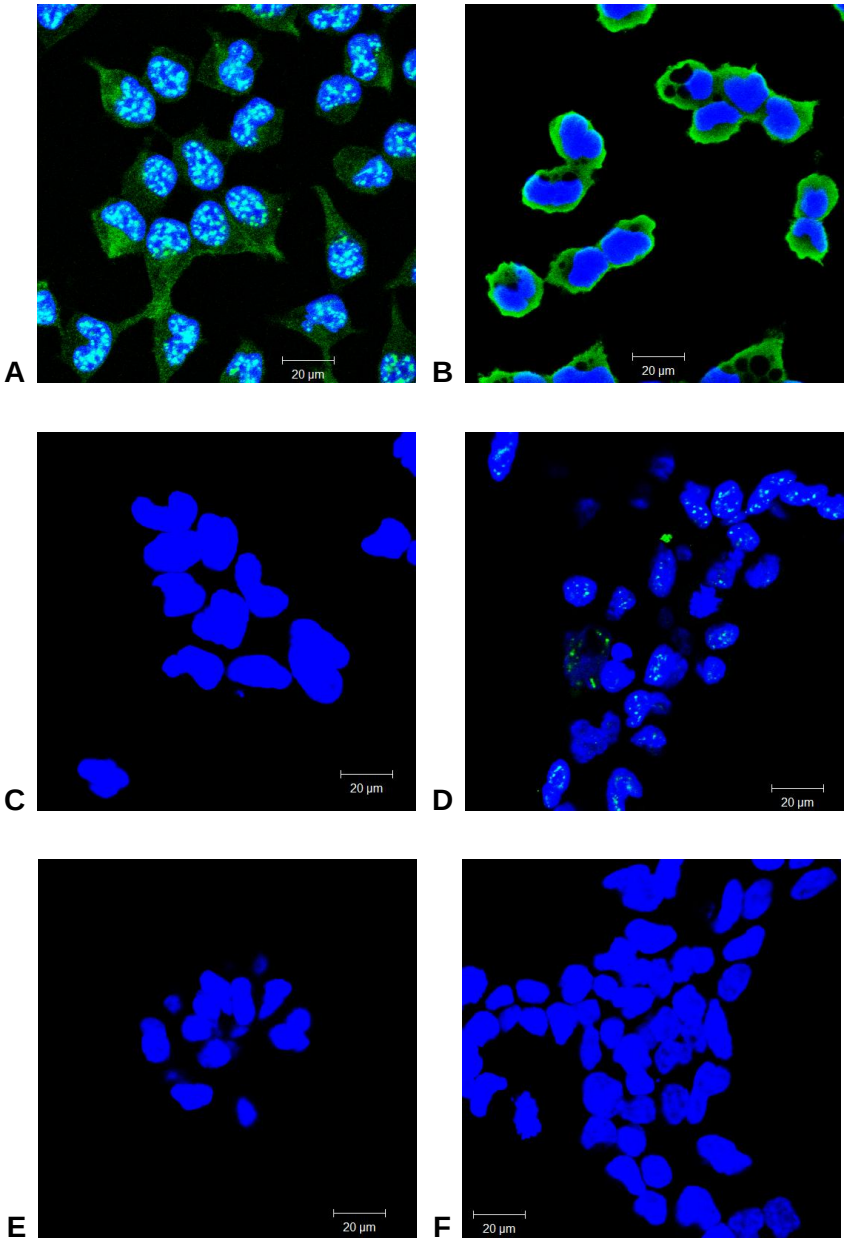

Figure 3.1 Identification of the $Ca_v3.2$ T-type Ca^{2+} channel in HEK293 cells

Immunocytochemistry of HEK293/$Ca_v3.2$ cells (P7) and WT HEK293 cells (P2) labelled with anti-$Ca_v3.2$ (green) from Alomone (panels A and D respecitvely), with anti-$Ca_v3.2$ from Santa Cruz (panels B and E respectively), and control without primary antibody (panels C and F respectively). Cell nuclei were stained blue with DAPI. Panels (A-C) are representative images of 6 fields of view from n=3 experimental repeats. Panels (D-F) are representative images of 4 fields of view from n=2 experimental repeats.

presence of $Ca_v3.2$ channels in HEK293/$Ca_v3.2$ cells and WT HEK293 cells using two different antibodies. Applying the $Ca_v3.2$ antibody from Alomone, the image in panel (A) shows the $Ca_v3.2$ T-type Ca^{2+} channel to be located throughout the cell, with nuclear puncta also visible. Using the $Ca_v3.2$ antibody from Santa Cruz, the image in panel (B) shows the $Ca_v3.2$ T-type Ca^{2+} channel to be denser at the cell membrane, with graded expression through the cytoplasm towards the nuclei. Images of WT HEK293 cells are shown in Figure 3.1, panels (D-F). Some isolated nuclear staining can be seen in panel (D) which exhibits the $Ca_v3.2$ antibody from Alomone. However, no staining is visible in panel (E) showing the $Ca_v3.2$ antibody from Santa Cruz.

Basal levels of $[Ca^{2+}]_i$ in the two cell lines were assessed by microfluorimetry. Figure 3.2 shows the changes in $[Ca^{2+}]_i$ levels in response to normal (Ca^{2+}-containing) or Ca^{2+}-free buffer. The representative trace of HEK293/$Ca_v3.2$ cells in panel (A), shows a significant change in $[Ca^{2+}]_i$ when the cells were subjected to Ca^{2+}-free buffer. In contrast, there were minimal changes in $[Ca^{2+}]_i$ in WT HEK293, shown in panel (B). The mean data in the bar graph in panel (C) demonstrate that HEK293/$Ca_v3.2$ cells (grey bars) have a significantly higher basal level of $[Ca^{2+}]_i$ than WT HEK293 cells (white bars) when subjected to normal buffer. The HEK293/$Ca_v3.2$ cells also demonstrated a larger response to Ca^{2+}-free buffer compared to WT HEK293 cells; $[Ca^{2+}]_i$ was reduced by 12% and 4% respectively.

Proliferation assays were performed to assess the growth characteristics of both HEK293/$Ca_v3.2$ and WT HEK293 cells, to determine whether over-expression of the $Ca_v3.2$ channel could influence cell proliferation. Figure 3.3 shows the differences in the growth characteristics of the two cell lines. The HEK293/$Ca_v3.2$ cells (grey bars) proliferated at a significantly faster rate over the three day assay than the WT HEK293 cells (white bars). Indeed, the over-expression of the $Ca_v3.2$ T-type Ca^{2+} channel augments proliferation, in addition to providing a route for an enhanced level of $[Ca^{2+}]_i$.

3.2.2 The effect of T-type Ca^{2+} channel inhibition on $[Ca^{2+}]_i$ and proliferation

To examine the effects of T-type Ca^{2+} channel inhibition on basal $[Ca^{2+}]_i$, 3µM mibefradil was assessed by microfluorimetry. The representative trace shown in Figure 3.4 (A) demonstrates the significant decrease in $[Ca^{2+}]_i$ caused by 3µM mibefradil in

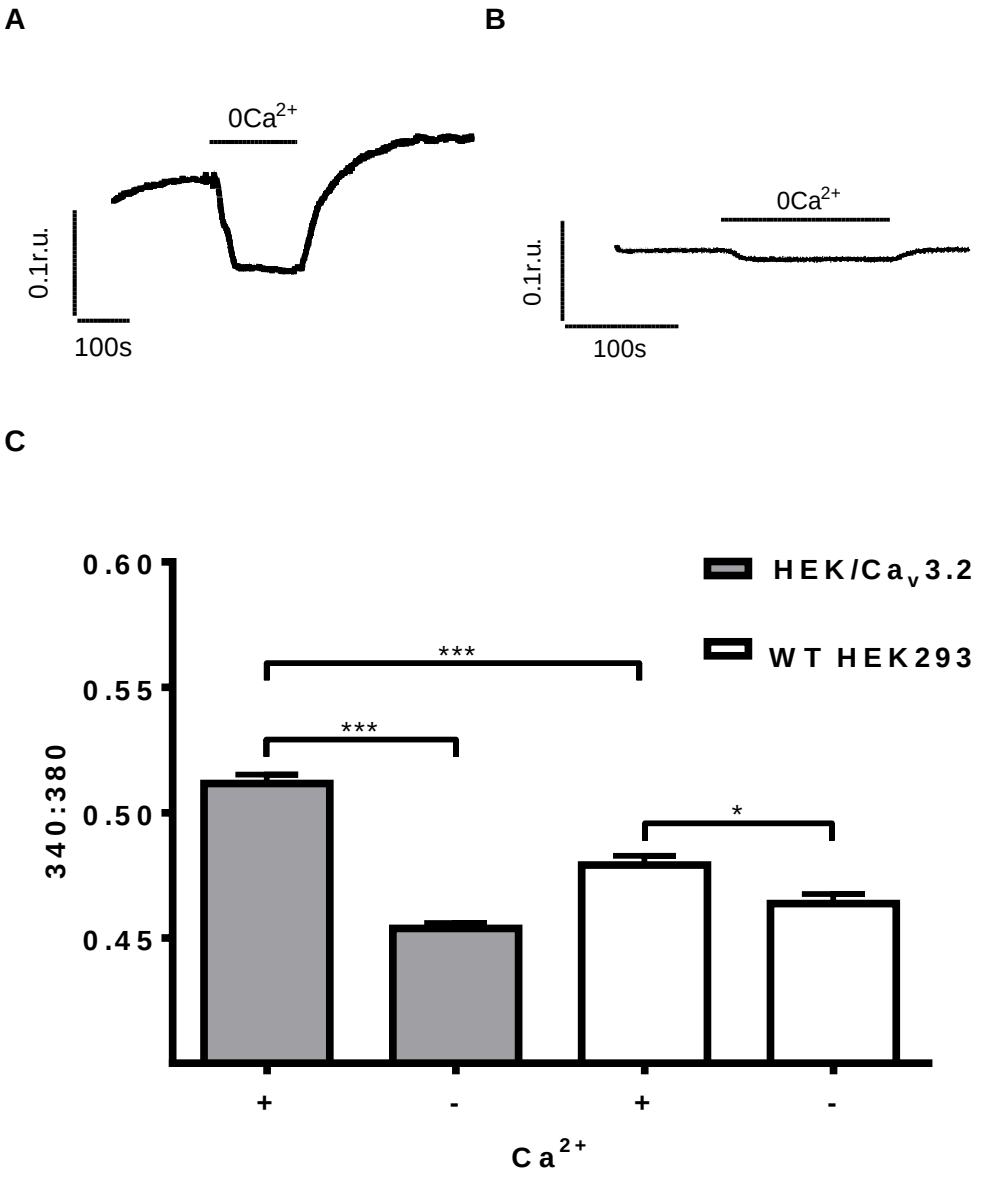

Figure 3.2 HEK293/Ca_v3.2 cells have elevated basal $[Ca^{2+}]_i$ levels

Representative traces of HEK293/Ca_v3.2 and WT HEK293 cells (A and B respectively) illustrate the disparate basal $[Ca^{2+}]_i$ levels in these two cell lines, and the different magnitude of the decrease in $[Ca^{2+}]_i$ in response to Ca^{2+}-free buffer. The bar graph (C) shows the mean (± s.e.m.) basal $[Ca^{2+}]_i$ levels in response to normal and Ca^{2+}-free buffers. Data were analysed by one-way ANOVA with Bonferroni's multiple comparison test; * $p<0.05$, *** $p<0.001$ as indicated above. n=108, r.u.=ratio units, s=seconds.

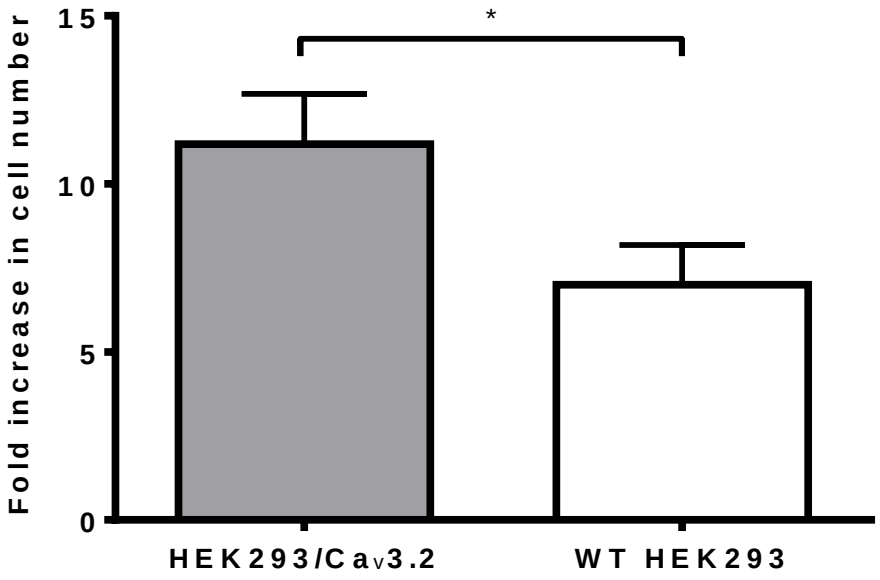

Figure 3.3 Augmented proliferation of HEK293/Ca_v3.2 cells

Bar graph showing the higher fold increase in cell number of HEK293/Ca_v3.2 cells compared to WT HEK293 cells, over a 3-day proliferation assay. Data are represented as fold increase (± s.e.m.), and were analysed by a two-tailed paired t-test, * $p<0.05$, n=7.

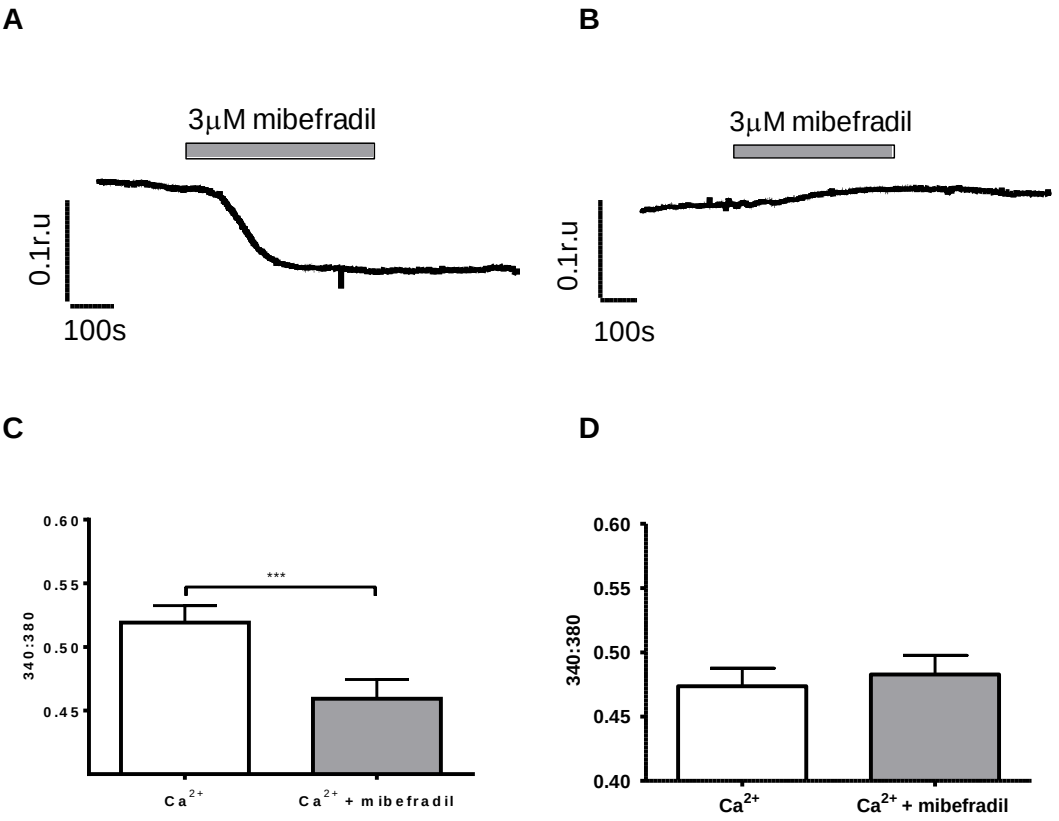

Figure 3.4 Treatment with 3μM mibefradil reduces $[Ca^{2+}]_i$ in HEK293/Ca_v3.2 cells

Representative traces showing the effect of 3μM mibefradil on basal $[Ca^{2+}]_i$ levels in HEK293/Ca_v3.2 (A) and WT HEK293 cells (B). Bar graphs showing the mean (± s.e.m.) decrease in Fura 2 ratio in HEK293/Ca_v3.2 cells (C) and WT HEK293 cells (D) when 3μM mibefradil was added to the normal buffer. Data were analysed by a two-tailed paired t-test, *** $p<0.001$, $n=6$.

HEK293/Ca_v3.2 cells. In contrast, Figure 3.4 (B) shows there is no effect of 3µM mibefradil on $[Ca^{2+}]_i$ in WT HEK293 cells. The slight and insignificant increase in Fura 2 ratio in WT HEK293 cells over time can be attributed to the natural behaviour of the cells during the experimental conditions, as it was noted that the Fura 2 ratio had a tendency to drift when the cells were constantly exposed to normal buffer. The bar graphs in Figure 3.4 (C) and (D) demonstrate the mean changes in $[Ca^{2+}]_i$ in response to mibefradil. $[Ca^{2+}]_i$ was reduced by 12% in HEK293/Ca_v3.2 cells, with no significant reduction in WT HEK293 cells. Proliferation assays were performed with the addition of 3µM mibefradil to determine whether inhibition of the Ca_v3.2 T-type Ca^{2+} channel would subsequently inhibit cell proliferation. The IC_{50} of Ca_v3.2 current inhibition in HEK293/Ca_v3.2 cells by mibefradil has been quoted to range between 1.1µM and 1.4µM (Cribbs *et al.*, 1998;Martin *et al.*, 2000). Although, the optimal concentration of mibefradil required to significantly inhibit proliferation, as determined from previous concentration response curves performed within our research group, was 3µM. Figure 3.5 shows the inhibition of HEK293/Ca_v3.2 proliferation by mibefradil on day 3 of the assay. 3µM mibefradil inhibited HEK293/Ca_v3.2 cell proliferation by 26% over the 3 day period. There was no significant difference in the proliferation of WT HEK293 cells.

The effect of NNC55-0396, a more selective T-type Ca^{2+} channel blocker, on $[Ca^{2+}]_i$ was also investigated. The IC_{50} of NNC55-0396 for HEK293/Ca_v3.2 cells is stated to be 7µM (Huang *et al.*, 2004). However, a preliminary proliferation assay involving HEK293/Ca_v3.2 and WT HEK293 cells revealed NNC55-0396 was more potent than mibefradil; and the drug was cytotoxic at concentrations above 5µM. Therefore, concentrations ranging from 1-3µM were tested using microfluorimetry, and 3µM was selective for HEK293/Ca_v3.2 cells. Figure 3.6 (A) demonstrates there was a significant decrease in $[Ca^{2+}]_i$ in HEK293/Ca_v3.2 cells in response to 3µM NNC55-0396, with no effect in WT HEK293 cells as shown in 3.6 (B). The bar graph in Figure 3.6 (C) shows a 12% decrease in $[Ca^{2+}]_i$ caused by 3µM NNC55-0396 in HEK293/Ca_v3.2 cells. Regarding WT HEK293 cells, Figure 3.6 (D) shows there is no significant reduction in the mean Fura 2 ratio with the addition of NNC55-0396.

The effect of Ni^{2+}, a differentially selective T-type Ca^{2+} channel blocker, was also investigated. The IC_{50} for Ni^{2+} in HEK293/Ca_v3.2 cells has been quoted to be 13µM

A

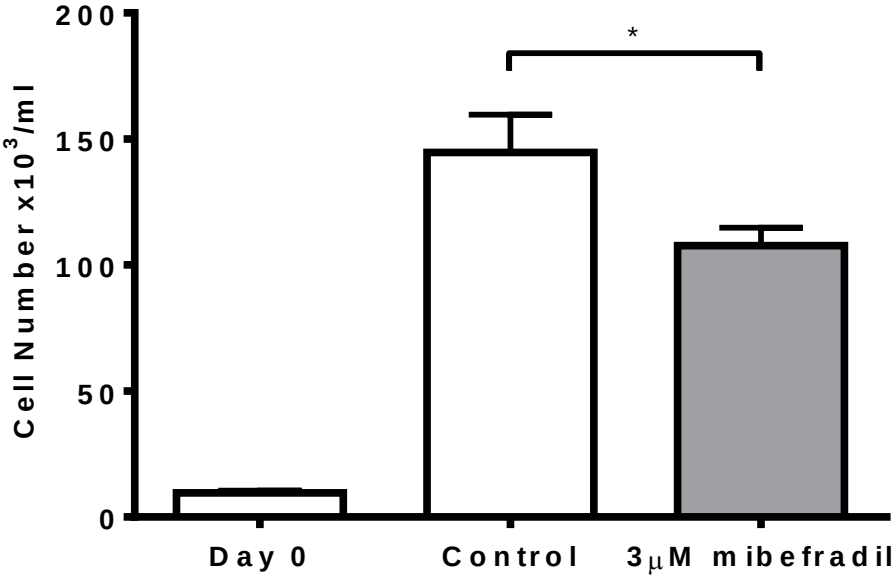

B

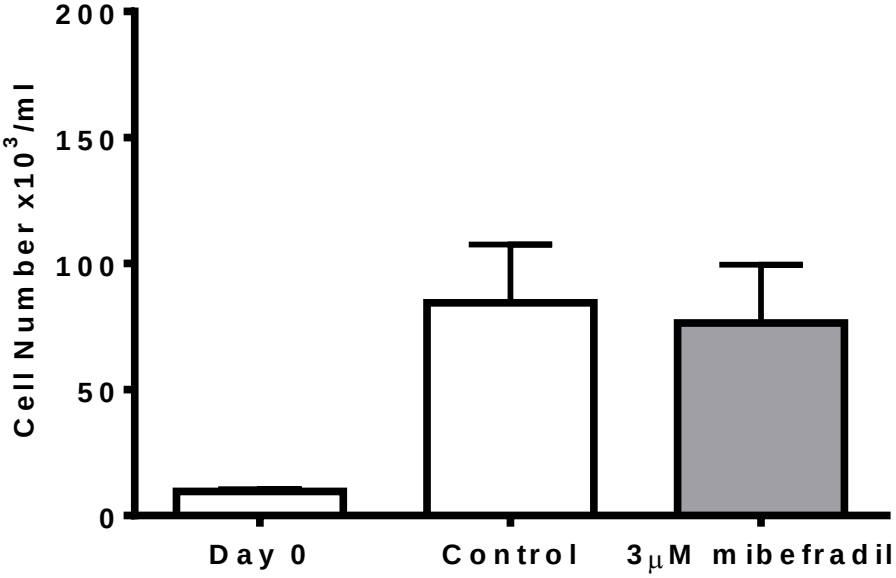

Figure 3.5 Mibefradil inhibits proliferation of HEK293/Ca_v3.2 cells

Bar graphs showing the mean (± s.e.m.) cell number of HEK293/Ca_v3.2 cells (A) and WT HEK293 cells (B). 3μM mibefradil inhibited HEK293/Ca_v3.2 cell proliferation on day 3 with no effect on WT HEK293 cells. Data were analysed by a two-tailed paired t-test * $p<0.05$, n=3.

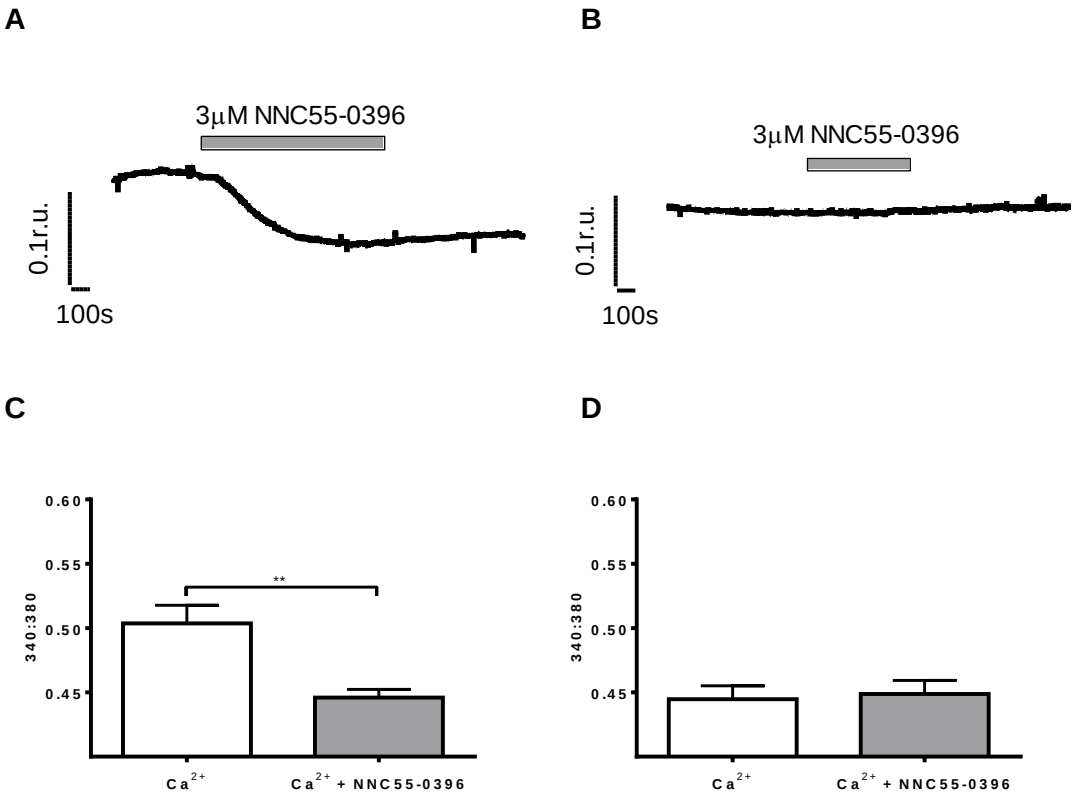

Figure 3.6 Treatment with 3μM NNC55-0396 reduces $[Ca^{2+}]_i$ in HEK293/Ca_v3.2 cells

Representative traces showing the effect of 3μM NNC55-0396 on $[Ca^{2+}]_i$ levels in HEK293/Ca_v3.2 (A) and WT HEK293 cells (B). Bar graphs showing the mean (± s.e.m.) decrease in Fura 2 ratio in HEK293/Ca_v3.2 cells (C) and WT HEK293 cells (D) when 3μM NNC55-0396 is added to the normal buffer. Data were analysed by a two-tailed paired t-test ** $p<0.001$, $n=8$.

(Lee *et al.*, 1999). In these experiments 30µM Ni^{2+} was utilised to ensure $Ca_v3.2$ channel block. Figure 3.7 (A) demonstrates that 30µM Ni^{2+} significantly decreases $[Ca^{2+}]_i$ in HEK293/$Ca_v3.2$ cells, in contrast to the lack of effect in WT HEK293 cells (B). The mean data shown in the bar graph in Figure 3.7 (C) illustrate that 30µM Ni^{2+} reduced $[Ca^{2+}]_i$ by 11%. Figure 3.7 (D) shows mean $[Ca^{2+}]_i$ was unchanged in the presence of 30µM Ni^{2+} in WT HEK293 cells.

In summary, inhibition of the $Ca_v3.2$ Ca^{2+} channel by Ni^{2+} NNC55-0396, and mibefradil decreases $[Ca^{2+}]_i$, and the latter also significantly inhibits augmented proliferation of HEK293/$Ca_v3.2$ cells, with no effect on WT HEK293 cells.

3.2.3 The effect of CO on $[Ca^{2+}]_i$ and proliferation

It has been previously demonstrated by our research group, using the patch-clamp technique, that CORM-2 can inhibit the $Ca_v3.2$ T-type Ca^{2+} current. The effect of CORM-3 on basal $[Ca^{2+}]_i$ in HEK293/$Ca_v3.2$ cells was assessed in this project by microfluorimetry, in order to validate such a novel finding using an alternative technique. A concentration of 3µM CORM-3 was employed in microfluorimetry experiments as this was the lowest concentration that was able to selectively reduce $[Ca^{2+}]_i$ in HEK293/$Ca_v3.2$ cells over WT HEK293 cells, after testing the effects of 1, 3, 10 and 30µM CORM-3. Figure 3.8 (A) shows a representative trace of the HEK293/$Ca_v3.2$ cells in response to 3µM CORM-3; $[Ca^{2+}]_i$ was significantly reduced by CO, in contrast to the lack of effect seen in WT HEK293 cells in panel (B). The bar graphs in panels (C) and (D) show the mean data; the presence of 3µM CORM-3 reduced $[Ca^{2+}]_i$ in HEK293/$Ca_v3.2$ cells by 11%. There was minimal change in Fura 2 ratio in WT HEK293 cells in response to CORM-3. The proliferation assays in panels (E) and (F) were produced by Dr Hannah E. Boycott previous to this PhD project. Panel (E) shows the proliferative response of HEK293/$Ca_v3.2$ cells to CORM-3 and iCORM-3, inactivated CORM-3, over a 3 day proliferation assay. There was a significant inhibition of HEK293/$Ca_v3.2$ cell proliferation by 3µM CORM-3, but not iCORM-3, demonstrating that CO has anti-proliferative effects in this cell line. Panel (F) shows the proliferative response of WT HEK293 cells to CORM-3 and iCORM-3 over a 3 day proliferation assay. The proliferation of WT HEK293 cells was not affected by CO, implying that CO is able to modulate the $Ca_v3.2$ T-type Ca^{2+} channel, which subsequently inhibits cell proliferation. Figure 3.9 shows the effect of 3µM iCORM-3 on $[Ca^{2+}]_i$. The representative trace of HEK293/$Ca_v3.2$ cells in panel (A) shows an unexpected,

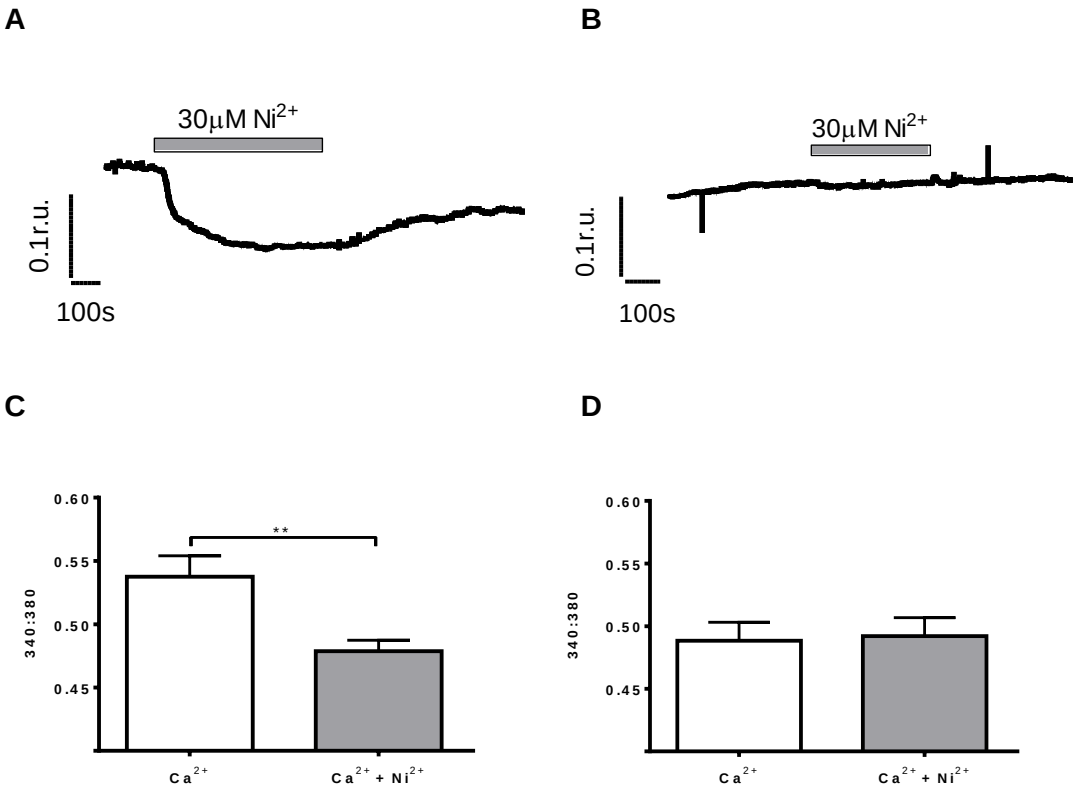

Figure 3.7 Treatment with 30μM Ni^{2+} reduces $[Ca^{2+}]_i$ in HEK293/Ca_v3.2 cells

Representative traces showing the effect of 30μM Ni^{2+} on $[Ca^{2+}]_i$ levels in HEK293/Ca_v3.2 (A) and WT HEK293 cells (B). Bar graphs showing the mean (± s.e.m.) decrease in Fura 2 ratio in HEK293/Ca_v3.2 cells (C) and WT HEK293 cells (D) when 30μM Ni^{2+} is added to the normal buffer. Data were analysed by a two-tailed paired t-test ** $p<0.001$, n=6.

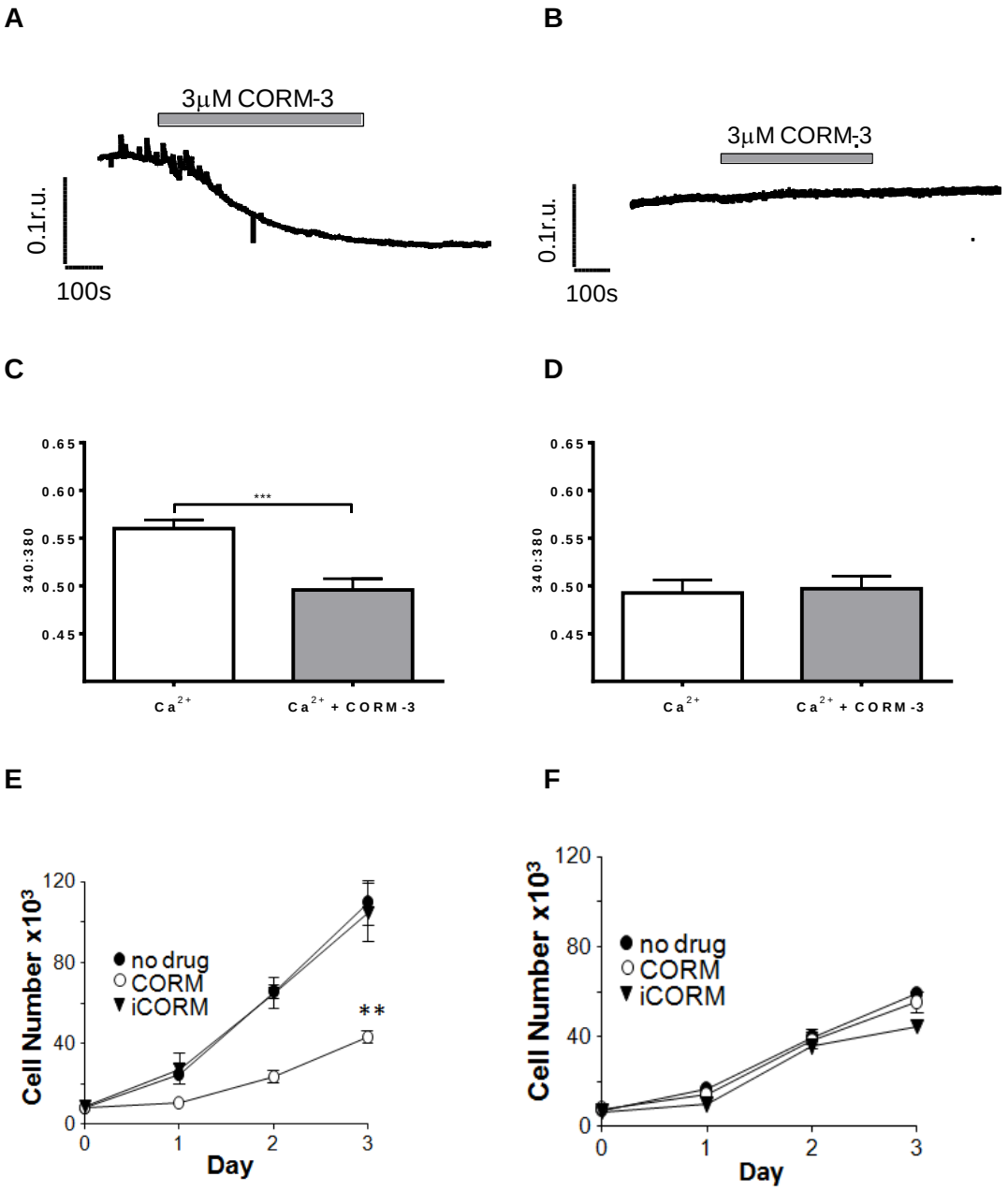

Figure 3.8 The effect of CORM-3 on $[Ca^{2+}]_i$ and proliferation

Representative traces showing the effect of 3μM CORM-3 on $[Ca^{2+}]_i$ levels in HEK293/Ca_v3.2 (A) and WT HEK293 cells (B). Bar graphs showing the mean (± s.e.m.) decrease in Fura 2 ratio in HEK293/Ca_v3.2 cells (C) and WT HEK293 cells (D) when 3μM CORM-3 is added to the normal buffer. Data were analysed by a two-tailed paired t-test, *** $p<0.001$, n=6. Line graphs showing mean (± s.e.m.) cell number monitored in HEK293/Ca_v3.2 (E) and WT HEK293 (F) cells. Cells were cultured in the absence of drugs (solid circles), or in the presence of either CORM-3 (30μM; open circles) or iCORM (30μM solid triangles), ** $p<0.01$, n=3. The data in panels (E) and (F) was generated by Dr Hannah E. Boycott.

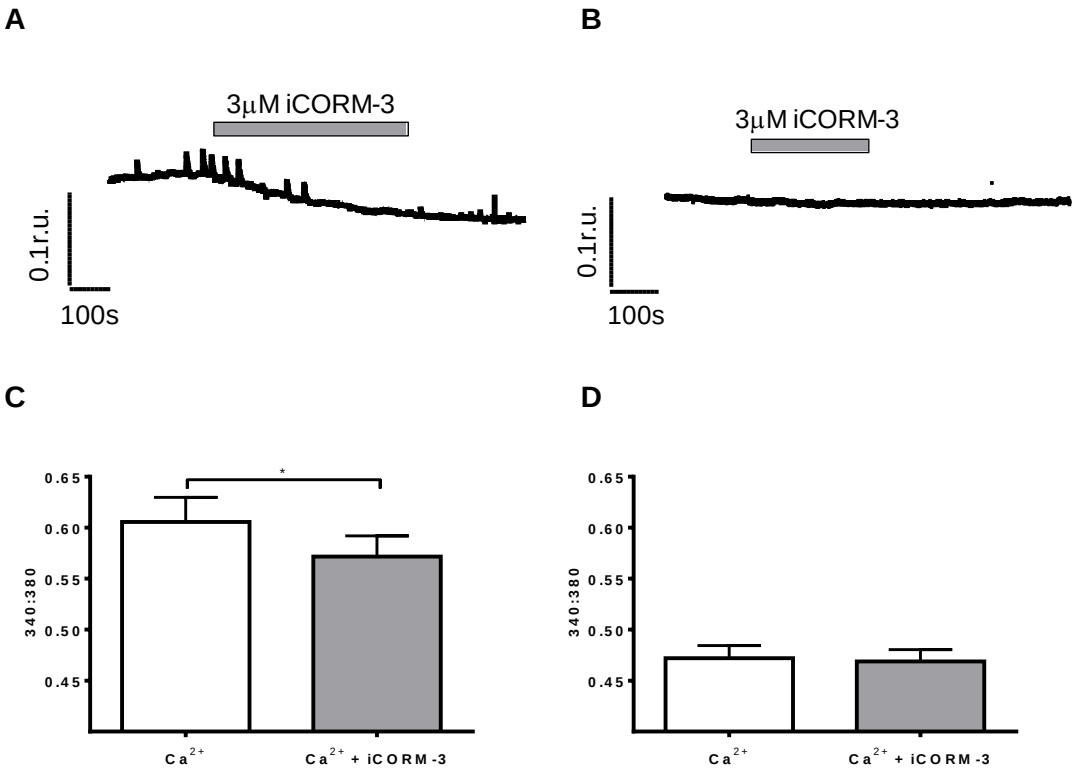

Figure 3.9 The effect of 3μM iCORM-3 on $[Ca^{2+}]_i$

Representative traces showing the effect of 3μM iCORM-3 on $[Ca^{2+}]_i$ levels in HEK293/Ca_v3.2 (A) and WT HEK293 cells (B). Bar graphs showing the mean (± s.e.m.) Fura 2 ratio in HEK293/Ca_v3.2 cells (C) and WT HEK293 cells (D) when 3μM iCORM-3 is added to the normal buffer. Data were analysed by a two-tailed paired t-test, * $p<0.05$, n=6.

significant decrease in $[Ca^{2+}]_i$, with a 7% reduction of mean Fura 2 ratio in the presence of iCORM-3. This is shown in panel (C). $[Ca^{2+}]_i$ was unchanged by iCORM-3 in WT HEK293 cells, which is demonstrated by the representative trace in panel (B), and the mean data in panel (D). In summary, CO is able to inhibit the $Ca_v3.2$ T-type Ca^{2+} channel, with a subsequent reduction in $[Ca^{2+}]_i$ and inhibition of proliferation.

3.2.4 The effect of HO-1 induction on $[Ca^{2+}]_i$ and proliferation

Immunocytochemistry was performed to demonstrate the induction of HO-1 by CoPPIX. Figure 3.10 (A) illustrates how HO-1 is induced by 10µM CoPPIX, and panel (B) illustrates HO-1 induction by 10µM hemin in HEK293/$Ca_v3.2$ cells. Panel (D) shows that HO-1 is induced by 3µM CoPPIX, and panel (E) illustrates HO-1 induction by 3µM hemin in WT HEK293 cells. There is minimal staining in panel (F), which shows the control image without induction. As the DAPI could not be visualised at this time, it is unclear as to where the cells are localised in Figure 3.10 (F).

A range of CoPPIX concentrations were applied to the cells for a 48h period to assess the corresponding level of HO-1 induction via western blotting, and subsequently decide on an adequate concentration to use in microfluorimetry experiments. Figure 3.11 (A) demonstrates that HO-1 was induced in HEK293/$Ca_v3.2$ cells to a level of 55 ± 11.50% of β-actin using 10µM CoPPIX, compared to 1.2 ± 0.14% the control group. Panel (B) shows a representative western blot of HO-1 protein with the corresponding β-actin loading control underneath. Figure 3.12 (A) demonstrates that HO-1 was induced in WT HEK293 cells to a level of 49.06 ± 12.90% of β-actin by 7µM, and 40.07 ± 20.16% by 10µM CoPPIX, vs 2.42 ± 2.30% for the control group. However, analysis via one-way ANOVA demonstrated a P value of 0.0647. Panel (B) shows a representative western blot of HO-1 protein with the corresponding β-actin loading control underneath.

To investigate whether the CO produced as a result of HO-1 induction could affect $[Ca^{2+}]_i$ levels, the cells were subjected to normal and Ca^{2+}-free buffers after a 48h incubation with CoPPIX. Disparate concentrations of 10µM and 3µM CoPPIX were applied to HEK293/$Ca_v3.2$ cells and WT HEK293 cells respectively. These

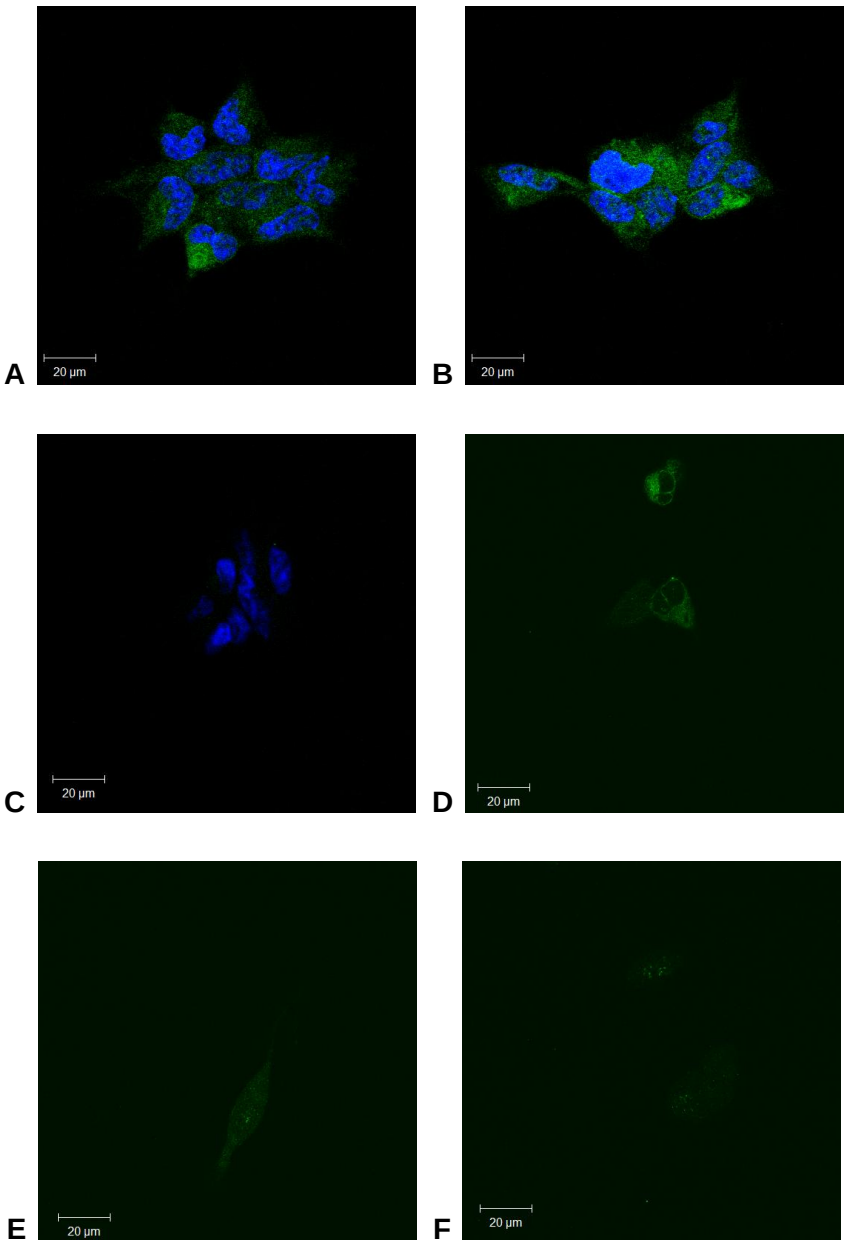

Figure 3.10 Identification of HO-1 induction in HEK293 cells

Immunocytochemistry of HEK293/Ca_v3.2 cells (P7) labelled with anti-HO-1 (green) after a 48h incubation with 10µM CoPPIX (panel A), with 10µM Hemin (panel B), and control without induction (panel C). Cell nuclei were stained blue with DAPI. Immunocytochemistry of WT HEK293 cells (P4) labelled with anti-HO-1 after a 24h incubation with 3µM CoPPIX (panel D), with 3µM Hemin (panel E), and control without induction (panel F). At the time of images D-F being taken, visualisation of DAPI was unavailable. Panels (A-C) are representative images of 10 fields of view from n=5. Panels (D-F) are representative images of 6 fields of view from n=3 experimental repeats.

A

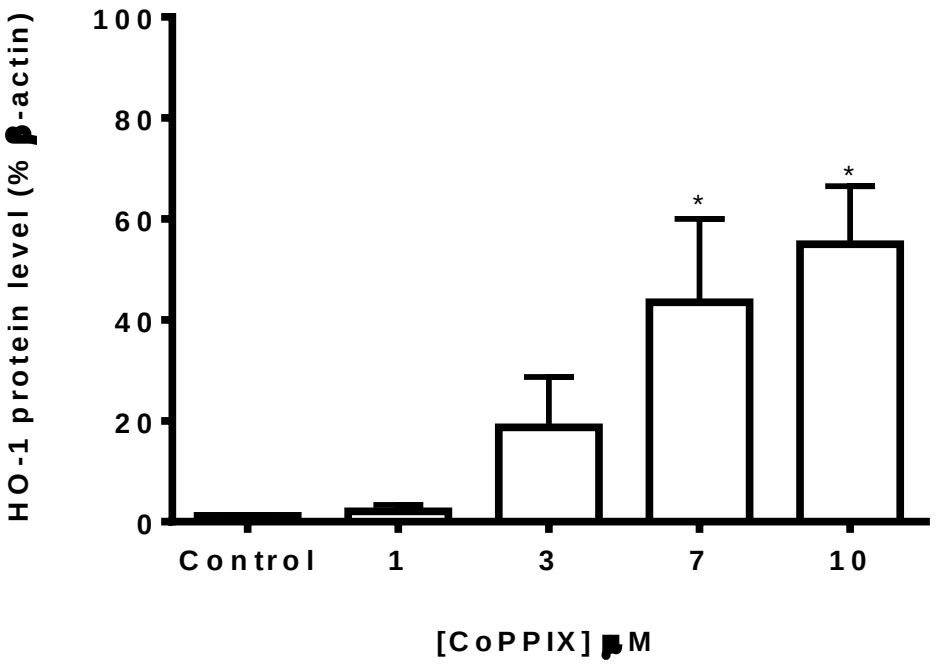

B

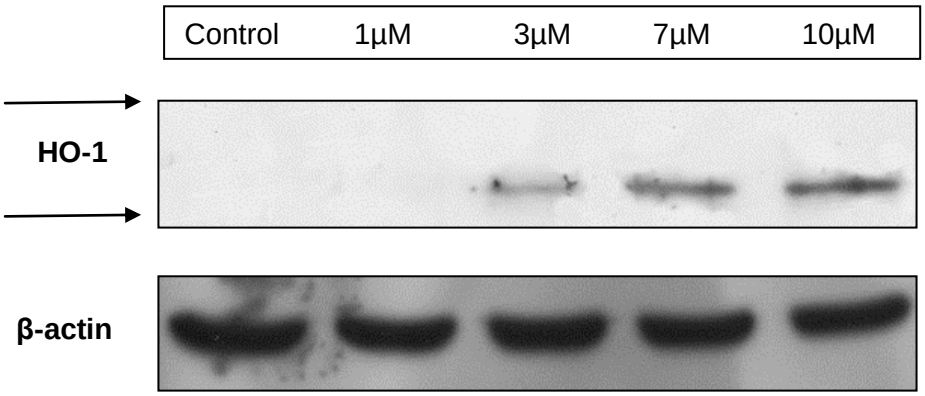

Figure 3.11 CoPPIX induces HO-1 protein expression in HEK293/Ca_v3.2 cells

Bar graph showing the mean (± s.e.m.) relative HO-1 protein expression in HEK293/Ca_v3.2 cells after normalisation of densitometric analyses relative to β-actin. (A). Data were analysed by one-way ANOVA with Dunnett's multiple comparison test, * $p<0.05$ vs control levels n=3. Representative Western Blot of HO-1 and the corresponding β-actin loading control (B). The arrows represent the position of the molecular weight markers (top, 37KDa; bottom, 25kDa).

A

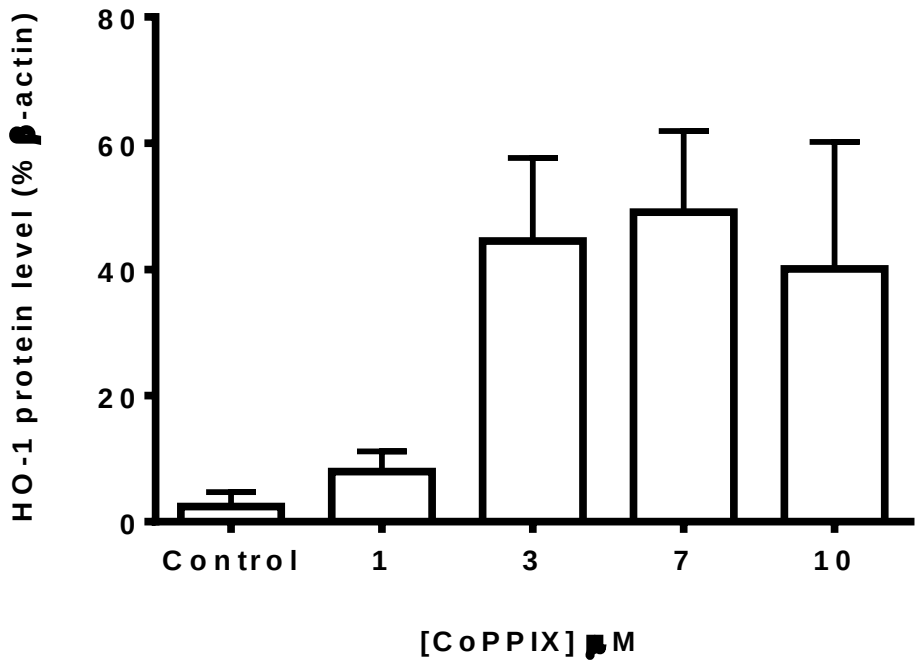

B

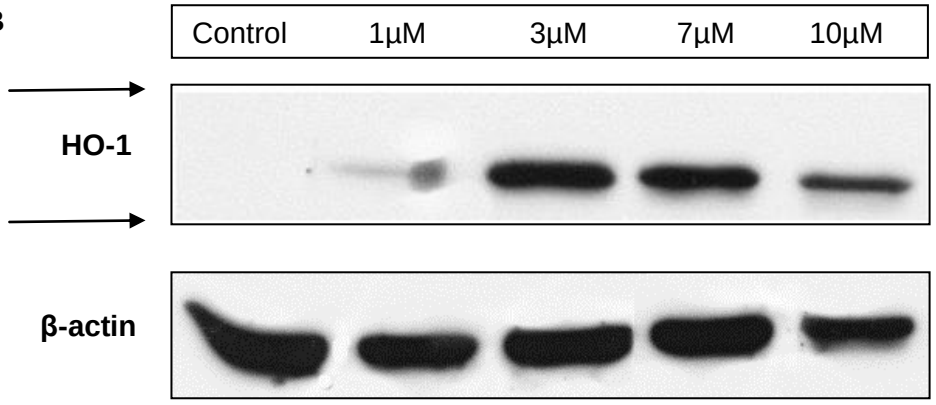

Figure 3.12 CoPPIX induces HO-1 protein expression in WT HEK293 cells

Bar graph showing the mean (± s.e.m.) relative HO-1 protein expression in WT HEK293 cells after normalisation of densitometric analyses relative to β-actin (A), n=3. Representative Western Blot of HO-1 and the corresponding β-actin loading control (B). The arrows represent the position of the molecular weight markers (top, 37KDa; bottom, 25kDa).

concentrations produced optimal HO-1 induction in the corresponding cell types, as determined from the data in Figures 3.11 and 3.12. Figure 3.13 (A) shows representative traces of experimental repeats. HEK293/Ca_v3.2 cells from both the control group and the CoPPIX treated group (black and blue traces respectively), aligned side by side on the same axis. Panel (B) shows the corresponding traces from WT HEK293 cells. Panels (C) and (D) show the mean data of control and CoPPIX treated groups for HEK293/Ca_v3.2 and WT HEK293 cells respectively. Concerning HEK293/Ca_v3.2 cells, it is demonstrated in both panels (A) and (C) that basal $[Ca^{2+}]_i$ was significantly lower in cells following HO-1 induction when compared to the control group. The mean Fura 2 ratio was 12% less in CoPPIX treated HEK293/Ca_v3.2 cells. The response of the control group to Ca^{2+}-free buffer showed a significant reduction in $[Ca^{2+}]_i$, in contrast the HO-1 group did not respond significantly; there was a 10% reduction compared to a 7% reduction in $[Ca^{2+}]_i$ respectively. Panels (B) and (D) in Figure 3.13 show minimal changes in $[Ca^{2+}]_i$ in WT HEK293 cells in response to HO-1 induction using 3µM CoPPIX.

To investigate the effect of HO-1 induction, and therefore subsequent CO production, on cellular proliferation, a concentration-response curve to the HO-1 inducer, CoPPIX, was performed. Figure 3.14 (A) shows the effect of CoPPIX on HEK293/Ca_v3.2 cell proliferation. 10µM CoPPIX significantly inhibited cell proliferation, demonstrating a 27% decrease in cell number. Panel (B) shows the effect of CoPPIX on WT HEK293 cell proliferation. 10µM CoPPIX surprisingly also inhibited the proliferation of WT cells, demonstrating a 79% reduction in cell number. However, it was observed that WT HEK293 cells became less viable when subjected to 10µM CoPPIX, which undoubtedly contributed to the lower cell counts. From this point in the experiments it was decided that corresponding cell media would also be processed alongside trypsinised cells, and any cells present counted and documented as floating, non-viable cells. Graphs containing this data are shown from Chapter 4 onwards.

In summary, HO-1 induction requires a higher concentration of CoPPIX in HEK293/Ca_v3.2 cells than WT HEK293 cells, which is reflected by western blots and proliferation assays. HO-1 induction significantly decreased $[Ca^{2+}]_i$ in HEK293/Ca_v3.2 cells, implying HO-1-derived CO is also able to inhibit the Ca_v3.2 T-type Ca^{2+} channel.

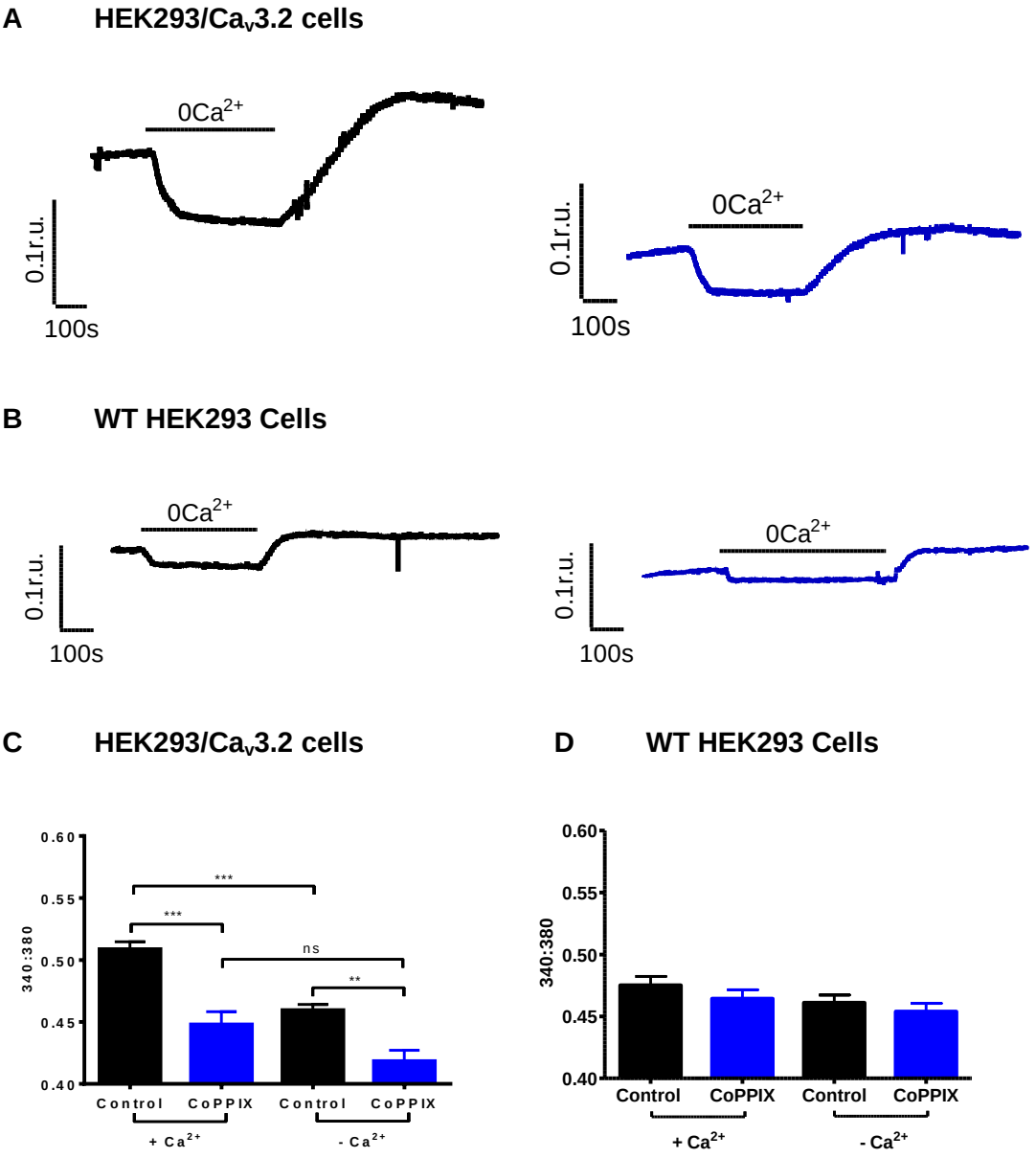

Figure 3.13 Treatment with CoPPIX reduces $[Ca^{2+}]_i$ in HEK293/Ca_v3.2 cells

Data showing the effects of a 48h pre-treatment with CoPPIX (blue traces and bars), in comparison to control cells without HO-1 induction (black traces and bars). Representative traces of HEK293/Ca_v3.2 cells (A) plus or minus incubation with 10µM CoPPIX. Representative traces of WT HEK293 cells (B) plus or minus incubation with 3µM CoPPIX. Bar graphs showing the mean (± s.e.m.) Fura 2 ratio in HEK293/Ca_v3.2 (C) n=16, and WT HEK293 cells (D) n=12, in response to Ca^{2+}-containing buffer and Ca^{2+}-free buffer. Data were analysed by one-way ANOVA with Bonferroni's multiple comparison test, *** p<0.001, ** p<0.01.

A

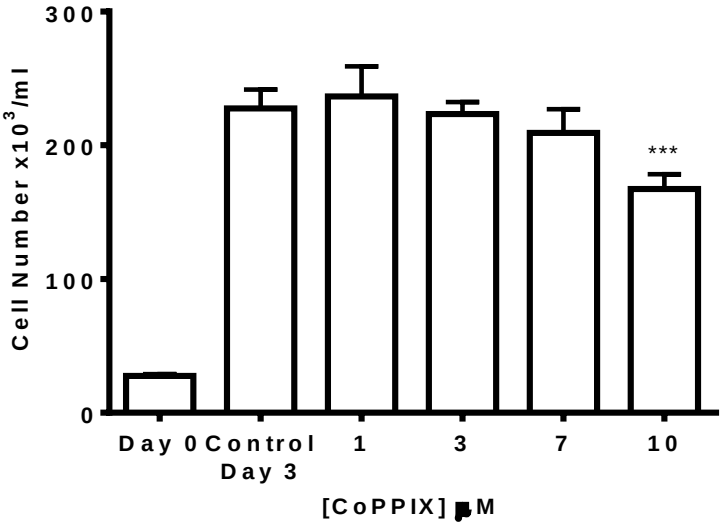

B

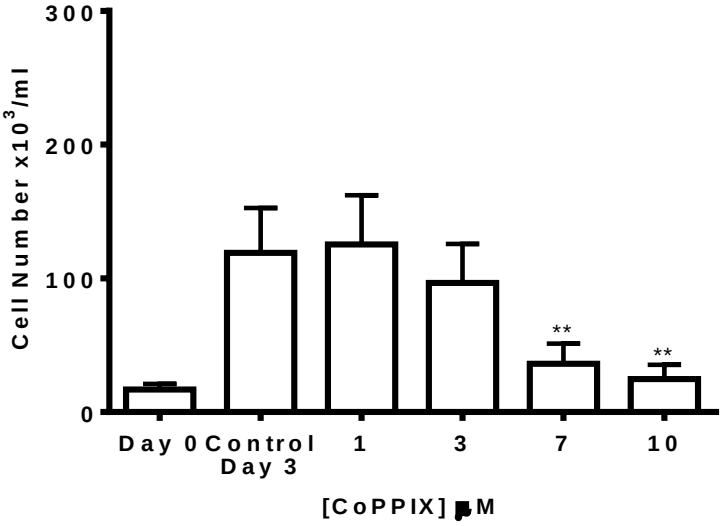

Figure 3.14 HO-1 induction by CoPPIX inhibits cell proliferation

Bar graphs showing the mean (± s.e.m.) day 3 cell number of HEK293/Ca_v3.2 cells (A) and WT HEK293 cells (B) in response to increasing concentrations of CoPPIX. Data were analysed by ratio repeated measures one-way ANOVA with Dunnett's multiple comparison test, *** $p<0.001$, ** $p<0.01$ vs day 3 control, n=3.

3.3 Discussion

The images in Figure 3.1 illustrate the differing T-type Ca^{2+} channel expression levels between the two cell lines. The $Ca_v3.2$ antibody from Alomone appears less specific as the image in panel (A) of both figures display varying degrees of punctate nuclear staining. The use of focus imaging, or Z-stack imaging, would be useful to allow greater depth of field and more specific localisation of the $Ca_v3.2$ T-type Ca^{2+} channels in question. The use of HEK293/$Ca_v3.2$ cells at P7 in this figure demonstrates that expression of the $Ca_v3.2$ T-type Ca^{2+} channel is maintained at the older passages employed in the experiments shown in this chapter.

An important property of the $Ca_v3.2$ T-type Ca^{2+} channel noted from these experiments is the influence this channel has on cell proliferation, as illustrated in Figure 3.3. The HEK293/$Ca_v3.2$ cells proliferated at a faster rate than the WT HEK293 cells over the course of the assay. This enhanced proliferation by the HEK293/$Ca_v3.2$ cells can be significantly inhibited by mibefradil, giving further integrity to the idea that T-type Ca^{2+} channels play a significant role in proliferation. A previous study, (Chemin *et al.*, 2000), reported no proliferative advantage of the $Ca_v3.2$ T-type Ca^{2+} channel using the same HEK293/$Ca_v3.2$ cells as detailed in this project. This study by Chemin *et al.* assessed proliferation via bromodeoxyuridine (BrdU) labelling. While this is an established assay for detecting BrdU incorporation into DNA, it is an indirect assessment of proliferation (Taupin, 2007). The method of cell counting employed in this PhD project is a direct measure of proliferation. However, these negative findings were contradicted by a later study from the same group, in which they describe a direct, non-linear relationship between Ca^{2+} entry by the $Ca_v3.2$ T-type Ca^{2+} channel, and proliferation of HEK293/$Ca_v3.2$ cells (Gray *et al.*, 2004). Together with another study, they link the augmented proliferation of HEK293/$Ca_v3.2$ cells to a cell cycle control mechanism (Wang *et al.*, 2002b). They describe a Ca^{2+} threshold that must be achieved in order to trigger an all or nothing proliferative response through the G_1/S cell cycle boundary. T-type Ca^{2+} currents have been strongly linked to specific cell cycle phases, with proliferating cells evidenced as having a higher level of expression of T-type Ca^{2+} channels, and a larger proportion of T-type Ca^{2+} currents in the G_1 and S phases of the cell cycle (Kuga *et al.*, 1996). As the cell cycle requires Ca^{2+} signalling to progress (Ciapa *et al.*, 1994), the T-type Ca^{2+} channel could provide the route through which proliferating cells maintain adequate $[Ca^{2+}]_i$ levels. The window current associated with

T-type Ca^{2+} channels is due to a proportion of these channels remaining open during the resting membrane potential of the cell, allowing Ca^{2+} to move in (Crunelli *et al.*, 2005). The disparate expression levels of the $Ca_v3.2$ T-type Ca^{2+} channel between HEK293/$Ca_v3.2$ and WT HEK293 cells, as shown in Figure 3.1, is consistent with the differing steady state levels of $[Ca^{2+}]_i$ as shown in Figure 3.2, which can be attributed to the window current available in HEK293/$Ca_v3.2$ cells. HEK293/$Ca_v3.2$ cells displayed a higher level of basal $[Ca^{2+}]_i$, together with a more pronounced response to Ca^{2+}-free buffer compared to WT HEK293 cells. The reduction of $[Ca^{2+}]_i$ by various T-type Ca^{2+} channel blockers; mibefradil, NNC55-0396, and Ni^{2+}, in HEK293/$Ca_v3.2$ cells but not in WT HEK293 cells, demonstrates that WT HEK cells express low levels of T-type Ca^{2+} channels, if any at all, and implicates the $Ca_v3.2$ T-type Ca^{2+} channel as being responsible for the higher basal $[Ca^{2+}]_i$ levels. In keeping with this idea, the effect of mibefradil on the proliferation of HEK293/$Ca_v3.2$ cells, but not WT HEK293 cells, implicates the $Ca_v3.2$ T-type Ca^{2+} channel as a determining factor of proliferation. The effects of mibefradil on T-type Ca^{2+} current inhibition in HEK293/$Ca_v3.2$ cells have been previously studied, with IC_{50} values quoted at 1.4µM (Cribbs *et al.*, 1998), and 1.1µM (Martin *et al.*, 2000). Although the extent of $Ca_v3.2$ current inhibition appears to depend upon the charge carrier, Ca^{2+} or Ba^{2+}, and also on temperature; the IC_{50} values increased with a shift from room temperature to physiological temperature (Martin *et al.*, 2000). As stated previously, mibefradil also inhibits L-type Ca^{2+} channels (Eller *et al.*, 2000). However, the concentration required to inhibit L-Type Ca^{2+} channels has been reported to be at least 10-fold higher than that for T-type Ca^{2+} channels (Bezprozvanny & Tsien, 1995;Martin *et al.*, 2000). Mibefradil has been shown to block L-type Ca^{2+} channels at higher concentrations; with an IC_{50} of 12.9µM in HEK293/$Ca_v1.2$ cells (Martin *et al.*, 2000). Given the fact that this chapter is concerned with data from HEK293 cells over-expressing the $Ca_v3.2$ channel, any effects of mibefradil on L-Type Ca^{2+} channels are likely to be insignificant. Concerning the effects of Ni^{2+}, the level of $[Ca^{2+}]_i$ begins to recover as the buffer is changed back to normal buffer, as shown in Figure 3.7 (A). In contrast to NNC55-0396, inhibition by Ni^{2+} is reversible (Lee *et al.*, 1999;Kang *et al.*, 2006), and if a longer wash-out period, or if a lower $[Ni^{2+}]$ closer to the IC_{50} of 13µM had been employed in these experiments, the restoration in $Ca_v3.2$ T-type Ca^{2+} channel function may have been demonstrated. The possibility of reversible $Ca_v3.2$ T-type Ca^{2+} channel inhibition by mibefradil was not assessed in these experiments, yet this has been shown previously (Martin *et al.*, 2000).

Preliminary data gathered by Dr H. E. Boycott prior to this PhD project demonstrate that CO, delivered via CORM-3, is anti-proliferative. Figure 3.8, in concordance with Figure 3.3, show that the HEK293/$Ca_v3.2$ cells proliferated at a faster rate than WT HEK293 cells, and that CO is able to inhibit this proliferation. The molecular backbone of CORM-3 that remains post CO release, namely iCORM-3, was shown to have no effect on proliferation, which supports existing studies demonstrating that CO is anti-proliferative in rat aortic VSMCs (Togane *et al.*, 2000;Peyton *et al.*, 2002;Peyton *et al.*, 2002), in human airway smooth muscle cells (Song *et al.*, 2002), in HO-1 transduced primary rat VSMCs, and primary mouse HO-$1^{-/-}$ smooth muscle cells (Otterbein *et al.*, 2003b). CO also significantly reduced $[Ca^{2+}]_i$ levels in HEK293/$Ca_v3.2$ cells, which validates the notion that CO acts by inhibiting the $Ca_v3.2$ T-type Ca^{2+} channel, as WT HEK293 cells were unaffected. However, iCORM-3 did also reduce $[Ca^{2+}]_i$ levels in HEK293/$Ca_v3.2$ cells. This could be attributed to incomplete inactivation of CORM-3. To inactivate the CORM-3 solution, which was made up with distilled water, the solution was exposed to the atmosphere for 48h to allow CO to be released. An alternative method to ensure complete inactivation would be to dissolve solid CORM-3 in Dulbecco's PBS as opposed to water, and then leave exposed for 48h (Motterlini *et al.*, 2003). However, the iCORM-3 employed by Dr H. E. Boycott in the proliferation assay was also made with distilled water. It is possible that any CO still available within the iCORM-3 solution was enough to produce a significant effect when applied acutely and monitored via Ca^{2+} microfluorimetry, which is essentially a snapshot of a short window of activity. iCORM-3 applied chronically over a proliferation assay did not produce any significant effects therefore, implying that any residual CO cannot prevent the level of $[Ca^{2+}]_i$ from falling below the required threshold to trigger cell cycle progression and proliferation, as discussed previously (Wang *et al.*, 2002b;Gray *et al.*, 2004). Together with the preliminary proliferation data produced by Dr H. E. Boycott, the effect of CORM-3 on $[Ca^{2+}]_i$ levels in HEK293/$Ca_v3.2$ cells demonstrates a novel finding that CO appears to inhibit the $Ca_v3.2$ T-type Ca^{2+} channel. This was investigated further by utilising the HEK293 HO-1 system to assess the effects of endogenous CO production.

CoPPIX successfully induced HO-1 in both HEK293/$Ca_v3.2$ and WT HEK293 cells, as illustrated by immunocytochemistry in Figure 3.10. The cellular location of HO-1 in these images appears to be generally cytoplasmic, with no clear organelle locale. In HEK293 cells, HO-1 has been localised to the nucleus (Lin *et al.*, 2007), whereas in other cell types, HO-1 has been localised to caveolae (Kim *et al.*, 2004), mitochondria

(Converso *et al.*, 2006), and the endoplasmic reticulum where it is synthesised (Shibahara *et al.*, 1980). Figure 3.13 shows that HO-1 induction by 10µM CoPPIX significantly reduced basal $[Ca^{2+}]_i$ in HEK293/Ca_v3.2 cells. Additionally, the response of the HO-1 group to Ca^{2+}-free buffer was lower than that of the control group. These data imply the window current was smaller as a result of HO-1 induction, which could be attributed to CO-mediated inhibition of the Ca_v3.2 T-type Ca^{2+} channels. The disparate concentrations of CoPPIX used to induce optimally, HO-1 in HEK293/Ca_v3.2 and WT HEK293 cells, is a limitation of the experiment. However, these concentrations were selected based on western blotting data in Figures 3.11 and 3.12, to ensure HO-1 was induced without cytotoxicity as a result of CoPPIX exposure.

The proliferative profile in response to CoPPIX in HEK293/Ca_v3.2 cells inversely correlates to the profile of HO-1 induction by CoPPIX, as validated by the increased expression of the HO-1 protein, shown in Figures 3.14 (A) and 3.11 respectively. However, there was no clear concentration-response to CoPPIX in WT HEK293 cells, shown in Figure 3.12, and HO-1 was also induced to higher levels than in HEK293/Ca_v3.2 cells. The pattern of HO-1 induction, and the extent of the physiological effect, was visibly different between the two cell lines. The proliferation of HEK293/Ca_v3.2 cells was reduced by 27% with 10µM CoPPIX, compared to a reduction of 79% by 10µM CoPPIX in WT HEK293 cells. One possible explanation for the fact that WT HEK293 cells are more susceptible to the effects of HO-1 induction than HEK293/Ca_v3.2 cells could be that the level of CO produced by HO-1 induction may not be as effective at inhibiting the Ca_v3.2 T-type Ca^{2+} channel when it is vastly over-expressed. There could be a proportion of Ca_v3.2 T-type Ca^{2+} channels that are unaffected by the available CO, which would leave a proportion of Ca_v3.2 T-type Ca^{2+} channels free to function normally. The window current would be active at these channels, and therefore CO inhibition at other Ca_v3.2 T-type Ca^{2+} channels would be ineffective at reducing $[Ca^{2+}]_i$ to a level that would fall short of the threshold trigger of the G_1/S cell cycle boundary, in order to subsequently prevent proliferation, as discussed earlier (Wang *et al.*, 2002b;Gray *et al.*, 2004).

An alternative explanation for the differing effects of CoPPIX could be that the WT HEK293 cells were simply more sensitive to this compound, and other effects were unsubstantiated. It is feasible that the HEK293/Ca_v3.2 cells are more robust due to their stable transfection. In WT HEK293 cells, there was a visible reduction in

proliferation by 3µM CoPPIX, albeit statistically non-significant. In contrast, HO-1 induction by 3µM CoPPIX had no effect on $[Ca^{2+}]_i$ in WT HEK293 cells. These data imply that HO-1 induction, and subsequent CO production, inhibit proliferation by an alternative mechanism to $Ca_v3.2$ T-type Ca^{2+} channel inhibition, as the immunocytochemistry in Figure 3.2 shows that there are no $Ca_v3.2$ T-type Ca^{2+} channels to inhibit. Although, the most plausible explanation is that CoPPIX is cytotoxic at concentrations higher than 3µM in WT HEK293 cells, and had any floating cells in the media been counted, this theory would have been corroborated. With regards to how CoPPIX induces HO-1, it appears that a region of DNA upstream of the murine HO-1 gene is the convergence point for the different signalling pathways from numerous HO-1 inducers, including hemin and CoPPIX (Alam *et al.*, 1995). It has also been demonstrated in chick embryonic liver cells that the response element for HO-1 induction by heme and CoPPIX differs from that of stress inducers such as heavy metals (Shan *et al.*, 2000;Shan *et al.*, 2002). The signalling pathway in human liver cells involves down-regulation of Bach1 and up-regulation of Nrf2 transcription factors (Shan *et al.*, 2006). In summary, the induction pathways of HO-1 appear to be complex and specific to the type of inducer.

It is unknown how the levels of CO produced via CoPPIX induction of HO-1 correlate to those produced by CORM-3 addition. Micromolar concentrations of CORM-3 are deemed to be comparable to endogenous CO (Foresti *et al.*, 2004). Conversely, it has been suggested that the exposure to exogenous, gaseous, CO would provide higher levels of CO than would be available as a result of HO-1 induction (Foresti *et al.*, 2008). The fact that proliferation was inhibited to a greater extent by CORM-3 than by HO-1 induction in HEK293/$Ca_v3.2$ cells, suggests more CO was available following CORM-3 exposure. It has also been suggested that a positive feedback loop exists within the HO-1/CO pathway, and that CO can directly induce the expression of HO-1 (Lee *et al.*, 2006;Kim *et al.*, 2007). This could explain why the more pronounced effects on proliferation were seen with CORM-3 exposure.

In conclusion, the data shown here demonstrate indirectly, that the $Ca_v3.2$ T-type Ca^{2+} channel can be inhibited by T-type Ca^{2+} channel antagonists, CO via CORM-3, and HO-1 induction. The effects of which manifest as inhibition of HEK293/$Ca_v3.2$ cell proliferation, and appear to be linked to the window current associated with T-type Ca^{2+} channels. The T-type Ca^{2+} channel window current is evidently the underlying

mechanism maintaining adequate $[Ca^{2+}]_i$ levels for numerous physiological processes. These include signal amplification in thalamacortical neurons, (Williams *et al.*, 1997), human myoblast fusion (Bijlenga *et al.*, 2000), and neuroendocrine differentiation of human prostate cancer cells, (Mariot *et al.*, 2002). There is also a wealth of data linking T-type Ca^{2+} channels currents to the pathological proliferation that underlies cancer development (Panner *et al.*, 2005;Panner & Wurster, 2006;Zhang *et al.*, 2012). In addition, the T-type Ca^{2+} current has been linked to the proliferation of primary aortic VSMCs; as the VSMCs become more confluent, the percentage of T-type Ca^{2+} current decreases, and the percentage of L-type current increases (Akaike *et al.*, 1989). This led to investigations into a role for T-type Ca^{2+} channels in pathological proliferation of VSMCs, reviewed by Cribbs, (2006). Therefore, to explore the effect of CO on the T-type Ca^{2+} channel in a more physiologically relevant model, a smooth muscle cell line was employed with the aim of assessing relevant findings in the context of data previously published on the anti-proliferative effects of CO in the vasculature (Morita *et al.*, 1997;Togane *et al.*, 2000;Song *et al.*, 2002;Otterbein *et al.*, 2003b;Raman *et al.*, 2006;Zuckerbraun *et al.*, 2006;Ramlawi *et al.*, 2007). This is examined in Chapter 4.

CHAPTER 4

Characterisation of Ca^{2+} channels in A7r5 cells

4.1 Introduction

VSMCs undergo a phenotypic switch, from a contractile to a proliferative state, in response to vascular injury (House *et al.*, 2008). This phenotypic switch is accompanied by an up-regulation of T-type Ca^{2+} channels, and a down-regulation of L-type Ca^{2+} channels (Akaike *et al.*, 1989;Richard *et al.*, 1992;Kuga *et al.*, 1996;Rodman *et al.*, 2005;House *et al.*, 2008). Pharmacological inhibition of T-type Ca^{2+} channels has been shown to inhibit cell proliferation in rat VSMCs (Schmitt *et al.*, 1995), human lung adenocarcinoma cells (Heo *et al.*, 2008), mouse glioblastoma cells (Keir *et al.*, 2012), and human glioblastoma cells (Schmitt *et al.*, 1995;Heo *et al.*, 2008;Keir *et al.*, 2012;Zhang *et al.*, 2012). Moreover, the maintenance of adequate $[Ca^{2+}]_i$ levels is central to the progression of the cell cycle (Ciapa *et al.*, 1994). The window current of T-type Ca^{2+} channels may be an important route through which $[Ca^{2+}]_i$ is maintained in proliferating cells; in VSMCs the window current is active at resting the membrane potential (-40mV to -55mV), providing a continuously functioning route of Ca^{2+} entry into the de-differentiated cells (Richard & Nargeot, 1998).

In order to study the effects of T-type Ca^{2+} channel modulation in the context of vascular biology, a VSMC line was employed. A7r5 cells are VSMCs that were originally isolated from embryonic rat aorta (Kimes & Brandt, 1976), and they have been shown to express both T- and L-type Ca^{2+} channels (Brueggemann *et al.*, 2005). A7r5 cell depolarisation using the vasoconstrictor vasopressin has been utilised to demonstrate the occurrence of Ca^{2+} oscillations in these cells (Otun *et al.*, 1992;Brueggemann *et al.*, 2005). Ca^{2+} oscillations within VSMCs promote a depolarising current that advances to neighbouring VSMCs via gap junctions, which synchronises a change in VSMC tone along the vessel (Peng *et al.*, 2001). The A7r5 cell line appears to be an ideal model in which to assess the contribution of T-type Ca^{2+} channels to changes of $[Ca^{2+}]_i$, in addition to the proliferative response.

4.2 Results

4.2.1 Characterisation of A7r5 cells

Immunocytochemistry was performed on A7r5 cells to confirm their smooth muscle cell properties. Figure 4.1 illustrates positive staining for smooth muscle α-actin (panel A), smooth muscle myosin heavy chain (panel B), and vimentin (panel C). In addition, co-localisation of smooth muscle α-actin and myosin heavy chain can be seen in panel Figure 4.1 (F), as demonstrated by the orange staining across the cells. All images in Figure 4.1 were produced from cells at the same passage, and using the same microscopy settings. The images in Figure 4.1 panels (D-F) were modified to the same extent by reducing the contrast in order to effectively discern the positive staining when the images were printed onto paper. The presence of T-type Ca^{2+} channels was also demonstrated by immunocytochemistry. Figure 4.2 shows positive staining for $Ca_v3.1$ and $Ca_v3.2$, with denser staining of $Ca_v3.1$ appearing in peri-nuclear regions. Anti-$Ca_v3.1$ and $Ca_v3.2$ antibodies sourced from Alomone were used to assess channel expression in A7r5 cells and human VSMC, as these antibodies produced consistent data upon experimental repeats. Demonstration of the presence of T-type Ca^{2+} channels by western blotting proved difficult; Figure 4.3 (A) shows the only successful identification of $Ca_v3.1$ from membrane enriched A7r5 samples, with HEK293/$Ca_v3.1$ cells used as the positive control. Figure 4.3 (B) shows the wide variation in mRNA expression levels of $Ca_v3.1$ from eleven samples of A7r5 cells, from five passages ranging from P2 to P6, as determined by RT-PCR. There was no correlation between passage number and degree of channel expression. Figure 4.4 shows the mRNA expression levels of $Ca_v3.2$, which was expressed at lower levels than $Ca_v3.1$, and $Ca_v3.2$ was undetected in some samples. Figure 4.5 shows example responses of A7r5 cells to 20mM K^+ buffer. This level of raised extracellular [K^+] was employed to cause modest depolarisation of the cell membranes, and therefore preferentially augment T-type voltage-gated Ca^{2+} channel activity. The example trace in panel (A) illustrates both the increase in $[Ca^{2+}]_i$ and the appearance of Ca^{2+} oscillations when A7r5 cells were exposed to 20mM K^+ buffer. The change in Fura 2 ratio for each of the three exposures to 20mM K^+ buffer is shown in panel (B). There was no significant difference between the first and second exposures. However, the response to 20mM K^+ buffer decreased on each subsequent exposure which is demonstrated by the significant difference in the change in Fura 2 ratio between exposure 1 and exposure 3. It was decided that only exposures 1 and 2 would be used in analyses of subsequent traces involving the assessment of a drug or compound. Panel (C) shows the spike frequency (i.e. the number of oscillations per second) for each exposure to 20mM K^+

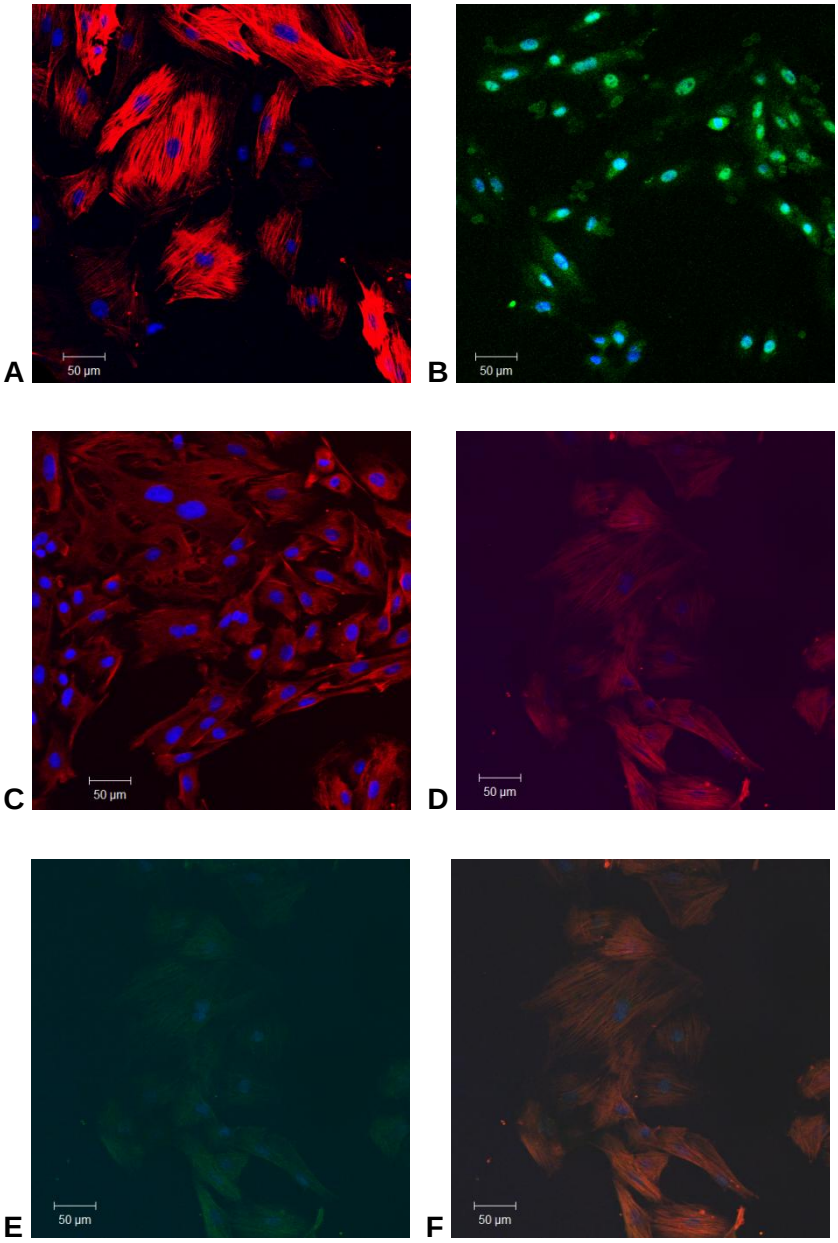

Figure 4.1 Characterisation of A7r5 cells

Immunocytochemistry of A7r5 cells showing staining for smooth muscle α-actin (red) (A), myosin heavy chain (green) (B), and vimentin (red) (C). The images in panels (D-F) were generated from simultaneous incubation with anti-smooth muscle α-actin and anti-myosin heavy chain antibodies; Panel (D) shows smooth muscle α-actin (red), panel (E) shows myosin heavy chain (green), and panel (F) shows smooth muscle α-actin and myosin heavy chain co-localisation. The contrast of images (D-F) was reduced by 15 units in order to distinguish the staining when the image is printed. Cell nuclei were stained blue with DAPI. Cells were utilised at P6, and are representative images of 4 fields of view from n=2 experimental repeats.

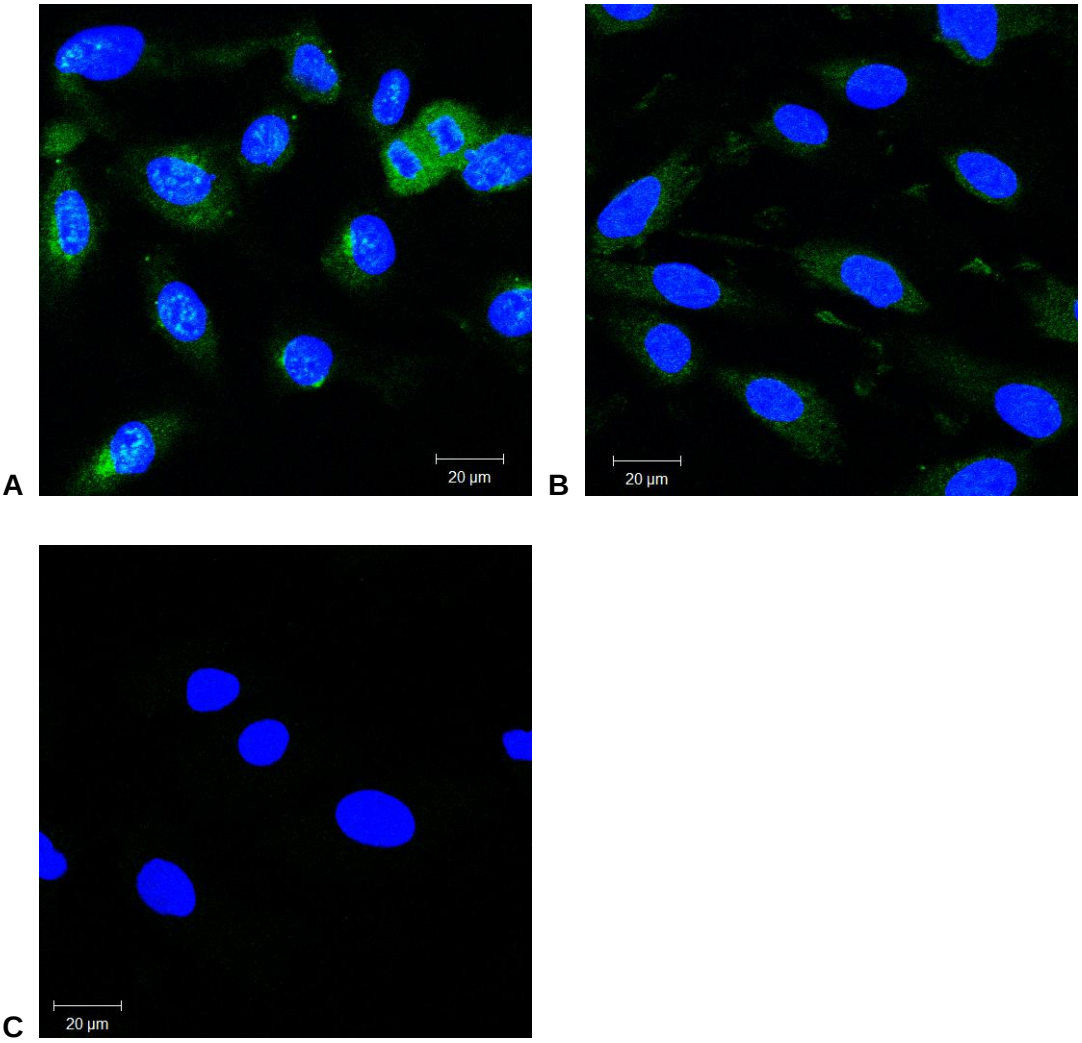

Figure 4.2 T-type Ca^{2+} channel expression in A7r5 cells

Immunocytochemistry of A7r5 cells showing staining for $Ca_v3.1$ (green) (A), and for $Ca_v3.2$ (green) (B). Antibodies sourced from Alomone. Panel (C) shows a control image without primary antibody. Cell nuclei were stained blue with DAPI. Cells were utilised at P4, and are representative images of 14 fields of view from n=7 experimental repeats.

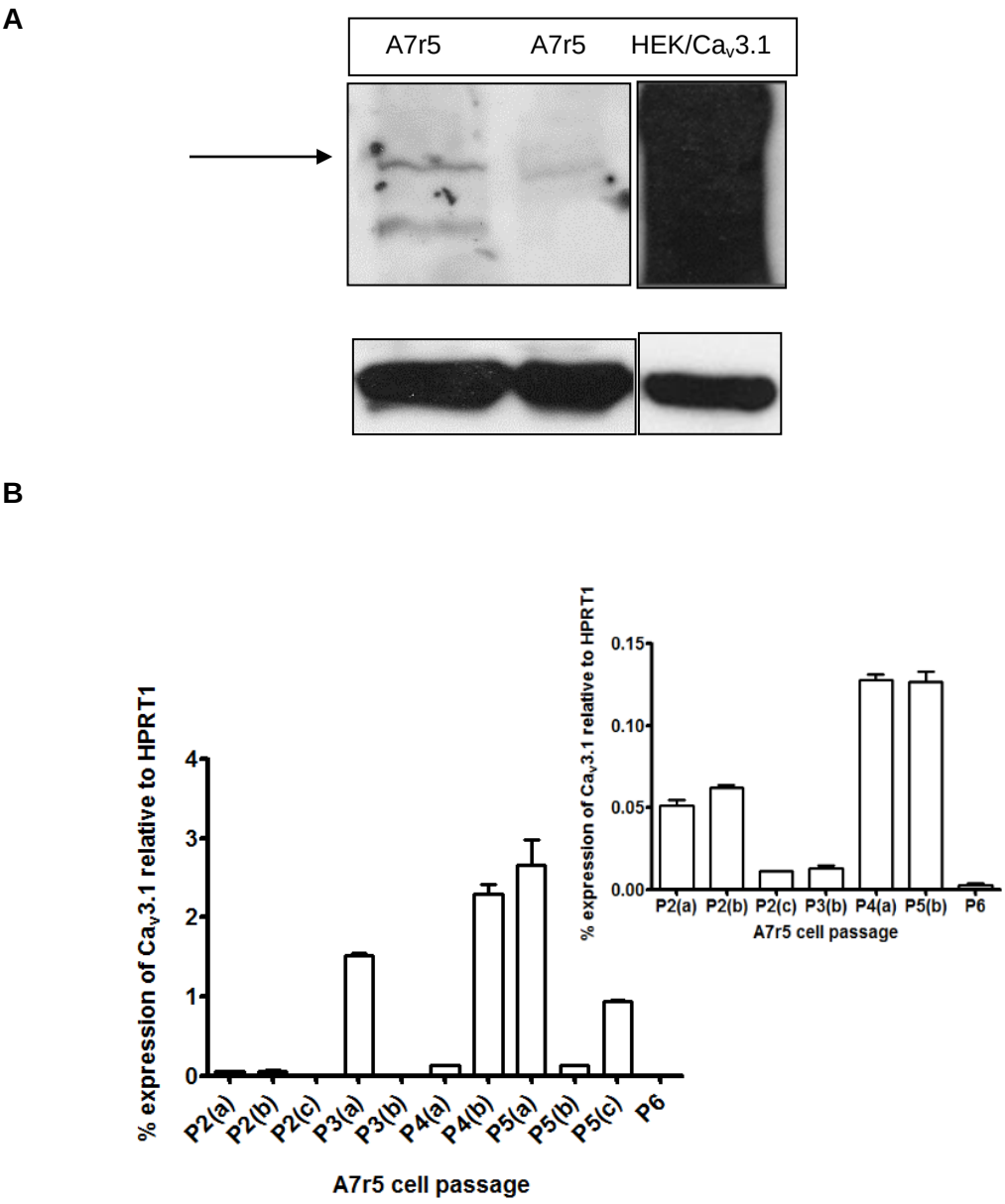

Figure 4.3 Expression of the $Ca_v3.1$ T-type Ca^{2+} channels in A7r5 cells

Panel (A) shows the only successful western blot of the $Ca_v3.1$ T-type Ca^{2+} channel, using anti-$Ca_v3.1$ antibody (Alomone), in various cell samples tested (A7r5: membrane enriched A7r5; HEK/$Ca_v3.1$: HEK293/$Ca_v3.1$ cells, positive control). The arrow represents the position of the 250kDa molecular weight marker. Below is the corresponding β-actin loading control blot. Panel (B) shows a bar graph of $Ca_v3.1$ mRNA expression, relative to the endogenous control, HPRT1 (hypoxanthine phosphoribosyltransferase 1), in eleven samples of A7r5 cells from five different passages, as indicated by the x-axis label. The inset bar graph shows the A7r5 samples with lower expression levels not clearly visible on the main bar graph. Samples were analysed in triplicate and represented as mean ± s.e.m.

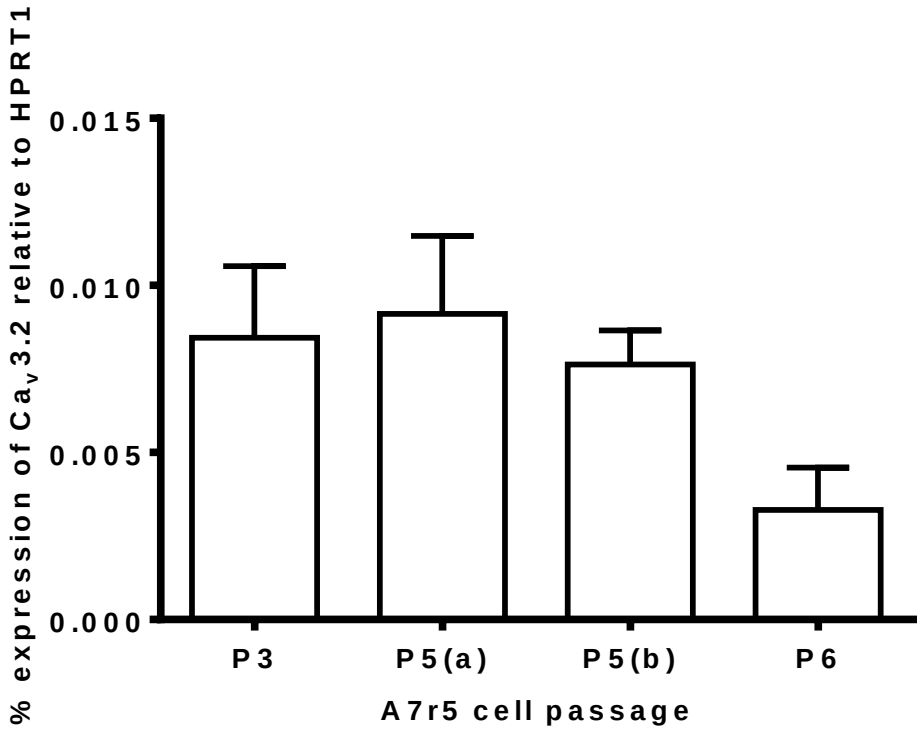

Figure 4.4 Expression of the $Ca_v3.2$ T-type Ca^{2+} channel in A7r5 cells

Bar graph of $Ca_v3.2$ mRNA expression, relative to the endogenous control, HPRT1. Twelve samples of A7r5 cells were analysed for $Ca_v3.2$ mRNA expression, and the channel was detectable in four samples from three passages, as indicated by the x-axis label. Samples were analysed in triplicate and represented as mean ± s.e.m.

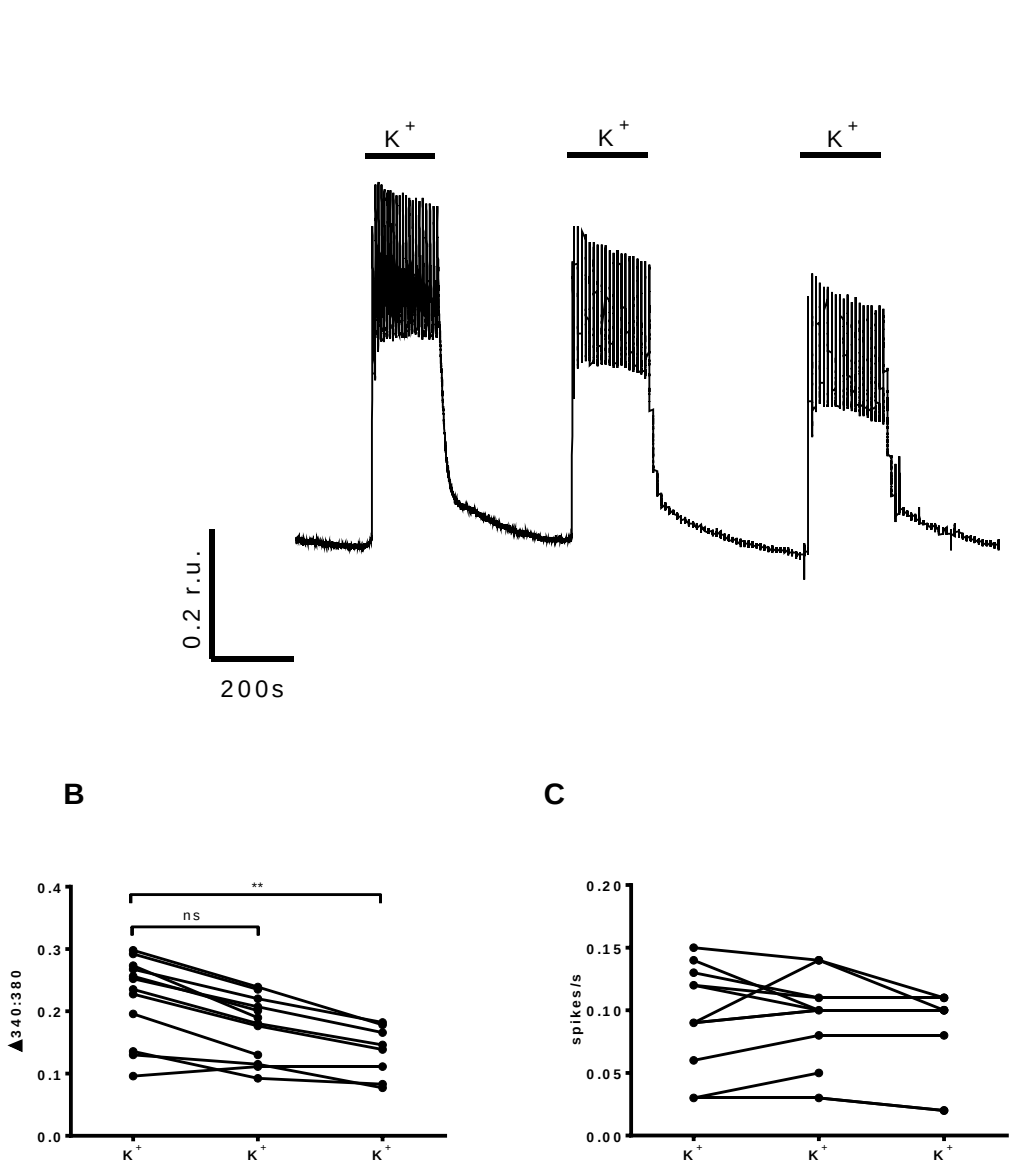

Figure 4.5 20mM K^+ buffer causes Ca^{2+} oscillations and an increase in $[Ca^{2+}]_i$

(A) Representative control trace showing the response of A7r5 cells to 20mM K^+ buffer. The switch from normal buffer (Ca^{2+}-containing) to 20mM K^+ buffer causes a rapid increase in $[Ca^{2+}]_i$ and Ca^{2+} oscillations, as shown by the three exposures. (B) Trend graph showing the change in Fura 2 ratio for the three exposures to 20mM K^+ buffer. (C) Trend graph showing the change in spikes/s for the three exposures to 20mM K^+ buffer. Data were analysed by one-way ANOVA with Bonferroni's multiple comparison test, ** $p<0.01$, $n=12$.

buffer. There were no significant differences between exposures 1-3. Figure 4.6 shows the minimal change in $[Ca^{2+}]_i$ when extracellular Ca^{2+} is removed; Fura 2 ratio was reduced by 4%, which is representative of a small window current. Figure 4.7 (A) shows the response of A7r5 cells to 80mM K^+ buffer. This level of extracellular $[K^+]$ was used to strongly depolarise the cell membranes, and thereby stimulate Ca^{2+} influx preferentially via L-type Ca^{2+} channels. There was a rapid increase in $[Ca^{2+}]_i$ as 80mM K^+ buffer was applied, which slowly declined during continued depolarisation, presumably because the L-type Ca^{2+} channels inactivate. Figure 4.7 (B) shows that removal of extracellular Ca^{2+} causes an almost complete loss of this response, as predicted, since Ca^{2+} was not available to move into the cell. Panel (C) shows the mean integrated response of five experiments, illustrated by Figure 4.7 (A) and (B).

In summary, $Ca_v3.1$ is the more prominent T-type Ca^{2+} channel in A7r5 cells. A7r5 cells produce Ca^{2+} oscillations in response to 20mM K^+ buffer, and rapid increases in $[Ca^{2+}]_i$ in response to both 20mM and 80mM K^+ buffer, implicating the presence of both T- and L-type Ca^{2+} channels in A7r5 cells.

4.2.2 The contribution of T-type and L-type Ca^{2+} channels to evoked $[Ca^{2+}]_i$ responses in A7r5 cells

Mibefradil was employed to assess the changes in $[Ca^{2+}]_i$ as a result of T-type Ca^{2+} channel inhibition. After an initial exposure to 20mM K^+ buffer, 3µM mibefradil was applied prior to, and throughout, the second exposure, which subsequently inhibited $[Ca^{2+}]_i$ by 58%, and also inhibited Ca^{2+} oscillations, as shown in Figure 4.8 (A). Unexpectedly, the responses of $[Ca^{2+}]_i$ to 80mM K^+ buffer were also significantly reduced by 65% in the presence of 3µM mibefradil, as shown by the example trace and the mean integral in Figure 4.9.

The effect of Ni^{2+}, a differentially selective T-type Ca^{2+} channel blocker, was also investigated. As the $Ca_v3.1$ Ca^{2+} channel is the dominant subtype in A7r5 cells, the inhibitory effects of Ni^{2+} on $Ca_v3.1$ channel activity in HEK293/$Ca_v3.1$ cells were assessed within our research group using whole-cell patch clamp recordings. Peak current-voltage (I-V) relationship curves in response to a range of Ni^{2+} concentrations are shown in Figure 4.10, and were generated by Dr Jacobo Elies. The IC_{50} was found

A

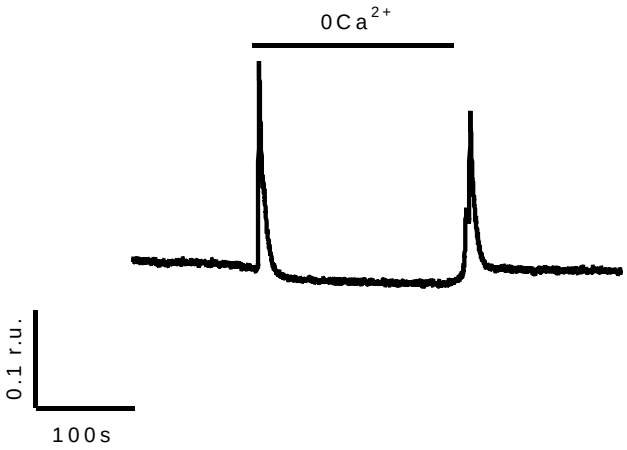

B

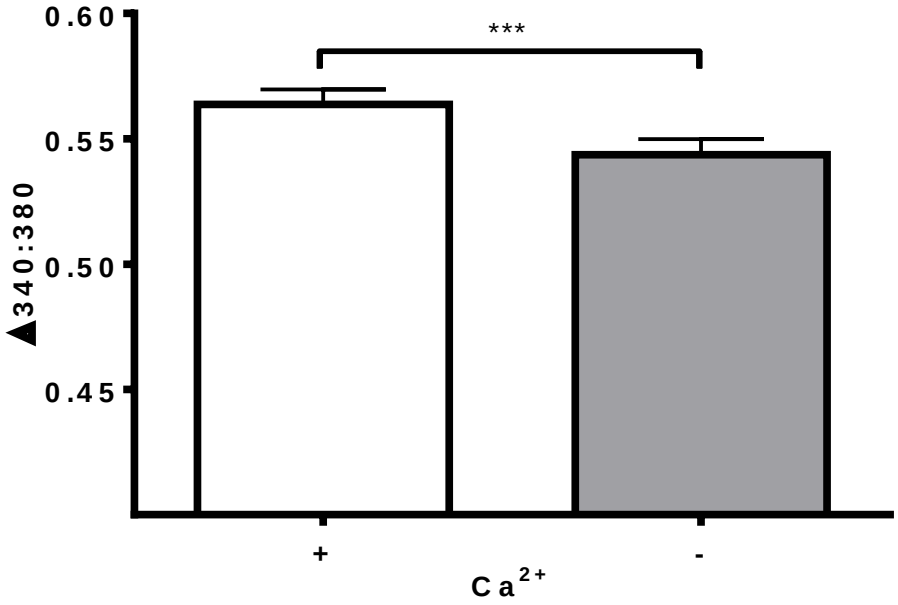

Figure 4.6 The response of $[Ca^{2+}]_i$ on exposure to Ca^{2+}-free extracellular buffer

Representative trace showing the response of A7r5 cells to Ca^{2+} free buffer (A). Bar graph of mean (± s.e.m.) Fura 2 ratio in response to Ca^{2+}-containing and Ca^{2+}-free extracellular buffer (B). Data were analysed by a two-tailed paired t-test, *** $p<0.001$, $n=3$.

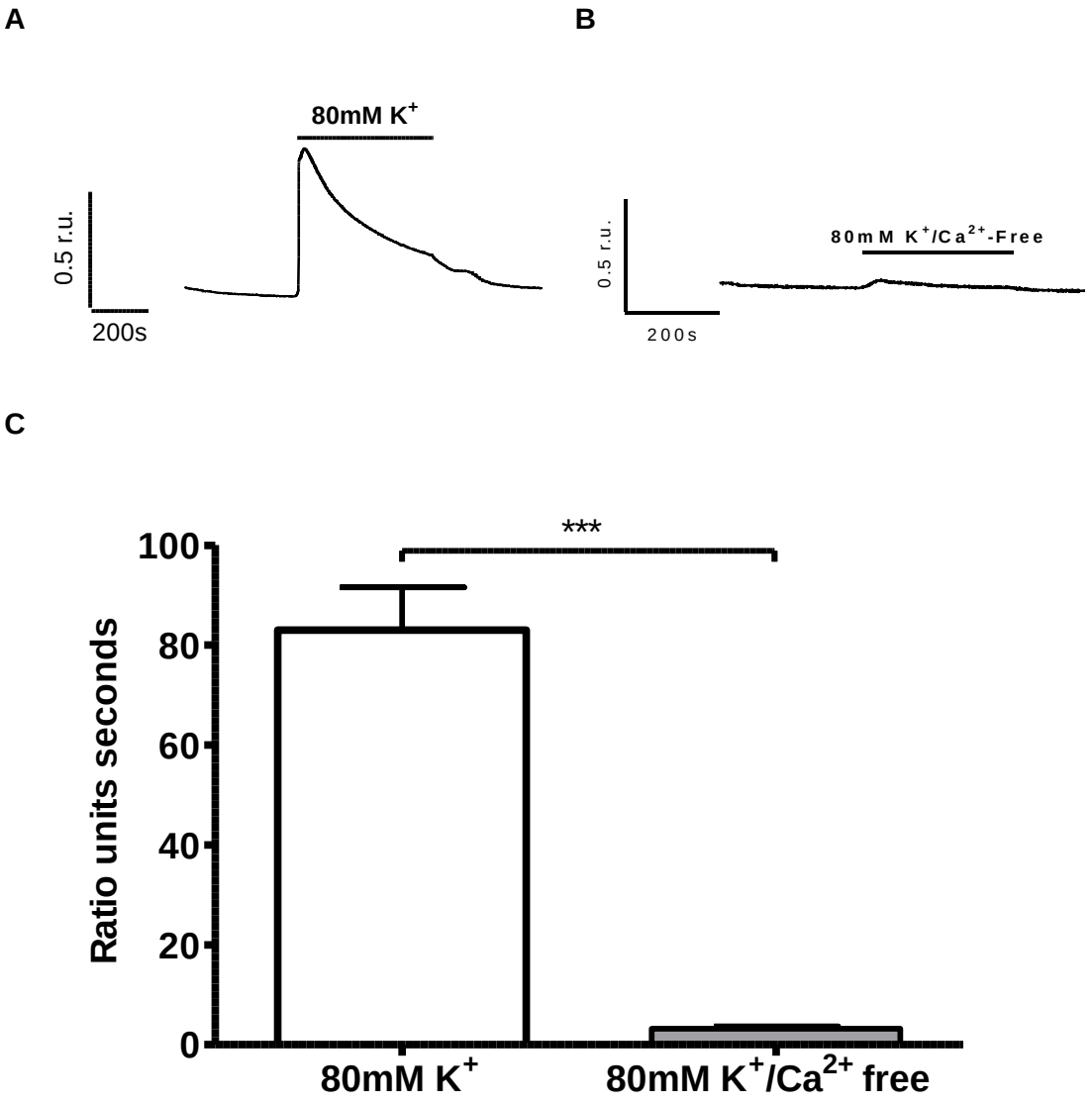

Figure 4.7 80mM K^+ buffer causes a rapid increase in $[Ca^{2+}]_i$

Representative control trace showing the response of A7r5 cells to cell depolarisation by 80mM K^+ (A), exhibited as an increase in Fura 2 ratio. This is the control condition to which subsequent drug applications will be compared to. Representative trace showing the minimal change in $[Ca^{2+}]_i$ in response to 80mM K^+/Ca^{2+}-free buffer (B). Bar graph showing the mean (± s.e.m.) integral of the responses evoked by 80mM K^+ or 80mM K^+/Ca^{2+} free buffer (C). Data were analysed by one-way ANOVA, *** $p<0.001$, $n=5$.

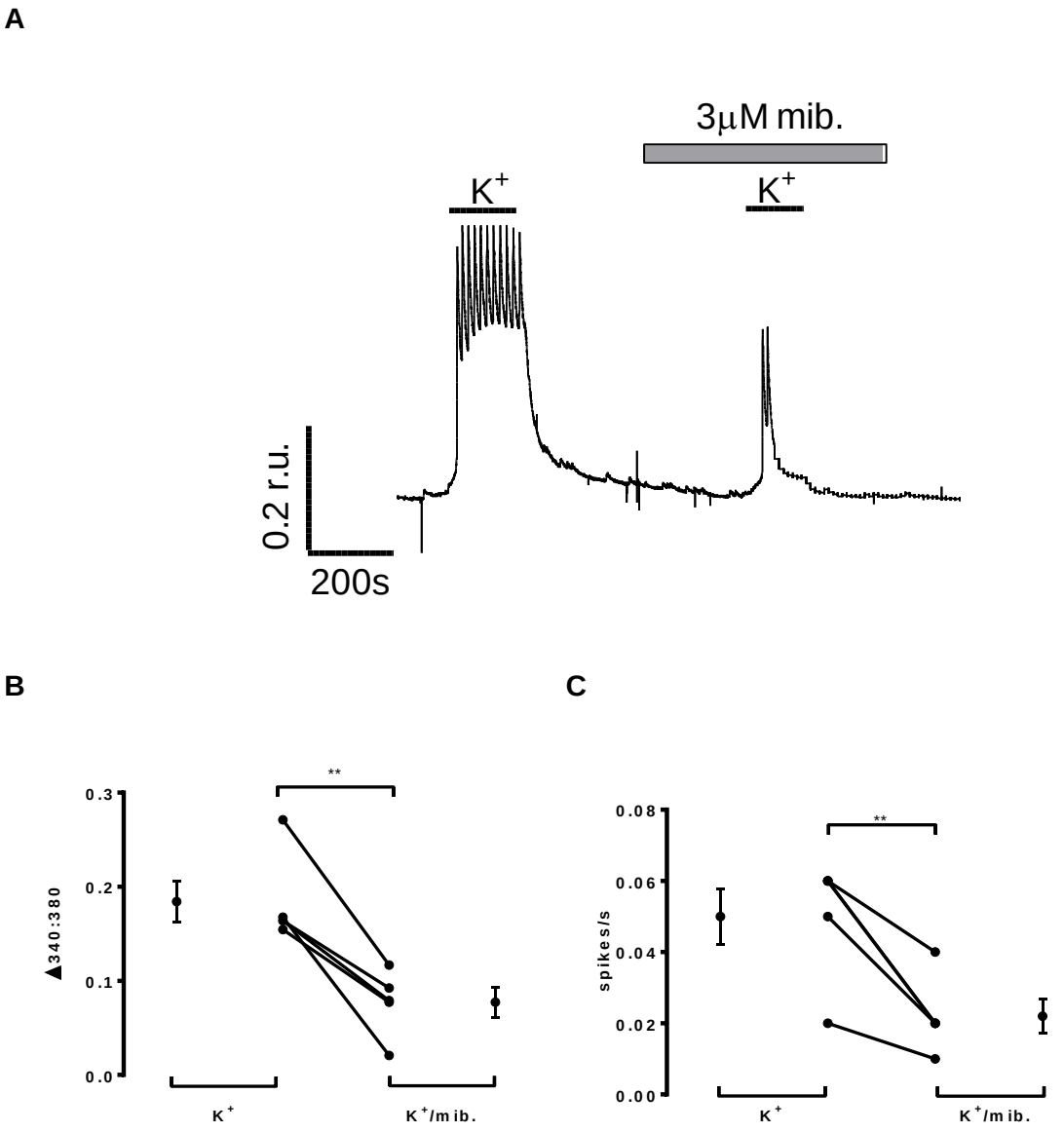

Figure 4.8 3µM mibefradil inhibits $[Ca^{2+}]_i$ and Ca^{2+} oscillations

Representative trace showing the response of A7r5 cells to 20mM K^+ buffer in the presence of 3µM mibefradil (A). Panel (B) shows a trend graph of the decrease in Fura 2 ratio in response to 20mM K^+ buffer followed by 20mM K^+ buffer in the presence of 3µM mibefradil. Panel (C) shows a trend graph of the decrease in spikes/s for exposure to 20mM K^+ buffer followed by 20mM K^+ buffer in the presence of 3µM mibefradil. The mean (± s.e.m.) response is shown to the right and left of the corresponding individual data points on each graph. Data were analysed by a two-tailed paired t-test, ** $p<0.01$, n=5. mib. = mibefradil

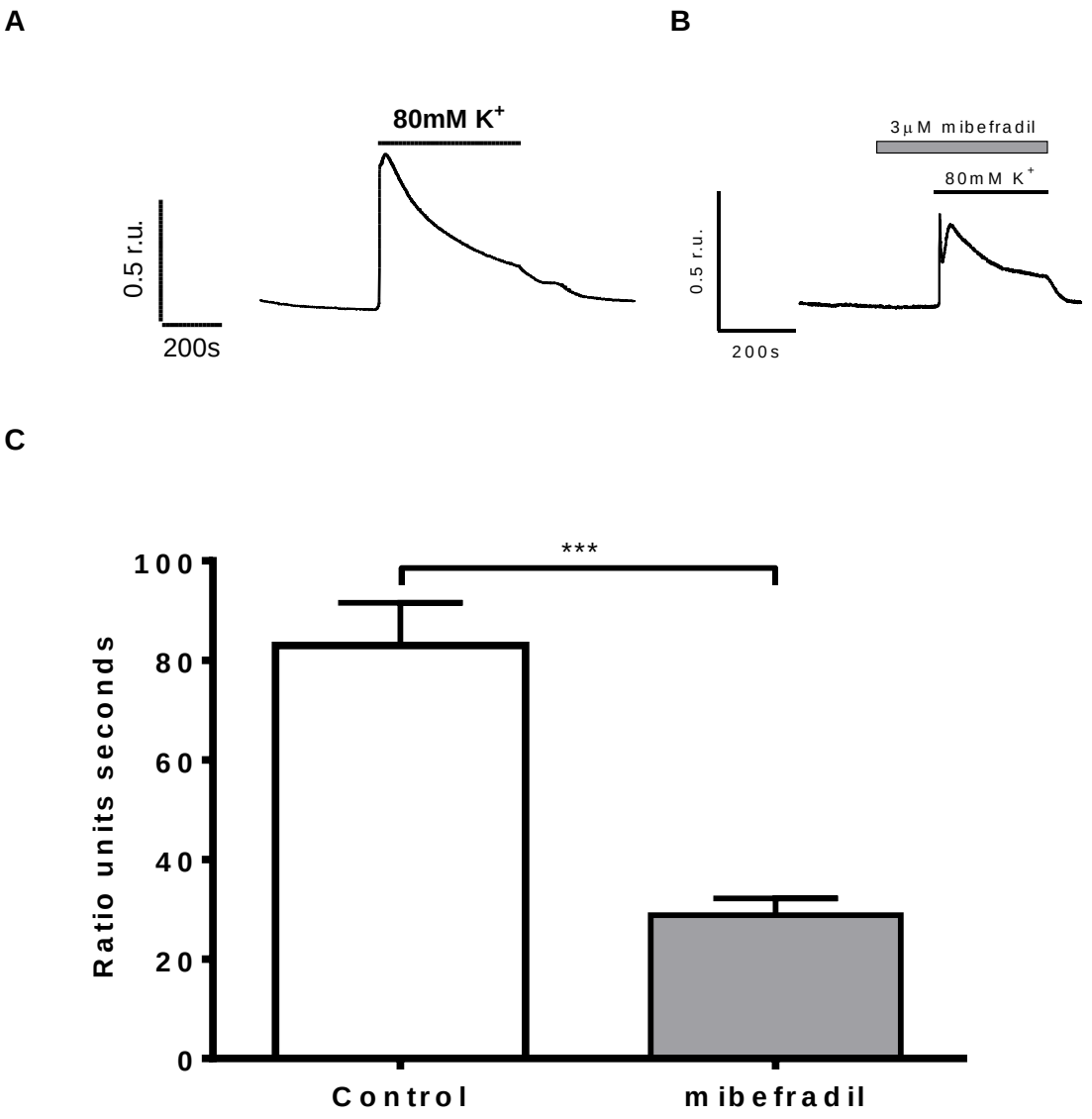

Figure 4.9 Response to 80mM K^+ buffer containing 3µM mibefradil

Representative trace showing the change of $[Ca^{2+}]_i$ in response to 80mM K^+ buffer (A) and the reduced response to 80mM K^+ containing 3µM mibefradil (B). Bar graph showing the mean (± s.e.m.) integral of the curves produced in response to 80mM K^+ buffer (control), and 80mM K^+ buffer containing 3µM mibefradil (C). Data were analysed by one-way ANOVA, *** $p<0.001$, n=5.

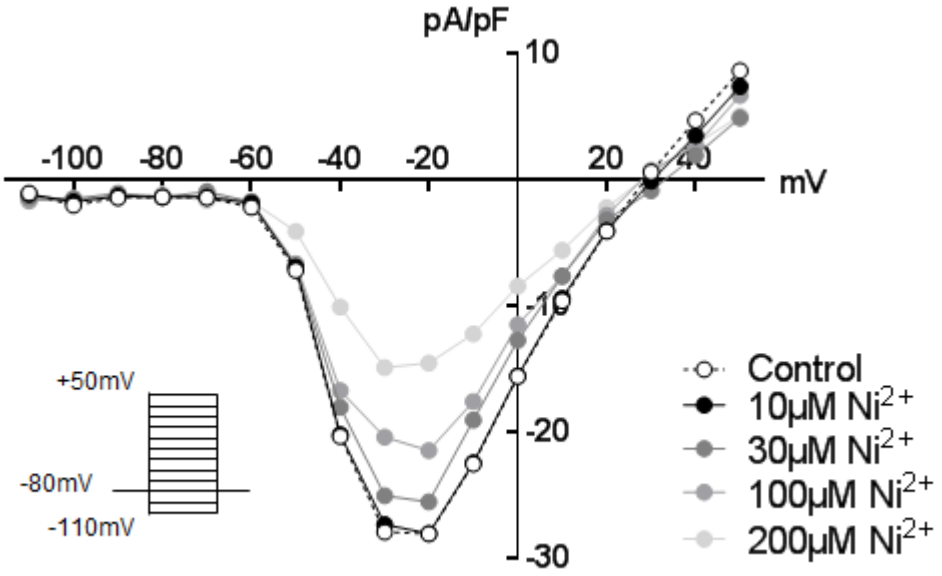

Figure 4.10 Inhibitory effects of Ni^{2+} on $Ca_v3.1$ channels

Representative peak I-V curves showing control and Ni^{2+} treated HEK293/$Ca_v3.1$ cells. Peak I-V relationships were measured by stepping from a holding potential of -80mV to voltages between -110mV and +50mV in 10mV increments for 100ms each. Data generated by Dr Jacobo Elies.

to be 289 ± 11.3µM (n=3). Preliminary experiments investigating the effect of 250µM Ni^{2+} demonstrated the complete abolition of the response to 20mM K^+ buffer. Therefore, a lower concentration of 30µM Ni^{2+} was utilised to assess the effects of low level T-type Ca^{2+} channel inhibition without producing off-target effects on L-type Ca^{2+} channels. Figure 4.11 shows the effects of 30µM Ni^{2+}. Mean $[Ca^{2+}]_i$ was significantly reduced by 37% via 30µM Ni^{2+}, yet Ca^{2+} oscillations were not significantly affected. The presence of 30µM Ni^{2+} did not alter the response to 80mM K^+ buffer; the mean curve integral was comparable to that of the control cells, as shown in Figure 4.12.

Nifedipine was employed to assess the effects of L-type Ca^{2+} channel inhibition on $[Ca^{2+}]_i$, with the aim of establishing which responses could be attributed solely to T-type Ca^{2+} channel activity. The representative trace in Figure 4.13 (A) shows that 2µM nifedipine reduces the response to 20mM K^+ buffer by 60%, and completely abolishes the Ca^{2+} oscillations. Figure 4.14 demonstrates that nifedipine also significantly inhibited the response to 80mM K^+ buffer. The mean curve integral was reduced by 68% in the presence of 2µM nifedipine.

The simultaneous addition of 2µM nifedipine and 3µM mibefradil completely prevented the response to 20mM K^+ buffer. There was no rise in $[Ca^{2+}]_i$ and no Ca^{2+} oscillations, as shown in Figure 4.15. Application of mibefradil and nifedipine, individually or simulataneously, significantly prevented an increase of $[Ca^{2+}]_i$, and the combined effect of both compounds on $[Ca^{2+}]_i$ was significantly different from each individual effect, as shown in Figure 4.15 (D). Simultaneous addition of 2µM nifedipine and 3µM mibefradil inhibited a significant rise in $[Ca^{2+}]_i$ in response to 80mM K^+ buffer, as shown in Figure 4.16. The mean curve integral was reduced by 92%, which is comparable to the response to Ca^{2+}-free 80mM K^+ buffer, suggesting essentially all voltage-gated Ca^{2+} channels were blocked, as expected. However, the combined effect of both compounds on $[Ca^{2+}]_i$ was not significantly different from each individual effect, as shown in Figure 4.16 (C). Application of 2µM nifedipine and 30µM Ni^{2+}, individually or simultaneously, significantly prevented an increase of $[Ca^{2+}]_i$, and completely abolished the oscillatory response to 20mM K^+ buffer, as shown in Figure 4.17. Although, the combined effect of both compounds on $[Ca^{2+}]_i$ was not significantly different from each individual effect, as shown in Figure 4.17 (D). Concerning the oscillation frequency, Ni^{2+} caused no significant effect on the response to 20mM K^+

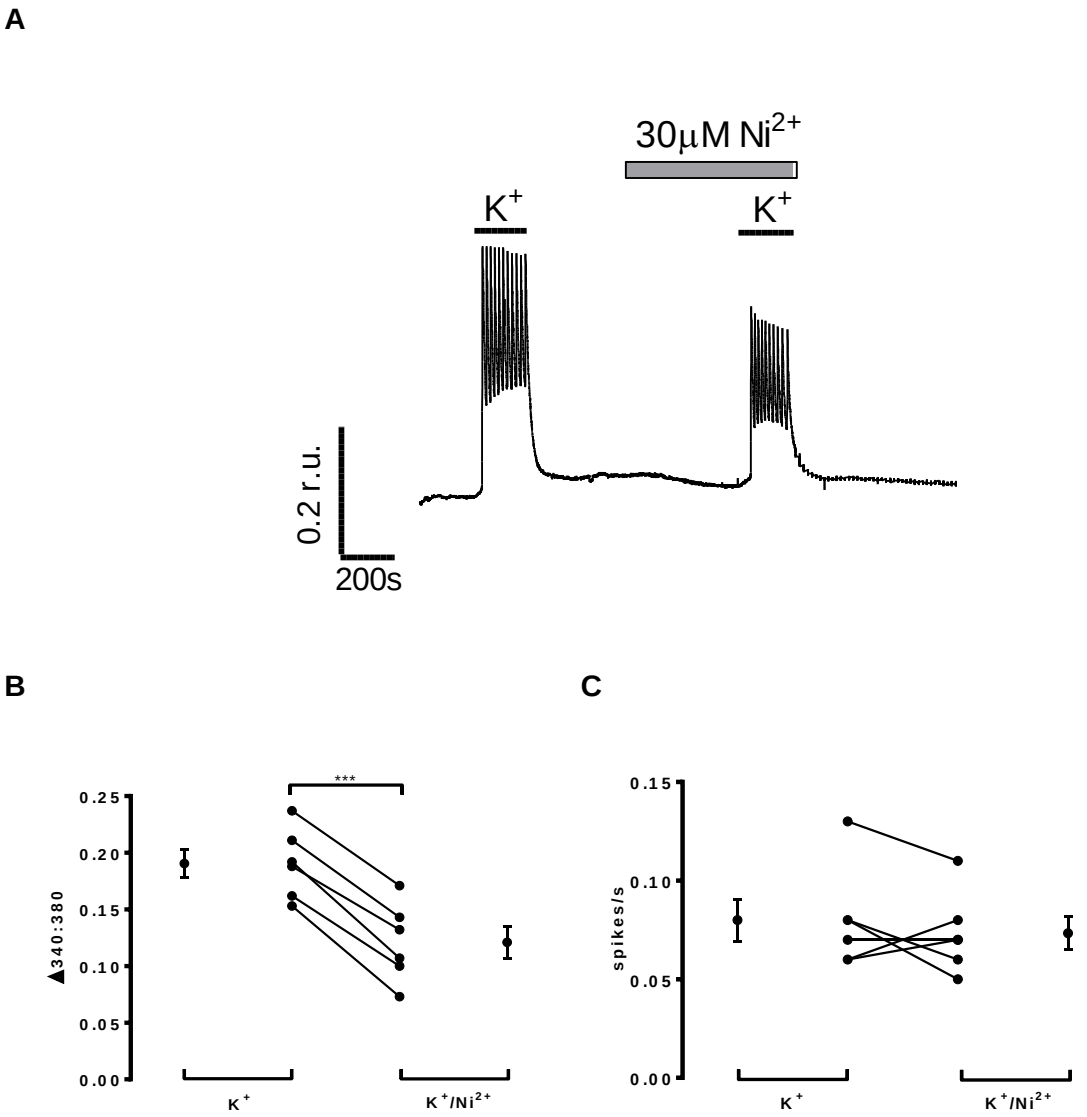

Figure 4.11 30µM Ni^{2+} inhibits $[Ca^{2+}]_i$ but not Ca^{2+} oscillations

Representative trace showing the response of A7r5 cells to 20mM K^+ buffer in the presence of 30µM Ni^{2+} (A). Panel (B) shows a trend graph of the decrease in Fura 2 ratio in response to 20mM K^+ buffer followed by 20mM K^+ buffer in the presence of 30µM Ni^{2+}. Panel (C) shows a trend graph of the change in spikes/s for exposure to 20mM K^+ buffer followed by 20mM K^+ buffer in the presence of 30µM Ni^{2+}. The mean (± s.e.m.) response is shown to the right and left of the corresponding individual data points on each graph. Data were analysed by a two-tailed paired t-test, *** $p<0.001$, $n=6$.

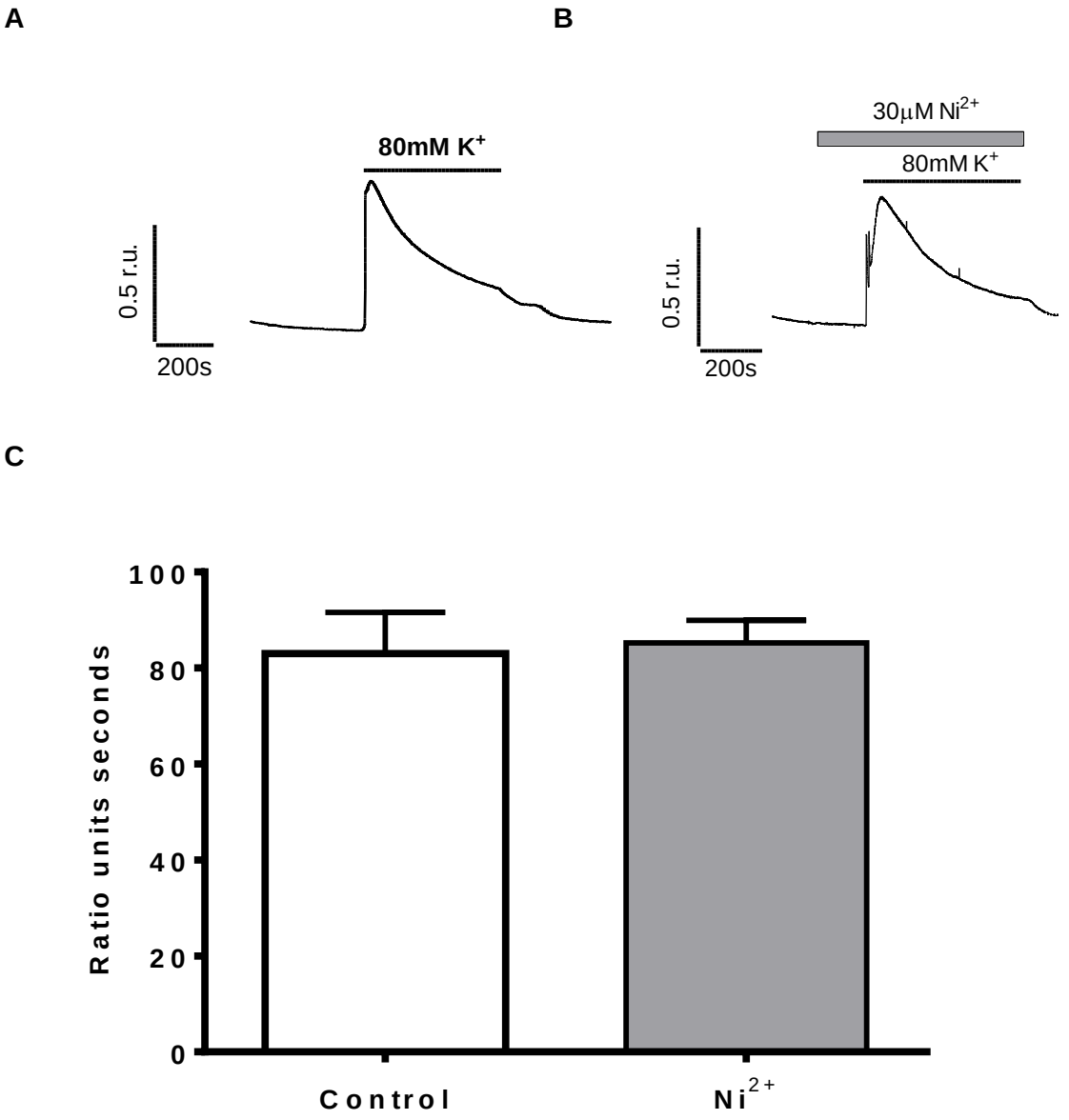

Figure 4.12 Response to 80mM K^+ buffer containing 30µM Ni^{2+}

Representative trace showing the change of $[Ca^{2+}]_i$ in response to 80mM K^+ buffer (A) and in response to 80mM K^+ buffer containing 30µM Ni^{2+} (B). Bar graph showing the mean (± s.e.m.) integral of the curves produced in response to 80mM K^+ buffer (control), and 80mM K^+ buffer containing 30µM Ni^{2+} (C), n=6.

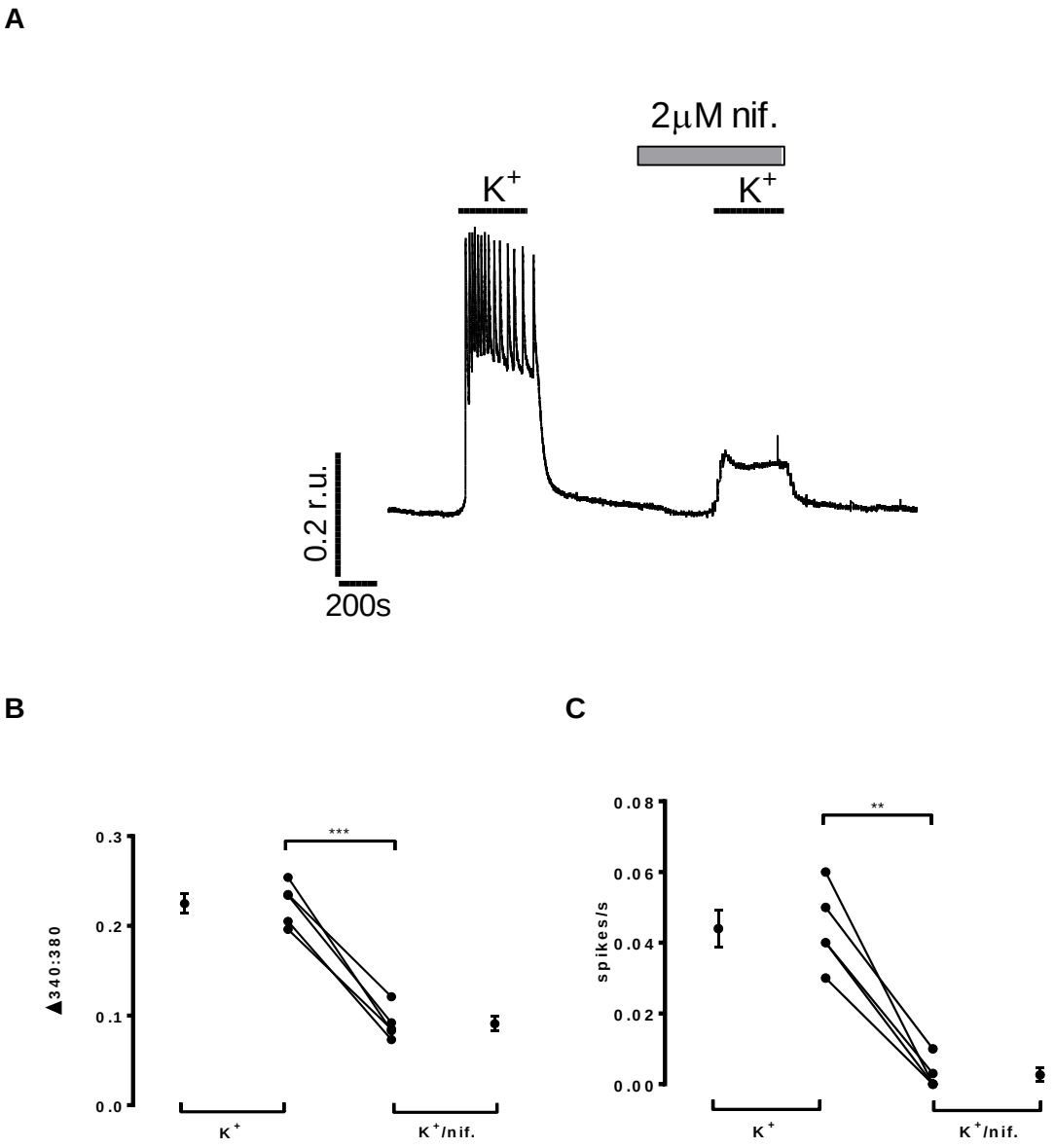

Figure 4.13 2μM nifedipine inhibits $[Ca^{2+}]_i$ and Ca^{2+} oscillations

Representative control trace showing the response of A7r5 cells to 20mM K^+ buffer in the presence of 2μM nifedipine (A). Trend graph showing the decrease in Fura 2 ratio in response to 20mM K^+ buffer followed by 20mM K^+ buffer in the presence of 2μM nifedipine. (B). Trend graph showing the decrease in spikes/s in response to 20mM K^+ buffer followed by 20mM K^+ buffer in the presence of 2μM nifedipine (C). The mean (± s.e.m.) response is shown to the right and left of the corresponding individual data points on each graph. Data were analysed by a two-tailed paired t-test, ** $p<0.01$, *** $p<0.001$, n=5. nif. = nifedipine

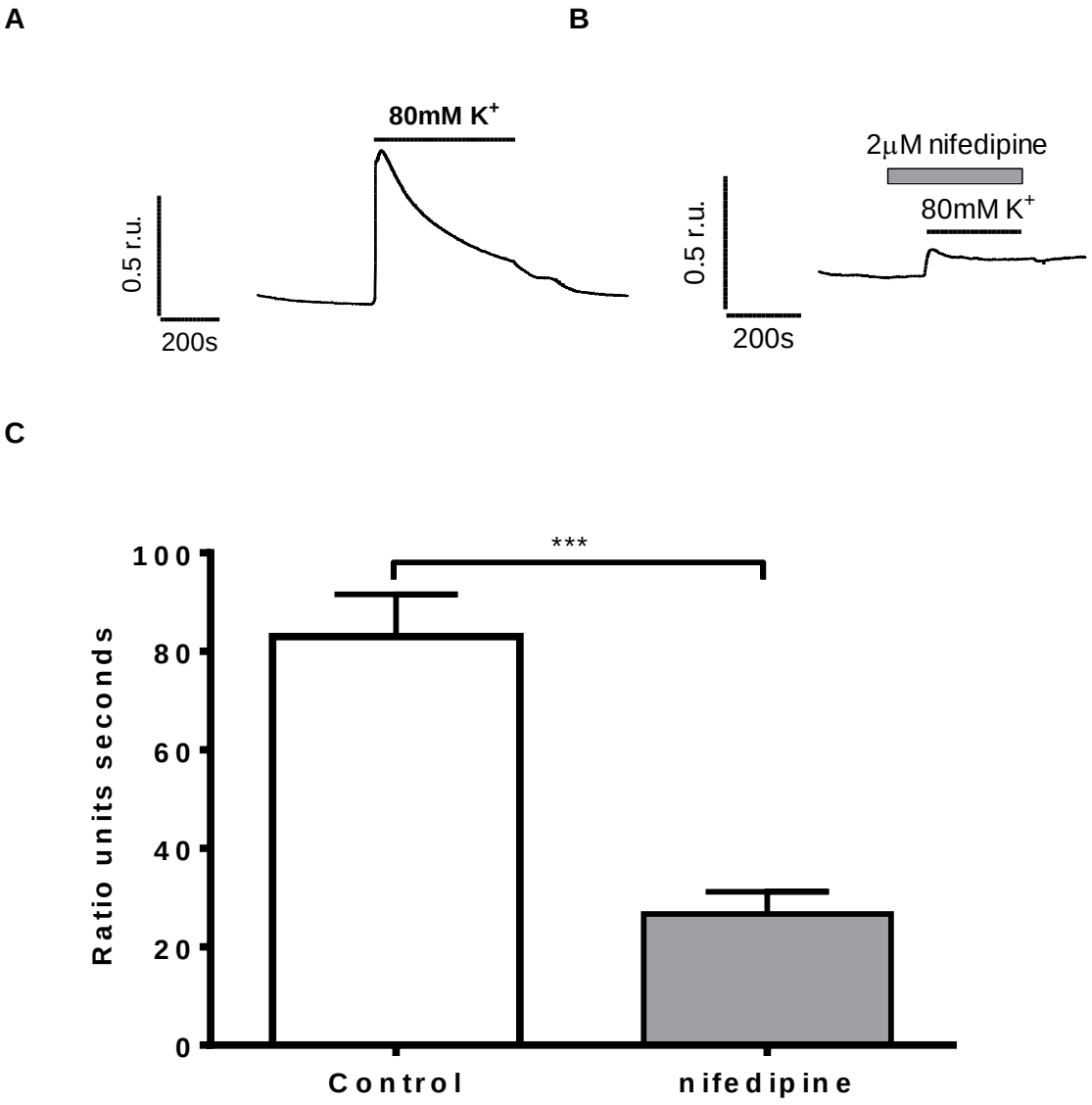

Figure 4.14 Response to 80mM K^+ buffer containing 2μM nifedipine

Representative trace showing the change of $[Ca^{2+}]_i$ in response to 80mM K^+ buffer (A) and the decreased response to 80mM K^+ buffer containing 2μM nifedipine (B). Bar graph showing the mean (± s.e.m.) integral of the curves produced in response to 80mM K^+ buffer (control), and 80mM K^+ buffer containing 2μM nifedipine (C). Data were analysed by one-way ANOVA, *** $p<0.001$, n=7.

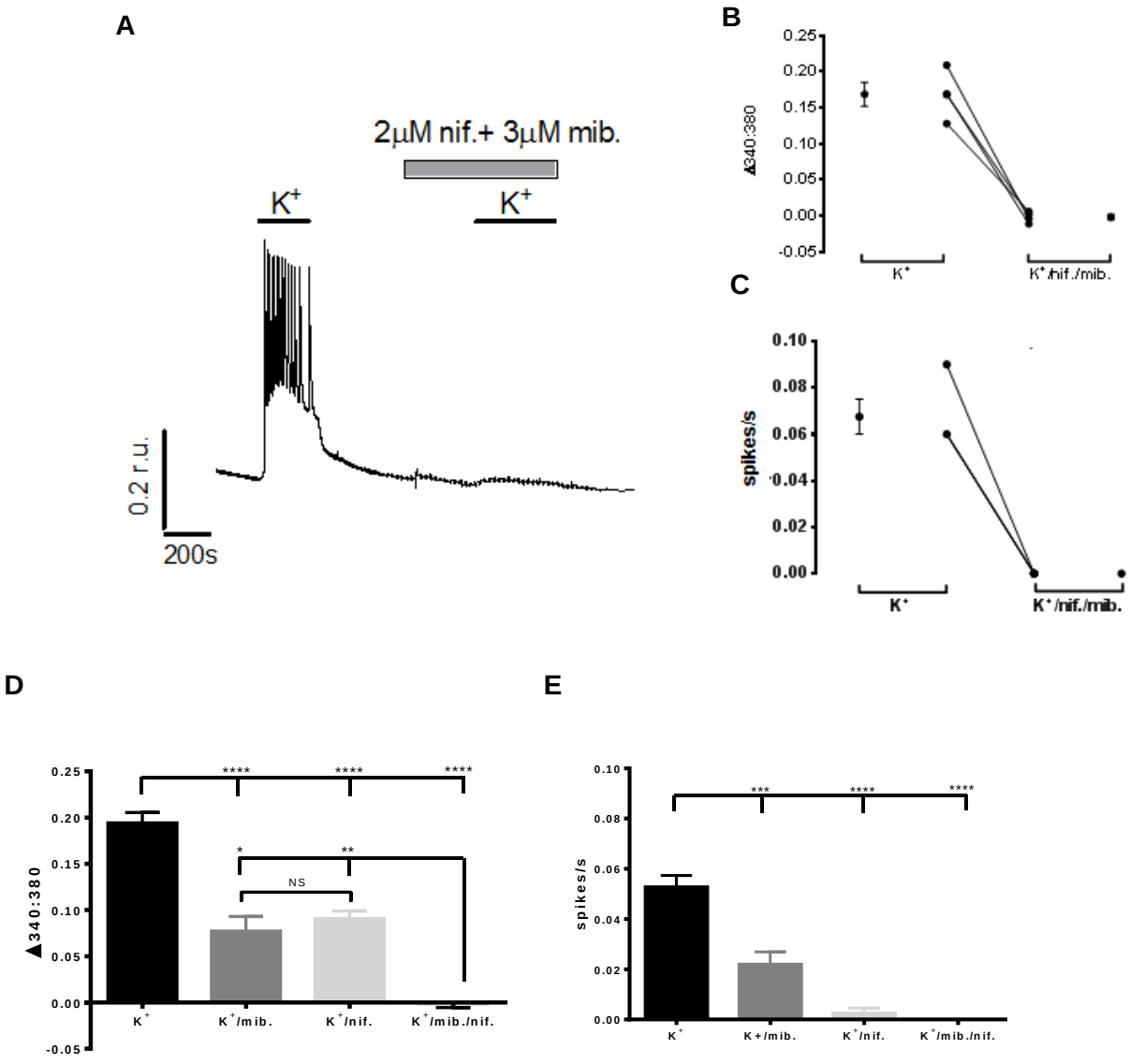

Figure 4.15 Simultaneous addition of 2µM nifedipine and 3µM mibefradil inhibits $[Ca^{2+}]_i$ and Ca^{2+} oscillations

Representative trace showing the response of A7r5 cells to 20mM K^+ buffer in the presence of 2µM nifedipine and 3µM mibefradil (A). Trend graph showing the decrease in Fura 2 ratio (B) and the decrease in spikes/s (C) within individual traces in response to 20mM K^+ buffer followed by 20mM K^+ buffer in the presence of 2µM nifedipine and 3µM mibefradil. The mean (± s.e.m.) response is shown to the right and left of the corresponding individual data points on each graph, n=4. Bar graph showing the mean (± s.e.m.) change in Fura 2 ratio (D) and the change in spikes/s (E) in response to 20mM K^+ buffer in the presence of the drug as indicated. Data analysed by one-way ANOVA followed by Tukey's multiple comparison test, * p<0.05, ** p<0.01 vs K^+/mib./nif. *** P<0.001, **** p<0.0001 vs K^+. nif. = nifedipine, mib. = mibefradil

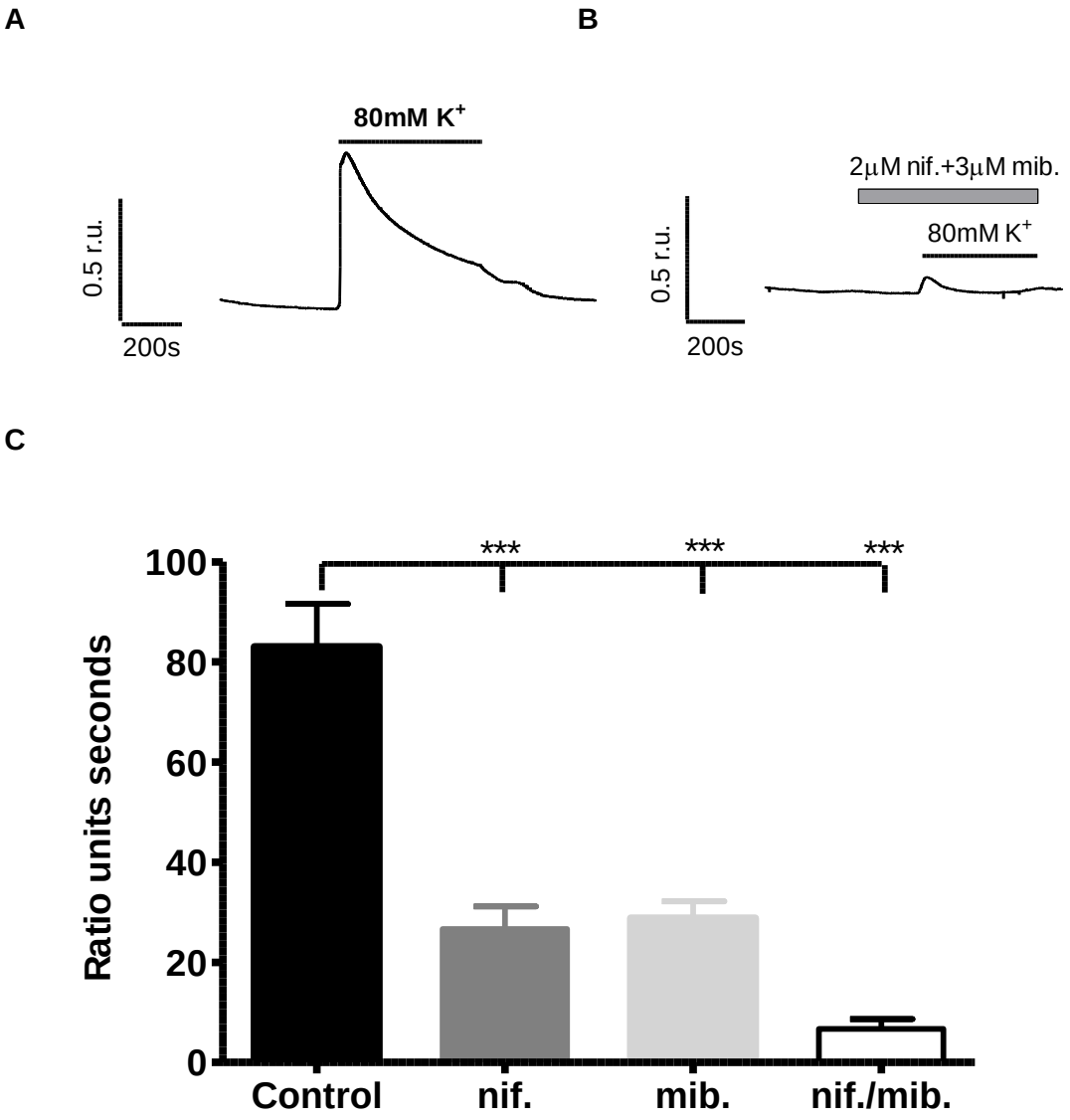

Figure 4.16 Response to 80mM K^+ buffer containing 2μM nifedipine and 3μM mibefradil

Representative trace showing the change of $[Ca^{2+}]_i$ in response to 80mM K^+ buffer (A) and the decreased response to 80mM K^+ buffer containing 2μM nifedipine and 3μM mibefradil (B). Bar graph showing the mean (± s.e.m.) integral of the curves produced in response to 80mM K^+ buffer (control), and 80mM K^+ buffer in the presence of the drug as indicated (C). Data were analysed by one-way ANOVA, *** $p<0.001$, n=6. nif. = nifedipine, mib. = mibefradil.

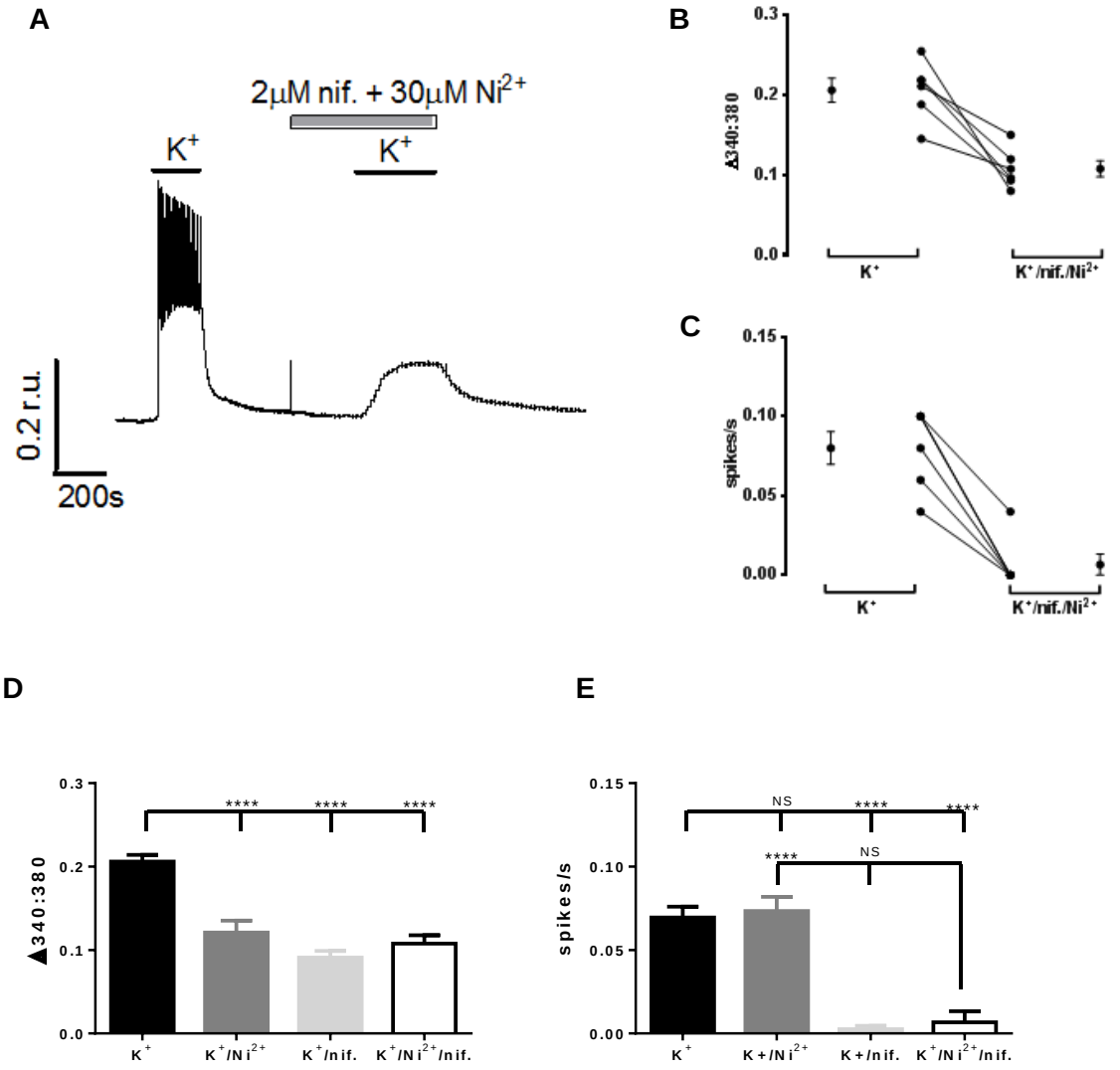

Figure 4.17 Simultaneous addition of 2μM nifedipine and 30μM Ni^{2+} inhibits $[Ca^{2+}]_i$ and Ca^{2+} oscillations

Representative trace showing the response of A7r5 cells to 20mM K^+ buffer in the presence of 2μM nifedipine and 30μM Ni^{2+} (A). Trend graph showing the decrease in Fura 2 ratio (B) and the decrease in spikes/s (C) within individual traces in response to 20mM K^+ buffer followed by 20mM K^+ buffer in the presence of 2μM nifedipine and 30μM Ni^{2+} The mean (± s.e.m.) response is shown to the right and left of the corresponding individual data points on each graph, n=6. Bar graph showing the mean (± s.e.m.) change in Fura 2 ratio (D) and the change in spikes/s (E) in response to 20mM K^+ buffer in the presence of the drug as indicated. Data analysed by one-way ANOVA followed by Tukey's multiple comparison test, **** $p<0.0001$ vs K^+ or K^+/Ni^{2+}/nif. nif. = nifedipine

buffer, and there was no significant difference between the response to nifedipine or nifedipine and Ni^{2+} combined. The differing extents of reductions of evoked $[Ca^{2+}]_i$ rises by the T-type Ca^{2+} channel blockers, mibefradil and Ni^{2+}, suggest that mibefradil has non-specific effects when used at 3µM. The lower level of $[Ca^{2+}]_i$ inhibition by 30µM Ni^{2+} is in accordance with the fact that the $Ca_v3.2$ T-type Ca^{2+} channels, which is the Ni^{2+} sensitive channel subtype, are expressed at low levels in A7r5 cells.

In summary, mibefradil appears to inhibit both T- and L-type Ca^{2+} channels when used at 3µM, whereas 30µM Ni^{2+} appears to selectively inhibit T-type Ca^{2+} channels. Nifedipine has significant effects during stimulation by 20mM K^+ buffer, implying that L-type Ca^{2+} channels are also active upon weak depolarisation of the cells. The insignificant effects of Ni^{2+} during stimulation by 80mM K^+ buffer confirm preferential activation of L-type Ca^{2+} channels upon strong depolarisation of the cells.

4.2.3 Inhibition of T-type and L-type Ca^{2+} channels and the effect on A7r5 proliferation

Proliferation of A7r5 cells was inhibited by mibefradil in a concentration dependent manner, as shown in Figure 4.18 (A). At higher concentrations of mibefradil, the non-viable cell count increased, as shown by the red line graph in panel (A). 3µM mibefradil decreased mean cell number by 32%, and caused 1.6% cell death. This concentration was subsequently applied to a three day time-course proliferation assay. Panel (B) shows the mean proliferative response over time; mibefradil reduced cell number by 40% on day 3. Cell Event™ was used as an indicator of caspase-3/7 activation, which is indicative of apoptosis. Representative images are shown in Figure 4.19 of 2µM staurosporine treated cells (positive control, panels A and B), and of 3µM mibefradil treated cells (panels C and D). The mean data of the percentage of Cell Event™ positive cells from all fields of view are shown in panel (E). Mibefradil treatment induced caspase-3/7 activation in 13% of cells, yet there was no significant effect on apoptosis by mibefradil vs negative control.

A7r5 cell proliferation was not affected by concentrations of Ni^{2+} ranging from 1µM to 30µM, and cell death was less than 0.5%, as shown in Figure 4.20. There was no concentration-dependent decrease in proliferation in response to increasing

A

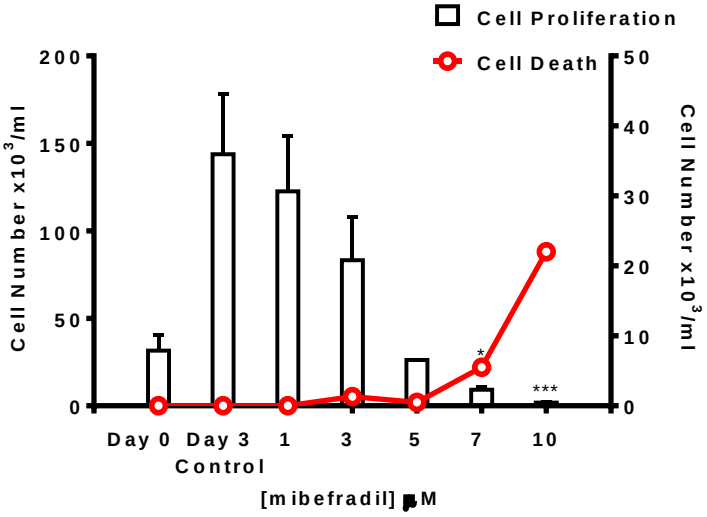

B

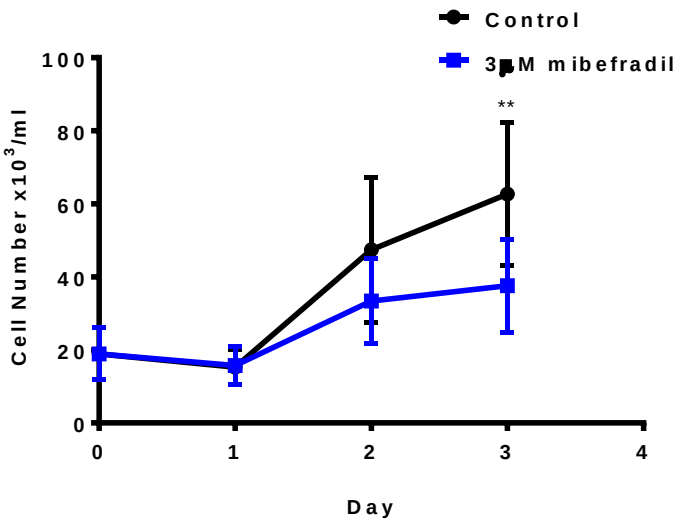

Figure 4.18 Mibefradil inhibits A7r5 cell proliferation

Bar graph showing the proliferative response of A7r5 cells to increasing concentrations of mibefradil (left y-axis) (A). The overlaid red plot shows the corresponding non-viable cell count (right y-axis). Data were analysed by a ratio repeated measures one-way ANOVA with Dunnett's multiple comparison test, * $p<0.05$, *** $p<0.001$ vs Day 3 Control, n=3. Line graph of the effects of 3µM mibefradil over a 3 day period. Data were analysed by two-way repeated measures ANOVA with sample matching by time point. This was followed by Sidak's multiple comparison test between control and treated groups for each time point, ** $p<0.01$, n=4. Data are represented as mean ± s.e.m.

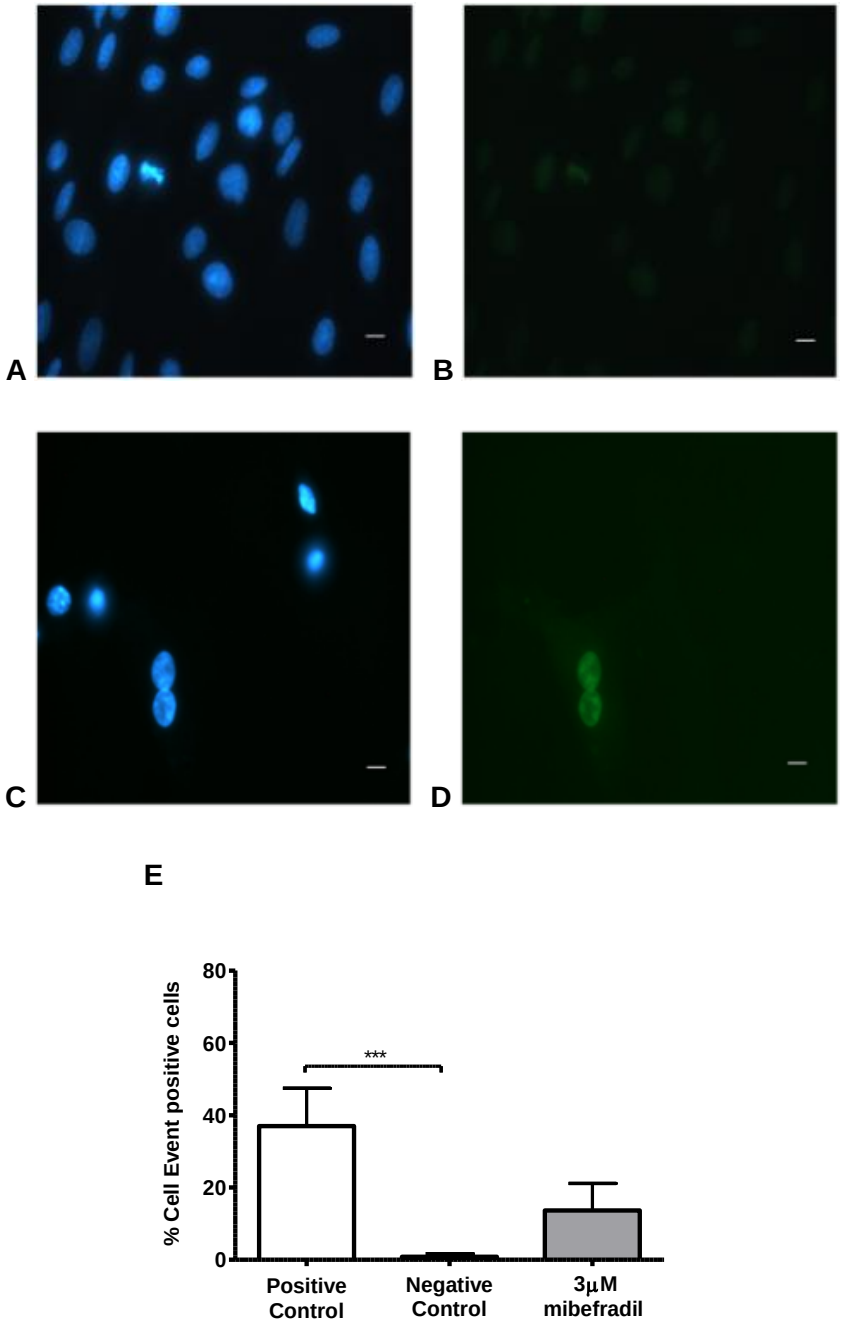

Figure 4.19 The effect of mibefradil on caspase-3/7 activation

Representative images of 2µM staurosporine treated A7r5 cells (positive control), Hoechst staining (A) and the corresponding Cell Event™ staining (B); and of 3µM mibefradil treated A7r5 cells, Hoechst staining (C) and the corresponding Cell Event™ staining (D). Scale bar=10µm. Bar graph of mean (± s.e.m.) % Cell Event positive cells for 2µM staurosporine treated A7r5 cells (positive control), untreated A7r5 cells (negative control) n=12 fields of view, and 3µM mibefradil treated cells, n=8 fields of view (E). Data were analysed by one-way ANOVA, with Bonferroni's multiple comparison test, *** $p<0.001$.

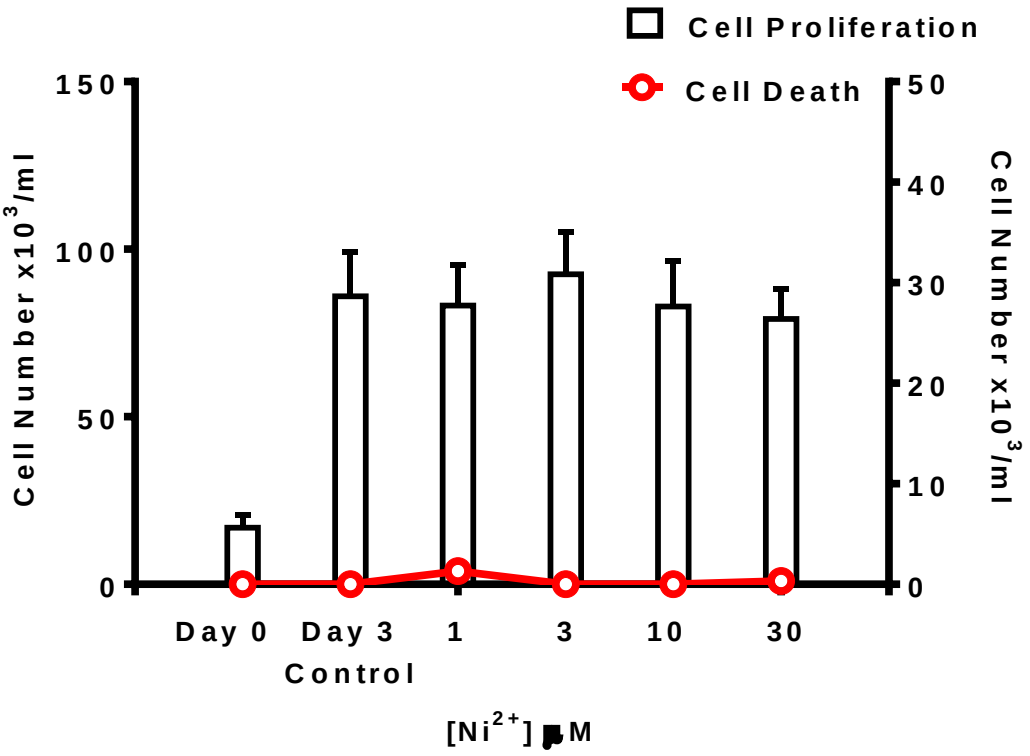

Figure 4.20 Low Ni^{2+} concentrations do not inhibit A7r5 cell proliferation

Bar graph showing the proliferative response of A7r5 cells to increasing concentrations of Ni^{2+} (left y-axis). The overlaid red plot shows the corresponding non-viable cell count (right y-axis). n=3, data are represented as mean ± s.e.m.

concentrations of nifedipine, nor did it affect cell viability, as shown in Figure 4.21. Only at a concentration of 4µM did nifedipine significantly inhibit cell proliferation, with cell death at less than 0.5%. As stated previously, the IC_{50} of T-type Ca^{2+} channels to Ni^{2+} differs for the channel subtypes, with $Ca_v3.1$ being less sensitive. $Ca_v3.1$ is expressed at higher levels than $Ca_v3.2$ in A7r5 cells, as described in section 4.2.1. As our research group has demonstrated that the IC_{50} of Ni^{2+} for the HEK293/$Ca_v3.1$ channel to be 289µM (see Figure 4.10), a higher concentration range of Ni^{2+} was applied to A7r5 cells to isolate the effects of $Ca_v3.1$ inhibition on cell proliferation. To block L-type Ca^{2+} channels, and thus prevent any off-target effects of 250µM Ni^{2+} on these channels, the assay was performed in the presence of 2µM nifedipine. Figure 4.21 has demonstrated that 2µM nifedipine had no effect on proliferation. Figure 4.22 demonstrates that 250µM Ni^{2+} significantly inhibits proliferation, with no effect on cell viability, as shown by the red line graph. Cell number was reduced by 75% by 250µM Ni^{2+}, and cell death was less than 0.5%.

In summary, the non-selective T-type Ca^{2+} channel blocker, mibefradil, significantly inhibited A7r5 cell proliferation. The L-type Ca^{2+} channel blocker, nifedipine, did not significantly inhibit A7r5 cell proliferation when used at a concentration of 2µM or less. Selective inhibition of $Ca_v3.2$ channels by low concentrations of Ni^{2+} did not limit cell proliferation, yet selective inhibition of $Ca_v3.1$ channels by high concentrations of Ni^{2+}, in the presence of 2µM nifedipine, did significantly inhibit A7r5 cell proliferation.

4.2.4 T-type Ca^{2+} channel modulation by $Ca_v3.1$ siRNA

As the $Ca_v3.1$ T-type Ca^{2+} channel is the more highly expressed sub-type in A7r5 cells, molecular techniques were employed to knock-down $Ca_v3.1$ channel expression using $Ca_v3.1$-targeting siRNA, with the aim of assessing subsequent effects on cell proliferation. Initial assessment of $Ca_v3.1$-targeting siRNA was performed at 24h and 48h time-points using a range of concentrations. HPRT1 was chosen as the endogenous control mRNA as the associated C_t values were comparable to the C_t values of the $Ca_v3.1$ mRNA in the A7r5 cell line. At the 24h time-point, 25nM and 50nM $Ca_v3.1$-targeting siRNA significantly reduced the expression of the $Ca_v3.1$ T-type Ca^{2+} channel, with 10nM, 25nM and 50nM all producing significant knock-down at 48h, as shown in Figure 4.23. A concentration of 25nM $Ca_v3.1$-targeting siRNA was then assessed over a 96h time-course, as shown in Figure 4.24. Significant knock-down of $Ca_v3.1$ mRNA expression was demonstrated at 24h and 48h, but this did not continue

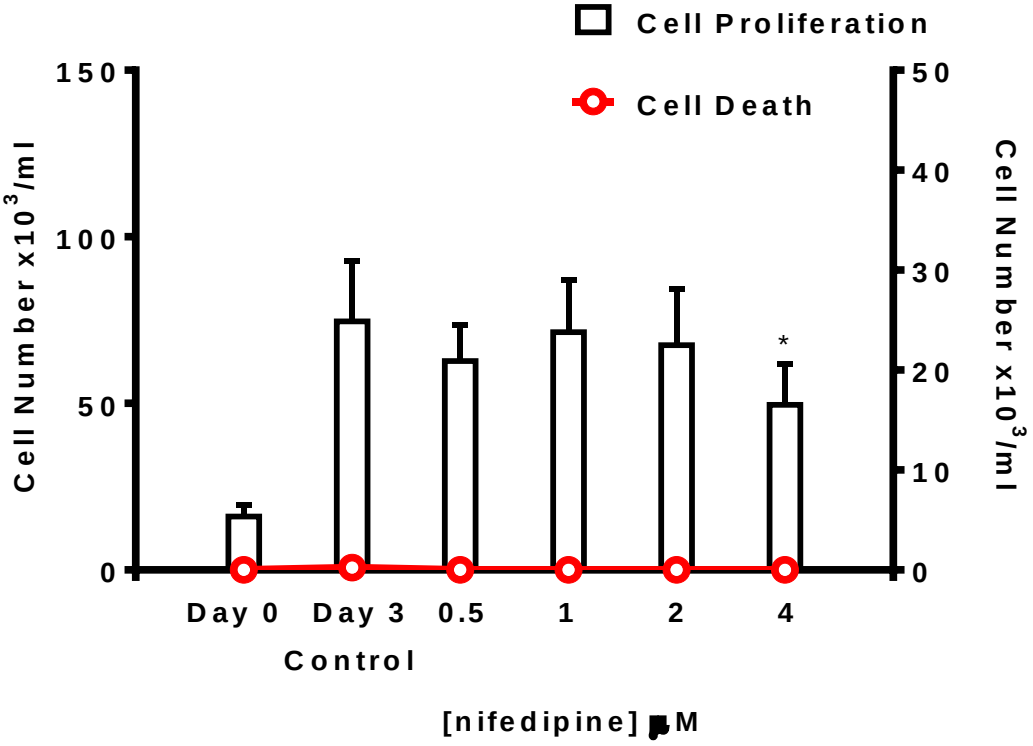

Figure 4.21 The effect of nifedipine on A7r5 cell proliferation

Bar graph showing the proliferative response of A7r5 cells to increasing concentrations of nifedipine (left y-axis). The overlaid red plot shows the corresponding non-viable cell count (right y-axis). Data were analysed by a ratio repeated measures one-way ANOVA with Dunnett's multiple comparison test, * $p<0.05$ vs Day 3 Control, n=3, data are represented as mean ± s.e.m.

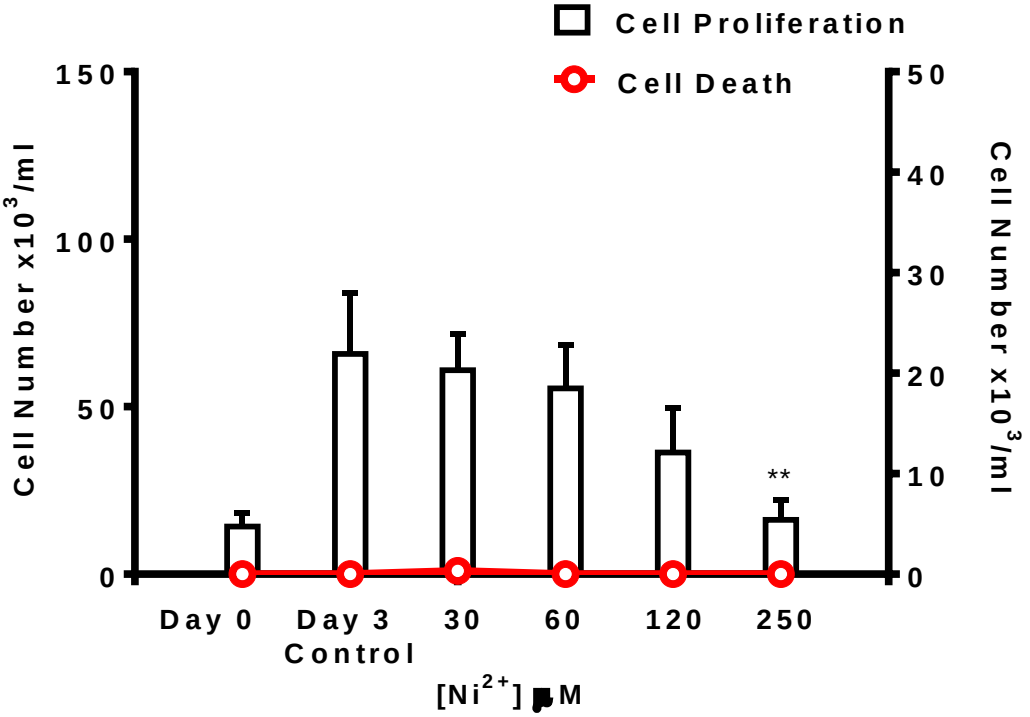

Figure 4.22 The effect of high Ni^{2+} concentrations and 2µM nifedipine on A7r5 proliferation

Bar graph showing the proliferative response of A7r5 cells to increasing concentrations of Ni^{2+}, in the presence of 2µM nifedipine (right y-axis). The overlaid red plot shows the corresponding non-viable cell count (left y-axis). Data were analysed by a ratio repeated measures one-way ANOVA with Dunnett's multiple comparison test, ** $p<0.01$ vs Day 3 Control, n=3, data are represented as mean ± s.e.m.

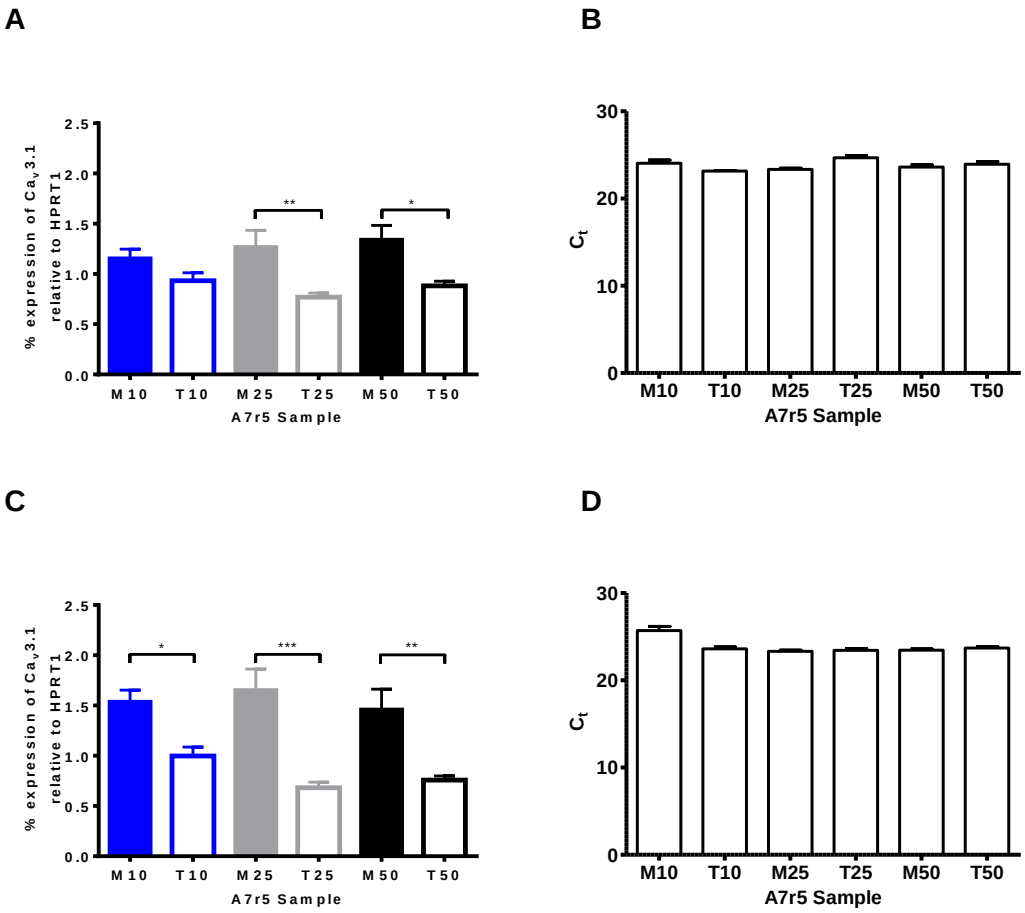

Figure 4.23 Preliminary assessment of $Ca_v3.1$-targeting siRNA at 24h and 48h

Bar graph showing the relative expression of $Ca_v3.1$ 24h post 10nM, 25nM, or 50nM $Ca_v3.1$-targeting siRNA treatment (A). Bar graph showing the corresponding HPRT1 C_t values at 24h (B). Bar graph showing the relative expression of $Ca_v3.1$ 48h post 10nM, 25nM, or 50nM $Ca_v3.1$-targeting siRNA treatment (C). Corresponding HPRT1 C_t values at 48h (D). M; Mock, T; transfected, 6-well format. Data were analysed by a ratio repeated measures one-way ANOVA with Bonferroni's multiple comparison test, * $p<0.05$, ** $p<0.01$, *** $p<0.001$, n=2, values in triplicate, data are represented as mean ± s.e.m. Cells at P3 and P4.

A

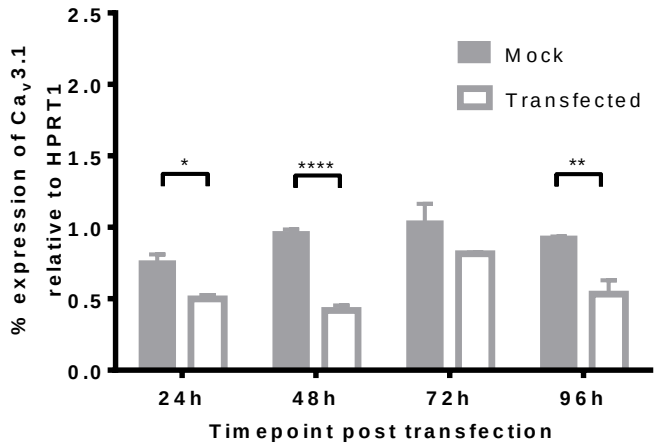

B

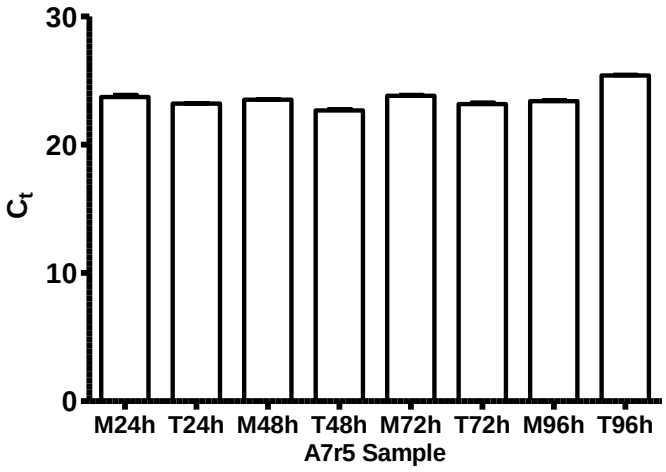

Figure 4.24 Assessment of 25nM $Ca_v3.1$-targeting siRNA over a 96h time-course

Bar graph showing the relative expression of $Ca_v3.1$ at time-points post 25nM $Ca_v3.1$-targeting siRNA treatment (A). Bar graph showing the corresponding HPRT1 C_t values (B). M; Mock, T; transfected, 6-well format. Data were analysed by a two-way ANOVA and matched within each treatment group (M or T), with Bonferroni's multiple comparison test, * $p<0.05$, ** $p<0.01$, **** $p<0.0001$, n=1, values in triplicate, data are represented as mean ± s.e.m. Cells at P5.

to 72h and 96h. Although mRNA knock-down was significant at 96h, this is likely due to the fact that the expression of the HPRT1 endogenous mRNA was increased in the transfected group at 96h. The assessment of 25nM $Ca_v3.1$-targeting siRNA over 96h was therefore repeated, as shown in Figure 4.25. Knock-down of $Ca_v3.1$ mRNA expression was demonstrated on day 0 at the start of the assay, but this was not maintained throughout the 96h time-course (panel A). The lack of effect on proliferation over this 96h time-course is shown in panel (B). As the expression of HPRT1 was variable in previous experiments, β2-microglobulin (β2M) was also employed as an endogenous control, although this mRNA was expressed at a higher level than both HPRT1 and $Ca_v3.1$ in A7r5 cells. β2M was employed to establish whether HPRT1 was affected by the transfection process itself, or whether such endogenous control mRNA was subject to fluctuation across A7r5 cell passages. However, as shown in Figures 4.25, 4.26, and 4.27, both HPRT1 and β2M fluctuate between samples in the same pattern. As 25nM $Ca_v3.1$-targeting siRNA caused no consistent effects on $Ca_v3.1$ mRNA expression, nor on proliferation, 50nM $Ca_v3.1$-targeting siRNA was assessed over a 96h time-course. There was a difference in cell proliferation at 48h using 50nM $Ca_v3.1$-targeting siRNA, as shown in Figure 4.26 (panel B). Cell number was reduced by 36% in the transfected group in comparison to the mock group. However, this was not maintained at 96h, and the proliferative response did not correlate with the mRNA knock-down shown in panel (A). It appeared that $Ca_v3.1$ mRNA knock-down was not attainable at 96h, therefore 50nM $Ca_v3.1$-targeting siRNA was employed once more over a 72h assay period, as shown in Figure 4.27. An untransfected group was also added to this experiment to establish whether the transfection process was adversely affecting the mRNA expression levels of the proteins being assessed. However, there was variability in $Ca_v3.1$ expression between the mock and untransfected groups, which suggests the transfection procedure itself adversely affected channel expression levels. Additionally, Figure 4.27 (A) demonstrates how the level of $Ca_v3.1$ expression varies over time in A7r5 cells. Both mock and untransfected groups show an increase in $Ca_v3.1$ expression between 0h and 24h, which then declines at 48h and 72h. However, this does not correlate with the proliferation data in Figure 4.27 (B), as the cell number did not increase until after 48h. Furthermore, $Ca_v3.1$ mRNA knock-down could not be accurately assessed due to fluctuations in levels of endogenous controls. Due to time constraints, the assessment of $Ca_v3.1$-targeting siRNA on A7r5 cell proliferation was not investigated further.

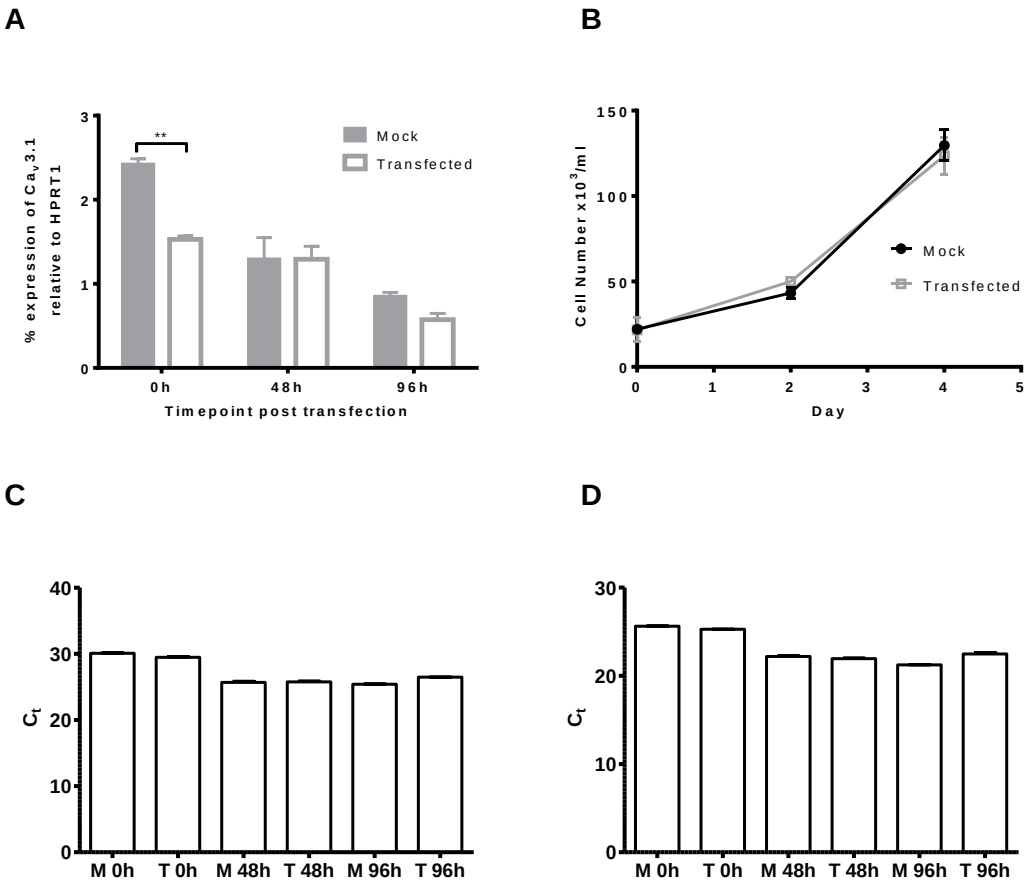

Figure 4.25 The effect of 25nM $Ca_v3.1$-targeting siRNA on A7r5 proliferation over a 96h time-course

Bar graph showing the relative expression levels of $Ca_v3.1$ at various time-points post 25nM $Ca_v3.1$-targeting siRNA treatment (A). Data were analysed by a two-way ANOVA and matched within each treatment group (M or T), with Bonferroni's multiple comparison test, ** $p<0.01$. Line graph showing the proliferative response of A7r5 cells post 25nM $Ca_v3.1$ siRNA treatment (B). Bar graphs (C and D) showing the corresponding housekeeper C_t values of HPRT1 and β2M respectively for 0h, 48h, and 96h time-points. M; Mock, T; transfected, 24-well format, n=1, values in triplicate, data are represented as mean ± s.e.m. Cells at P5.

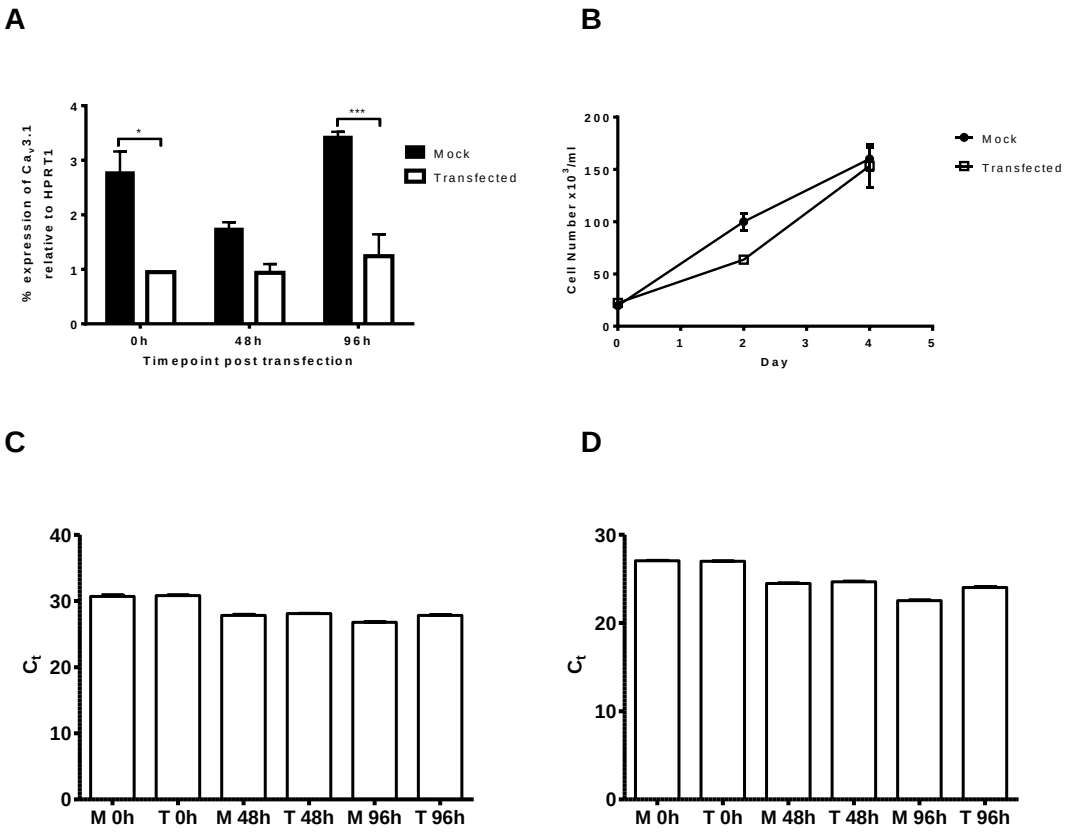

Figure 4.26 The effect of 50nM $Ca_v3.1$-targeting siRNA on A7r5 proliferation over a 96h time-course

Bar graph showing the relative expression levels of $Ca_v3.1$ at various time-points post 50nM $Ca_v3.1$-targeting siRNA treatment (A). Data were analysed by a two-way ANOVA and matched within each treatment group (M or T), with Bonferroni's multiple comparison test, * $p<0.05$, *** $p<0.001$. Line graph showing the proliferative response of A7r5 cells post 50nM $Ca_v3.1$-targeting siRNA treatment (B). Bar graphs (C and D) showing the corresponding housekeeper C_t values of HPRT1 and β2M respectively for 0h, 48h, and 96h time-points. M; Mock, T; transfected, 24-well format, n=1, values in triplicate, data are represented as mean ± s.e.m. Cells at P4.

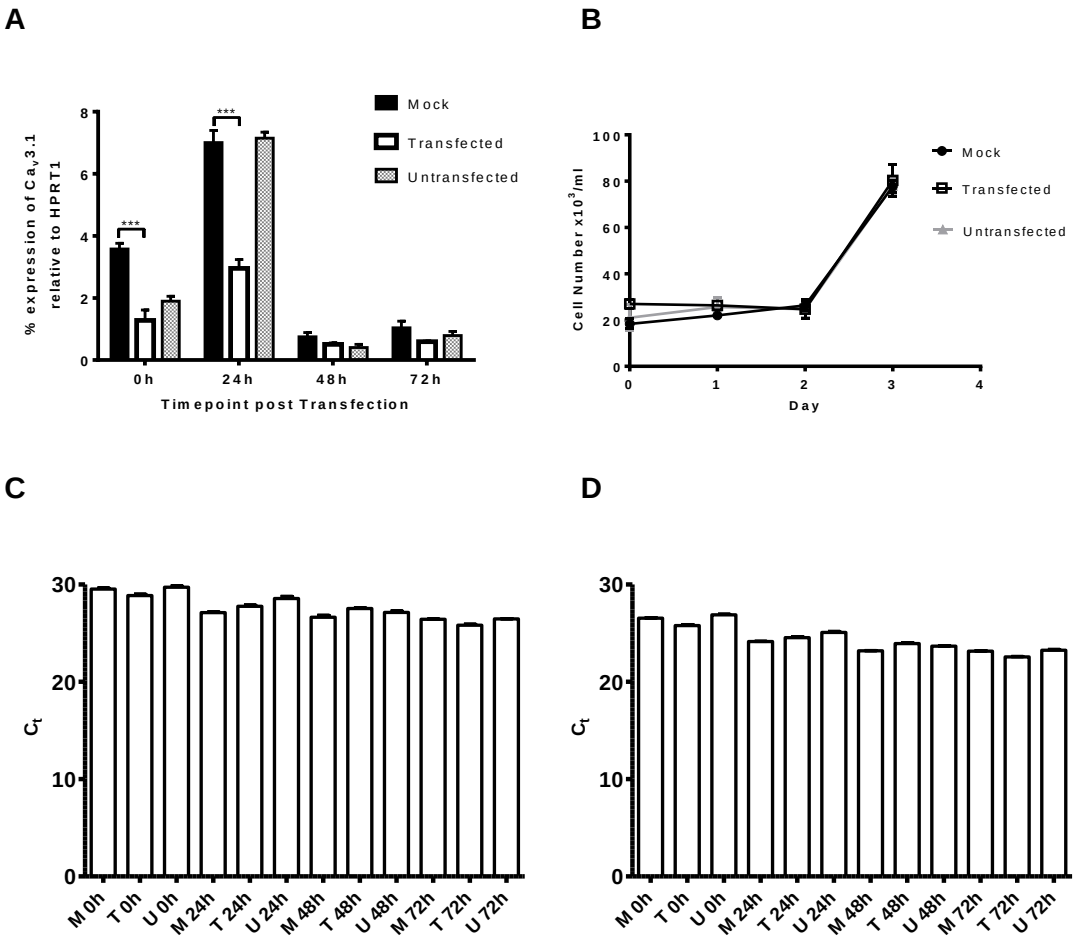

Figure 4.27 The effect of 50nM $Ca_v3.1$-targeting siRNA on A7r5 proliferation over a 72h time-course

Bar graph showing the relative expression levels of $Ca_v3.1$ at various time-points post 50nM $Ca_v3.1$ siRNA treatment (A). Data were analysed by a two-way ANOVA and matched within each treatment group (M or T), with Bonferroni's multiple comparison test, *** $p<0.001$. Line graph showing the proliferative response of A7r5 cells post 50nM $Ca_v3.1$-targeting siRNA treatment (B). Bar graphs (C and D) showing the corresponding housekeeper C_t values of HPRT1 and β2M respectively for 0h, 48h, and 72h time-points. M; Mock, T; transfected, U; untransfected, 24-well format, n=1, values in triplicate, data are represented as mean ± s.e.m. Cells at P5.

4.3 Discussion

Figure 4.1 confirms positive staining for smooth muscle cell markers in A7r5 cells. The co-stained images in panels (D-F) exhibited fainter staining, despite being captured using the same microscopy settings, the same antibody dilutions, and using the same cells. This suggested that the presence of both antibodies prevented the effective binding and visualisation of either antibody. The expression of both $Ca_v3.1$ and $Ca_v3.2$ T-type Ca^{2+} channels was demonstrated by immunocytochemistry and RT-PCR, and both methods show $Ca_v3.1$ to be the more prominently expressed T-type Ca^{2+} channel subtype in A7r5 cells, despite variable expression levels across passages. Such variation could be a result of the proliferative state of the cells and how confluent the cell monolayer was, as T-type Ca^{2+} channel expression is down-regulated by cell contact in confluent cell monolayers (Akaike *et al.*, 1989;Richard *et al.*, 1992). To try and minimise such variation, all A7r5 cell samples were retrieved when the monolayer was 80% confluent. However, differences in expression levels were still apparent, although a link to passage number was ruled out. Another group has also demonstrated that $Ca_v3.1$ is more prominent than $Ca_v3.2$ in rat arteries and A7r5 cells, in addition to a similar $Ca_v3.1$ peri-nuclear staining pattern (Brueggemann *et al.*, 2005). Membrane enrichment of A7r5 cell samples prior to western blotting produced limited success of $Ca_v3.1$ detection (Figure 4.3). These findings correlate to the fact that immunocytochemistry demonstrated minimal positive staining of the channels at the cell membrane (Figure 4.2). Therefore, even though $Ca_v3.1$ expression is more prominent, absolute expression levels are still low.

A7r5 cells respond rapidly to modest membrane depolarisation caused by 20mM K^+ buffer, with a rise of $[Ca^{2+}]_{i,}$ superimposed on which was the appearance of Ca^{2+} oscillations. The diminished response to consecutive exposures of 20mM K^+ buffer, as shown in Figure 4.5, could be due to Ca^{2+} channel inactivation. T-type Ca^{2+} channels open in bursts during prolonged depolarisation, and the channels cycle between open, inactivated, and closed states (Perez-Reyes, 2003). Indeed, $Ca_v3.1$ T-type Ca^{2+} channel gating has been shown to be modulated by Ca^{2+} ions, as free $[Ca^{2+}]_i$ promote the cycling between channel states (Lacinova *et al.*, 2006). The inactivation of L-type Ca^{2+} channels is voltage and also Ca^{2+} dependent, and these channels inactivate more slowly than T-type Ca^{2+} channels (Hille, 1992). As the length of the trace increased, the Ca^{2+} channels may have taken longer to recover, therefore preventing subsequent activation. This is more likely of T-type Ca^{2+} channels, which have longer tail currents (Hille, 1992). The phenomenon of ‘run-down’, described as the decline of Ca^{2+} current

over long recordings, is a documented problem associated with the whole-cell patch clamp technique (Belles *et al.*, 1988). Run-down was proposed to be due to a loss of cellular constituents via the patch pipette, a rise in $[Ca^{2+}]_{i,}$ and loss of high energy compounds. The idea of Ca^{2+} current run-down could be extrapolated to the diminished response of A7r5 cells seen here. Although, recording $[Ca^{2+}]_i$ by microfluorimetry does not involve a loss of cellular constituents as whole-cell patch clamp does, the co-ordination of the cellular responses could change over time. Furthermore, gap junctions have been shown to mediate the diffusion of Ca^{2+} to neighbouring human smooth muscle cells (Christ *et al.*, 1992), and in HEK293 cells transfected with connexin-43 and the ryanodine receptor (Toyofuku *et al.*, 1998). However, rises in $[Ca^{2+}]_i$ have been shown to reduce junctional conductance (Loewenstein, 1981). The contribution of gap junctions to the cell response to 20mM K^+ buffer could be investigated by the use of a gap junction modulator, such as carbenoxolone. During long microfluorimetry traces, as illustrated in Figure 4.5, the depolarising response could diminish across the cell monolayer, which could produce variable movements of Ca^{2+} between cells. Taking this notion into account, with the additional possibility that voltage-gated Ca^{2+} channels may take longer to cycle through inactivated and deactivated states, as Lacinova *et al* (2006) demonstrated that $[Ca^{2+}]_i$ facilitated $Ca_v3.1$ T-type Ca^{2+} channel inactivation, these effects would likely be reflected by a smaller change in Fura 2 ratio as the length of the trace increases.

A pharmacological approach was taken to try to isolate the individual contributions of T-type and L-type Ca^{2+} channels to the response to 20mM K^+ buffer. Taken together, the effects of all the compounds applied to A7r5 cells during 20mM K^+ buffer exposure imply that both T-type and L-type Ca^{2+} channels are involved in the response. However, the data suggest that L-type Ca^{2+} channels have a more prominent role in the mediation of Ca^{2+} oscillations. The L-type Ca^{2+} channel blocker, nifedipine, significantly inhibited $[Ca^{2+}]_i$, reducing the response to 20mM K^+ buffer by 60% relative to control, and nifedipine also abolished the Ca^{2+} oscillations. The T-type Ca^{2+} channel blocker mibefradil produced a similar effect, reducing the response to 20mM K^+ buffer by 58%, although the oscillatory response was not completely abolished. Simultaneous application of nifedipine and mibefradil completely inhibited any change in $[Ca^{2+}]_i$. Nanomolar concentrations of mibefradil have been shown to inhibit A7r5 Ca^{2+} oscillations, and this study concluded that both T-type and L-type Ca^{2+} channels are involved in the oscillatory response in A7r5 cells (Brueggemann *et al.*, 2005). However, this study also found that T-type Ca^{2+} channel over-expression did not increase Ca^{2+}

oscillation frequency, implying that T-type Ca^{2+} channels are not the major influence of such oscillations. Mibefradil has been shown to block L-type Ca^{2+} channels at higher concentrations; with an IC_{50} of 12.9µM in HEK293/Ca_v1.2 cells (Martin *et al.*, 2000), an IC_{50} of 18.6µM in L-type transfected Chinese hamster ovary cells (Mehrke *et al.*, 1994), and an IC_{50} of 3µM in rat ventricular cells (Leuranguer *et al.*, 2000). It would seem likely, therefore, that 3µM mibefradil employed in these experiments also had inhibitory effects on L-type Ca^{2+} channels. The possible inhibition of L-type Ca^{2+} channels by mibefradil is also evidenced by the response to 80mM K^+ buffer, which promotes strong membrane depolarisation and preferential activation of L-type Ca^{2+} channels. Mibefradil reduced the integrated response by 65%, nifedipine by 68%, and simultaneous application of both drugs by 92%. Contrastingly, one study has demonstrated that nifedipine can inhibit endogenous and recombinant T-type Ca^{2+} channels with an IC_{50} of 109µM for Ca_v3.1, and 5µM for Ca_v3.2 (Shcheglovitov *et al.*, 2005). Although a concentration of 2µM was used in the current experiments, and the fact that A7r5 cells express Ca_v3.1 channels more abundantly, the data concerning proliferation suggest it is highly unlikely that nifedipine had any inhibitory effects on T-type Ca^{2+} channels.

The IC_{50} of Ni^{2+} for Ca_v3.1 and Ca_v3.2 has been shown to be 250µM and 13µM respectively for recombinant channels expressed in HEK293 cells (Lee *et al.*, 1999), and 304.8µM and 4.9µM (Kang *et al.*, 2006) respectively for recombinant channels expressed in xenopus oocytes. 200µM Ni^{2+} was able to reversibly inhibit T-type Ca^{2+} currents in A7r5 cells (Brueggemann *et al.*, 2005), and we have quantified the IC_{50} to be 289µM in HEK293/Ca_v3.1 cells. Preliminary microfluorimetry experiments using 250µM Ni^{2+} demonstrated complete abolition of the response to 20mM K^+ buffer, therefore a lower concentration 30µM Ni^{2+} was utilised to assess the effects of partial T-type Ca^{2+} channel block, without producing off-target effects on L-type Ca^{2+} channels. The response to 20mM K^+ buffer in the presence 30µM Ni^{2+} was reduced by 37% without altering oscillation frequency, and the simultaneous addition of Ni^{2+} and nifedipine inhibited the change in Fura 2 ratio by 48%. This implies that the effects of 30µM Ni^{2+} are limited to T-type Ca^{2+} channels, which is verified by the lack of effect of 30µM Ni^{2+} on $[Ca^{2+}]_i$ when the cells were exposed to 80mM K^+ buffer. Indeed, Ni^{2+} was shown to inhibit L-Type Ca^{2+} channels with an ED_{50} of 65µM quoted in human smooth muscle cells (Hollywood *et al.*, 2003). Proliferation of A7r5 cells was not affected by concentrations of Ni^{2+} up to 30µM. This concentration of Ni^{2+} is selective for Ca_v3.2 over Ca_v3.1 channels, and the former are expressed at low levels in A7r5 cells, as demonstrated by Figure 4.4. The significant effects of 30µM Ni^{2+} on $[Ca^{2+}]_i$, but not on

cell proliferation, suggest that $Ca_v3.2$ channels do not notably contribute to proliferation of A7r5 cells. It is possible that chronic inhibition of $Ca_v3.2$ channels over a period of 3 days during a proliferation assay did not reduce $[Ca^{2+}]_i$ to sub-threshold levels, which would subsequently limit cell proliferation (Gray *et al.*, 2004), as discussed previously in Chapter 3. Figure 4.11 demonstrates that acute inhibition of $Ca_v3.2$ channels does significantly affect $[Ca^{2+}]_i$, yet Figure 4.20 implies that chronic inhibition of $Ca_v3.2$ channels does not lead to significant effects on proliferation. In the presence of 2µM nifedipine, concentrations of Ni^{2+} increasing from 30µM to 250µM caused a concentration-dependent decrease in proliferation. It is likely that $Ca_v3.2$ channels were inhibited by lower concentrations of Ni^{2+}, with $Ca_v3.1$ channels additionally inhibited by concentrations of 120µM Ni^{2+} and above. Significant inhibition of proliferation occurred in response to chronic exposure of 250µM Ni^{2+}, implying $Ca_v3.1$ channels are central to the proliferative capacity of A7r5 cells, and to the maintenance of adequate $[Ca^{2+}]_i$ levels to trigger cell cycle progression. Interestingly, sub-confluent A7r5 cells have been shown to have higher resting $[Ca^{2+}]_i$ and are less excitable than confluent A7r5 cells (Otun *et al.*, 1992). These data are consistent with the fact that T-type Ca^{2+} channels are expressed at higher levels in proliferating cells (Kuga *et al.*, 1996), and become less prominent on contact inhibition and in contractile cells (Akaike *et al.*, 1989;House *et al.*, 2008). The inhibitory effects on proliferation exerted by 3µM mibefradil can be attributed to T-type Ca^{2+} channel inhibition and not off-target effects, as proliferation was not affected by L-type Ca^{2+} channel inhibition. Non-viable cell counts show mibefradil to be cytotoxic at concentrations above 5µM, which is corroborated by the fact that 3µM mibefradil did not cause significant activation of caspase-3/7.

In the context of the $[Ca^{2+}]_i$ responses shown in this chapter, the data may show an under-estimate of T-type Ca^{2+} channel contribution. As coverslips of confluent A7r5 cells were utilised for microfluormetry experiments, T-type Ca^{2+} channel expression could have declined, and therefore the effects of Ni^{2+} upon moderate depolarisation demonstrated to be less significant than in sub-confluent proliferating cells. The higher resting $[Ca^{2+}]_i$ in sub-confluent A7r5 cells described by Otun *et al*. (1992) could be attributed to the window current caused by T-type Ca^{2+} channels. A negligible window current was demonstrated in A7r5 cells in the present experiments, as shown in Figure 4.6. This is consistent with the low level of T-type Ca^{2+} channel expression shown in Figures 4.3 and 4.4. The sharp increases in $[Ca^{2+}]_i$ shown on the trace in Figure 4.6 as the buffer is changed from Ca^{2+}-containing to Ca^{2+}-free may be indicative of internal

Ca^{2+} store emptying. The upsurge of $[Ca^{2+}]_i$ when the buffer is switched back to a Ca^{2+}-containing buffer is likely attributable to the availability of extracellular Ca^{2+}, and possibly in conjunction with Ca^{2+}-induced Ca^{2+}-release (CICR). Although further experiments involving a sarcoplasmic endoplasmic reticulum Ca^{2+} ATPase (SERCA) inhibitor, such as cyclopiazonic acid for example, would need to be performed to conclude reliably how the internal Ca^{2+} stores contribute to the $[Ca^{2+}]_i$ changes and the oscillatory response. Although, Otun *et al.* (1992) concluded that the oscillatory response of confluent A7r5 cells occurs as a result of extracellular Ca^{2+}, and therefore via voltage-gated Ca^{2+} channels, the possibility of a role for CICR was not assessed in this study.

The limited data produced from the experiments involving $Ca_v3.1$-targeting siRNA were not consistent or elucidative. These experiments were carried out to validate the pharmacological findings involving Ni^{2+} at a molecular level. However, the level of $Ca_v3.1$ mRNA expression fluctuated in mock samples, both within and among time-course experiments, but there was no correlation with passage number. This is illustrated in Figures 4.25 to 4.27. Indeed, T-type Ca^{2+} channels have been shown to be affected by the proliferative state of VSMCs, as a confluent cell monolayer influences the down-regulation of channel expression (Akaike *et al.*, 1989;Richard *et al.*, 1992). Panels (A and B) in Figure 4.25 illustrate this; as the time-course proceeds, the A7r5 cells became more confluent and $Ca_v3.1$ mRNA expression in the mock samples declined. The fluctuations in HPRT1 values between mock and transfected groups within experiments undoubtedly had an effect on the calculation of relative $Ca_v3.1$ expression levels. The amount of RNA within each sample was not normalised prior to the RT-PCR assay as the relative quantification of $Ca_v3.1$ expression to HPRT1 expression is designed to remove RNA loading variability. Additionally, samples were assessed in triplicate. However, β2M also fluctuated in the same pattern as HPRT1, therefore the transfection process itself could have caused variations in the mRNA expression levels of all the proteins assessed. Alternatively, the mRNA levels in the cell samples from different time-points could have contained such large variation that the relative expression is not an accurate assessment. This is supported by the fact that the untransfected group shown in Figure 4.27 (A) did not follow the pattern of mock $Ca_v3.1$ mRNA expression. Other commonly used endogenous controls such as β-actin and glyceraldehyde phosphate dehydrogenase (GAPDH) are expressed at much higher levels than $Ca_v3.1$, and GAPDH expression has also been shown to be modulated by proliferation (Suzuki *et al.*, 2000), so were therefore not utilised. The

siRNA employed in these experiments was chosen specifically as it was ON-TARGETplus® SMARTpool® siRNA marketed to reduce off-target effects, but it is possible that the correct target in A7r5 cells was not hit. If time had permitted, the next stage of experiments could have involved short hairpin RNA (shRNA) to knock-down $Ca_v3.1$ mRNA expression. The use of shRNA has proven to be more efficient than siRNA, as shRNA is incorporated directly into the endogenous miRNA pathway (Rao *et al.*, 2009). Higher concentrations of siRNA are required to produce mRNA knock-down in comparison to the required number of shRNA copies, and this can subsequently cause siRNA-mediated off-target effects (Rao *et al.*, 2009). Knock-down of mRNA via shRNA can be constitutive or inducible, although the use of an inducible system offers more control of mRNA suppression regulation (Gossen & Bujard, 1992). The use of the tetracycline inducible system produces reversible mRNA suppression which has been utilised in colorectal cancer cells for the analysis of cell cycle arrest (van de Wetering *et al.*, 2003). This suggests it would be a suitable system for the investigation of the proliferative effects of mRNA knock-down. This system has previously been employed in our laboratory group.

In summary, these data suggest that both T-type and L-type Ca^{2+} channels are activated upon modest cell depolarisation, yet L-type Ca^{2+} channels appear to have a more prominent role in the generation of Ca^{2+} oscillations. L-type Ca^{2+} channels do not have a role in the proliferative response, but the $Ca_v3.1$ T-type Ca^{2+} channel is central to A7r5 cell proliferation. As T-type Ca^{2+} channels have been demonstrated to be present and functional in A7r5 cells, the effects of CO and HO-1 were next examined.

CHAPTER 5

The effect of HO-1 and CO on proliferation and $[Ca^{2+}]_i$ in A7r5 cells

5.1 Introduction

VSMCs are responsible for the maintenance of normal blood pressure and blood flow, and have a contractile phenotype in healthy vessels (Owens, 1995). In response to vascular injury, VSMCs undergo a phenotypic switch from contractile to synthetic cells, which migrate to the site of injury and proliferate. This proliferative response is a central feature of several cardiovascular disorders, such as atherosclerosis, hypertension, and restenosis (Rzucidlo *et al.*, 2007). The environment encompassing such injury promotes HO-1 induction, which plays a role in limiting vessel damage (Durante, 2003). HO-1, via subsequent CO and bilirubin production, limits apoptosis, inflammation, oxidation, platelet aggregation, and proliferation. Indeed, the protective role of CO within the vasculature has been well defined, (Morita *et al.*, 1997;Togane *et al.*, 2000;Song *et al.*, 2002;Otterbein *et al.*, 2003b;Raman *et al.*, 2006;Zuckerbraun *et al.*, 2006;Ramlawi *et al.*, 2007). CO has numerous intracellular targets, including heme-containing proteins such as NOS, catalase, peroxidase, cytochrome c oxidase, cytochrome P450, sGC, in addition to NADPH oxidase and BK_{Ca} channels (Motterlini & Otterbein, 2010). What remains to be fully elucidated are the cellular targets by which this gasotransmitter exerts specific anti-proliferative effects.

Redox signalling appears to be important for many effects associated with CO, including anti-proliferative effects. CO was shown to limit the proliferation of human airway smooth muscle cells by the inhibition of NADPH oxidase in addition to the production of mitochondrial ROS (Taille *et al.*, 2005). This anti-proliferative mechanism involved a reduction of ERK1/2 phosphorylation and a subsequent increase in cyclin D1 expression. The involvement of ERK1/2 and the MAPK pathway, in addition to sGC and the cGMP pathway, have both been detailed as signalling pathways involved in the anti-proliferative effects of CO (Song *et al.*, 2002;Stanford *et al.*, 2003). Redox regulation also appears to have a role in the phenotypic switch of VSMCs; dehydroepiandrosterone is able to inhibit the phenotypic switch by enhancing the levels of glutaredoxin and glutathione (Urata *et al.*, 2010), which are involved in the defence against oxidative stress (Fernandes & Holmgren, 2004). Our research group has demonstrated that CO can inhibit the L-type Ca^{2+} channel, with an IC_{50} of 14.8μM in

HEK/Ca_v1.2 cells, and given these channels provide an important route for Ca^{2+} entry in VSMCs, this has important implications during situations of vascular stress, when CO production is enhanced via HO-1 induction (Scragg *et al.*, 2008). CO was shown to increase mitochondrial ROS, which caused redox modulation of cysteine residues within the L-type Ca^{2+} channel. Inhibition of the T-type Ca^{2+} channel by CO has been recently demonstrated via electrophysiological methods by our research group, and it is possible that redox modulation may also underlie this mechanism. CO and HO-1 induction, in addition to the use of a reducing agent, were therefore examined in A7r5 cells, and the effects on $[Ca^{2+}]_i$ and proliferation assessed.

5.2 Results

5.2.1 The effect of CO on $[Ca^{2+}]_i$ and cell proliferation

The effect of CO on $[Ca^{2+}]_i$ was assessed by application of CORM-3. After an initial exposure to 20mM K^+ buffer, 10µM CORM-3 was applied prior to, and throughout the second exposure, which subsequently inhibited $[Ca^{2+}]_i$ and reduced the Ca^{2+} oscillation frequency, as shown in Figure 5.1 panels (A), (D), and (G). There was no difference in the mean change in Fura 2 ratio or in mean oscillation frequency upon addition of 10µM iCORM-3, as shown in Figure 5.1 panels (B), (E), and (H). To assess whether the redox state of the cellular environment affected the response to CORM-3, A7r5 cells were pre-treated with a reducing agent, dithiothreitol (DTT), before applying CORM-3. Pre-treatment with 2µM DTT prior to 10µM CORM-3 application did not significantly reduce the Ca^{2+} oscillation frequency, as shown in Figure 5.1 (I), yet there appears to be a trend towards a lower oscillation frequency on the representative trace in panel (C). DTT pre-treatment did not completely prevent a decrease in $[Ca^{2+}]_i$, as shown in Figure 5.1 panels (C) and (F). When compared to the effect of CORM-3 alone via one-way ANOVA, DTT pre-treatment caused no significant difference in $[Ca^{2+}]_i$ or oscillation frequency, as shown in Figure 5.2. The response of A7r5 cells to 80mM K^+ buffer in the presence of 10µM CORM-3 was comparable to the control cell response, as shown in Figure 5.3. CORM-3 had no inhibitory effect on the mean integrated response when the cells were strongly depolarised; $[Ca^{2+}]_i$ was not affected. CORM-3 was assessed in a proliferation assay; A7r5 cell number was reduced by 5%, 8%, and 16% in response to 3µM, 10µM, and 30µM CORM-3 respectively, yet proliferation was not significantly inhibited, as shown in Figure 5.4. Cell death was limited to 1% or less.

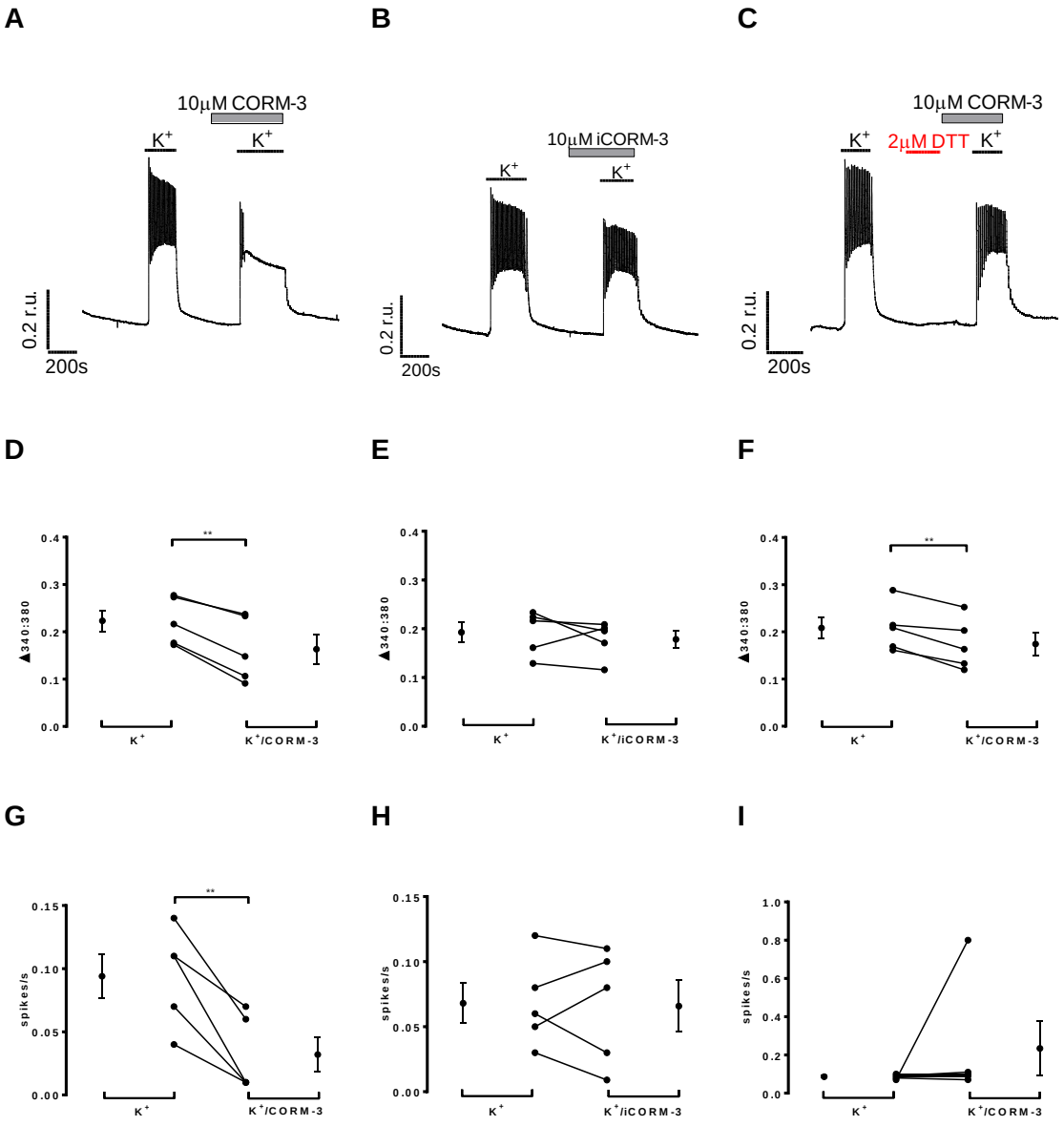

Figure 5.1 The effect of 10μM CORM-3, iCORM-3 and 2μM DTT on $[Ca^{2+}]_i$ and Ca^{2+} oscillations

Representative traces showing the response of A7r5 cells to 20mM K^+ buffer in the presence of 10μM CORM-3, 10μM iCORM-3, and 10μM CORM-3 post 2μM DTT pre-treatment (panels A-C). Trend graphs showing the change in Fura 2 ratio between K^+ exposures, in the presence of 10μM CORM-3, 10μM iCORM-3, and 10μM CORM-3 post 2μM DTT pre-treatment (panels D-F). Trend graphs showing the change in spikes/s between K^+ exposures, in the presence of 10μM CORM-3, 10μM iCORM-3, and 10μM CORM-3 post 2μM DTT pre-treatment (panels G-I). The mean (± s.e.m.) response is shown to the right and left of the corresponding individual data points on each graph. Data were analysed by a two-tailed, paired t-test, ** $p<0.01$, $n=5$.

A

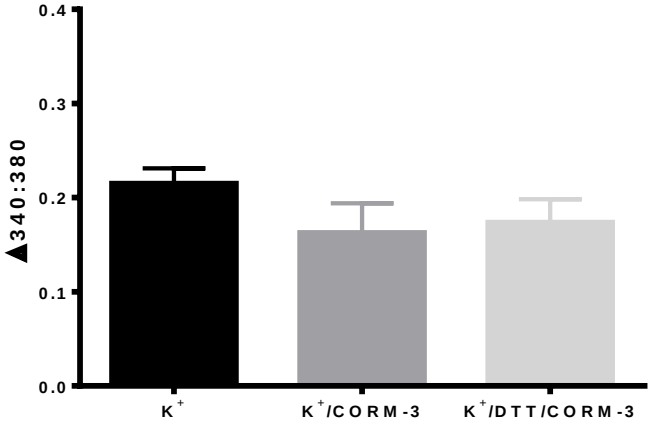

B

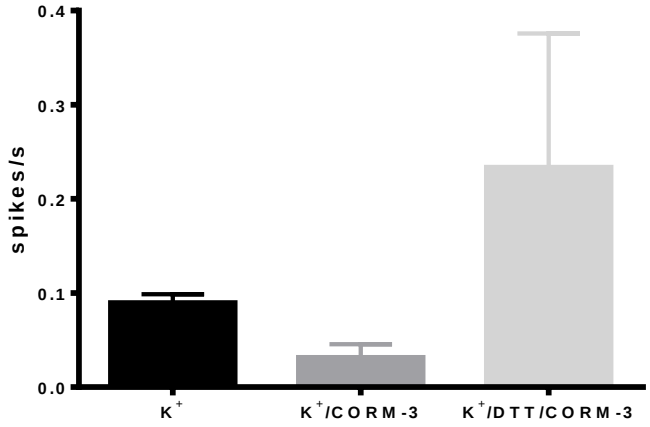

Figure 5.2 DTT does not significantly prevent the effects of CORM-3

Bar graph showing the mean (± s.e.m.) change in Fura 2 ratio (A) and the change in spikes/s (B) in response to 20mM K^+ buffer in the presence of 10µM CORM-3, plus or minus pre-treatment with 2µM DTT. n=5

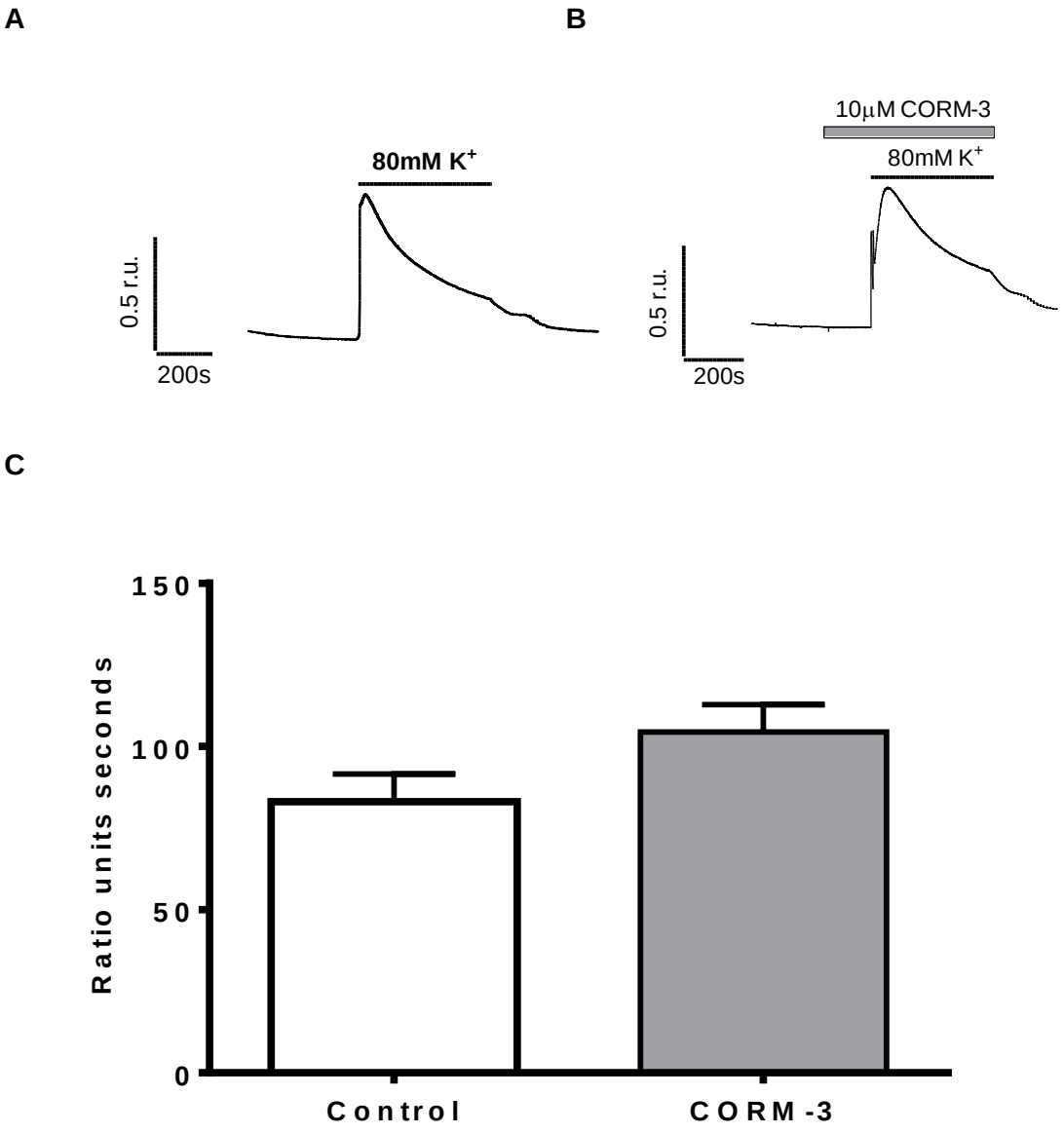

Figure 5.3 The change in $[Ca^{2+}]_i$ in response to 80mM K^+ buffer containing 10μM CORM-3

Representative trace showing the change of $[Ca^{2+}]_i$ in response to 80mM K^+ buffer (A) and in response to 80mM K^+ buffer containing 10μM CORM-3 (B). Bar graph showing the mean (± s.e.m.) integrated response to 80mM K^+ buffer, plus or minus the addition of 10μM CORM-3 (C). n=6.

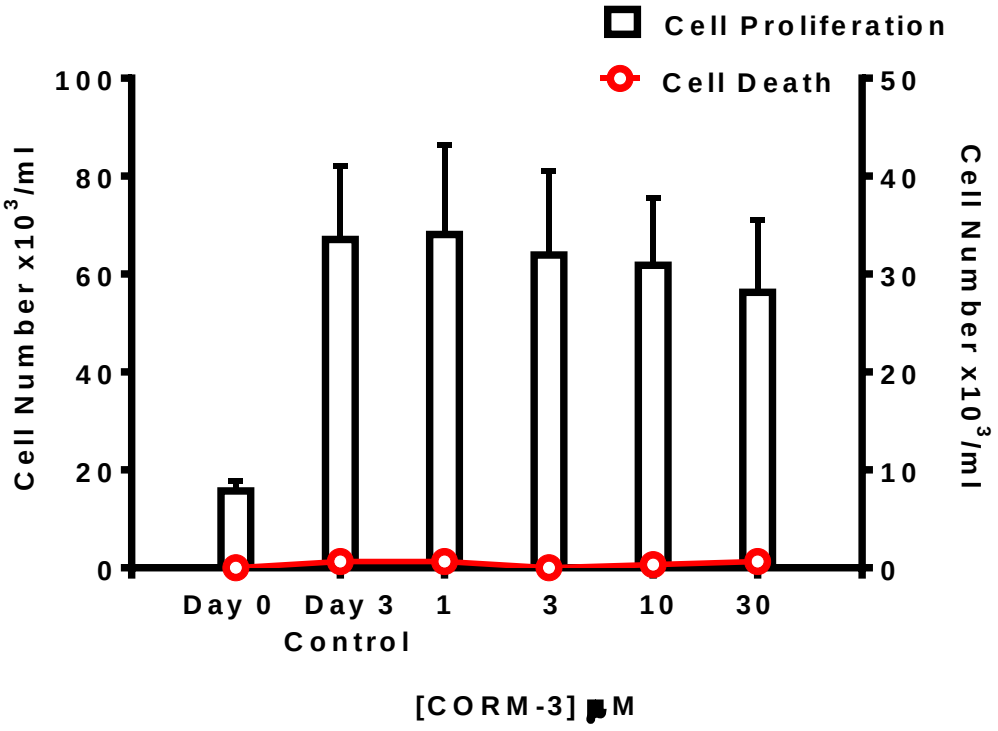

Figure 5.4 CORM-3 has no effect on A7r5 proliferation

Bar graph showing the proliferative response of A7r5 cells to increasing concentrations of CORM-3 (left y-axis). The overlaid red plot shows the corresponding non-viable cell count (right y-axis). Data are represented as ± s.e.m., n=6.

Co-application of 3µM mibefradil with concentrations of CORM-3 ranging from 1µM to 30µM significantly inhibited cell proliferation without affecting cell viability, as shown in Figure 5.5. Cell death was limited to 1.6% or less. The application of 3µM mibefradil in isolation caused a 43% reduction of proliferation, as shown in the inset of Figure 5.5, whereas the co-application of 3µM mibefradil with 1µM, 3µM, 10µM and 30µM CORM-3 caused a 26%, 34%, 35%, and a 36% reduction of proliferation respectively. These data imply competition for the same cellular target, namely the T-type Ca^{2+} channel. Although, no direct comparison can be made between the inset and the main graph in Figure 5.5, as the assays were performed at different times. The lack of effect of 10µM CORM-3 on cell viability demonstrated by the red line graph in Figure 5.4 was verified by the lack of caspase-3/7 activation shown in Figure 5.6.

The simultaneous application of 2µM nifedipine and 10µM CORM-3 was examined to see how the response compared to the effects of nifedipine and Ni^{2+} co-application, and assess whether both the T-type and L-type components of the response to 20mM K^+ buffer could be inhibited. Together, nifedipine and CORM-3 completely abolished the oscillatory response and significantly reduced $[Ca^{2+}]_i$ by 48%, as shown in Figure 5.7 (A). The co-application of nifedipine and Ni^{2+} also significantly reduced $[Ca^{2+}]_i$ by 48%, as shown in Figure 4.17 in chapter 4. Simultaneous application of 2µM nifedipine and 10µM CORM-3 significantly prevented the response to 20mM K^+ buffer, as shown in Figure 5.7 (D) and (E). There was no siginificant difference between the response to CORM-3 and nifedipine vs the response to CORM-3 or nifedipine alone. Cell proliferation was inhibited by co-application of a range of CORM-3 concentrations with 2µM nifedipine, as shown in Figure 5.8. 1µM, 3µM, 10µM, and 30µM CORM-3 caused a 41%, 62%, 68%, and a 62% reduction of cell number respectively. Cell death was limited to 6% or less.

In summary, CORM-3 significanlty limited a rise in $[Ca^{2+}]_i$ in response to moderate depolarisation, and also significantly inhibited Ca^{2+} oscillations. This effect was not significantly prevented by redox modulation. CORM-3 had no effect on $[Ca^{2+}]_i$ when the cells were strongly depolarised, nor did CORM-3 have a significant effect on cell proliferation. The simultaneous application of CORM-3 and nifedipine caused no additive effect on $[Ca^{2+}]_i$ levels, yet this combination significantly inhibited cell proliferation.

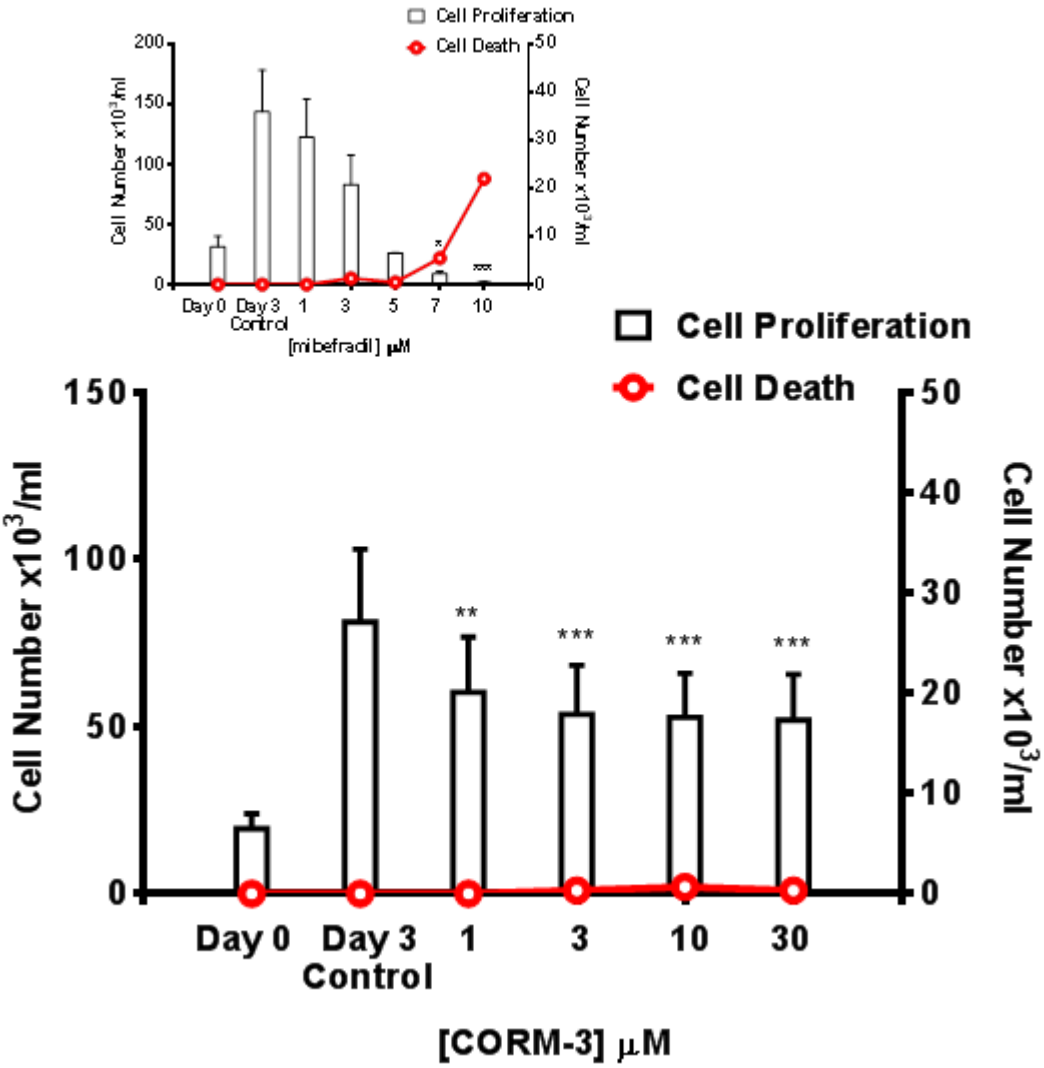

Figure 5.5 Co-application of CORM-3 and mibefradil inhibits A7r5 proliferation

Bar graph showing the proliferative response of A7r5 cells to increasing concentrations of CORM-3, in the presence of 3µM mibefradil (left y-axis). The overlaid red plot shows the corresponding non-viable cell count (right y-axis). Data were analysed by a ratio repeated measures one-way ANOVA with Dunnett's multiple comparison test, ** $p<0.01$, *** $p<0.001$ vs Day 3 Control. Data are represented as ± s.e.m., n=6. Inset is a replication of Figure 4.18 showing the effects of mibefradil on A7r5 cell proliferation.

A

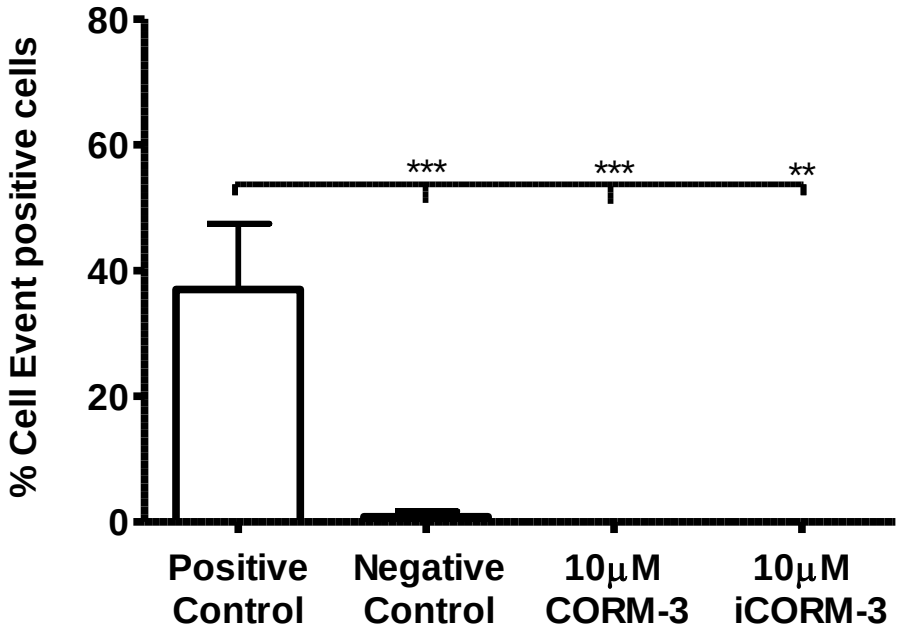

Figure 5.6 CORM-3 and iCORM-3 do not induce caspase-3/7 activation

Bar graph showing that neither 10μM CORM-3, nor 10μM iCORM-3, induced activation of caspase-3/7, n=11 and n=7 fields of view respectively. 2μM staurosporine treatment represented the positive control, A7r5 cells acted as the negative control, n=12 fields of view. Data are represented as mean ± s.e.m. Data were analysed by one-way ANOVA, with Bonferroni's multiple comparison test, ** $p<0.01$, *** $p<0.001$ vs positive control.

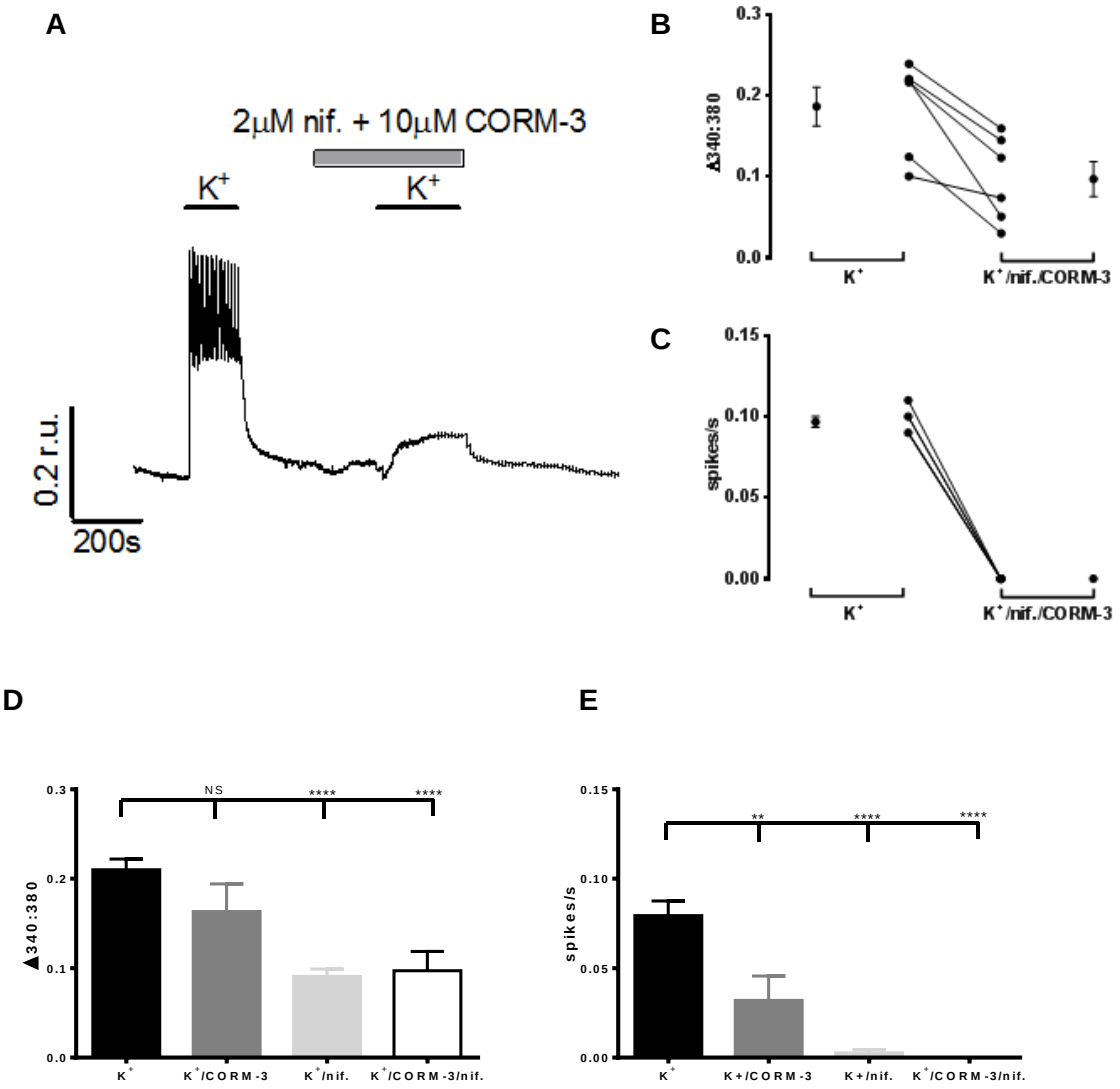

Figure 5.7 Simultaneous addition of 10μM CORM-3 and 2μM nifedipine inhibits $[Ca^{2+}]_i$ and Ca^{2+} oscillations

Representative trace showing the response of A7r5 cells to 20mM K^+ buffer in the presence of 10μM CORM-3 and 2μM nifedipine (A). Trend graph showing the decrease in Fura 2 ratio (B) and the decrease in the change in spikes/s (C) in response to 20mM K^+ buffer followed by 20mM K^+ buffer in the presence of 10μM CORM-3 and 2μM nifedipine. The mean (± s.e.m.) response is shown to the right and left of the corresponding individual data points on each graph. Bar graph showing the mean (± s.e.m.) change in Fura 2 ratio (D) and the change in spikes/s (E) in response to 20mM K^+ buffer in the presence of the drug as indicated. Data were analysed by one-way ANOVA, followed by Tukey's multiple comparison test, ** $p<0.01$, **** $p<0.0001$ vs K^+, n=6. nif. = nifedipine.

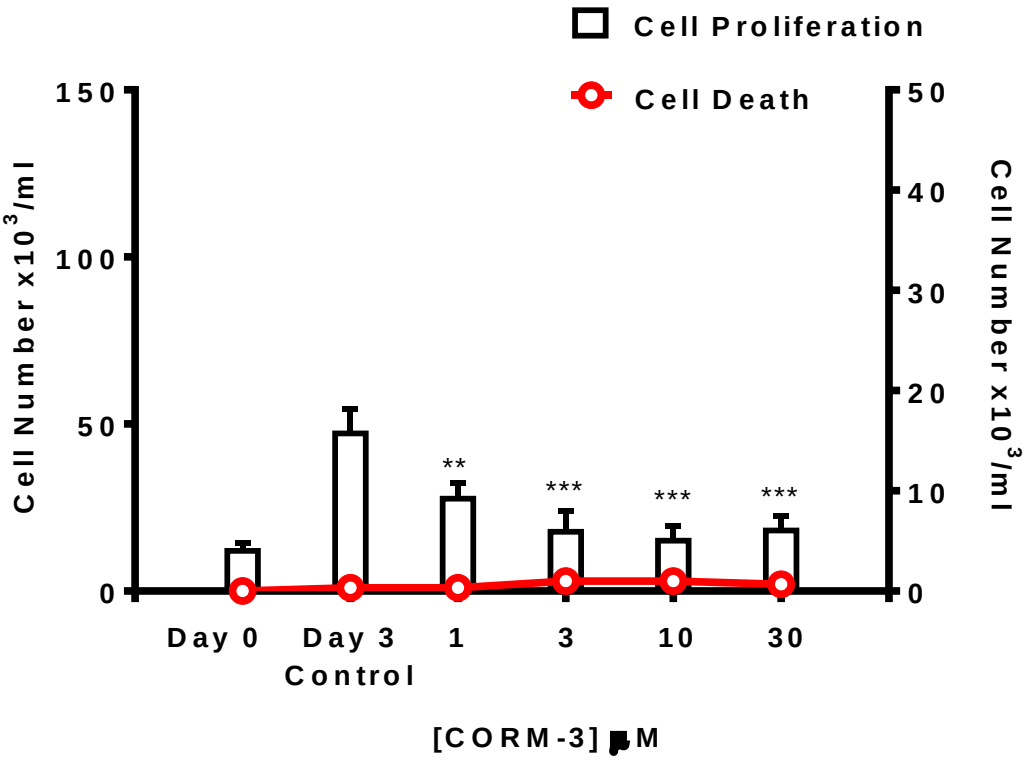

Figure 5.8 CORM-3 inhibits A7r5 proliferation in combination with nifedipine

Bar graph showing the proliferative response of A7r5 cells to increasing concentrations of CORM-3, in the presence of 2µM nifedipine (left y-axis). The overlaid red plot shows the corresponding non-viable cell count (right y-axis). Data were analysed by ratio repeated measures one-way ANOVA with Dunnett's multiple comparison test, ** $p<0.01$, *** $p<0.001$ vs Day 3 Control. Data are represented as mean ± s.e.m., n=3.

5.2.2 The effect of HO-1 modulation on $[Ca^{2+}]_i$ and cell proliferation

HO-1 induction by 10μM CoPPIX and 10μM hemin over a 24h period was verified by immunocytochemistry and is shown in Figure 5.9. The effects of HO-1 induction in response to modest depolarisation are shown in Figure 5.10. The level of $[Ca^{2+}]_i$ was visibly lower in cells with HO-1 induction as shown by the example traces in panels (A) and (B); the mean change in Fura 2 ratio was reduced by 30% with respect to the control group, as shown in panel (C). The oscillation frequency was also visibly reduced, as shown in Figure 5.10 (D). It appears that there was a trend towards lower $[Ca^{2+}]_i$ and Ca^{2+} oscillation frequency in response to CoPPIX pre-treatment, yet the data did not reach statistical significance. Figure 5.11 (A) shows the effect of nifedipine in comparison to the effects of nifedipine post HO-1 induction in Figure 5.11 (B). As stated in Chapter 4, nifedipine significantly reduced $[Ca^{2+}]_i$ by 60% in comparison to control data. The addition of 2μM nifedipine after a 48h incubation with 10μM CoPPIX also completely abolished the Ca^{2+} oscillations, and significantly reduced $[Ca^{2+}]_i$ by 70% in comparison to control data. The representative trace in Figure 5.11 (B) shows the diminished response to 20mM K^+ buffer, as indicated by the lower baseline of the Ca^{2+} oscillations. Furthermore, the amplitude of the oscillations appears to be increased, although this was not quantitatively assessed. Incubation of the cells with 10μM CoPPIX, individually or followed by application of 2μM nifedipine, prevented a significant increase of $[Ca^{2+}]_i$, in response to 20mM K^+ buffer, as shown in Figure 5.11 (C). Incubation of the cells with 10μM CoPPIX followed by application of 2μM nifedipine, completely abolished Ca^{2+} oscillations, as shown in Figure 5.11 (D).

HO-1 induction by a range of CoPPIX concentrations was verified by western blotting and is shown in Figure 5.12. At the 48h time-point, HO-1 protein expression was induced to a level of 57.72 ± 20.55% of β-actin in response to 10μM CoPPIX, and to a level of 55.92 ± 11.60% of β-actin in response to 30μM CoPPIX. CoPPIX was added to the cells as a single application on Day 0, and subsequent induction of the HO-1 protein is shown in Figure 5.13. However, without re-application of CoPPIX, HO-1 expression appears to begin to decline over the 3 day period, although not to a level of statistical significance. A7r5 cell proliferation was inhibited in a concentration dependent manner, as shown in Figure 5.14 (A), with no effect on cell viability as shown by the red line graph. Mean cell number was reduced by 30% and 41% for 10μM and 30μM CoPPIX respectively, and cell death was limited to 1.6% or less. Cell

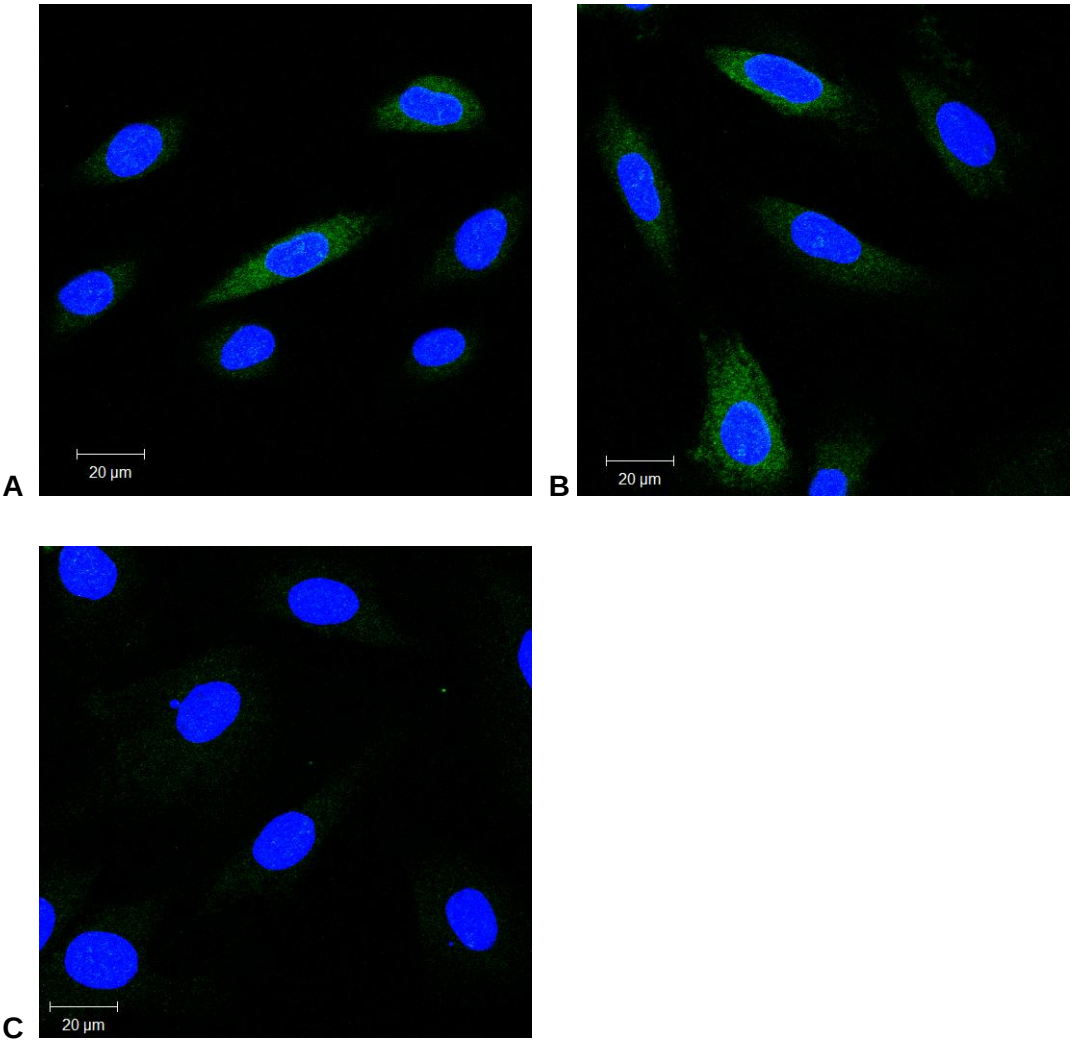

Figure 5.9 HO-1 induction by CoPPIX and hemin

Immunocytochemistry of HO-1 induction (green) in A7r5 cells. Panel (A) illustrates HO-1 expression after a 24h incubation with 10µM CoPPIX. Panel (B) illustrates HO-1 expression after a 24h incubation with 10µM hemin. Panel (C) shows a control image without HO-1 induction. Cell nuclei were stained blue with DAPI. Cells were utilised at P6, and are representative images of 12 fields of view from n=6 experimental repeats.

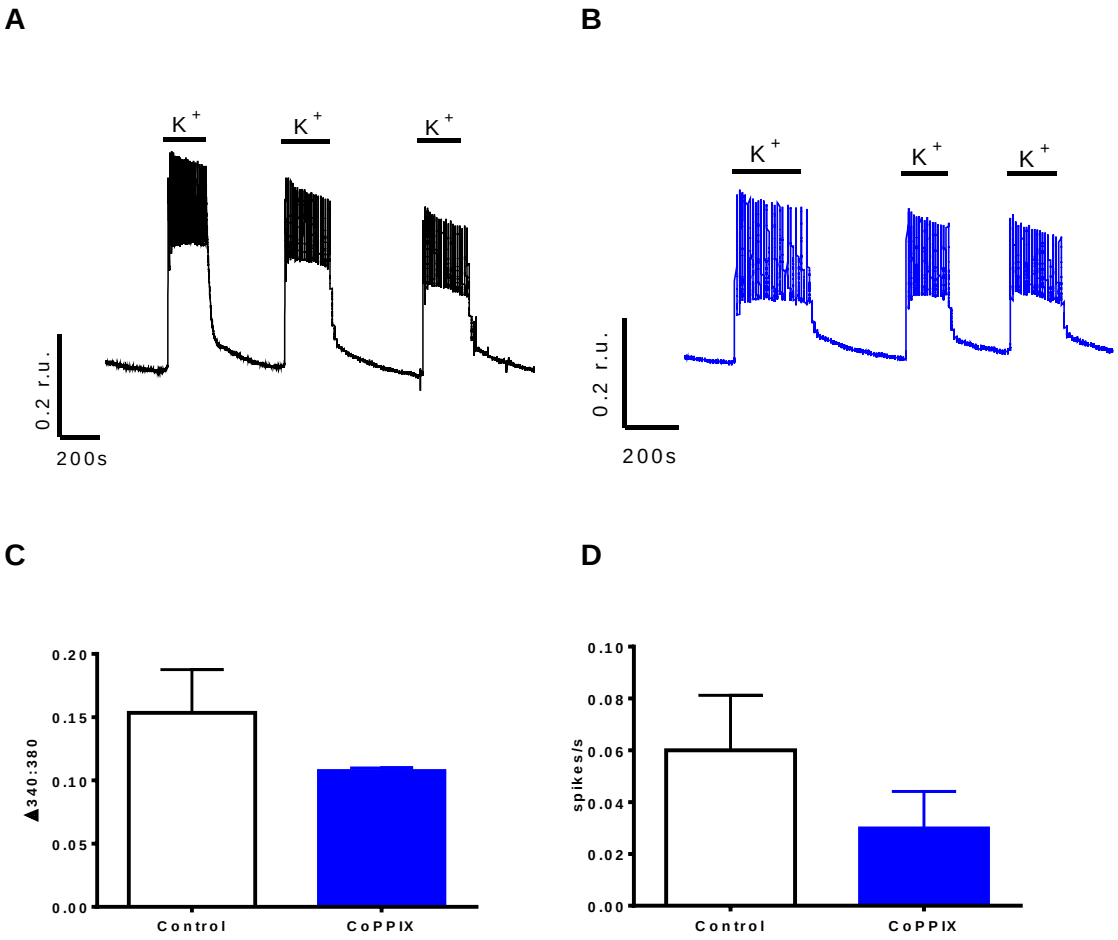

Figure 5.10 The effect of 10µM CoPPIX on $[Ca^{2+}]_i$ and Ca^{2+} oscillations

Representative control trace showing the response of A7r5 cells to 20mM K^+ buffer (A), and the response of A7r5 cells to 20mM K^+ buffer after a 48h incubation with 10µM CoPPIX (B). Bar graph showing the mean (± s.e.m.) change in Fura 2 ratio in response to 20mM K^+ buffer, plus or minus pre-treatment with 10µM CoPPIX (C). Bar graph showing the mean (± s.e.m.) spikes/s in response to 20mM K^+ buffer, plus or minus pre-treatment with 10µM CoPPIX (D). n=4.

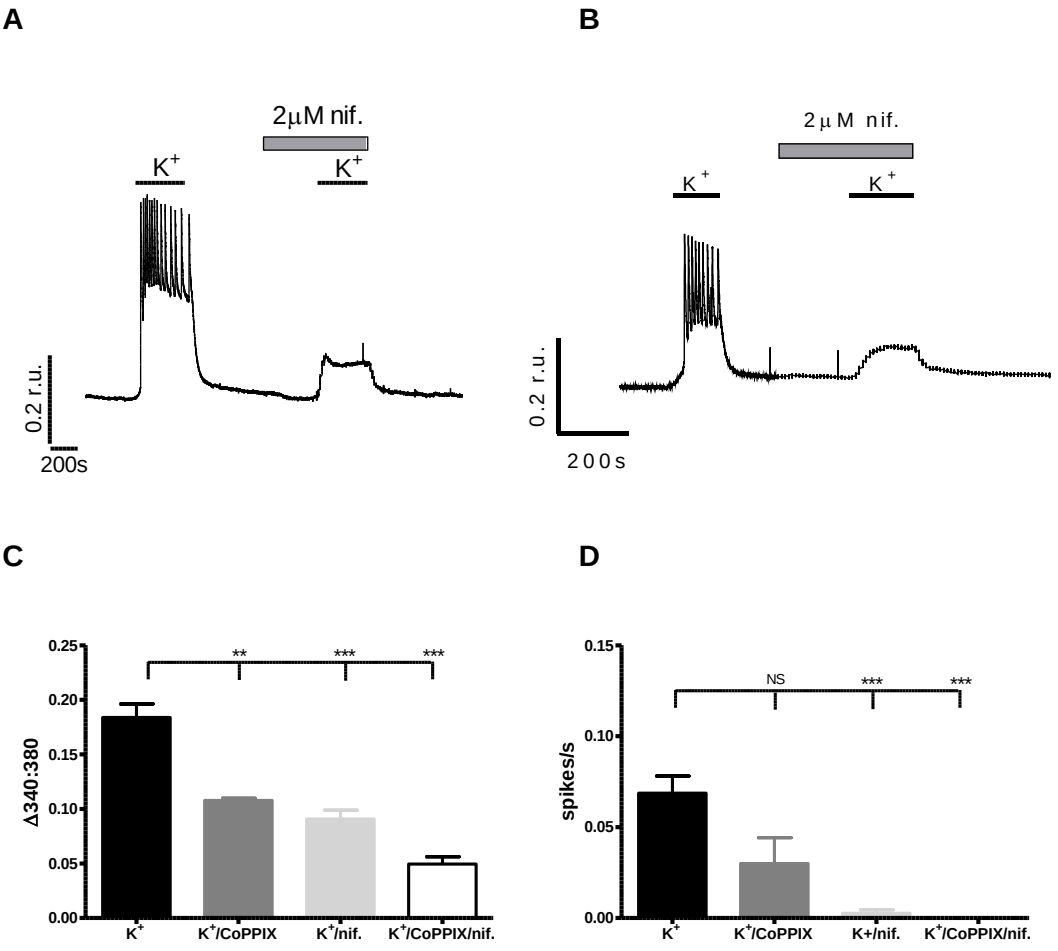

Figure 5.11 A7r5 $[Ca^{2+}]_i$ and Ca^{2+} oscillations are inhibited by simultaneous CoPPIX and nifedipine treatment

Representative trace showing the response of A7r5 cells to 20mM K^+ buffer in the presence of 2μM nifedipine (A). Representative trace showing the response of A7r5 cells, after a 48h incubation with 10μM CoPPIX, to 20mM K^+ buffer in the presence of 2μM nifedipine (B). Bar graph showing the change in Fura 2 ratio (C) and the change in spikes/s (D) in response to 20mM K^+ buffer in the presence of the drug as indicated. Data are represented as mean (± s.e.m.) and were analysed by one-way ANOVA, followed by Tukey's multiple comparison test, ** $p<0.01$, *** $p<0.001$ vs K^+, n=6. nif. = nifedipine.

A

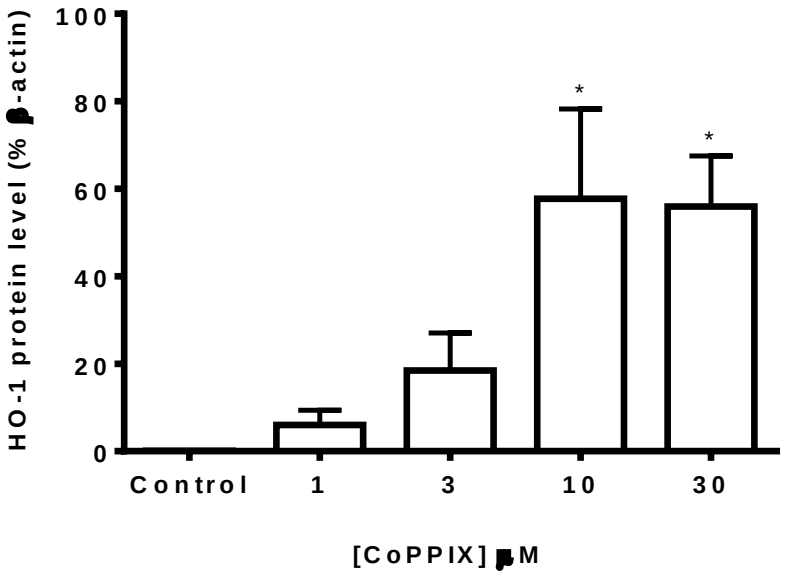

B

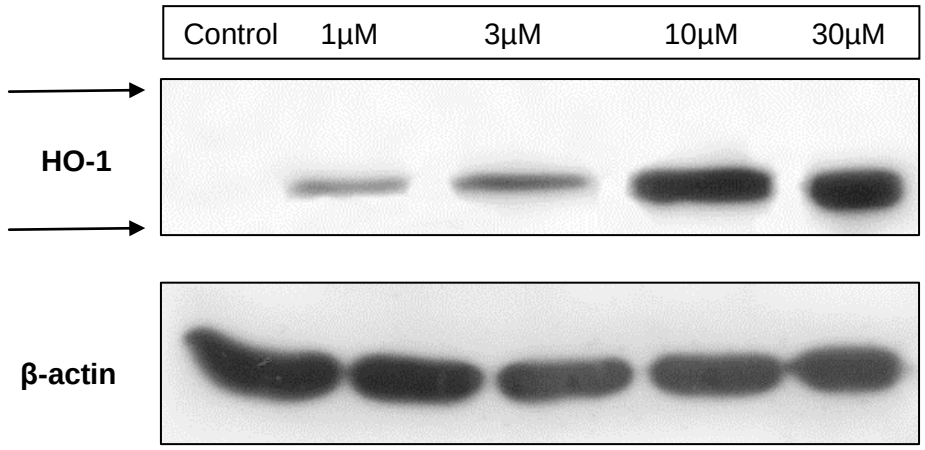

Figure 5.12 CoPPIX induces HO-1 protein expression in A7r5 cells

Bar graph showing relative HO-1 protein expression in A7r5 cells in response to a 48h incubation with a range of CoPPIX concentrations, densitometric analyses were normalised relative to β-actin (A). Data are represented as mean ± s.e.m. and were analysed by one-way ANOVA with Dunnett's multiple comparison test, * $p<0.05$ vs Control levels, n=3. Representative western blot of HO-1 and the corresponding β-actin loading control (B). The arrows represent the position of the molecular weight markers (top, 37KDa; bottom, 25kDa).

A

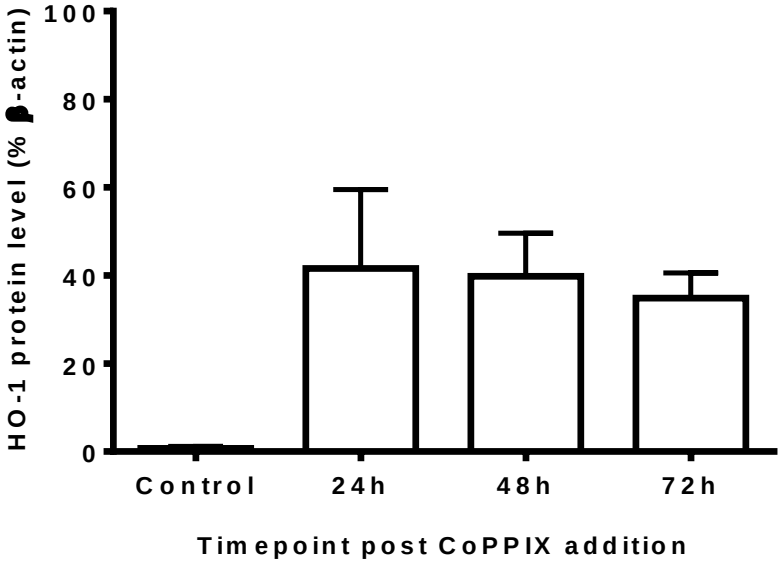

B

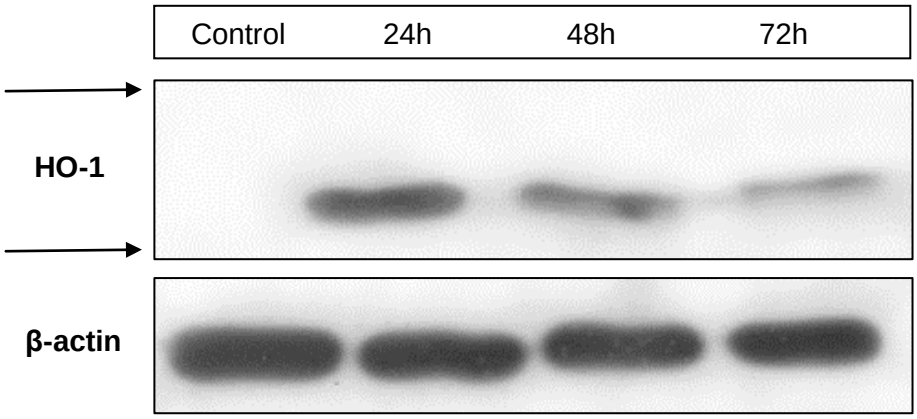

Figure 5.13 HO-1 induction by CoPPIX over a 3 day period

Bar graph showing relative HO-1 protein expression in A7r5 cells following incubation with 10μM CoPPIX for 24h, 48h, and 72h, densitometric analyses were normalised relative to β-actin (A). Data are represented as mean ± s.e.m., n=3. Representative western blot of HO-1 and the corresponding β-actin loading control (B). The arrows represent the position of the molecular weight markers (top, 37KDa; bottom, 25kDa).

A

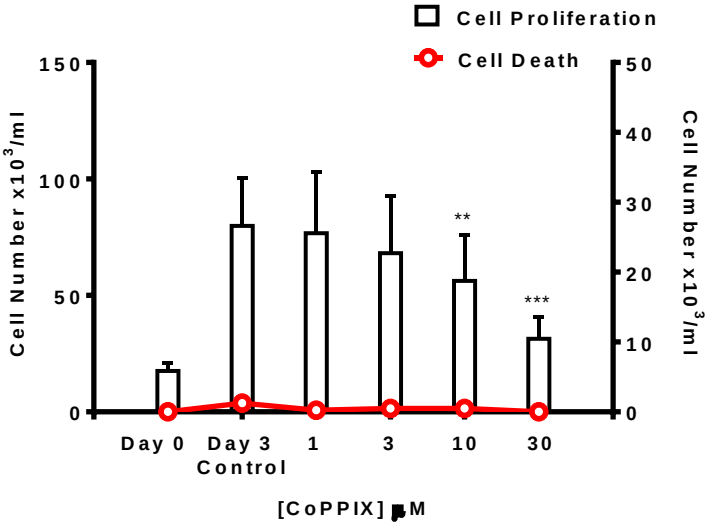

B

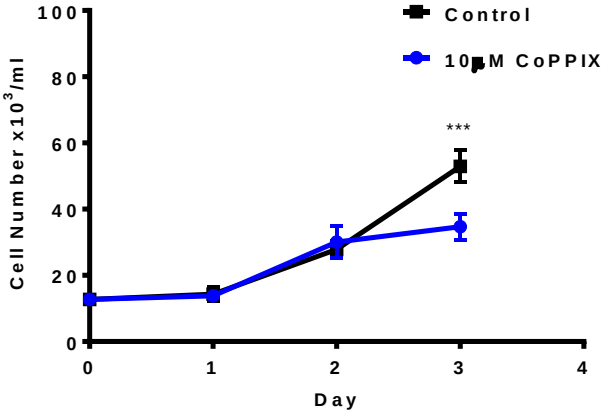

Figure 5.14 HO-1 induction by CoPPIX inhibits A7r5 cell proliferation in a concentration-dependent manner

Panel (A) shows a bar graph of the proliferative response of A7r5 cells to increasing concentrations of CoPPIX (left y-axis). The overlaid red plot shows the corresponding non-viable cell count (right y-axis). Data were analysed by ratio repeated measures ANOVA with Dunnett's multiple comparison test, ** $p<0.01$, *** $p<0.001$ vs Day 3 Control, n=5. Line graph showing the effects of 10µM CoPPIX over a three day period; cell counts were taken daily to produce a 3 day time-course (B). Data were analysed by a two-way repeated measures ANOVA, with sample matching by time point. This was followed by Sidak's multiple comparison test between control and treated groups for each time point, *** $p<0.001$, n=4. Data are represented as mean ± s.e.m.

number in response to 10µM CoPPIX was monitored daily for a period of 3 days to produce a 3 day time-course of proliferation. The line graph in Figure 5.14 (B) demonstrates that 10µM CoPPIX significantly reduced cell number by day 3. The minimal effect of 10µM CoPPIX on cell viability demonstrated by media counts in Figure 5.14 (A) was verified by the lack of caspase-3/7 activation shown in Figure 5.15.

HO-1 induction by 10µM hemin over a 24h period was verified by immunocytochemistry and is shown in Figure 5.9 (B). HO-1 induction by a range of hemin concentrations was verified by western blotting and is shown in Figure 5.16. At the 48h time-point, HO-1 was induced to a level of 51.99 ± 1.73% of β-actin for 10µM hemin. After the addition of hemin on Day 0, the HO-1 protein was induced, but expression decreased over a 3 day period, as shown in Figure 5.17. Mean A7r5 cell number was reduced by 18% and 50% in response to 10µM and 30µM hemin respectively, as shown in Figure 5.18 (A). Cell death was 1% or less. Over a 3 day time-course, hemin inhibited the proliferative response of A7r5 cells, although not to a level of statistical significance, as shown in Figure 5.18 (B).

A7r5 cells stably over-expressing human HO-1 (A7r5/hHO-1 cells) demonstrated a decline in HO-1 expression as they were passaged weekly over a three week period, which is demonstrated in Figure 5.19. The response of A7r5 cells and A7r5/hHO-1 cells to moderate depolarisation by 20mM K^+ buffer is shown in Figure 5.20. A7r5/hHO-1 cells demonstrated a smaller change in Fura 2 ratio than A7r5 cells, as shown by the bar graph in Figure 5.20 (C), yet the data did not reach statistical significance. There was a wide variation in the oscillatory response of A7r5/hHO-1 cells, as shown by Figure 5.20 (D). Figure 5.21 shows the proliferative response of A7r5 cells and A7r5/hHO-1 cells in the presence or absence of 10µM CoPPIX over a 3 day time-course. The application of 10µM CoPPIX to A7r5 cells reduced the mean cell number by 38%. The addition of CoPPIX to the A7r5/hHO-1 cell group had an additional effect on the proliferative response, reducing mean cell number by a further 11% on day 3. The proliferative response between A7r5 cells and A7r5/hHO-1 cells was significantly different on day 2 and day 3, as shown in Figure 5.21 (B).

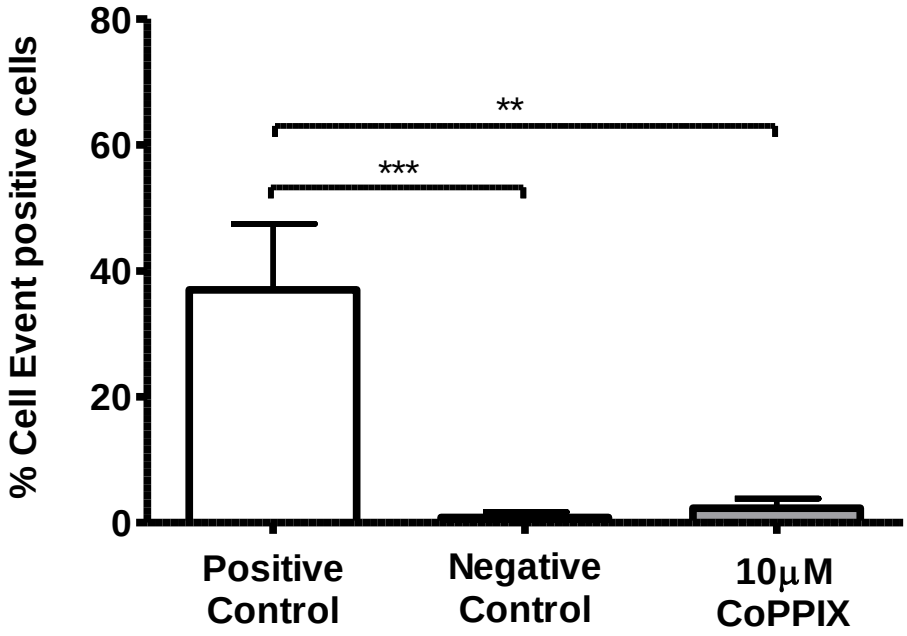

Figure 5.15 CoPPIX does not induce caspase-3/7 activation

Bar graph showing that 10μM CoPPIX does not induce apoptosis by caspase-3/7 activation. 2μM staurosporine treatment represented the positive control, untreated A7r5 cells acted as the negative control, n=12 fields of view for each group. CoPPIX treated, n=6 fields of view. Data were analysed by a one-way ANOVA, with Bonferroni's multiple comparison test, ** $p<0.01$, *** $p<0.001$. Data are represented as ± s.e.m.

A

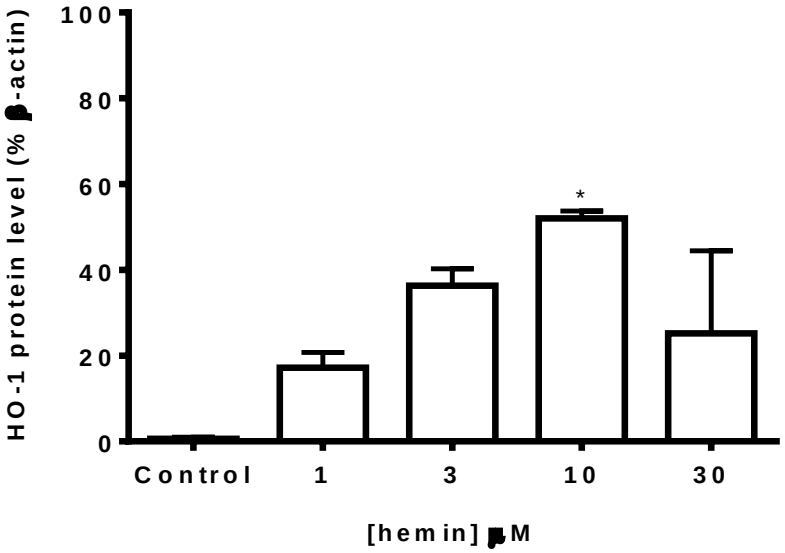

B

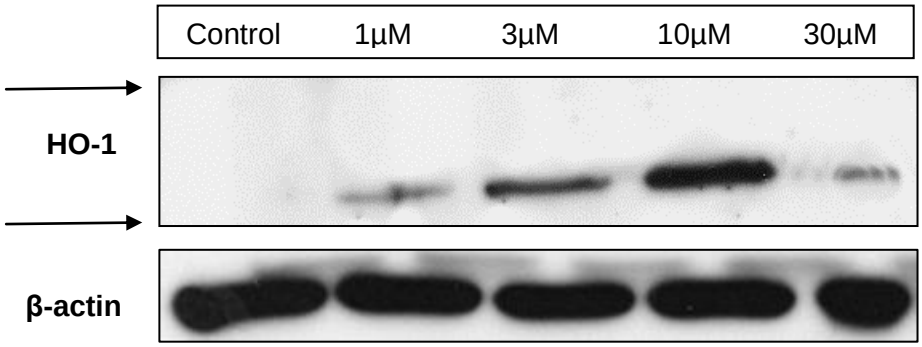

Figure 5.16 Hemin induces HO-1 protein expression in A7r5 cells

Bar graph showing relative HO-1 protein expression in A7r5 cells in response to a 48h incubation with a range of hemin concentrations, densitometric analyses were normalised relative to β-actin (A). Data are represented as mean ± s.e.m., and data were analysed by one-way ANOVA with Dunnett's multiple comparison test, * $p<0.05$ vs Control levels, n=3. Representative western blot of HO-1 and the corresponding β-actin loading control (B). The arrows represent the position of the molecular weight markers (top, 37KDa; bottom, 25kDa).

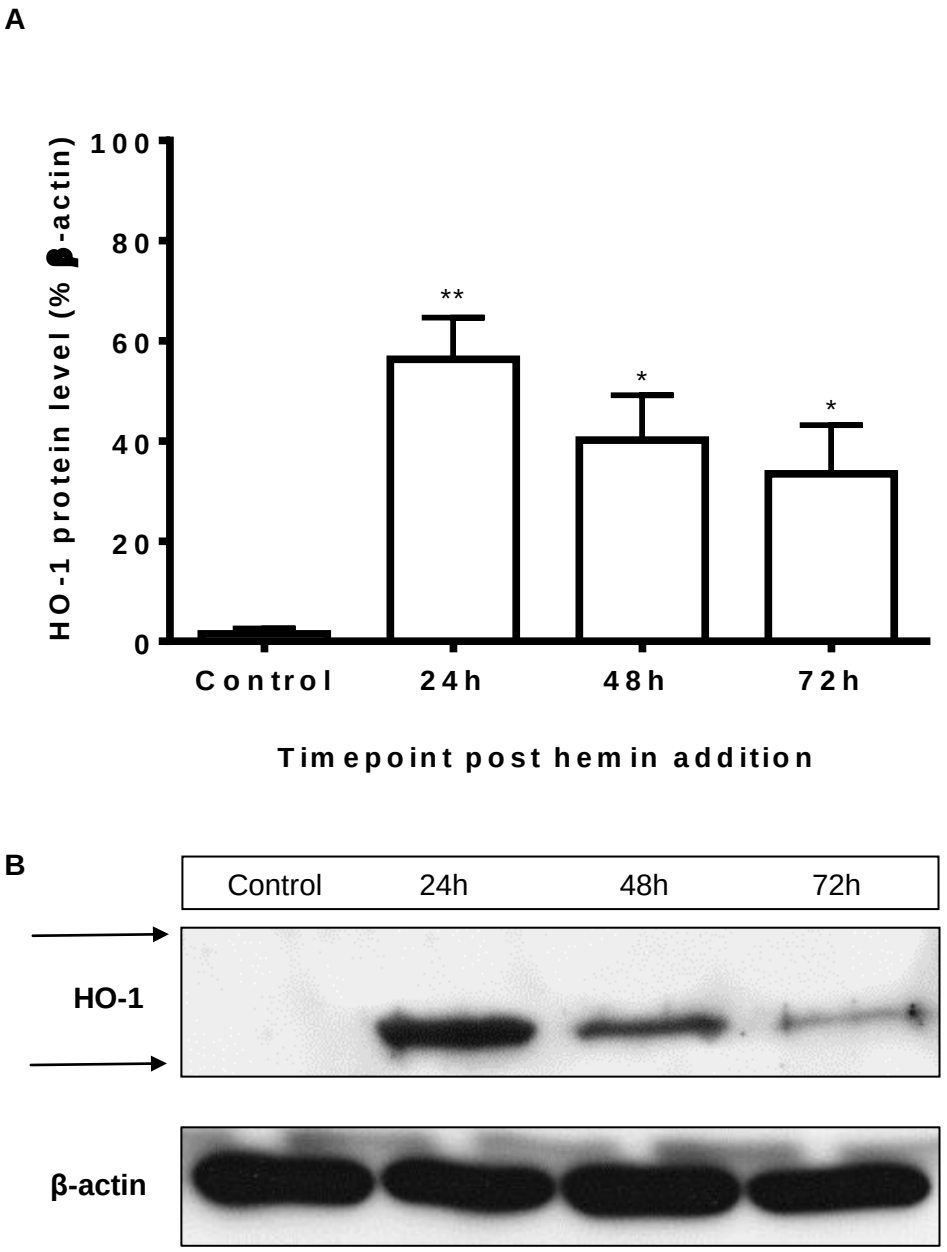

Figure 5.17 HO-1 induction by hemin declines over a 3 day period

Bar graph showing relative HO-1 protein expression in A7r5 cells following incubation with 10µM hemin for 24h, 48h, and 72h, densitometric analyses were normalised relative to β-actin (A). Data are represented as mean ± s.e.m., and data were analysed by one-way ANOVA with Dunnett's multiple comparison test, * $p<0.05$, ** $p<0.01$ vs Control levels, n=3. Representative western blot of HO-1 and the corresponding β-actin loading control (B). The arrows represent the position of the molecular weight markers (top, 37KDa; bottom, 25kDa).

A

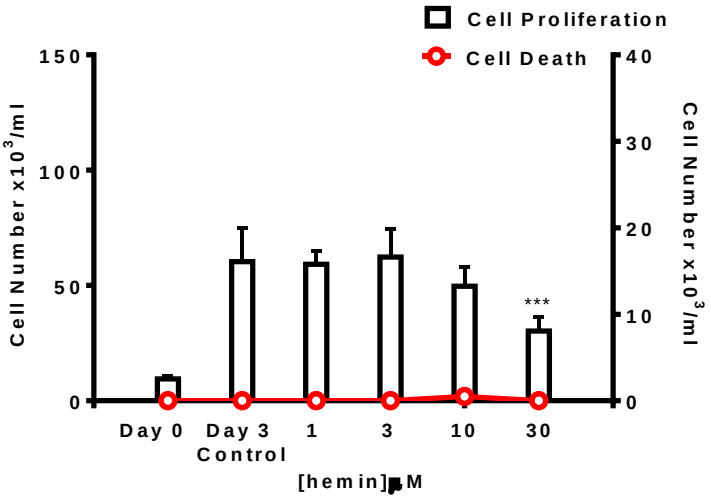

B

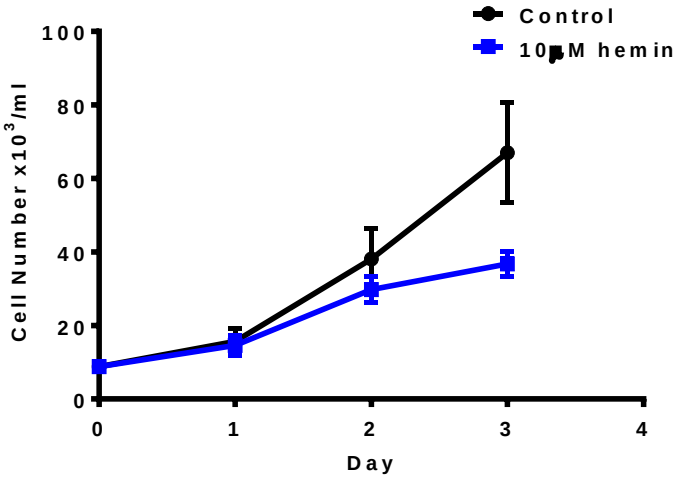

Figure 5.18 The effect of hemin on A7r5 cell proliferation

Panel (A) shows a bar graph of the proliferative response of A7r5 cells to increasing concentrations of hemin (left y-axis). The overlaid red plot shows the corresponding non-viable cell count (right y-axis). Data were analysed by ratio repeated measures one-way ANOVA with Dunnett's multiple comparison test, *** $p<0.001$ vs Day 3 Control, n=3. Line graph showing the effects of 10µM hemin; cell counts were taken daily to produce a three day time-course (B), n=3. Data are represented at mean ± s.e.m.

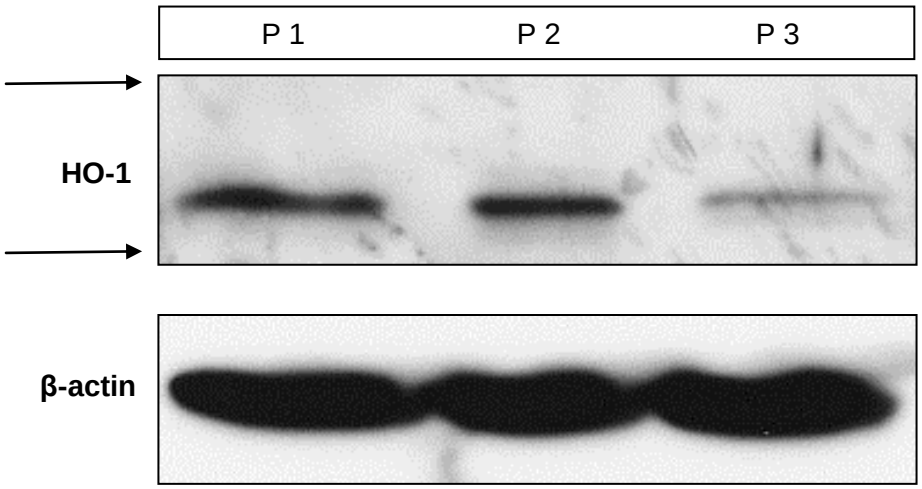

Figure 5.19 HO-1 expression by A7r5/hHO-1 cells

Illustrative western blot showing the decline in HO-1 protein expression by A7r5/hHO-1 cells over 3 passages. Underneath is the corresponding β-actin loading control. The arrows represent the position of the molecular weight markers (top, 37KDa; bottom, 25kDa). n=1

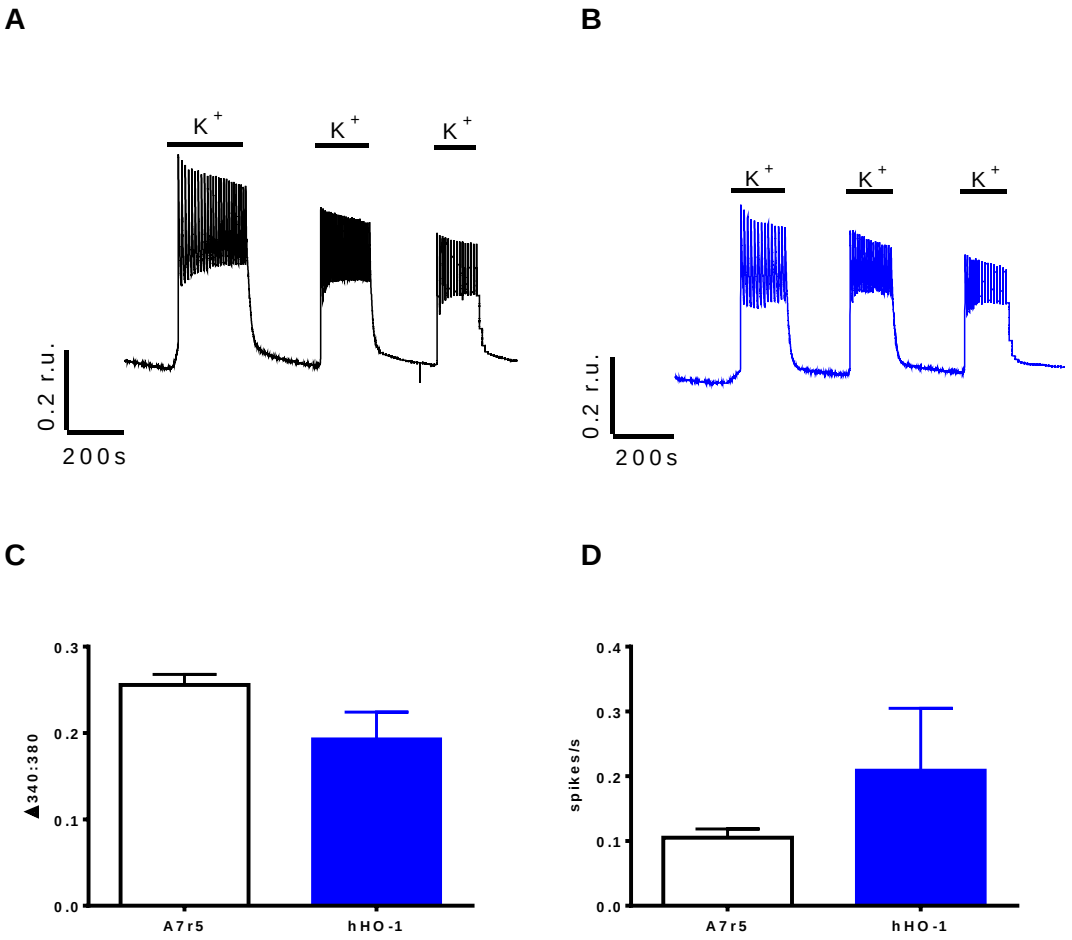

Figure 5.20 $[Ca^{2+}]_i$ and Ca^{2+} oscillations in A7r5 vs A7r5/hHO-1 cells

Representative control trace showing the response of A7r5 cells to 20mM K^+ buffer (A). Representative trace showing the response of A7r5/hHO-1 cells to 20mM K^+ buffer (B). Bar graph showing the mean change in Fura 2 ratio in response to 20mM K^+ buffer, for A7r5 cells and A7r5/hHO-1 cells. (C). Bar graph showing the mean spikes/s in response to 20mM K^+ buffer, for A7r5 cells and A7r5/hHO-1 cells. Data are represented mean ± s.e.m., n=9.

A

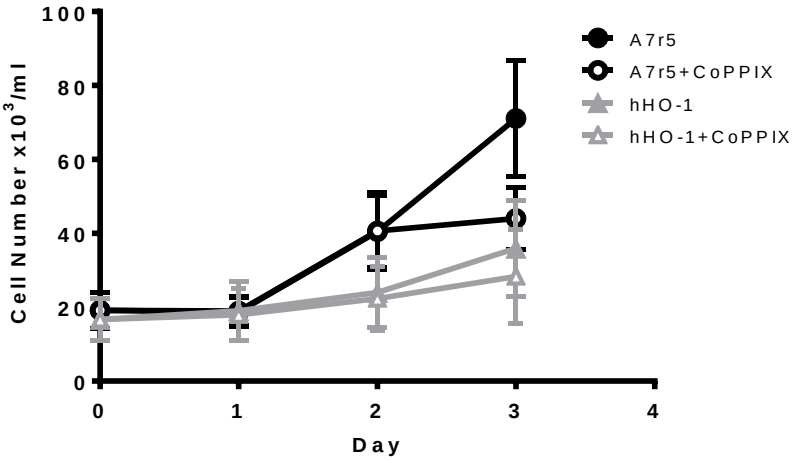

B

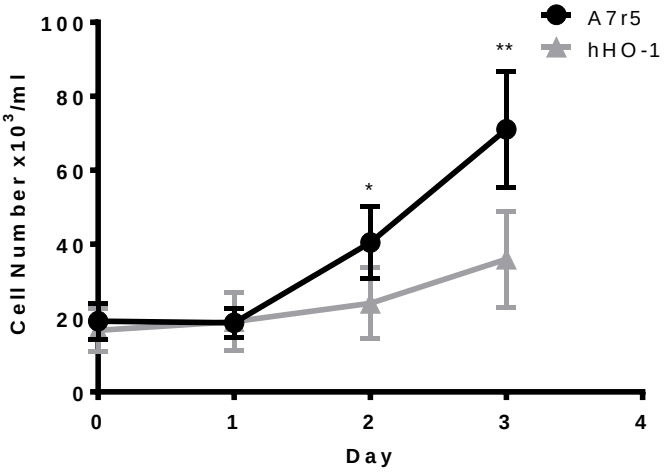

Figure 5.21 Stable over-expression of HO-1 inhibits A7r5 cell proliferation

Line graph showing the proliferative response of A7r5 cells and hHO-1/A7r5 cells ±10μM CoPPIX over a 3 day period; cell counts were taken daily to produce a 3 day time-course (A). Line graph showing the significant difference in proliferation between A7r5 cells and hHO-1/A7r5 cells on days 2 and 3 of the assay (B). Data were analysed by two-way repeated measures ANOVA, with sample matching by time point. This was followed by Sidak's multiple comparison test between A7r5 and hHO-1 cell groups for each time point, * $p<0.05$, ** $p<0.01$ hHO-1 vs A7r5, n=5. Data are represented as mean ± s.e.m.

QC-15 is a non-competitive inhibitor of HO-1 that binds to the distal side of the heme binding pocket within the enzyme (Rahman *et al.*, 2012). Various combinations of CoPPIX and QC-15 (a gift from Prof. Kanji Nakatsu, Queen's University, Kingston, Canada) were assessed in attempt to establish how the effects of this novel HO-1 inhibitor were exerted. One group of cells were treated with QC-15 and this was added to media already containing CoPPIX, to investigate whether inhibition was possible in the presence of an inducer. Another group of cells were treated with QC-15, but this was added to fresh media after the cells had been previously exposed to CoPPIX, in order to establish whether the effect of the inducer could be reversed. Figure 5.22 shows that QC-15 was able to reduce the level of CoPPIX induced HO-1 expression when CoPPIX containing media was removed from the cells, and fresh media added containing 10μM QC-15. This is shown by the HO-1 protein levels; 3.91 ± 1.30% of β-actin for 24h CoPPIX/48h QC-15, and 33.84 ± 4.58% of β-actin for 48h CoPPIX/24h QC-15. The level of HO-1 induction was higher when CoPPIX remained in the media with QC-15; 62.95 ± 26.91% of β-actin for 24h CoPPIX+48h QC-15, 53.46 ± 5.66% of β-actin for 48h CoPPIX+24h QC-15. With regards to the proliferative response of A7r5 cells to such combinations of CoPPIX and QC-15, the presence of CoPPIX in any combination significantly inhibited proliferation, as shown in Figure 5.23. The effect of QC-15 independent of CoPPIX also appeared to reduce cell proliferation, but did not reach statistical significance. There was no effect on cell viability by CoPPIX or QC-15, as demonstrated by the red line graph.

In summary, HO-1 induction by CoPPIX and hemin was verified by immunocytochemistry and westen blotting. CoPPIX treatment caused a trend towards lower $[Ca^{2+}]_i$ and Ca^{2+} oscillations, but did not reach a level of statistical significance. Treatment of A7r5 cells with CoPPIX also appeared to increase the amplitude of Ca^{2+} oscillations. The combined effect of CoPPIX and nifedipine treatment produced additive effects on $[Ca^{2+}]_i$ compared to nifedipine alone. HO-1 induction by CoPPIX significantly inhibited cell proliferation. Treatment with hemin produced a trend towards lower cell number, but data did not reach statistical significance. hHO-1/A7r5 cells proliferated significantly less than A7r5 cells, yet no significant effect were seen on $[Ca^{2+}]_i$ levels. The novel HO-1 inhibitor, QC-15, was able to limit HO-1 induction to a greater extent in the absence of CoPPIX, but QC-15 also appeared to negatively regulate A7r5 cell proliferation.

A

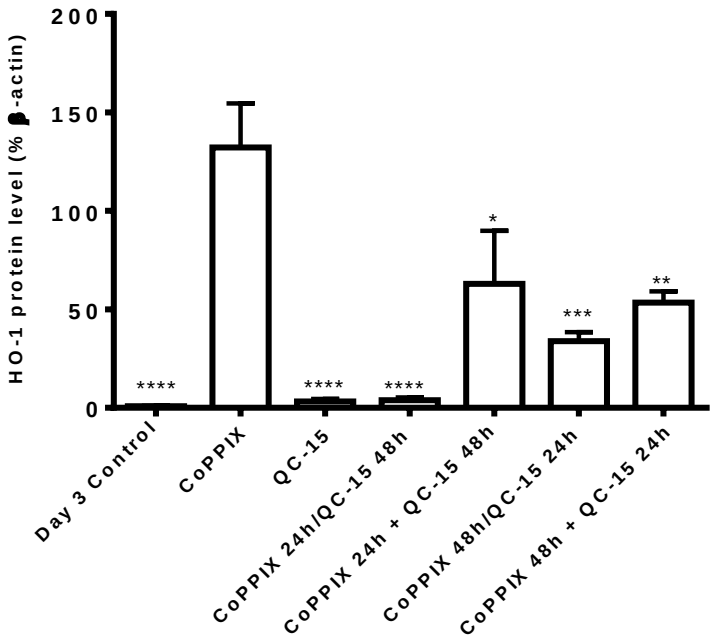

B

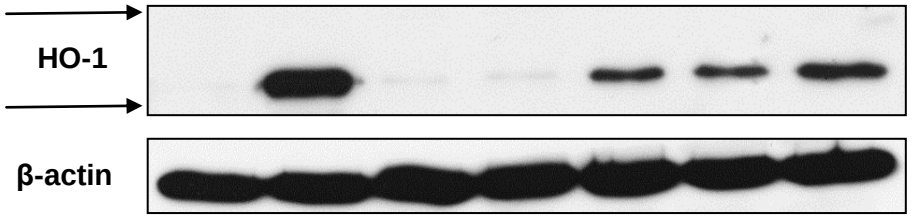

Figure 5.22 The effect of QC-15 on HO-1 induction by CoPPIX

(A) Bar graph showing relative HO-1 protein expression in A7r5 cells in response to 10µM CoPPIX, 10µM QC-15, or combinations of the two compounds; CoPPIX initially for 24h then fresh media with QC-15 for 48h; CoPPIX initially for 24h, then QC-15 for 48h in addition to the existing media; CoPPIX initially for 48h then fresh media with QC-15 for 24h; CoPPIX initially for 48h, then QC-15 for 24h in addition to the existing media. Densitometric analyses were normalised relative to β-actin, n=3. Data are represented as mean ± s.e.m., and data were analysed by one-way ANOVA with Dunnett's multiple comparison test, * $p<0.05$, ** $p<0.01$, *** $p<0.001$, **** $p<0.0001$ vs CoPPIX levels. (B) Representative western blot of HO-1 and the corresponding β-actin loading control. Each lane corresponds to the above bar on the graph. The arrows represent the position of the molecular weight markers (top, 37KDa; bottom, 25kDa).

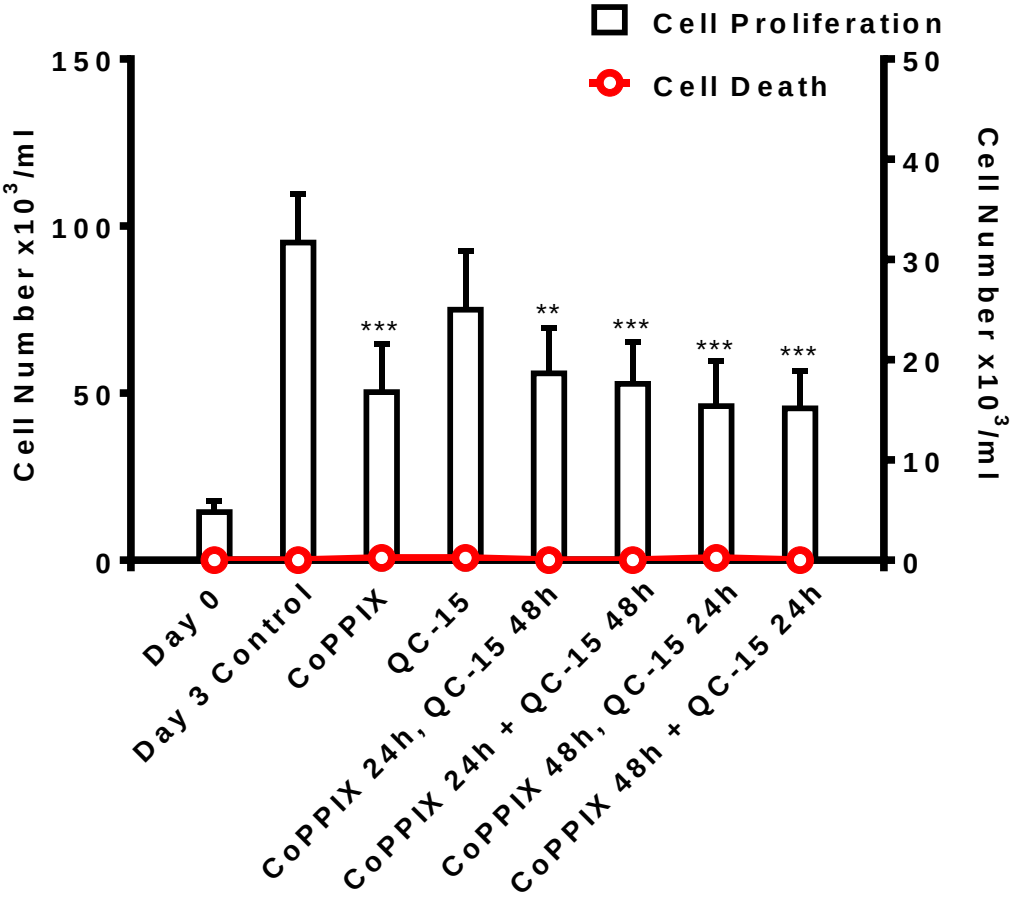

Figure 5.23 The effect of QC-15 on A7r5 cell proliferation

Bar graph showing the proliferative response of A7r5 cells to 10µM CoPPIX, 10µM QC-15, or combinations of the two compounds (left y-axis); CoPPIX initially for 24h then fresh media with QC-15 for 48h; CoPPIX initially for 24h, then QC-15 for 48h in addition to the existing media; CoPPIX initially for 48h then fresh media with QC-15 for 24h; CoPPIX initially for 48h, then QC-15 for 24h in addition to the existing media. The overlaid red plot shows the corresponding non-viable cell count (right y-axis). Data are represented as mean ± s.e.m., and data were analysed by one-way ANOVA with Dunnett's multiple comparison test, ** $p<0.01$, *** $p<0.001$ vs Day 3 Control, n=4.

5.3 Discussion

Taken together, Figures 5.1 and 5.3 suggest that CORM-3 is able to inhibit T-type Ca^{2+} channels. Significant effects on $[Ca^{2+}]_i$ and Ca^{2+} oscillations were demonstrated when the cells were modestly depolarised (20mM K^+ buffer), but not when they were strongly depolarised (80mM K^+ buffer), implying T-type Ca^{2+} channels were preferentially inhibited. Given that Ni^{2+} did not affect Ca^{2+} oscillation frequency (Figure 4.11, Chapter 4), but mibefradil did significantly reduce Ca^{2+} oscillations (Figure 4.8, Chapter 4), possibly as a result of non-selective effects on L-type Ca^{2+} channels, it appears logical to conclude that by significantly reducing Ca^{2+} oscillations, CORM-3 also has non-selective effects. However, the fact that CORM-3 had no effect on $[Ca^{2+}]_i$ when L-type Ca^{2+} channels were preferentially activated, suggests that CORM-3 preferentially inhibits T-type Ca^{2+} channels. CORM-3 caused a significant decrease in $[Ca^{2+}]_i$ regardless of DTT pre-treatment, yet Ca^{2+} oscillations were not significantly affected, despite there being a trend towards a lower oscillation frequency. Our research group has demonstrated that CO can inhibit L-type Ca^{2+} currents in cardiac myocytes and HEK293 cells expressing the human $Ca_v1.2$ subunit, although at a higher concentration of 30µM CORM-2, and also that DTT is able to prevent the effects of CO on this channel (Scragg *et al.*, 2008). Therefore, the non-significant effect of DTT pre-treatment on Ca^{2+} oscillations could also be attributed to the preventative effect on L-type Ca^{2+} channels. CO has also been shown to augment human recombinant interstitial smooth muscle L-type Ca^{2+}channels (Lim *et al.*, 2005). The study by Scragg *et al*. details how reactive oxygen species produced by electron transport chain modulation alter the redox state of the cell and the L-type Ca^{2+} channel, thereby altering the channel function. T-type Ca^{2+} channels have been shown to be modulated by a variety of endogenous ligands and pathways. The reducing agent L-cysteine has been demonstrated to augment T-type Ca^{2+} currents in sensory neurons (Nelson *et al.*, 2005). The neurotransmitter Zn^{2+} has been shown to preferentially inhibit $Ca_v3.2$ channels via an extracellular histidine residue at position 191 (His191) in domain I of the $Ca_v3.2$ α_1 subunit (Traboulsie *et al.*, 2007), and this can be prevented by Zn^{2+} ion chelation via reducing agents (Nelson *et al.*, 2007b). His191 is also the site implicated in preferential Ni^{2+} inhibition (Kang *et al.*, 2006), and the site of metal-catalysed oxidation by ascorbate, which subsequently inhibits the channel (Nelson *et al.*, 2007a). Evidently, redox sites within the T-type Ca^{2+} channel are important for modulation. DTT has been shown to inhibit $Ca_v3.1$ T-type Ca^{2+} channels in HEK293/$Ca_v3.1$ cells by causing a hyperpolarising shift of current activation (Karmazinova *et al.*, 2010). Through $Ca_v3.1$ mutagenesis, this study demonstrated that extracellular cysteine residues are required for current inhibition by DTT. If DTT had produced significant

effects on $[Ca^{2+}]_i$ in the present study, further experiments to elucidate which residues were affected by CO and DTT would be required. T-type Ca^{2+} channel mutagenesis followed by electrophysiological assessment of channel currents would be the logical next step. Cysteine residues are modified by the redox status of the cell (Chung *et al.*, 2013), and are a likely target for redox modulation within the $Ca_v3.1$ T-type Ca^{2+} channel protein (Karmazinova *et al.*, 2010).

CORM-3 did not significantly inhibit A7r5 cell proliferation, and in combination with 3µM mibefradil, CORM-3 caused no additive inhibitory effects in comparison to the effect of mibefradil alone. CORM-3 is stable for over 24h at 37ºC when dissolved in water, and releases CO upon ligand exchange in physiological solutions with a half-life of 4-18 minutes (Clark *et al.*, 2003). It has been proposed that CORM-3 reacts with plasma proteins *in vivo* to form ruthenium-protein adducts, and these adducts then decay slowly to liberate CO (Santos *et al.*, 2012). In the present experiment, CORM-3 was applied to the medium twice daily to ensure the cells were consistently exposed to CO. The myoglobin assay provides a method for the quantitation of CO released from CORMs, (Motterlini *et al.*, 2002;Atkin *et al.*, 2011), and was employed by our research group during preliminary investigations of CORM-3 activity prior to the use of this compound in proliferation assays. However, the low expression levels of T-type Ca^{2+} channels in A7r5 cells likely constrained the elucidation of the anti-proliferative effects of CO within this cell line. When CORM-3 was applied in combination with 2µM nifedipine, proliferation was significantly inhibited. The proliferative response of the cells in Figure 5.8 was lower than in other proliferation assays. An explanation for this could be that as the cells reached P6, it was discovered that they proliferated at a slower rate. The passages used in the Figure 5.8 were a combination of passages 4, 5, and 6. However, the effects of both nifedipine and CORM-3 on $[Ca^{2+}]_i$ when applied simultaneously were less than the effect of nifedipine alone; $[Ca^{2+}]_i$ reached a higher level in the presence of both compounds. The fact that the proliferative response to both compounds does not reflect the change $[Ca^{2+}]_i$ levels is unexpected. These data imply that L-type Ca^{2+} channels, or a proportion of these channels, are active upon modest depolarisation therefore, it is possible that this activity is masking the activity of T-type Ca^{2+} channels. The effects of 2µM nifedipine on $[Ca^{2+}]_i$ levels, as shown in Figure 4.13 in Chapter 4, demonstrate that L-type channels are prominent in A7r5 cells, yet Figure 4.21 shows that 2µM nifedipine has no inhibitory effect on proliferation. As CO has been shown to modulate both L-type and T-type Ca^{2+} channel activity, it is possible that when L-type Ca^{2+} channels are inhibited by nifedipine, the inhibitory effect

of CO on T-type Ca^{2+} channels is unmasked. This is likely to be more apparent in the setting of a proliferation assay, as a proportion of T-type Ca^{2+} channels are active at RMP, and the contribution of these channels to resting $[Ca^{2+}]_i$ levels is greater than that of L-type Ca^{2+} channels.

HO-1 induction via 10µM CoPPIX pre-treatment reduced $[Ca^{2+}]_i$ and Ca^{2+} oscillation frequency, but not to a level of statistical significance. However, the trends may have proven significant if the number of experimental repeats was increased. The application of nifedipine after CoPPIX pre-treatment reduced $[Ca^{2+}]_i$ levels by a greater extent than nifedipine treatment alone; implying HO-1 induction and subsequent CO exposure is able to reduce $[Ca^{2+}]_i$ by a mechanism independent of L-type Ca^{2+} channels. This additional effect by CoPPIX, which was not produced by CORM-3 in the presence of nifedipine, may be attributable to the prolonged exposure of the cells to CO as a result of a 48h exposure to CoPPIX. Interestingly, the amplitude of the Ca^{2+} oscillations produced in response to HO-1 induction in both Figures 5.10 and 5.11 appear to be increased in comparison to the control traces. In hindsight, analysis of the Ca^{2+} oscillation amplitude between control and HO-1-induced traces should have been performed. Figure 5.11 (C) shows that Fura 2 ratio was significantly reduced by HO-1 induction, yet the representative traces in Figures 5.10 and 5.11 (B) imply that Ca^{2+} oscillation frequency decreases with HO-1 induction. These observations suggest that HO-1-derived CO is able to limit $[Ca^{2+}]_i$, possibly by inhibition of T-type Ca^{2+} channels (as suggested by Figures 3.13 and 5.10), but that Ca^{2+} movement with each oscillation is increased, possibly via L-type Ca^{2+} channels. The potential inhibition of T-type Ca^{2+} channels by HO-1-derived CO may have revealed the full response of L-type Ca^{2+} channels and their influence on Ca^{2+} oscillations.

Proliferation of A7r5 cells was significantly inhibited by 10µM CoPPIX. There was also a general trend of decreased cell proliferation in response to hemin, although a level of statistical significance was not reached. The anti-proliferative effects of hemin were less potent than the effects of CoPPIX. This is surprising as hemin also acts as a substrate for HO-1, therefore one would expect higher enzyme activity and more CO production. If time had permitted, the levels of HO-1 activity after induction by the two metalloporphyrins could have been assessed using the biliverdin reductase assay (Huber, III *et al.*, 2009). Taking into consideration the significant effects of CORM-3 and CoPPIX on HEK293/Ca_v3.2 cell proliferation and $[Ca^{2+}]_i$, it is tempting to speculate that

the significant inhibitory effects of CoPPIX on A7r5 proliferation are due to T-type Ca^{2+} channel inhibition. However, this cannot be reliably concluded given the insignificant effects of CORM-3 on proliferation, and of CoPPIX on $[Ca^{2+}]_i$ levels.

As the level of HO-1 expression deterioratied during the passage of A7r5/hHO-1 cells, early passage numbers were utilised in the proliferation assays and microfluorimetry recordings. A7r5/hHO-1 proliferation was significantly lower than A7r5 cell proliferation, implying the level of HO-1 activity as a result of over-expression is comparable to the effects of 10μM CoPPIX and 30μM hemin. As A7r5/hHO-1 proliferation was lower than the CoPPIX induced anti-proliferative effects in A7r5 cells, it is feasible that the constant level of over-expressed HO-1 activity, and subsequent CO production, continuously limited the proliferative response. Indeed, rat VSMC proliferation was also inhibited by HO-1 over-expression using a retroviral vector (Zhang *et al.*, 2002). However, the mechanism underlying this response was not fully elucidated. As the application of CoPPIX reduces the proliferative response of A7r5/hHO-1 by a further 12%, it appears there is scope for further HO-1 induction. The level of A7r5/hHO-1-mediated CO production was not high enough to reduce $[Ca^{2+}]_i$ significantly in A7r5/hHO-1 cells. The mircofluorimetry data provide a snapshot of Ca^{2+} handling over a short time window, whereas proliferation assays provide a continuous assessment of the cell response. Therefore, the chronic exposure of the cells to HO-1 and CO is more accurately assessed by the latter.

The densitometry data in Figure 5.22 (A) imply that QC-15 is able to inhibit HO-1 induction by CoPPIX after a 24h exposure, but induction will still occur if CoPPIX is maintained in the media. This suggests that there was a level of competition between the two compounds because, if CoPPIX was present in addition to QC-15, HO-1 induction ensued. The inhibition of A7r5 proliferation in Figure 5.23 by QC-15 was surprising given that this compound was developed as a HO-1 inhibitor, as it is HO-1 induction that has demonstrated anti-proliferative effects previously (Duckers *et al.*, 2001;Tulis *et al.*, 2001;Peyton *et al.*, 2002;Zhang *et al.*, 2002;Choi *et al.*, 2009;Hyvelin *et al.*, 2010). The anti-proliferative effects of combinations of QC-15 and CoPPIX cannot be solely attributed to the induction of HO-1, as QC-15 also negatively affected the proliferative response. Further evidence of this notion is given by the fact that HO-1 was not induced by the 24h incubation with CoPPIX which was then replaced by QC-15 for a further 48h, as demonstrated in Figure 5.22, yet proliferation was inhibited by

this combination. HO-1 is inhibited more potently by QC-15 than HO-2, and QC-15 has been shown to have little effect on other heme-containing enzymes, such as sGC and NOS (Kinobe *et al.*, 2006). However, there appears to be additional off-target effects with regards to A7r5 proliferation. Indeed, neointima formation has been shown to be reduced in iNOS knockout mice (Chyu *et al.*, 1999), therefore even minimal off-target effects of QC-15, on NOS for example, may have limited the proliferative response of A7r5 cells.

In summary, despite the minimal effects of CORM-3 alone on A7r5 cell proliferation, microfluorimetry data indirectly imply that CO can inhibit native T-type Ca^{2+} channels in these cells. HO-1 induction or over-expression, and subsequent CO production, have anti-proliferative effects and visibly reduce $[Ca^{2+}]_i$. Although, the inhibitory effect of CORM-3 on $[Ca^{2+}]_i$ was not significantly prevented by redox modulation, transient receptor potential channels have been shown to be modulated by the extracellular redox protein, thioredoxin (Beech & Sukumar, 2007). Thioredoxin has an important role in maintaining cellular redox status (Yamawaki *et al.*, 2003), and oxidative stress is a feature of many cardiovascular disorders (Paravicini & Touyz, 2006;Kim *et al.*, 2011b;Chung *et al.*, 2013). Excess pathological proliferation and T-type Ca^{2+} channel up-regulation (Rodman *et al.*, 2005;Cribbs, 2006;Pluteanu & Cribbs, 2011), in addition to HO-1 induction and subsequent CO production (Wang & Chau, 2010), are central to such disorders, therefore a possible role for thioredoxin as a modulator of T-type Ca^{2+} channels warrants investigation. Indeed, ROS have been shown to increase VSMC differentiation (Su *et al.*, 2001), therefore the redox status of VSMCs during the response to injury may provide the specific environment for CO to exert effects on the T-type Ca^{2+} channel.

CHAPTER 6

The effect of T-type Ca^{2+} channel inhibition, HO-1 induction, and CO on human smooth muscle cell proliferation

6.1 Introduction

Vascular injury and ensuing complications arise from endothelial dysfunction or damage. Interventions such as stenting and angioplasty, and disorders such as hypertension and atherosclerosis, compromise the integrity of the endothelium and a an inflammatory response ensues, followed by an increase in oxidative stress and remodelling (Rzucidlo *et al.*, 2007). In response to this injury, VSMCs de-differentiate, re-enter the cell cycle, migrate to the site of injury and proliferate (Rzucidlo *et al.*, 2007). Excessive VSMC proliferation can be detrimental to vascular function, as they produce extracellular matrix that contributes to the formation of atherosclerotic plaques and hyperplastic lesions (Rzucidlo *et al.*, 2007), and neointima formation can reduce or even occlude blood flow. Under such conditions of oxidative and inflammatory stress, HO-1 is induced, and the by-product of HO-1 activity, CO, has been shown to have anti-proliferative effects in VSMCs (Kim *et al.*, 2011b). The anti-proliferative effects of HO-1 and CO have been demonstrated across different species. HO-1 induction was shown to limit vascular remodelling *in vivo* following balloon injury in rats (Tulis *et al.*, 2001), and HO-1 derived CO reduced neointima formation and inhibited proliferation of rat aortic VSMCs (Togane *et al.*, 2000;Peyton *et al.*, 2002). VSMC proliferation was reduced in a pig model of arterial injury after HO-1 induction (Duckers *et al.*, 2001), and HO-1 induction in stented rat aorta and rabbit iliac arteries limited neointimal hyperplasia, in addition to apoptosis and inflammation (Hyvelin *et al.*, 2010).

Previous chapters have detailed the anti-proliferative effects of CO in HEK293/$Ca_v3.2$ cells and rat aortic VSMCs. The hypothesis that the T-type Ca^{2+} channel is a target of CO has been strengthened by the data generated thus far. Primary VSMCs were employed in order to assess the effects of HO-1 induction, CO and T-type Ca^{2+} channel inhibition on proliferation in a model with greater relevance to human disease. Both human saphenous vein smooth muscle cells (HSVSMC) and human coronary artery smooth muscle cells (HCASMC) were utilised.

6.2 Results

6.2.1 Characterisation of HSVSMCs

Immunocytochemistry was performed on HSVSMCs to confirm their smooth muscle cell properties. Figure 6.1 illustrates positive staining for smooth muscle α-actin (panels A and E), smooth muscle myosin heavy chain (panels B and F), and vimentin (panel C). In addition, a degree of co-localisation of smooth muscle α-actin and myosin heavy chain can be seen in Figure 6.1 panel (D), as demonstrated by the orange staining in the cell in the centre of the image. The corresponding α-actin and myosin heavy chain images are shown in panels (E) and (F). The presence of T-type Ca^{2+} channels were also demonstrated by immunocytochemistry. Figure 6.2 shows positive staining for $Ca_v3.1$ and $Ca_v3.2$, with denser staining of $Ca_v3.1$ in peri-nuclear regions and what appears to be an association with the Golgi network. Figure 6.3 (A) shows the only successful identification of $Ca_v3.1$ via western blot. The channel is represented most clearly in lanes 2 and 4, which correspond to a membrane enriched and an untreated HSVSMC sample respectively. HEK293/$Ca_v3.1$ cells were used as the positive control. Immunoprecipitation of the T-type Ca^{2+} channels was attempted on two occasions without success. Figure 6.3 (B) shows the wide variation in mRNA expression levels of $Ca_v3.1$ from six patient samples of HSVSMCs, the cell passages ranged from P2 to P6. Figure 6.4 shows the mRNA expression levels of $Ca_v3.2$, detectable in only two patient samples, which exhibit a trend of considerably lower expression than $Ca_v3.1$. Figure 6.5 demonstrates the growth characteristics of HSVSMCs in response to 0.4% or 10% serum-containing medium. The 10% serum-containing medium was utilised to encourage cell proliferation, whilst the 0.4% serum-containing medium was employed to induce cell senescence. There was a significant difference in cell number between the 10% and 0.4% experimental groups at days 3 and 4 of the assay. Subsequent proliferation assays involving human VSMCs were therefore performed over 4 days in order to detect reliably, the significant effects of compounds used in this study.

6.2.2 The effect of T-type Ca^{2+} channel inhibition on HSVSMC and HCASMC proliferation

Proliferation of both HSVSMCs and HCASMCs was significantly inhibited by mibefradil, as shown in Figures 6.6 and 6.7 respectively. There was a concentration-dependent decrease in HSVSMC proliferation, as shown in Figure 6.6 (A), yet concentrations of 10μM and 30μM mibefradil reduced cell viability to 50%. Cells were counted daily for a

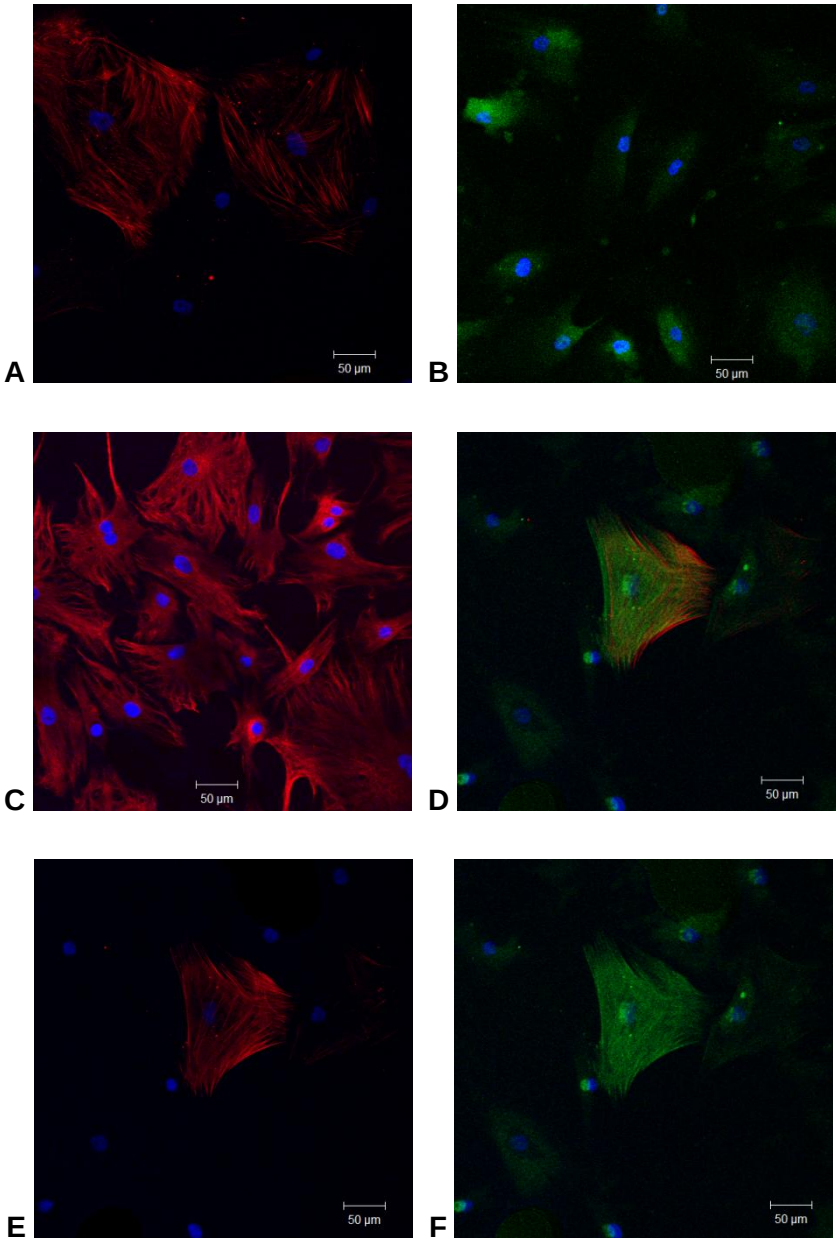

Figure 6.1 Characterisation of HSVSMCs

Immunocytochemistry of HSVSMCs showing smooth muscle α-actin staining (red) (A), smooth muscle myosin heavy chain staining (green) (B), vimentin staining (red) (C), smooth muscle α-actin and myosin heavy chain co-localisation (D). Panels (E) and (F) show the corresponding smooth muscle α-actin (red) and smooth muscle myosin heavy chain (green) of image (D). Cell nuclei were stained blue with DAPI. Cells were utilised at P5, and are representative images of 12 fields of view from n=6 experimental repeats.

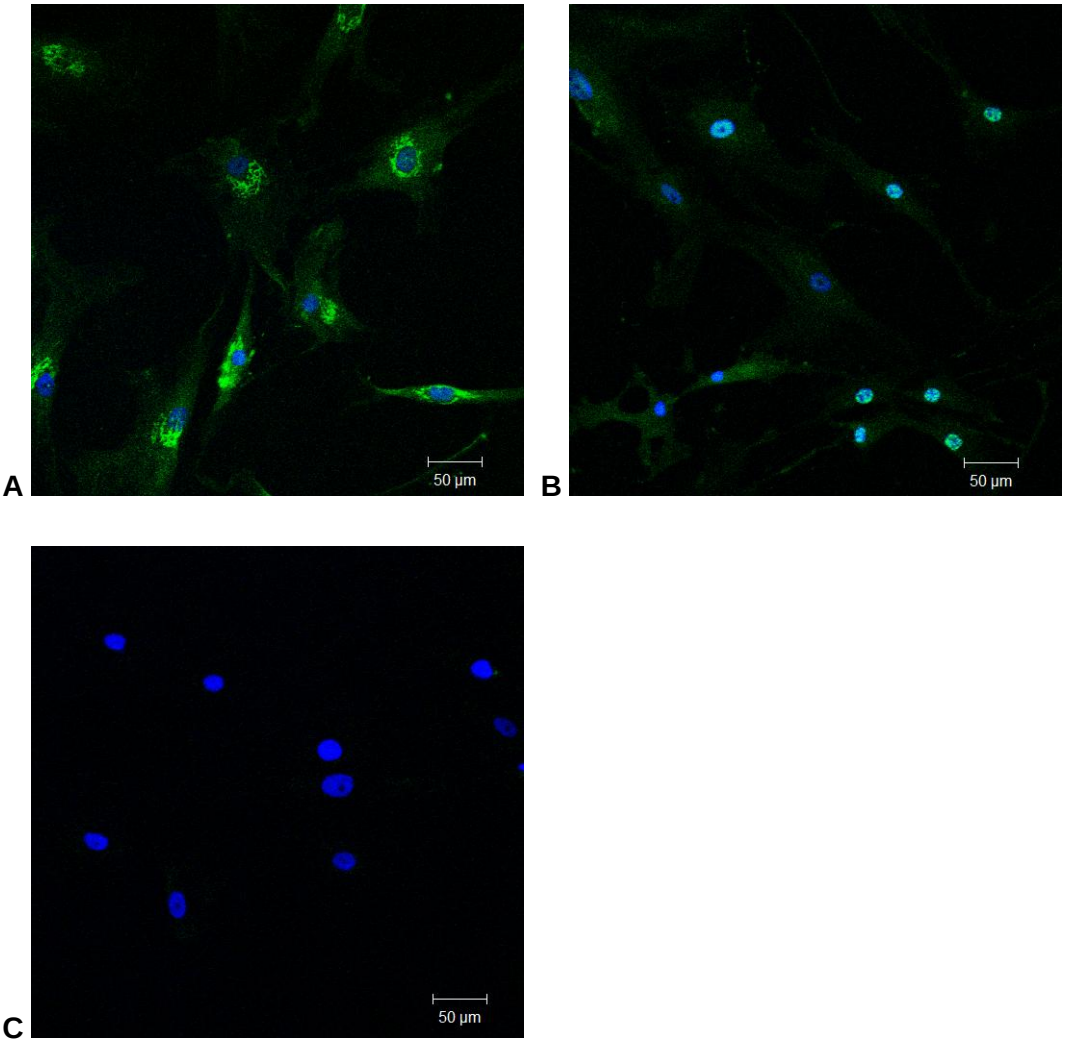

Figure 6.2 Expression of $Ca_v3.1$ and $Ca_v3.2$ in HSVSMCs

Immunocytochemistry of HSVSMCs showing staining for $Ca_v3.1$ (green) (A), and for $Ca_v3.2$ (green) (B). Panel (C) shows a control image without primary antibody. Cell nuclei were stained blue with DAPI. Cells were utilised at P3, and are representative images of 10 fields of view from n=5 experimental repeats.

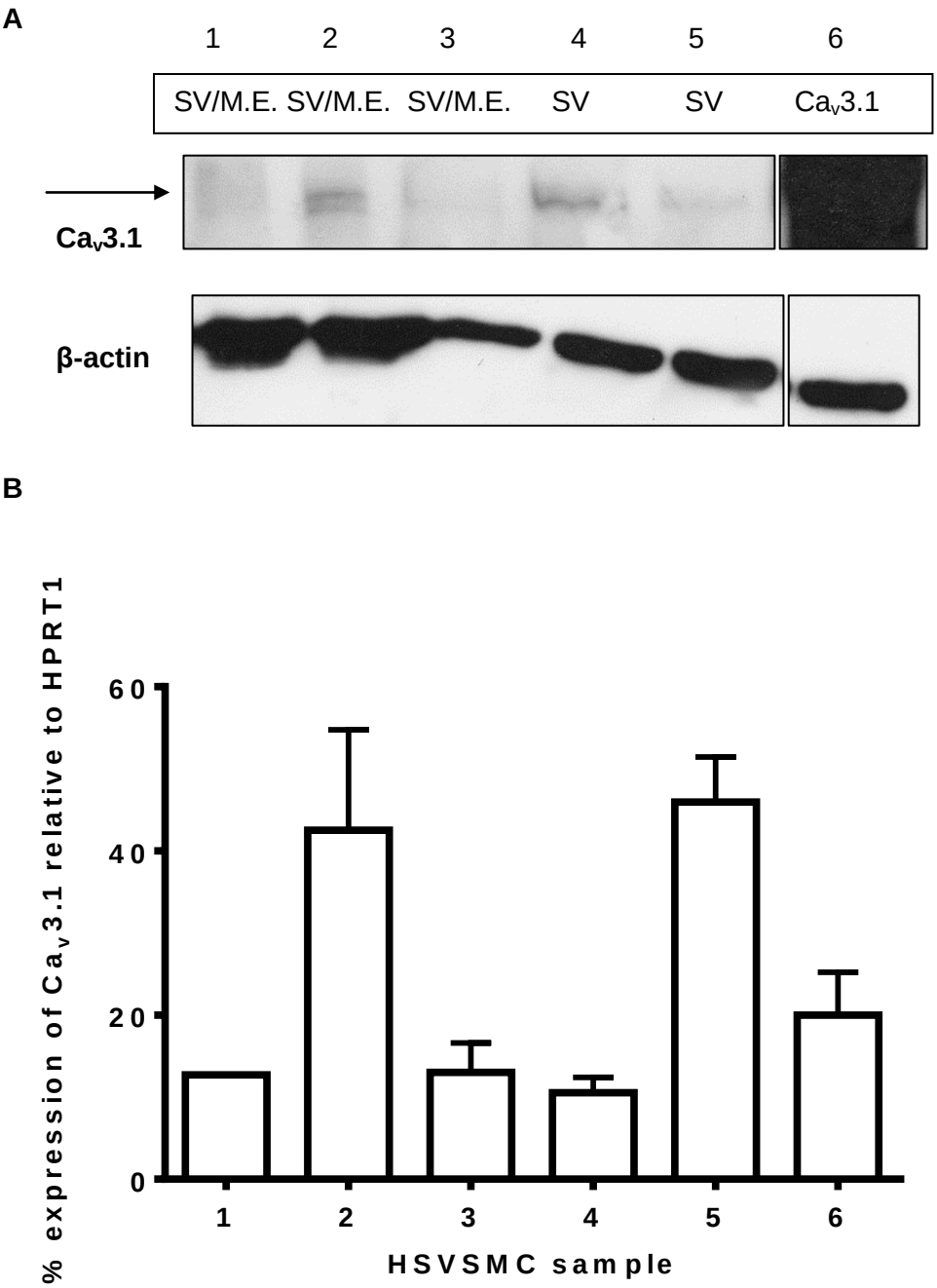

Figure 6.3 Expression of the $Ca_v3.1$ T-type Ca^{2+} channel in HSVSMCs

Western blot of $Ca_v3.1$ T-type Ca^{2+} channel expression using an anti-$Ca_v3.1$ antibody from Alomone (A), in various cell samples (SV; control HSVSMC, SV/M.E.; membrane enriched HSVSMC, $Ca_v3.1$; HEK293/$Ca_v3.1$ cells). The arrow represents the position of the 250kDa molecular weight marker, and of the $Ca_v3.1$ protein. Below is the corresponding β-actin loading control. Panel (B) shows a bar graph of $Ca_v3.1$ mRNA expression, relative to the endogenous control, HPRT1 (Hypoxanthine phosphoribosyltransferase 1), in samples of HSVSMCs from 6 different patients at P2 to P6. Samples were analysed in triplicate and represented as mean ± s.e.m.

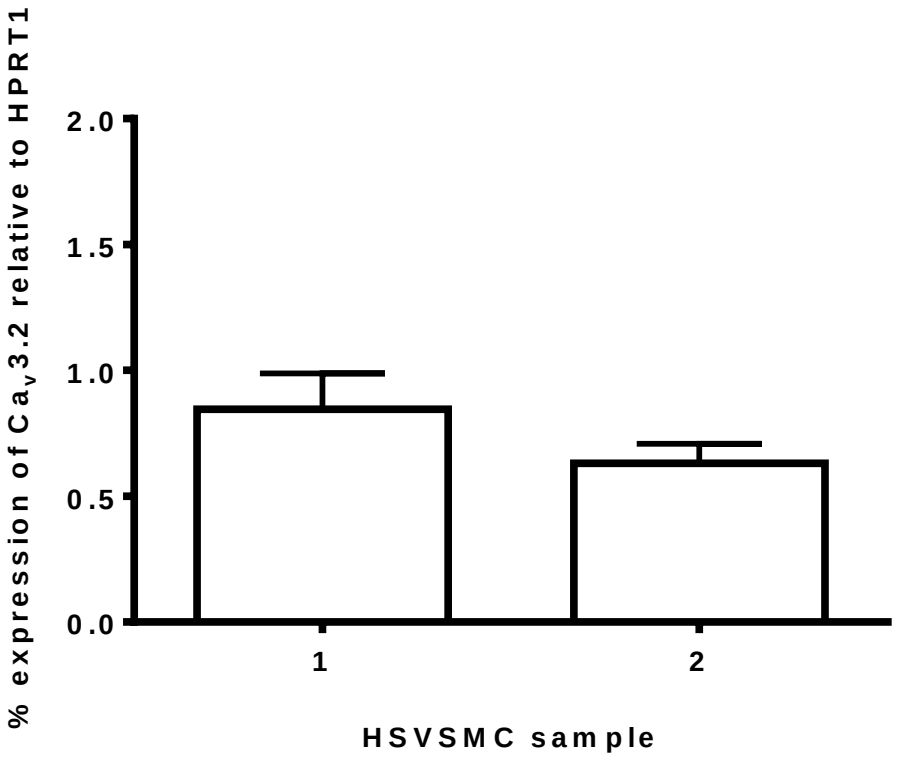

Figure 6.4 Expression of the $Ca_v3.2$ T-type Ca^{2+} channel in HSVSMCs

Bar graph of $Ca_v3.2$ mRNA expression relative to the endogenous control, HPRT1, detectable in only two patient samples of HSVSMCs. Samples were at P3 and P4, analysed in triplicate and represented as mean ± s.e.m.

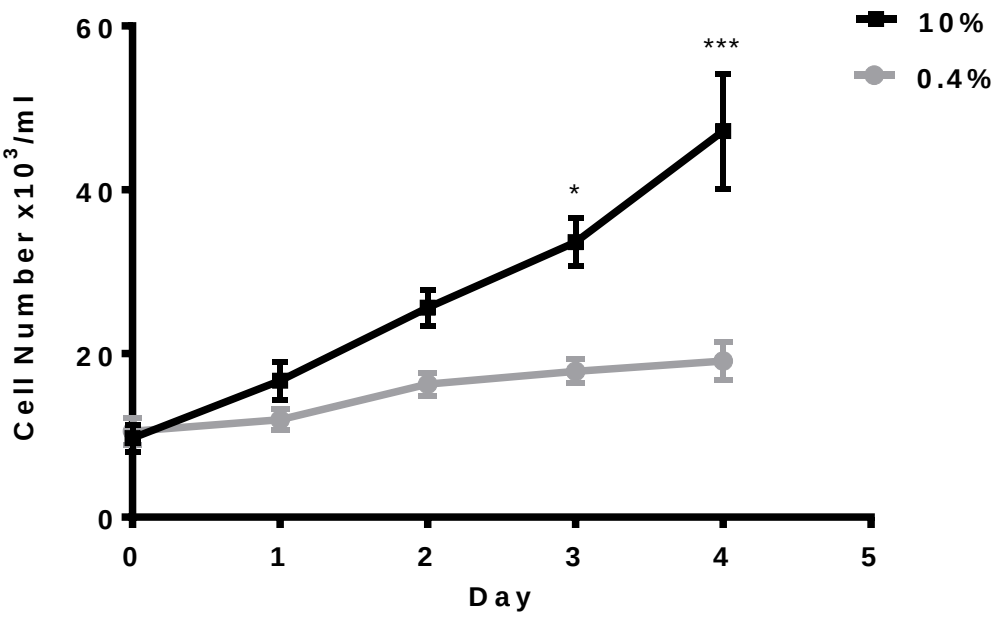

Figure 6.5 Growth characteristics of HSVSMCs

Line graph showing the daily counts of HSVSMCs in response to 0.4% (grey line) or 10% serum-containing media (black line), over a 4 day time-course, n=4. Data are represented as mean ± s.e.m., and data were analysed by two-way repeated measures ANOVA with sample matching by time point. This was followed by Sidak's multiple comparison test between control and treated groups for each time point, * $p<0.05$, *** $p<0.001$.

A

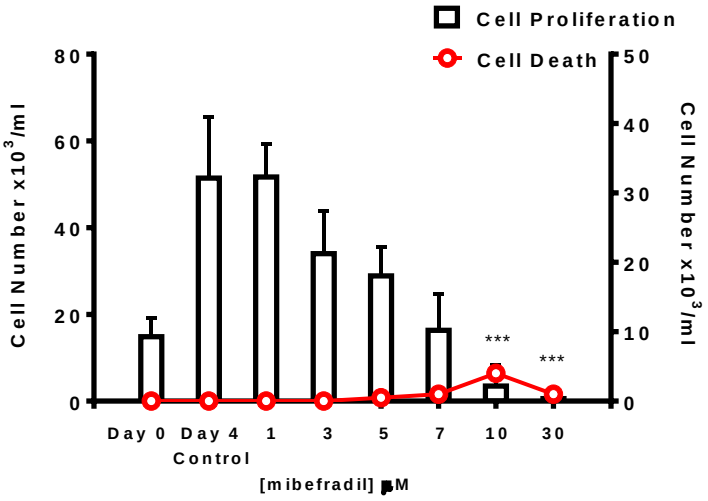

B

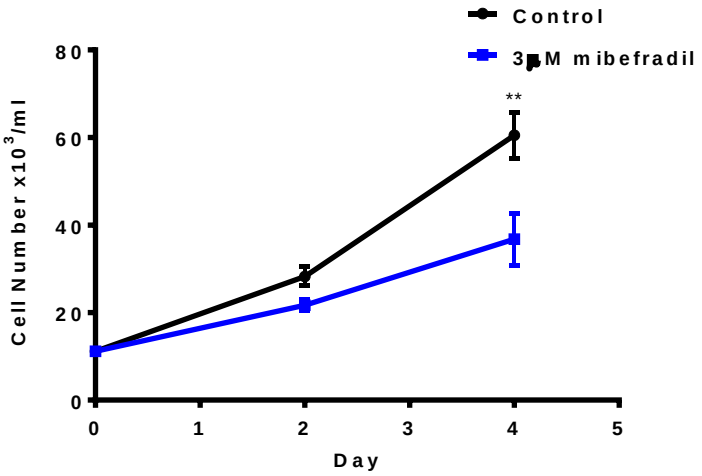

Figure 6.6 Mibefradil inhibits HSVSMC proliferation

Bar graph showing the proliferative response of HSVSMCs (left y-axis) to increasing concentrations of mibefradil (A). The overlaid red plot (right y-axis) shows the corresponding non-viable cell count. Data were analysed by ratio repeated measures one-way ANOVA with Dunnett's multiple comparison test, *** $p<0.001$ vs Day 4 Control, n=4. Line graph of the effects of 3µM mibefradil over a 4 day time-course (B), data were analysed by two-way repeated measures ANOVA with sample matching by time point. This was followed by Sidak's multiple comparison test between control and treated groups for each time point, ** $p<0.01$, n=4. Data are represented as mean ± s.e.m.

A

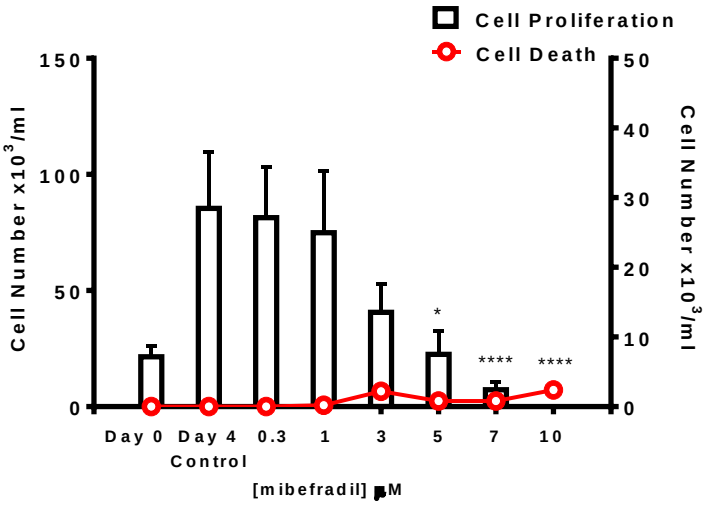

B

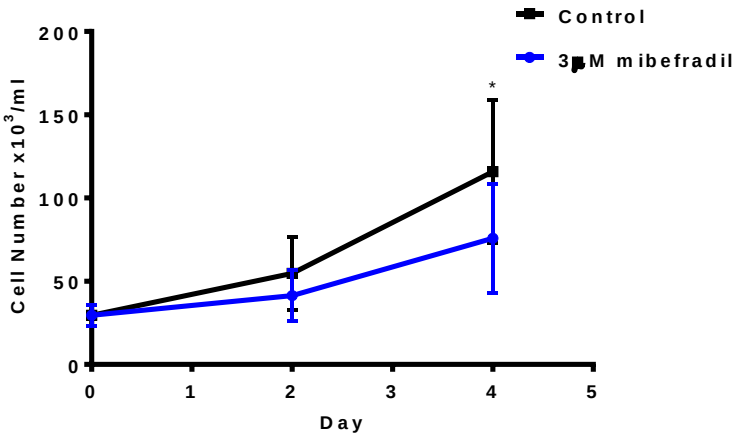

Figure 6.7 Mibefradil inhibits HCASMC proliferation

Bar graph showing the proliferative response of HCASMCs (left y-axis) to increasing concentrations of mibefradil (A). The overlaid red plot shows the corresponding non-viable cell count (right y-axis). Data were analysed by ratio repeated measures one-way ANOVA with Dunnett's multiple comparison test, * $p<0.05$, **** $p<0.0001$ vs Day 4 Control, n=5. Line graph of the effects of 3µM mibefradil over time (B), data were analysed by two-way repeated measures ANOVA with sample matching by time point. This was followed by Sidak's multiple comparison test between control and treated groups for each time point, * $p<0.05$, n=4. Data are represented as mean ± s.e.m.

period of 4 days to assess the proliferative response of 3µM mibefradil over time; producing a 4 day time-course. Cell proliferation was inhibited by 34% and 39% in the presence of 3µM mibefradil on day 4, as shown in Figure 6.6 (A) and (B) respectively. Despite the fact that 3µM mibefradil has been demonstrated to have non-selective effects in A7r5 cells, this concentration produced visible effects on human VSMC proliferation, without causing cytotoxicity as assessed via non-viable cell counts. Given that inhibition of L-type Ca^{2+} channels by 2µM nifedipine did not cause significant inhibition of cell proliferation in A7r5 cells, as shown in Figure 4.21 (Chapter 4), one can speculate that any off-target effects of mibefradil on L-type Ca^{2+} channels would therefore, not significantly inhibit cell proliferation. Additionally, mibefradil was the most selective T-type blocker available at the time of these experiments. HCASMCs appeared more sensitive; 3µM mibefradil caused 5% cell death, and higher concentrations were increasingly cytotoxic, as shown in Figure 6.7 (A). Cell proliferation was inhibited by 52% and 35% in the presence of 3µM mibefradil on day 4, as shown in Figure 6.7 (A) and (B) respectively. However, the combination of all day 4 counts to produce n=9 demonstrates that cell proliferation was inhibited by 43% in the presence of 3µM mibefradil (graph not shown). In summary, T-type Ca^{2+} channel inhibiton by 3µM mibefradil limits proliferation of HSVSMC and HCASMC to similar extents.

6.2.3 The effect of CO on HSVSMC and HCASMC proliferation

CORM-3 inhibited the proliferation of HSVSMCs and HCASMCs in a concentration dependent manner without causing effects on cell viability. HSVSMC number was reduced by 45% in the presence of 10µM CORM-3, as shown in Figure 6.8. HCASMC number was reduced by 22% and 34% in the presence of 10µM CORM-3, as shown in Figure 6.9 (A) and (B) respectively. However, the combination of all day 4 counts to produce n=7 indicated that cell proliferation was inhibited by 25% in the presence of 10µM CORM-3 (graph not shown).

6.2.4 The effect of HO-1 modulation on HSVSMC and HCASMC proliferation

Immunocytochemistry of HSVSMC in Figure 6.10 illustrates that HO-1 is induced by 3µM CoPPIX (panel A) and 3µM hemin (panel B) over 24h. Figure 6.11 illustrates the change in HO-1 protein expression after treatment with increasing concentrations of CoPPIX. Panels (A) and (B) show the levels of HO-1 protein expression at 48h and at

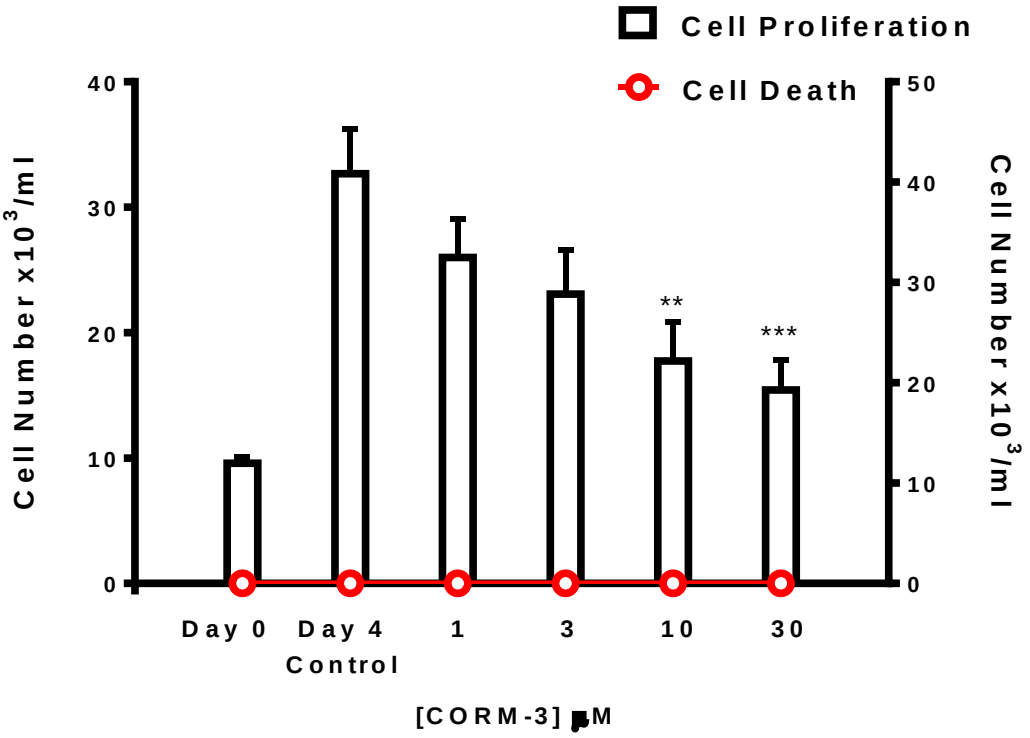

Figure 6.8 CORM-3 inhibits HSVSMC proliferation

Bar graph showing the proliferative response of HSVSMCs (left y-axis) to increasing concentrations of CORM-3 (right y-axis). The overlaid red plot shows the corresponding non-viable cell count. Data are represented as mean ± s.e.m., and data were analysed by ratio repeated measures one-way ANOVA with Dunnett's multiple comparison test, ** $p<0.01$, *** $p<0.001$ vs Day 4 Control, n=4.

A

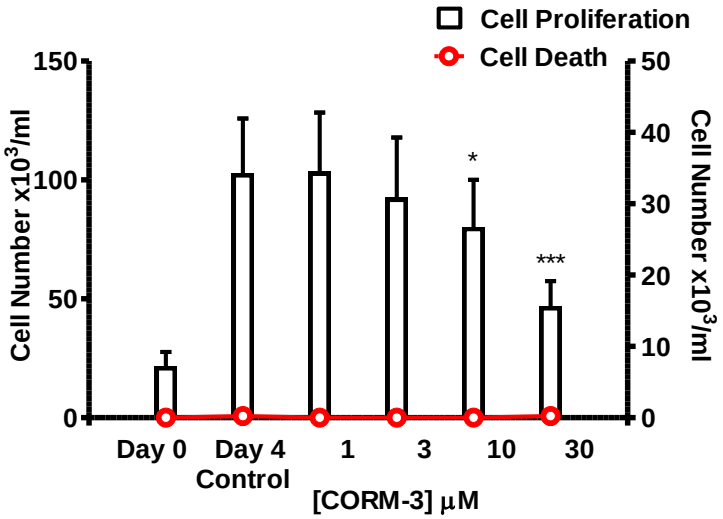

B

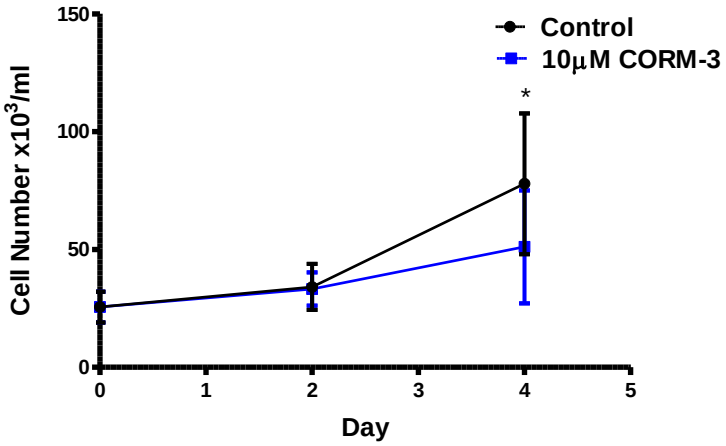

Figure 6.9 CORM-3 inhibits HCASMC proliferation

Bar graph showing the proliferative response of HCASMCs (left y-axis) to increasing concentrations of CORM-3 (A). The overlaid red plot shows the corresponding non-viable cell count (right y-axis). Data were analysed by ratio repeated measures one-way ANOVA with Dunnett's multiple comparison test, * $p<0.05$, *** $p<0.001$ vs Day 4 Control, n=4. Line graph of the effects of 10µM CORM-3 over time (B). Data were analysed by two-way repeated measures ANOVA with sample matching by time point. This was followed by Sidak's multiple comparison test between control and treated groups for each time point, * $p<0.05$, n=3. Data are represented as mean ± s.e.m.

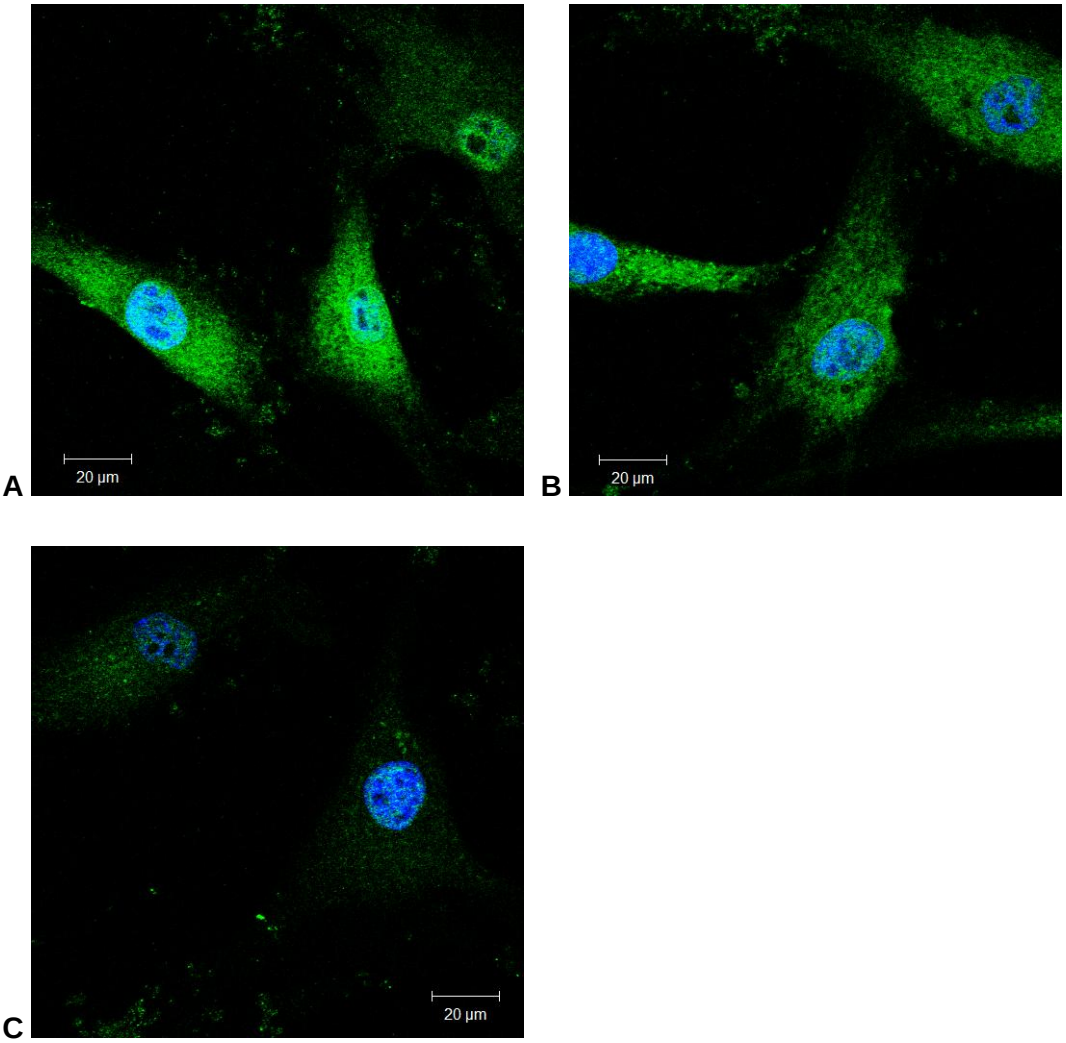

Figure 6.10 HO-1 induction in HSVSMCs

Immunocytochemistry of HO-1 induction (green) in HSVSMCs. Panel (A) illustrates HO-1 induction after a 24h incubation with 3µM CoPPIX. Panel (B) illustrates HO-1 induction after a 24h incubation with 3µM hemin. Panel (C) shows a control image without HO-1 induction. Cell nuclei were stained blue with DAPI. Cells were utilised at P4, and are representative images of 8 fields of view from n=4 experimental repeats.

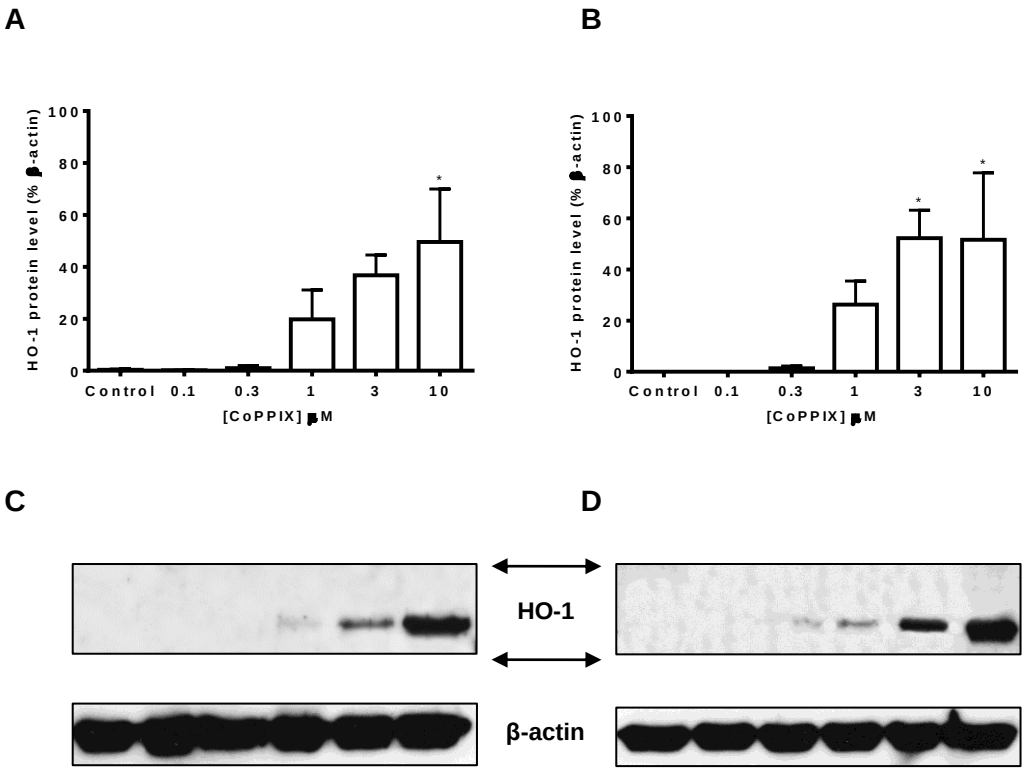

Figure 6.11 CoPPIX induces HO-1 protein expression in HSVSMCs

Bar graphs showing the relative HO-1 protein expression in HSVSMCs; densitometric analyses were normalised to β-actin at 48h (A) and 96h (B), n=3. CoPPIX treatment was added at 0h and 48h. Data are represented as mean ± s.e.m. and data were analysed by one-way ANOVA with Dunnett's multiple comparison test, * $p<0.05$ vs Control levels. Representative western blots of HO-1 and the corresponding β-actin loading control at 48h (C) and 96h (D). The arrows represent the position of the molecular weight markers (top, 37KDa; bottom, 25kDa).

96h, and corresponding representative western blots are shown in panels (C) and (D). HO-1 expression was increased in a concentration-dependent manner in response to CoPPIX. Expression was maintained at 96h by re-application of CoPPIX when the media was changed at 48h, and HO-1 was subsequently induced to a higher level at 96h. Figure 6.12 (A) shows the proliferative response of HSVSMCs to increasing concentrations of CoPPIX, with no effect on cell viability, as shown by the red line plot. Proliferation of HSVSMCs was significantly inhibited by 3µM and 10µM CoPPIX; cell number was reduced by 42% and 45% respectively. The proliferative response of HSVSMCs to 3µM CoPPIX was assessed daily over a 4 day period to produce a time-course; HSVSMC proliferation was inhibited by 39% on day 4, as shown in Figure 6.12 (B), which is comparable to the extent of inhibition demonstrated in response to 3µM CoPPIX shown in Figure 6.12 (A). Co-application of 3µM mibefradil and 3µM CoPPIX did not cause additive inhibitory effects on HSVSMC proliferation when assessed over a 4 day time-course, as shown in Figure 6.13. Cell number was reduced by 10% and 47% in response to CoPPIX and mibefradil respectively. However, cell number was reduced by 47% in response to simultaneous application of CoPPIX and mibefradil. CoPPIX limited cell proliferation in HCASMCs at a concentration of 3µM or higher. Cell death was less than 1%, 1.6%, and 3% in response to 3µM, 10µM and 30µM CoPPIX respectively. HCASMC number was reduced by 43% and 52% in the presence of 3µM CoPPIX, as shown in Figure 6.14 (A) and (B) respectively. However, the combination of all day 4 counts to produce n=8 indicates that cell proliferation was inhibited by 48% in the presence of 3µM CoPPIX (graph not shown).

HO-1-targeting siRNA was employed to prevent basal HO-1 expression and HO-1 induction in HSVSMCs, in order to assess the subsequent proliferative response. A range of HO-1-targeting siRNA concentrations were applied to the cells for 48h, and western blots performed to evaluate HO-1 protein knock-down. As HO-1 is an inducible protein, the optimal time-point at which to apply CoPPIX to the cells was investigated to ensure that the optimal window of mRNA knock-down was utilised. The cell response to the application of CoPPIX immediately post transfection or on the day following transfection was assessed. Figure 6.15 (A) shows HO-1 protein expression levels in response to 3µM CoPPIX application immediately after the transfection solutions were removed, proceeding transfection with 25nM, 50nM, and 100nM HO-1-targeting siRNA. From these western blots it was concluded that 100nM HO-1-targeting siRNA was the optimal concentration to knock-down HO-1 expression. Figure 6.15 panels (B) and (C)

A

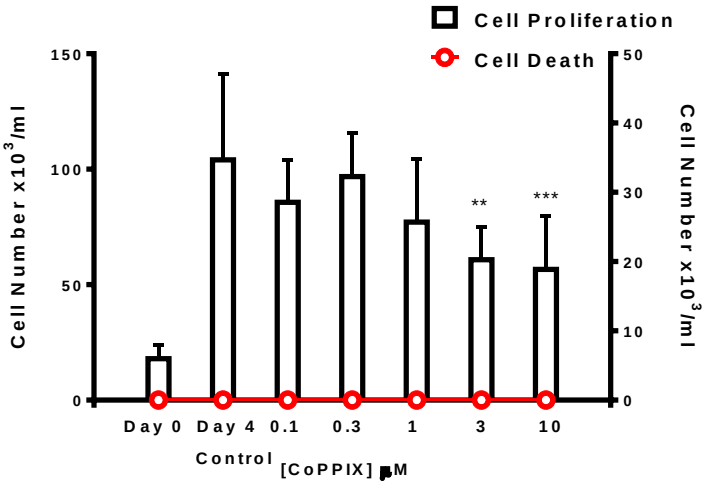

B

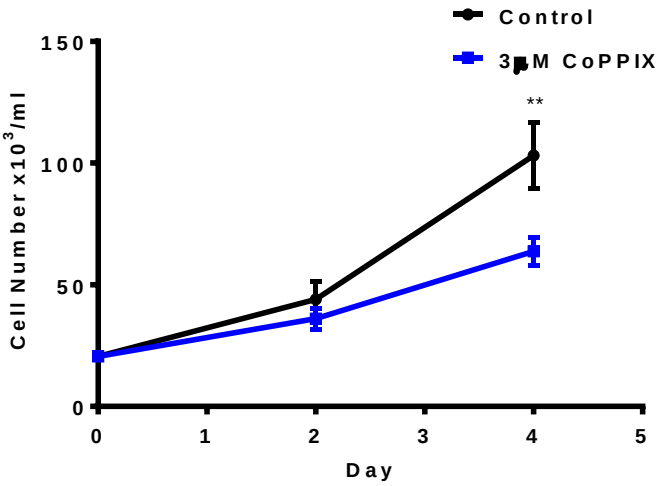

Figure 6.12 CoPPIX inhibits HSVSMC proliferation

Bar graph showing the proliferative response of HSVSMC (left y-axis) to increasing concentrations of CoPPIX. The overlaid red plot shows the corresponding non-viable cell count (right y-axis). Data were analysed by ratio repeated measures one-way ANOVA with Dunnett's multiple comparison test, ** $p<0.01$, *** $p<0.001$ vs Day 4 Control, n=4. Line graph of the effects of 3µM CoPPIX over time (B). Data were analysed by two-way repeated measures ANOVA with sample matching by time point. This was followed by Sidak's multiple comparison test between control and treated groups for each time point, ** $p<0.01$, n=3. Data are represented as mean ± s.e.m.

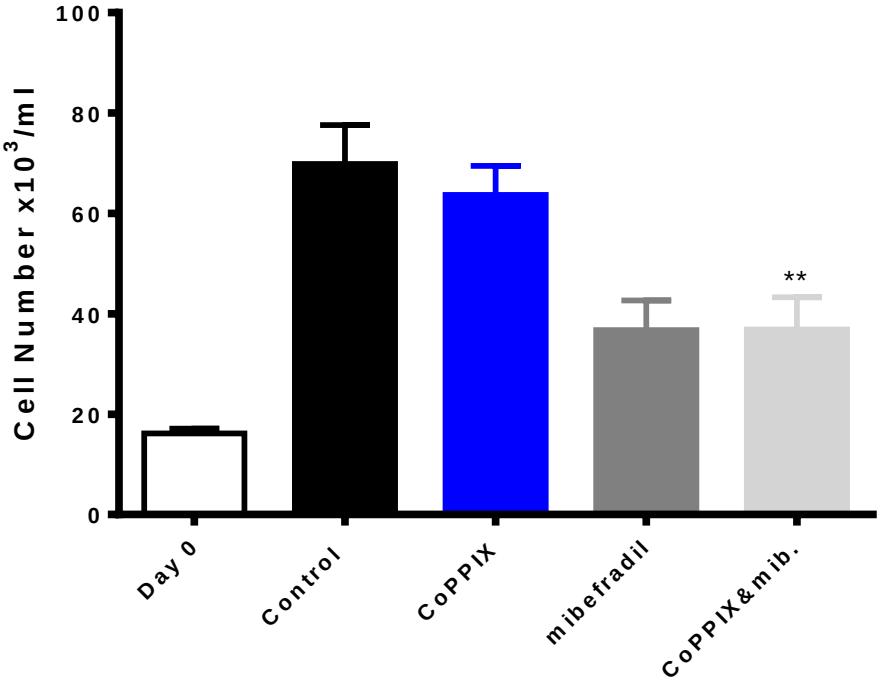

Figure 6.13 Co-application of CoPPIX and mibefradil inhibits HSVSMC proliferation

Bar graph showing the mean (±s.e.m.) day 4 counts of HSVSMC after treatment with 3µM CoPPIX, 3µM mibefradil, or simultaneous application of 3µM mibefradil and 3µM CoPPIX. Data were analysed by one-way ANOVA followed by Tukey's multiple comparison test, ** $p<0.01$ vs control. Control n=12, CoPPIX n=3, mibefradil n=4, CoPPIX and mibefradil n=5.

A

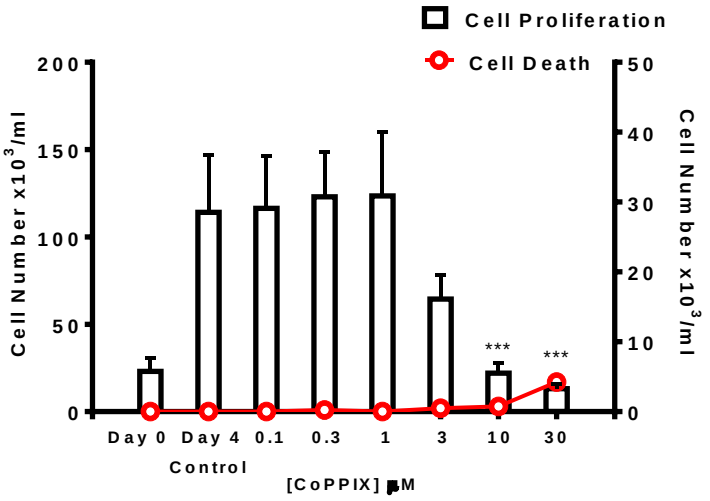

B

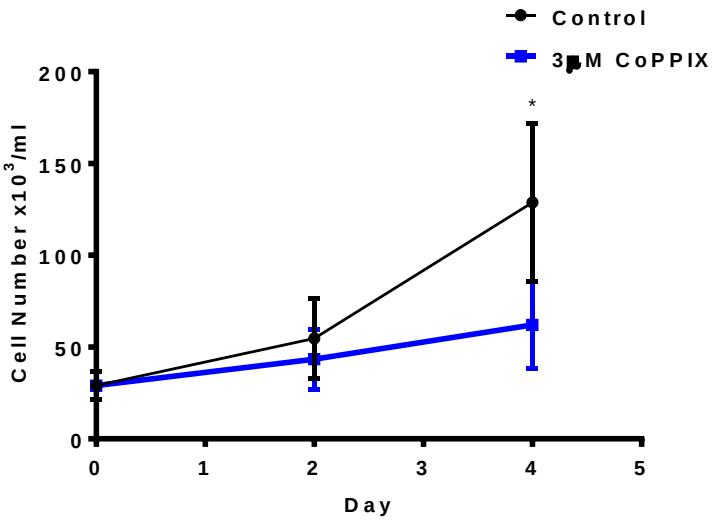

Figure 6.14 CoPPIX inhibits HCASMC proliferation

Bar graph showing the proliferative response of HCASMCs (left y-axis) to increasing concentrations of CoPPIX (A). The overlaid red plot shows the corresponding non-viable cell count (right y-axis). Data were analysed by ratio repeated measures one-way ANOVA with Dunnett's multiple comparison test, *** $p<0.001$ vs Day 4 Control, n=4. Line graph showing the effects of 3µM CoPPIX over a 4 day time-course (B). Data were analysed by two-way repeated measures ANOVA with sample matching by time point. This was followed by Sidak's multiple comparison test between control and treated groups for each time point, * $p<0.05$, n=4. Data are represented as mean ± s.e.m.

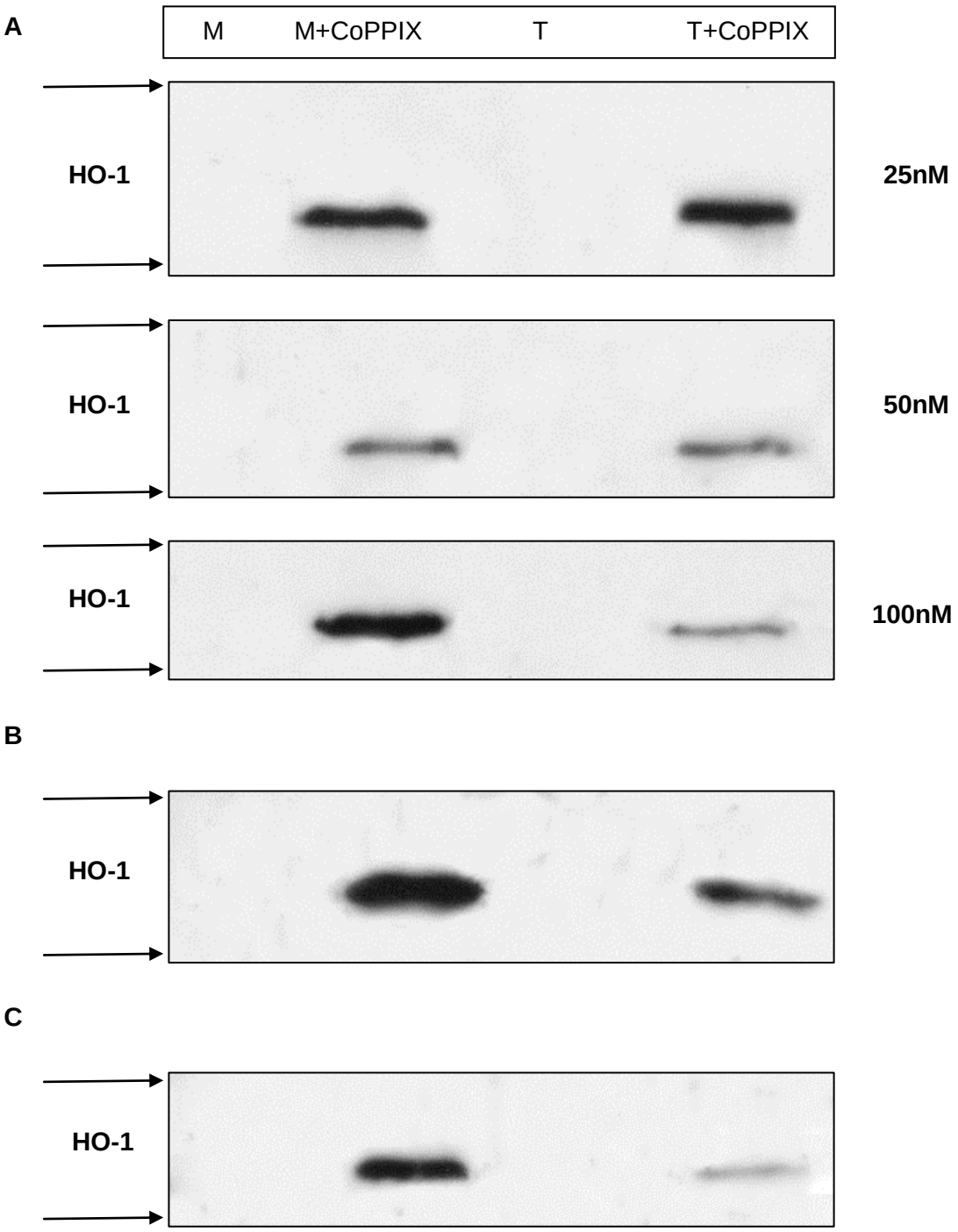

Figure 6.15 Optimisation of HO-1-targeting siRNA in HSVSMCs

Western blots of HO-1 expression after transfection with 25nM, 50nM, and 100nM HO-1-targeting siRNA (A); 3μM CoPPIX was added to the cells upon removal of the transfection solution. Panels (B) and (C) show western blots of HO-1 expression after transfection with 100nM HO-1-targeting siRNA; 3μM CoPPIX was added to the cells the day following transfection (B), or added to the cells upon removal of the transfection solution (C). The arrows represent the position of the molecular weight markers (top, 37KDa; bottom, 25kDa). M=Mock, T=Transfected.

show HO-1 induction in response to 3µM CoPPIX applied the day following transfection, or applied immediately post-transfection respectively, proceeding transfection with 100nM. These western blots show that the window of adequate HO-1 knock-down begins immediately post-transfection, therefore CoPPIX was applied at this time-point in subsequent experiments. Proliferation was assessed by a 4 day time-course immediately following transfection with 100nM HO-1-targeting siRNA; day 0 counts were taken at this time-point. The western blots in Figure 6.16 (A) demonstrate that the HO-1 mRNA was sufficiently knocked-down for the 4 day period, as CoPPIX did not induce protein expression in the transfected cell group. Figure 6.16 (B) shows the proliferative response of the mock and transfected groups, with or without the addition of 3µM CoPPIX. CoPPIX inhibited the cell proliferation of the mock cells by 22% on day 4, with no effect on the transfected cells. This also demonstrates that the HO-1 mRNA was sufficiently knocked-down. However, the presence of the HO-1-targeting siRNA negatively affected the proliferative response of the HSVSMCs. Unexpectedly, cell proliferation was reduced by 57% in the presence of HO-1-targeting siRNA.

In summary, 3µM CoPPIX limits proliferation of HSVSMC and HCASMC to similar extents. The anti-proliferative effect of CoPPIX and mibefradil simultaneously does not appear to be additive. 100nM HO-1-targetting siRNA prevents HO-1 induction by CoPPIX, yet the presence of the siRNA negatively regulated cell proliferation.

6.3 Discussion

Smooth muscle α-actin is the most abundant protein in smooth muscle cells, and smooth muscle myosin heavy chain is the most distinguishing marker of smooth muscle cells (Owens *et al.*, 2004). Despite the abundance of smooth muscle α-actin, this protein was not demonstrated clearly in all cells in Figure 6.1 (A) and (E). The synthesis of smooth muscle α-actin has been shown to decrease in the presence of serum stimulation in parallel with cell proliferation, as demonstrated by thymidine incorporation (Owens *et al.*, 1986). Indeed, smooth muscle α-actin was shown to decrease during culture conditions and remain at low levels during cell proliferation (Campbell *et al.*, 1989). As HSVSMCs were plated at sparse densities for immunocytochemistry, the expression of smooth muscle α-actin may therefore have

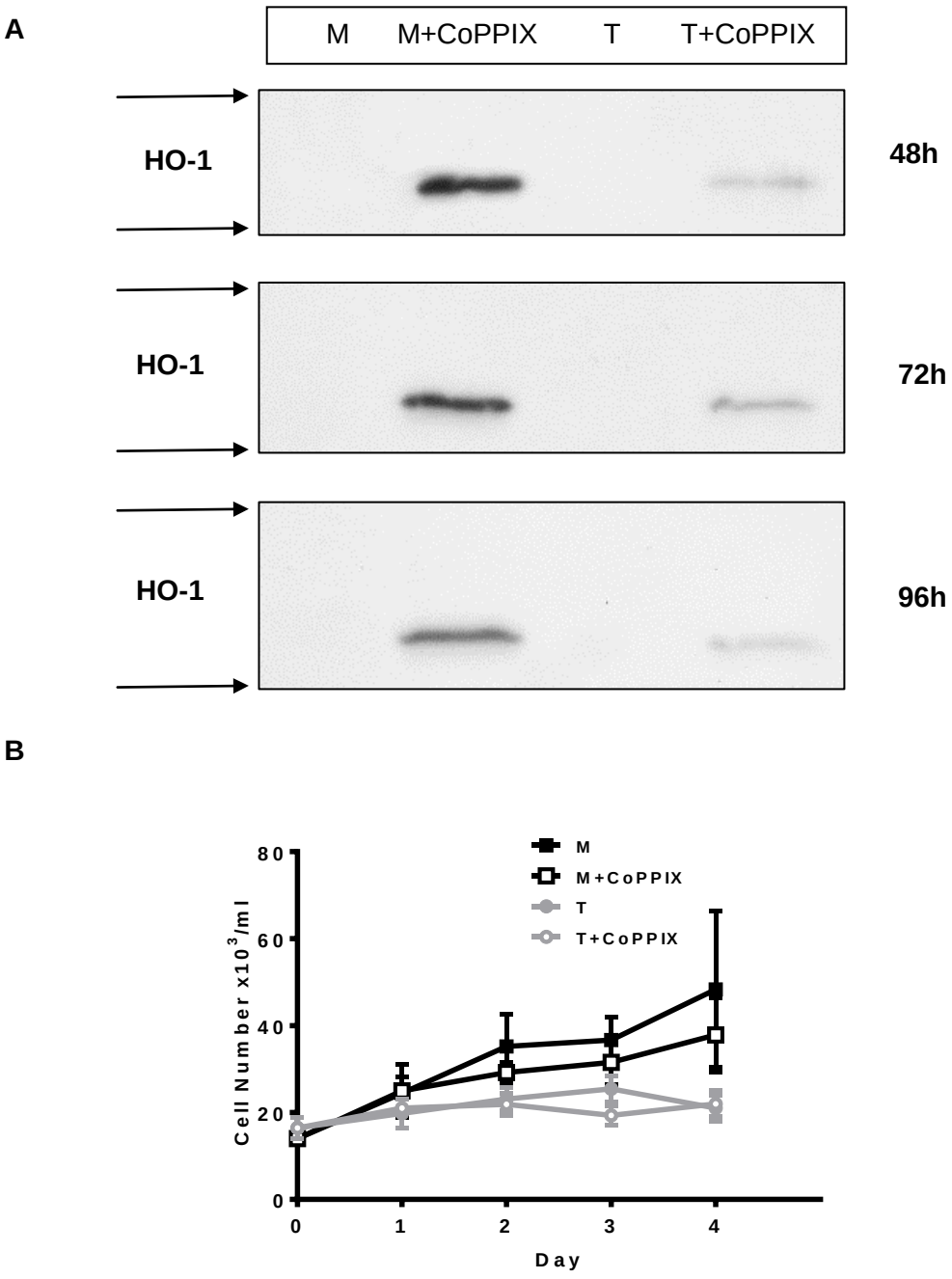

Figure 6.16 The effect of 100nM HO-1-targeting siRNA in HSVSMCs

Western blots of HO-1 expression after transfection with 100nM HO-1-targeting siRNA at 48h, 72h, and 96h (A); 3µM CoPPIX was added to the cells immediately upon removal of the transfection solution. The arrows represent the position of the molecular weight markers (top, 37KDa; bottom, 25kDa). Line graph showing the proliferative response over 4 days of Mock and Transfected cells, ± 3µM CoPPIX treatment, after transfection with 100nM HO-1-targeting siRNA (B), n=3, data are represented as mean ± s.e.m. M=Mock, T=Transfected.

been limited during these conditions. This is in line with a more recent study which demonstrated that the expression of contractile proteins; (smooth muscle α-actin and smooth muscle myosin heavy chain), was lower in synthetic VSMCs than in contractile VSMCs (Worth *et al.*, 2001). Furthermore, the cytoskeletal protein, vimentin, was expressed at higher levels in synthetic cells, indicating that expression of this intermediate filament is increased upon phenotypic modulation of VSMCs (Kocher *et al.*, 1985;Worth *et al.*, 2001). In canine airway smooth muscle cells, vimentin expression increased in proliferating cells, and decreased as cells reached confluence, implying vimentin could be a marker of smooth muscle cell dedifferentiation (Halayko *et al.*, 1996). Limited co-localisation of smooth muscle α-actin and smooth muscle myosin heavy chain has been demonstrated in synthetic cells (Worth *et al.*, 2001), which coincides with the limited co-localisation illustrated in Figure 6.1 (D). The HSVSMCs examined in the present study were synthetic VSMCs, and the arrangement of cytoskeletal and contractile proteins shown in Figure 6.1 reflected this cell phenotype. The images of the cells in Figure 6.1 represent HSVSMC at P5, implying that the maintenance of these cells in culture for 5 weeks sustains a proliferative phenotype, which was also ensured by preventing the cells from reaching confluence (Campbell *et al.*, 1989).

The expression levels of $Ca_v3.1$ and $Ca_v3.2$ in HSVSMCs, as shown in Figures 6.3 and 6.4, are much higher than the expression levels in A7r5 cells (Chapter 4, Figures 4.3 and 4.4), yet there was no correlation with passage number in either cell type. Despite these higher levels of expression, identification of $Ca_v3.1$ by membrane enrichment remained challenging, and $Ca_v3.2$ could not be detected. Immunoprecipitation of the T-type Ca^{2+} channels was attempted on two occasions without success. $Ca_v3.1$ is expressed at higher levels than $Ca_v3.2$ in both cell types, which is also suggested by immunocytochemistry in Figure 6.2. Indeed, the $Ca_v3.1$, but not the $Ca_v3.2$ T-type Ca^{2+} channel has been shown to be a requirement for murine VSMC proliferation (Tzeng *et al.*, 2012). The localisation of $Ca_v3.1$ positive staining at peri-nuclear regions, as shown in Figure 6.2, could be indicative of increased $Ca_v3.1$ protein synthesis and trafficking in response to the synthetic phenotype of the HSVSMCs. The Golgi network and the rough endoplasmic reticulum have been described as prominent features of injured VSMCs, and are likely to play a role in the regenerative response of VSMCs (Poole *et al.*, 1971;Chamley-Campbell *et al.*, 1979). The β1b auxiliary subunit has been shown to increase functional $Ca_v3.1$ T-type Ca^{2+} channel expression, and a possible role as a

chaperone was suggested (Dolphin *et al.*, 1999). This study also demonstrated that the α2-δ auxiliary subunit influenced the expression of the $Ca_v3.1$ T-type Ca^{2+} channel at the cell membrane, in addition to the amplitude of the current. Yet, recombinant $Ca_v3.1$ T-type Ca^{2+} channels exhibit similar currents to those of native channels, therefore α1 subunits do not require accessory subunits to function adequately (Perez-Reyes, 2006). To validate the idea that the $Ca_v3.1$ T-type Ca^{2+} channel becomes localised within the Golgi network during proliferative phases, a fluorescent probe targeted against the Golgi, such as CellLight® Golgi marker (Molecular Probes), could be employed simultaneously with a $Ca_v3.1$ targeted probe to assess co-localisation.

HCASMCs consistently proliferated to a greater extent than HSVSMCs in all proliferation assays. Contrastingly, HCASMC proliferation was inhibited to a lesser extent by CORM-3 than HSVSMC proliferation, as shown in Figure 6.8 and 6.9 (A). Based on the proliferative responses one could speculate that HCASMCs have a higher expression level of T-type Ca^{2+} channels than HSVSMCs, yet this contradicts the hypothesis that CO inhibits cell proliferation via T-type Ca^{2+} channels. If time had permitted, elucidation of the T-type Ca^{2+} channel expression levels via immunocytochemistry and RT-PCR could have explained these disparate proliferative profiles. Venous VSMCs have been shown to proliferate more than paired arterial VSMCs (Turner *et al.*, 2007), however the arterial and venous VSMCs employed in the present study were not paired, and different cell requirements necessitated different growth media, which negates any physiological conclusions drawn from direct comparisons. The fact that HSVSMCs have a higher expression level of the T-type Ca^{2+} channel subtypes than A7r5 cells may explain the differing responses of the cell types to CORM-3. Figure 5.4 in Chapter 5 demonstrates the minimal inhibition of proliferation of A7r5 cells in response to CORM-3, in contrast to the significant inhibition of HSVSMC proliferation shown in Figure 6.8.

The proliferative responses of HSVSMCs and HCASMCs to the T-type inhibitor mibefradil were similar when the drug was applied at 3μM. The corresponding non-viable cell counts, as demonstrated by the red plots in Figures 6.6 and 6.7, corroborate the effects seen on A7r5 cells (Chapter 4); that mibefradil is cytotoxic at high concentrations. However, there was an apparent difference in the extent of the anti-proliferative effects produced in response to 3μM mibefradil in HCASMCs in Figure 6.7

(A) and (B). The cells utilised in the concentration-response assay ranged from P2 to P6, whereas the cells utilised in the time-course assay ranged from P3 to P6, therefore the cell ages were similar. The control cell group for the time-course assay proliferated to a greater extent than the control group for the concentration-response assay, which may explain why 3µM mibefradil limited cell growth to a greater extent in the concentration-response assay.

There is a larger standard error associated with day 4 counts of HCASMCs than with HSVSMCs, as the proliferative response of the former cell type diminished with subsequent cell passage, and was particularly apparent at P5 and P6. Higher passage numbers were utilised for the time-course assays assessing the effects of CORM-3 and CoPPIX. This suggests the development of replicative senescence. Senescent cell cultures can be described as those exhibiting a decline in cell proliferation after a phase of exponential proliferation (Matsumura *et al.*, 1979), although the cell cultures detailed in this study were examined over much longer periods of 60 weeks, compared to the 6 week period over which HCASMCs were assessed in the present study. Increased cell doubling time and lower population densities have been attributed to an ageing process of sub-cultured VSMCs (Chamley-Campbell *et al.*, 1979). The number of senescent human VSMCs was shown to be directly related to the age of the donor (Ruiz-Torres *et al.*, 1999), although studies in different species are less consistent. Replication efficiency of rat aortic VSMCs is higher in cells isolated from aged animals than from young animals (McCaffrey *et al.*, 1988;Li *et al.*, 1997), whereas the data regarding mouse aortic VSMCs is conflicting (Moon *et al.*, 2001;Moon *et al.*, 2003). It is possible that the phenotype of the HCASMCs was modified with each subsequent passage, producing an increasing number of senescent cells. An assessment of T-type Ca^{2+} channel expression at each passage would have been advantageous to assess whether the expression of the channels declined over the 6 week period.

HO-1 induction in HSVSMCs was demonstrated by immunocytochemistry following a 24h incubation with CoPPIX, and the associated western blots show that HO-1 protein expression is maintained at 48h and 96h. CoPPIX did not inhibit proliferation in a concentration-dependent manner in both HSVSMCs and HCASMCs, suggesting that low concentrations of CoPPIX do not reach the threshold required to induce HO-1 protein expression. This is verified by the lack of HO-1 protein bands in response to 0.1µM and 0.3µM CoPPIX in Figure 6.11. As noted previously, there was a large

variation in day 4 HCASMC counts due to the use of older passages. The inhibitory effects of CoPPIX on HSVSMCs and HCASMCs proliferation begin to appear at day 2, whereas the inhibitory effects on A7r5 cells appear at day 3. This could be due to the fact that A7r5 cells have lower expression levels of T-type Ca^{2+} channels than HSVSMCs. Co-application of mibefradil and CoPPIX did not cause additive effects on proliferation. Moreover, the extent of proliferation inhibition by simultaneous application of the compounds equalled that of mibefradil treatment, implying there was competition for the same cellular target. However, the extent of inhibition by CoPPIX in Figure 6.13 was much lower than that shown in Figure 6.12, which is due to the combination of control data from 12 assays. These HSVSMC were sourced from 12 different patients therefore, inherent differences will have undoubtably contributed to the extent of which the cells proliferated, and possibly how they responded to the HO-1 inducer, CoPPIX.

In contrast to the effects of CORM-3, CoPPIX inhibited HCASMC proliferation to a greater extent than HSVSMC proliferation. The fact that the HSVSMCs utilised in the present study were isolated from patients undergoing coronary artery bypass graft (CABG) surgery is noteworthy. To necessitate the need for CABG surgery, these patients will no doubt have coronary artery disease (CAD), and therefore the corresponding HSVSMCs may have inherent modifications as a result. In contrast, the HCASMCs were derived from normal, plaque free coronary arteries. The saphenous vein is subject to lower blood pressure and less shear stress than an artery (Turner *et al.*, 2007), yet the risk factors of CAD, such as hypercholesterolemia, diabetes mellitus, and cigarette smoke, will likely be detrimental to all vessels (Vogel, 1997). Furthermore, such risk factors have been linked with a long microsatellite polymorphism $(GT)_n$ in the HO-1 promoter, and with the development of CAD (Kaneda *et al.*, 2002). Another study also found that longer $(GT)_n$ repeats were associated with CAD susceptibility in patients with diabetes mellitus (Chen *et al.*, 2002). Although neither study found a significant correlation between the long length polymorphism and CAD without such risk factors, there was a trend towards this relationship. The longer $(GT)_n$ genotype has been shown to limit HO-1 expression, which suggests that patients with risk factors for CAD have a reduced capacity for HO-1 induction and vessel protection in response to stresses such as ROS and oxLDL (Chen *et al.*, 2002;Kaneda *et al.*, 2002). These findings can be extended to the data shown here; proliferation was inhibited to a greater extent in HCASMCs than in HSVSMCs, which could be a result of differing extents of HO-1 induction. If time had permitted, western blots of HO-1 induction in HCASMCs could have clarified this hypothesis.

Preliminary assessment of the effect of HO-1-targeting siRNA indicated that 100nM was the optimal concentration, and the adequate window of HO-1 knock-down began immediately post-transfection. The finding that HO-1 knock-down negatively regulated cell proliferation was unexpected, although the fact that CoPPIX had no further inhibitory effect on the transfected cells implies that the siRNA effectively targeted HO-1 mRNA. Therefore, the inhibitory effects of HO-1 knock-down are difficult to explain. The mock cells proliferated 3.5 fold over the course of the assay, yet the growth of the control cells in all proliferation assays involving HSVSMCs ranged from 3.3 to 5.8 fold. This range can be explained by the fact that cells were sourced from numerous different patients and consequently will contain inherent differences. It can be assumed, therefore, that the transfection procedure itself was not the cause of the diminished proliferative response of the transfected cells. HO-1 has markedly different effects on proliferation depending on the cell type. In contrast to the anti-proliferative effects of HO-1 in VSMCs and fibroblasts, HO-1 is pro-proliferative in keratinocytes, endothelial cells, pancreatic cancer cells, lung cancer cells, hepatoma, sarcoma, and melanoma (Jozkowicz *et al.*, 2007). In numerous cancers HO-1 is induced or constitutively expressed, which confers resistance to apoptosis (Jozkowicz *et al.*, 2007). Indeed, our research group has demonstrated that HO-1-derived CO confers resistance to apoptosis in medulloblastoma DAOY cells (Al-Owais *et al.*, 2012). As reported by Jozkowicz *et al.* (2007), the effects of HO-1 on proliferation are conflicting, and the involvement of numerous mediators confers complex cellular responses. Despite the fact that HO-1 has been shown to have definitive anti-proliferative effects in VSMCs (Kim *et al.*, 2011b), it is possible that in addition to HO-1 mRNA knock-down, the siRNA caused off-target effects which subsequently affected proliferation.

The use of human VSMCs in the present study has added a clinically relevant aspect to the project as a whole, which has progressed from the use of a recombinant expression system, to a vascular cell line, to primary cells. The anti-proliferative effects of HO-1 and CO are conserved in human VSMCs, and the role of the T-type Ca^{2+} channel in proliferation has been indicated by the use of mibefradil. The previously documented non-specific effects associated with mibefradil are a limiting factor of these experiments. A novel, selective T-type Ca^{2+} channel inhibitor, ML218, has demonstrated inhibition of T-type Ca^{2+} current in subthalamic neurons (Xiang *et al.*, 2011). Additional experiments assessing ML218 as a pharmacological tool would be useful. Stronger conclusions could be drawn about the effects of CO on T-type Ca^{2+} channels in human VSMCs if microfluorimetry data was available. However, such data

proved difficult to acquire, as stable baseline recordings of $[Ca^{2+}]_i$ could not be obtained. To test further the hypothesis of T-type Ca^{2+} channel inhibition by CO, electrophysiological recordings via whole-cell patch clamp would generate more specific data about T-type Ca^{2+} channel currents, as these currents could be isolated and pharmacological modulation assessed. However, this is technically demanding given the small currents shown in previous reports, as reviewed by (Kuo *et al.*, 2011).

CHAPTER 7

Conclusions

7.1 Principle Findings

HEK293/Ca_v3.2 cells

- Over-expression of the Ca_v3.2 T-type Ca^{2+} channel produced higher basal $[Ca^{2+}]_i$ which was reduced by T-type Ca^{2+} channel inhibition, CO exposure, and HO-1 induction
- The Ca_v3.2 T-type Ca^{2+} channel augments proliferation
- Augmented proliferation is decreased by T-type Ca^{2+} channel inhibition, therefore T-type Ca^{2+} channels are central to the proliferative response
- CO is anti-proliferative and potentially acts via the T-type Ca^{2+} channel

A7r5 cells

- Ca_v3.1 T-type Ca^{2+} channels are the more prominent subtype in A7r5 cells
- Both L-type and T-type Ca^{2+} channels are expressed in A7r5 cells, and L-type Ca^{2+} channels appear to have a more prominent role in Ca^{2+} oscillations
- L-type Ca^{2+} channels do not have a role in cell proliferation
- Ca_v3.1 T-type Ca^{2+} channels do have a role in cell proliferation, as evidenced by the effects of Ni^{2+}
- CORM-3, but not iCORM-3, reduced $[Ca^{2+}]_i$ and Ca^{2+} oscillation frequency in A7r5 cells upon modest depolarisation
- CORM-3 did not affect Ca^{2+} influx when A7r5 cells were strongly depolarised
- CORM-3 had minimal anti-proliferative effects in isolation, but was anti-proliferative when L-type Ca^{2+} channels were blocked
- HO-1 induction and over-expression inhibited A7r5 cell proliferation and there was a trend towards reduced $[Ca^{2+}]_i$

Human VSMCs

- T-type Ca^{2+} channels are expressed at higher levels in HSVSMCs than A7r5 cells
- $Ca_v3.1$ T-type Ca^{2+} channels are the more prominent subtype in HSVSMCs
- T-type Ca^{2+} channel inhibition, CO exposure and HO-1 induction have anti-proliferative effects in human VSMCs
- Simultaneous HO-1 induction and T-type Ca^{2+} channel inhibition do not cause additive inhibitory effects on proliferation
- HO-1 induction and CO exposure had a greater inhibitory capacity in conjunction with a higher expression level of the $Ca_v3.1$ T-type Ca^{2+} channel in HSVSMC than A7r5 cells

7.2 Summary and clinical relevance

As the level of T-type Ca^{2+} channel expression has been shown to increase in synthetic VSMCs (House *et al.*, 2008), along with the concurrent induction of HO-1 activity (Kim *et al.*, 2011b), and the fact that our research group has recently demonstrated that CO is able to inhibit the T-type Ca^{2+} current, the possibility that the T-type Ca^{2+} channel is a therapeutic target for HO-1 was investigated. My data indicate that CO can inhibit the T-type Ca^{2+} channel. The physiological effects of this inhibition present as a decrease in cell proliferation and a reduction in $[Ca^{2+}]_i$. This conclusion is strengthened by the fact that both CO exposure and HO-1 induction conferred a greater anti-proliferative effect in cells with higher expression levels of the T-type Ca^{2+} channels. CO appears to affect both the $Ca_v3.1$ and $Ca_v3.2$ T-type Ca^{2+} channels, as shown by the effects on HEK293/$Ca_v3.2$ cells and HSVSMCs. The T-type Ca^{2+} channel is an important mediator of VSMC proliferation (Cribbs, 2006), yet the commonly used pharmacological antagonist of this channel, mibefradil, has limited specificity and associated side effects *in vivo* (Nilius et al., 1997;Mullins et al., 1998;Eller et al., 2000;Strege et al., 2005). The inhibitory effect of CO on the T-type Ca^{2+} current is a novel finding by our research group, and as CO is an endogenous signalling molecule, the associated anti-proliferative effects could be exploited as a therapy for cardiovascular disorders involving excessive VSMC proliferation. By directly enhancing CO availability at the site of vascular injury, or by increasing HO-1 expression and activity in VSMCs, pathological proliferation could be reduced, thereby limiting the ensuing complications associated with a compromised vessel. The idea of gaseous CO as a therapy is not unreasonable, considering the fact that nitric oxide gas is currently

used as a treatment for pulmonary hypertension (Bloch *et al.*, 2007). However, there is a narrow margin between the cytoprotective and detrimental effects of gaseous CO exposure, and targeting the gas to the desired endogenous tissues could pose difficulties. Adequate monitoring of blood COHb levels would also be necessary (Motterlini & Otterbein, 2010). The advent of CORMs suggests that CO delivery could be specifically directed to the site of injury, for instance, by the use of a CORM-coated stent to limit restenosis (Motterlini & Otterbein, 2010). This notion is particularly appealing given that CO has the ability to limit VSMC proliferation and concurrently promote endothelial cell proliferation (Wu & Wang, 2005). Experimentation of such a specifically targeted drug-eluting stent was recently discussed by Curcio *et al.* (2011), whereby delivery of the phosphatidylinositide-3-kinase, p85, limited VSMC proliferation without effecting endothelial cells. Regarding the potential therapeutic use of gaseous CO, a CO delivery system has recently been developed; the Covox DS (Ikaria), and both gaseous CO and CORMs are currently being assessed for safety and efficacy in Phase III clinical trials. (Motterlini & Otterbein, 2010). The suggestion that CO can limit VSMC proliferation by inhibiting T-type Ca^{2+} channel activity is an important finding and certainly offers potential for further investigation. However, an understanding of the exact mechanism of inhibition is required in order to support the development of a therapy tailored to this endogenous pathway.

7.3 Further Work

Investigating native T-type Ca^{2+} channel activity poses numerous challenges. Identification of the T-type Ca^{2+} channel by western blotting and RT-PCR has proved difficult, due to the relatively low level of expression in VSMCs, in combination with the fact that expression levels can vary in proliferative cells. The use of microfluorimetry recordings added scope to the data generated from proliferation assays, yet the elucidation of the specific T-type Ca^{2+} channel response using this methodology on cells expressing both voltage-gated T- and L-type Ca^{2+} channels was dependent on the use of pharmacological agents. Therefore, whole-cell patch clamp electrophysiological recordings would provide further information about distinct T-type Ca^{2+} channel activity, and the extent of T-type Ca^{2+} current inhibition by both antagonists and CO. The inclusion of electrophysiology data demonstrating the inhibitory effects of CO on the T-type Ca^{2+} current would allow a more definitive conclusion to be drawn. The availability of a novel, more specific, T-type Ca^{2+} channel blocker, ML218, will aid the verification of T-type Ca^{2+} channel effects in subsequent investigations (Xiang *et al.*, 2011).

The limited data shown here regarding the potential involvement of redox modulation on T-type Ca^{2+} channel activity warrants further investigation. Oxidative stress is a feature of many cardiovascular disorders (Paravicini & Touyz, 2006;Kim *et al.*, 2011b;Chung *et al.*, 2013); therefore, exploration of the various sources of ROS and their subsequent effects on T-type Ca^{2+} channel activity and CO-mediated inhibition may help elucidate the exact mechanism of modulation. Endogenous ROS are produced from numerous sources including NADPH oxidase, xanthine oxidase, uncoupled NOS, and the mitochondria (Mueller *et al.*, 2005), and CO has been shown to modulate NADPH oxidase (Taille *et al.*, 2005) and cytochrome c oxidase (Zuckerbraun *et al.*, 2007). Therefore, the use of anti-oxidants such as MitoQ, and inhibitors of potential sources of ROS such as allopurinol, apocynin, and antimycin A, as previously examined by our research group with respect to L-type Ca^{2+} channel inhibition by CO (Scragg *et al.*, 2008), are pertinent pathways to explore. This may be aided by T-type Ca^{2+} channel mutagenesis in order to specifically isolate potential redox sites within the channel protein. The thioredoxin and glutaredoxin systems serve to maintain cellular redox balance (Yamawaki *et al.*, 2003), and transient receptor potential channels have been shown to be modulated by thioredoxin (Beech & Sukumar, 2007), therefore these systems may be another potential direction of investigation.

To extend the clinical relevance of this project, *in vivo* experiments assessing CO-mediated modulation of the T-type Ca^{2+} channel would be appropriate. The effects of CO on neointima formation could be assessed in T-type knock-out mice. It would be advantageous to examine the effects of CO on both $Ca_v3.1^{-/-}$ and $Ca_v3.2^{-/-}$ mice, as one group found that the $Ca_v3.1$ T-type Ca^{2+} channel is required for intimal hyperplasia (Tzeng *et al.*, 2012), yet the $Ca_v3.2$ subtype is documented as the prominent subtype in the cardiovascular system (Catterall *et al.*, 2005;Cribbs, 2006).

Reference List

Abraham NG & Kappas A (2008). Pharmacological and clinical aspects of heme oxygenase. *Pharmacol Rev* **60**, 79-127.

Akaike N, Kanaide H, Kuga T, Nakamura M, Sadoshima J, & Tomoike H (1989). Low-voltage-activated calcium current in rat aorta smooth muscle cells in primary culture. *J Physiol* **416**, 141-160.

Al-Owais MM, Scragg JL, Dallas ML, Boycott HE, Warburton P, Chakrabarty A, Boyle JP, & Peers C (2012). Carbon Monoxide Mediates the Anti-apoptotic Effects of Heme Oxygenase-1 in Medulloblastoma DAOY Cells via K+ Channel Inhibition. *J Biol Chem* **287**, 24754-24764.

Alam J, Camhi S, & Choi AM (1995). Identification of a second region upstream of the mouse heme oxygenase-1 gene that functions as a basal level and inducer-dependent transcription enhancer. *J Biol Chem* **270**, 11977-11984.

Albert AP & Large WA (2003). Store-operated Ca2+-permeable non-selective cation channels in smooth muscle cells. *Cell Calcium* **33**, 345-356.

Aley PK, Wilkinson JA, Bauer CC, Boyle JP, Porter KE, & Peers C (2008). Hypoxic remodelling of Ca(2+) signalling in proliferating human arterial smooth muscle. *Mol Cell Biochem* **318**, 101-108.

Atkin AJ, Lynam JM, Moulton BE, Sawle P, Motterlini R, Boyle NM, Pryce MT, & Fairlamb IJ (2011). Modification of the deoxy-myoglobin/carbonmonoxy-myoglobin UV-vis assay for reliable determination of CO-release rates from organometallic carbonyl complexes. *Dalton Trans* **40**, 5755-5761.

Atochin DN & Huang PL (2010). Endothelial nitric oxide synthase transgenic models of endothelial dysfunction. *Pflugers Arch* **460**, 965-974.

Ball CJ, Wilson DP, Turner SP, Saint DA, & Beltrame JF (2009). Heterogeneity of L- and T-channels in the vasculature: rationale for the efficacy of combined L- and T-blockade. *Hypertension* **53**, 654-660.

Bathoorn E, Slebos DJ, Postma DS, Koeter GH, van Oosterhout AJ, van der Toorn M, Boezen HM, & Kerstjens HA (2007). Anti-inflammatory effects of inhaled carbon monoxide in patients with COPD: a pilot study. *Eur Respir J* **30**, 1131-1137.

Beech DJ & Sukumar P (2007). Channel regulation by extracellular redox protein. *Channels (Austin)* **1**, 400-403.

Belles B, Malecot CO, Hescheler J, & Trautwein W (1988). "Run-down" of the Ca current during long whole-cell recordings in guinea pig heart cells: role of phosphorylation and intracellular calcium. *Pflugers Arch* **411**, 353-360.

Bergdahl A, Gomez MF, Wihlborg AK, Erlinge D, Eyjolfson A, Xu SZ, Beech DJ, Dreja K, & Hellstrand P (2005). Plasticity of TRPC expression in arterial smooth muscle: correlation with store-operated Ca2+ entry. *Am J Physiol Cell Physiol* **288**, C872-C880.

Bertrand R, Solary E, O'Connor P, Kohn KW, & Pommier Y (1994). Induction of a common pathway of apoptosis by staurosporine. *Exp Cell Res* **211**, 314-321.

Bezprozvanny I & Tsien RW (1995). Voltage-dependent blockade of diverse types of voltage-gated Ca2+ channels expressed in Xenopus oocytes by the Ca2+ channel antagonist mibefradil (Ro 40-5967). *Mol Pharmacol* **48**, 540-549.

Bijlenga P, Liu JH, Espinos E, Haenggeli CA, Fischer-Lougheed J, Bader CR, & Bernheim L (2000). T-type alpha 1H Ca2+ channels are involved in Ca2+ signaling during terminal differentiation (fusion) of human myoblasts. *Proc Natl Acad Sci U S A* **97**, 7627-7632.

Bilban M, Haschemi A, Wegiel B, Chin BY, Wagner O, & Otterbein LE (2008). Heme oxygenase and carbon monoxide initiate homeostatic signaling. *J Mol Med* **86**, 267-279.

Blank RS & Owens GK (1990). Platelet-derived growth factor regulates actin isoform expression and growth state in cultured rat aortic smooth muscle cells. *J Cell Physiol* **142**, 635-642.

Blank RS, Thompson MM, & Owens GK (1988). Cell cycle versus density dependence of smooth muscle alpha actin expression in cultured rat aortic smooth muscle cells. *J Cell Biol* **107**, 299-306.

Blanks AM, Zhao ZH, Shmygol A, Bru-Mercier G, Astle S, & Thornton S (2007). Characterization of the molecular and electrophysiological properties of the T-type calcium channel in human myometrium. *J Physiol* **581**, 915-926.

Bloch KD, Ichinose F, Roberts JD, Jr., & Zapol WM (2007). Inhaled NO as a therapeutic agent. *Cardiovasc Res* **75**, 339-348.

Boczkowski J, Poderoso JJ, & Motterlini R (2006). CO-metal interaction: Vital signaling from a lethal gas. *Trends Biochem Sci* **31**, 614-621.

Braudeau C, Bouchet D, Tesson L, Iyer S, Remy S, Buelow R, Anegon I, & Chauveau C (2004). Induction of long-term cardiac allograft survival by heme oxygenase-1 gene transfer. *Gene Ther* **11**, 701-710.

Braunstein TH, Inoue R, Cribbs L, Oike M, Ito Y, Holstein-Rathlou NH, & Jensen LJ (2009). The role of L- and T-type calcium channels in local and remote calcium responses in rat mesenteric terminal arterioles. *J Vasc Res* **46**, 138-151.

Brueggemann LI, Martin BL, Barakat J, Byron KL, & Cribbs LL (2005). Low voltage-activated calcium channels in vascular smooth muscle: T-type channels and AVP-stimulated calcium spiking. *Am J Physiol Heart Circ Physiol* **288**, H923-H935.

Brune B & Ullrich V (1987). Inhibition of platelet aggregation by carbon monoxide is mediated by activation of guanylate cyclase. *Mol Pharmacol* **32**, 497-504.

Brunt KR, Fenrich KK, Kiani G, Tse MY, Pang SC, Ward CA, & Melo LG (2006). Protection of human vascular smooth muscle cells from H2O2-induced apoptosis through functional codependence between HO-1 and AKT. *Arterioscler Thromb Vasc Biol* **26**, 2027-2034.

Buhler FR (1997). Cardiovascular care with the new T-type calcium channel antagonist: possible role of attendant sympathetic nervous system inhibition. *J Hypertens Suppl* **15**, S3-S7.

Campbell JH, Kocher O, Skalli O, Gabbiani G, & Campbell GR (1989). Cytodifferentiation and expression of alpha-smooth muscle actin mRNA and protein during primary culture of aortic smooth muscle cells. Correlation with cell density and proliferative state. *Arteriosclerosis* **9**, 633-643.

Capiod T (2011). Cell proliferation, calcium influx and calcium channels. *Biochimie* **93**, 2075-2079.

Catterall WA (2000). Structure and regulation of voltage-gated Ca2+ channels. *Annu Rev Cell Dev Biol* **16**, 521-555.

Catterall WA, Perez-Reyes E, Snutch TP, & Striessnig J (2005). International Union of Pharmacology. XLVIII. Nomenclature and structure-function relationships of voltage-gated calcium channels. *Pharmacol Rev* **57**, 411-425.

Chamley-Campbell J, Campbell GR, & Ross R (1979). The smooth muscle cell in culture. *Physiol Rev* **59**, 1-61.

Chamley-Campbell JH, Campbell GR, & Ross R (1981). Phenotype-dependent response of cultured aortic smooth muscle to serum mitogens. *J Cell Biol* **89**, 379-383.

Chang T, Wu L, & Wang R (2008). Inhibition of vascular smooth muscle cell proliferation by chronic hemin treatment. *Am J Physiol Heart Circ Physiol* **295**, H999-H1007.

Chao TS, Byron KL, Lee KM, Villereal M, & Rosner MR (1992). Activation of MAP kinases by calcium-dependent and calcium-independent pathways. Stimulation by thapsigargin and epidermal growth factor. *J Biol Chem* **267**, 19876-19883.

Chemin J, Monteil A, Briquaire C, Richard S, Perez-Reyes E, Nargeot J, & Lory P (2000). Overexpression of T-type calcium channels in HEK-293 cells increases intracellular calcium without affecting cellular proliferation. *FEBS Lett* **478**, 166-172.

Chen CC, Lamping KG, Nuno DW, Barresi R, Prouty SJ, Lavoie JL, Cribbs LL, England SK, Sigmund CD, Weiss RM, Williamson RA, Hill JA, & Campbell KP (2003). Abnormal coronary function in mice deficient in alpha1H T-type Ca2+ channels. *Science* **302**, 1416-1418.

Chen YH, Lin SJ, Lin MW, Tsai HL, Kuo SS, Chen JW, Charng MJ, Wu TC, Chen LC, Ding YA, Pan WH, Jou YS, & Chau LY (2002). Microsatellite polymorphism in promoter of heme oxygenase-1 gene is associated with susceptibility to coronary artery disease in type 2 diabetic patients. *Hum Genet* **111**, 1-8.

Chiang CS, Huang CH, Chieng H, Chang YT, Chang D, Chen JJ, Chen YC, Chen YH, Shin HS, Campbell KP, & Chen CC (2009). The Ca(v)3.2 T-type Ca(2+) channel is required for pressure overload-induced cardiac hypertrophy in mice. *Circ Res* **104**, 522-530.

Choi HC, Lee KY, Lee DH, & Kang YJ (2009). Heme oxygenase-1 induced by aprotinin inhibits vascular smooth muscle cell proliferation through cell cycle arrest in hypertensive rats. *Korean J Physiol Pharmacol* **13**, 309-313.

Christ GJ, Moreno AP, Melman A, & Spray DC (1992). Gap junction-mediated intercellular diffusion of Ca2+ in cultured human corporal smooth muscle cells. *Am J Physiol* **263**, C373-C383.

Chung HS, Wang SB, Venkatraman V, Murray CI, & Van Eyk JE (2013). Cysteine oxidative posttranslational modifications: emerging regulation in the cardiovascular system. *Circ Res* **112**, 382-392.

Chyu KY, Dimayuga P, Zhu J, Nilsson J, Kaul S, Shah PK, & Cercek B (1999). Decreased neointimal thickening after arterial wall injury in inducible nitric oxide synthase knockout mice. *Circ Res* **85**, 1192-1198.

Ciapa B, Pesando D, Wilding M, & Whitaker M (1994). Cell-cycle calcium transients driven by cyclic changes in inositol trisphosphate levels. *Nature* **368**, 875-878.

Clark JE, Naughton P, Shurey S, Green CJ, Johnson TR, Mann BE, Foresti R, & Motterlini R (2003). Cardioprotective actions by a water-soluble carbon monoxide-releasing molecule. *Circ Res* **93**, e2-e8.

Clowes AW, Reidy MA, & Clowes MM (1983). Mechanisms of stenosis after arterial injury. *Lab Invest* **49**, 208-215.

Converso DP, Taille C, Carreras MC, Jaitovich A, Poderoso JJ, & Boczkowski J (2006). HO-1 is located in liver mitochondria and modulates mitochondrial heme content and metabolism. *FASEB J* **20**, 1236-1238.

Cribbs LL (2006). T-type Ca2+ channels in vascular smooth muscle: multiple functions. *Cell Calcium* **40**, 221-230.

Cribbs LL, Lee JH, Yang J, Satin J, Zhang Y, Daud A, Barclay J, Williamson MP, Fox M, Rees M, & Perez-Reyes E (1998). Cloning and characterization of alpha1H from human heart, a member of the T-type Ca2+ channel gene family. *Circ Res* **83**, 103-109.

Crunelli V, Toth TI, Cope DW, Blethyn K, & Hughes SW (2005). The 'window' T-type calcium current in brain dynamics of different behavioural states. *J Physiol* **562**, 121-129.

Curcio A, Torella D, & Indolfi C (2011). Mechanisms of smooth muscle cell proliferation and endothelial regeneration after vascular injury and stenting: approach to therapy. *Circ J* **75**, 1287-1296.

Dallas ML, Boyle JP, Milligan CJ, Sayer R, Kerrigan TL, McKinstry C, Lu P, Mankouri J, Harris M, Scragg JL, Pearson HA, & Peers C (2011). Carbon monoxide protects against oxidant-induced apoptosis via inhibition of Kv2.1. *FASEB J* **25**, 1519-1530.

del Toro R, Levitsky KL, Lopez-Barneo J, & Chiara MD (2003). Induction of T-type calcium channel gene expression by chronic hypoxia. *J Biol Chem* **278**, 22316-22324.

Deramaudt BM, Braunstein S, Remy P, & Abraham NG (1998). Gene transfer of human heme oxygenase into coronary endothelial cells potentially promotes angiogenesis. *J Cell Biochem* **68**, 121-127.

Dolmetsch RE, Lewis RS, Goodnow CC, & Healy JI (1997). Differential activation of transcription factors induced by Ca2+ response amplitude and duration. *Nature* **386**, 855-858.

Dolphin AC, Wyatt CN, Richards J, Beattie RE, Craig P, Lee JH, Cribbs LL, Volsen SG, & Perez-Reyes E (1999). The effect of alpha2-delta and other accessory subunits on expression and properties of the calcium channel alpha1G. *J Physiol* **519 Pt 1**, 35-45.

Duchen MR (1992). Fluorescence - Monitoring cell chemistry *in vivo*. In *Monitoring Neuronal Activity: A Practical Approach*, ed. Stamford JA, pp. 231-260. IRL Press, Oxford.

Duckers HJ, Boehm M, True AL, Yet SF, San H, Park JL, Clinton WR, Lee ME, Nabel GJ, & Nabel EG (2001). Heme oxygenase-1 protects against vascular constriction and proliferation. *Nat Med* **7**, 693-698.

Durante W (2002). Carbon monoxide and bile pigments: surprising mediators of vascular function. *Vasc Med* **7**, 195-202.

Durante W (2003). Heme oxygenase-1 in growth control and its clinical application to vascular disease. *J Cell Physiol* **195**, 373-382.

Durante W, Peyton KJ, & Schafer AI (1999). Platelet-derived growth factor stimulates heme oxygenase-1 gene expression and carbon monoxide production in vascular smooth muscle cells. *Arterioscler Thromb Vasc Biol* **19**, 2666-2672.

Eisenberg MJ & Konnyu KJ (2006). Review of randomized clinical trials of drug-eluting stents for the prevention of in-stent restenosis. *Am J Cardiol* **98**, 375-382.

Eller P, Berjukov S, Wanner S, Huber I, Hering S, Knaus HG, Toth G, Kimball SD, & Striessnig J (2000). High affinity interaction of mibefradil with voltage-gated calcium and sodium channels. *Br J Pharmacol* **130**, 669-677.

Feng MG, Li M, & Navar LG (2004). T-type calcium channels in the regulation of afferent and efferent arterioles in rats. *Am J Physiol Renal Physiol* **286**, F331-F337.

Fernandes AP & Holmgren A (2004). Glutaredoxins: glutathione-dependent redox enzymes with functions far beyond a simple thioredoxin backup system. *Antioxid Redox Signal* **6**, 63-74.

Ferns GA, Raines EW, Sprugel KH, Motani AS, Reidy MA, & Ross R (1991). Inhibition of neointimal smooth muscle accumulation after angioplasty by an antibody to PDGF. *Science* **253**, 1129-1132.

Firth AL, Remillard CV, & Yuan JX (2007). TRP channels in hypertension. *Biochim Biophys Acta* **1772**, 895-906.

Foresti R, Bani-Hani MG, & Motterlini R (2008). Use of carbon monoxide as a therapeutic agent: promises and challenges. *Intensive Care Med* **34**, 649-658.

Foresti R, Hammad J, Clark JE, Johnson TR, Mann BE, Friebe A, Green CJ, & Motterlini R (2004). Vasoactive properties of CORM-3, a novel water-soluble carbon monoxide-releasing molecule. *Br J Pharmacol* **142**, 453-460.

Freidja ML, Toutain B, Caillon A, Desquiret V, Lambert D, Loufrani L, Procaccio V, & Henrion D (2011). Heme oxygenase 1 is differentially involved in blood flow-dependent

arterial remodeling: role of inflammation, oxidative stress, and nitric oxide. *Hypertension* **58**, 225-231.

Gackiere F, Bidaux G, Lory P, Prevarskaya N, & Mariot P (2006). A role for voltage gated T-type calcium channels in mediating "capacitative" calcium entry? *Cell Calcium* **39**, 357-366.

Galis ZS, Muszynski M, Sukhova GK, Simon-Morrissey E, Unemori EN, Lark MW, Amento E, & Libby P (1994). Cytokine-stimulated human vascular smooth muscle cells synthesize a complement of enzymes required for extracellular matrix digestion. *Circ Res* **75**, 181-189.

GE Healthcare. Amersham ECL Western Blotting System. 2012.
Ref Type: Online Source

Gollasch M, Haase H, Ried C, Lindschau C, Morano I, Luft FC, & Haller H (1998). L-type calcium channel expression depends on the differentiated state of vascular smooth muscle cells. *FASEB J* **12**, 593-601.

Golovina VA (1999). Cell proliferation is associated with enhanced capacitative Ca(2+) entry in human arterial myocytes. *Am J Physiol* **277**, C343-C349.

Golovina VA, Platoshyn O, Bailey CL, Wang J, Limsuwan A, Sweeney M, Rubin LJ, & Yuan JX (2001). Upregulated TRP and enhanced capacitative Ca(2+) entry in human pulmonary artery myocytes during proliferation. *Am J Physiol Heart Circ Physiol* **280**, H746-H755.

Gomez MF, Stevenson AS, Bonev AD, Hill-Eubanks DC, & Nelson MT (2002). Opposing actions of inositol 1,4,5-trisphosphate and ryanodine receptors on nuclear factor of activated T-cells regulation in smooth muscle. *J Biol Chem* **277**, 37756-37764.

Gonzalez-Cobos JC & Trebak M (2010). TRPC channels in smooth muscle cells. *Front Biosci* **15**, 1023-1039.

Gossen M & Bujard H (1992). Tight control of gene expression in mammalian cells by tetracycline-responsive promoters. *Proc Natl Acad Sci U S A* **89**, 5547-5551.

Gozzelino R, Jeney V, & Soares MP (2010). Mechanisms of cell protection by heme oxygenase-1. *Annu Rev Pharmacol Toxicol* **50**, 323-354.

Gray LS, Perez-Reyes E, Gomora JC, Haverstick DM, Shattock M, McLatchie L, Harper J, Brooks G, Heady T, & Macdonald TL (2004). The role of voltage gated T-type Ca2+ channel isoforms in mediating "capacitative" Ca2+ entry in cancer cells. *Cell Calcium* **36**, 489-497.

Grynkiewicz G, Poenie M, & Tsien RY (1985). A new generation of Ca2+ indicators with greatly improved fluorescence properties. *J Biol Chem* **260**, 3440-3450.

Halayko AJ, Salari H, MA X, & Stephens NL (1996). Markers of airway smooth muscle cell phenotype. *Am J Physiol* **270**, L1040-L1051.

Hall J, Jones RD, Jones TH, Channer KS, & Peers C (2006). Selective inhibition of L-type Ca2+ channels in A7r5 cells by physiological levels of testosterone. *Endocrinology* **147**, 2675-2680.

Heo JH, Seo HN, Choe YJ, Kim S, Oh CR, Kim YD, Rhim H, Choo DJ, Kim J, & Lee JY (2008). T-type Ca2+ channel blockers suppress the growth of human cancer cells. *Bioorg Med Chem Lett* **18**, 3899-3901.

Higashi Y, Noma K, Yoshizumi M, & Kihara Y (2009). Endothelial function and oxidative stress in cardiovascular diseases. *Circ J* **73**, 411-418.

Hill-Eubanks DC, Gomez MF, Stevenson AS, & Nelson MT (2003). NFAT regulation in smooth muscle. *Trends Cardiovasc Med* **13**, 56-62.

Hille B (1992). Calcium Channels. In *Ionic Channels of Excitable Membranes* pp. 83-114. Sinauer Associates, Massachusetts.

Hollywood MA, Woolsey S, Walsh IK, Keane PF, McHale NG, & Thornbury KD (2003). T- and L-type Ca2+ currents in freshly dispersed smooth muscle cells from the human proximal urethra. *J Physiol* **550**, 753-764.

House SJ, Ginnan RG, Armstrong SE, & Singer HA (2007). Calcium/calmodulin-dependent protein kinase II-delta isoform regulation of vascular smooth muscle cell proliferation. *Am J Physiol Cell Physiol* **292**, C2276-C2287.

House SJ, Potier M, Bisaillon J, Singer HA, & Trebak M (2008). The non-excitable smooth muscle: calcium signaling and phenotypic switching during vascular disease. *Pflugers Arch* **456**, 769-785.

House SJ & Singer HA (2008). CaMKII-delta isoform regulation of neointima formation after vascular injury. *Arterioscler Thromb Vasc Biol* **28**, 441-447.

Huang HM, Liang YC, Cheng TH, Chen CH, & Juan SH (2005). Potential mechanism of blood vessel protection by resveratrol, a component of red wine. *Ann N Y Acad Sci* **1042**, 349-356.

Huang L, Keyser BM, Tagmose TM, Hansen JB, Taylor JT, Zhuang H, Zhang M, Ragsdale DS, & Li M (2004). NNC 55-0396 [(1S,2S)-2-(2-(N-[(3-benzimidazol-2-

yl)propyl]-N-methylamino)ethyl)-6-fluoro-1,2, 3,4-tetrahydro-1-isopropyl-2-naphtyl cyclopropanecarboxylate dihydrochloride]: a new selective inhibitor of T-type calcium channels. *J Pharmacol Exp Ther* **309**, 193-199.

Huber WJ, III, Marohnic CC, Peters M, Alam J, Reed JR, Masters BS, & Backes WL (2009). Measurement of membrane-bound human heme oxygenase-1 activity using a chemically defined assay system. *Drug Metab Dispos* **37**, 857-864.

Huc S, Monteil A, Bidaud I, Barbara G, Chemin J, & Lory P (2009). Regulation of T-type calcium channels: signalling pathways and functional implications. *Biochim Biophys Acta* **1793**, 947-952.

Hyvelin JM, Maurel B, Uzbekov R, Motterlini R, & Lermusiaux P (2010). Hemin prevents in-stent stenosis in rat and rabbit models by inducing heme-oxygenase-1. *J Vasc Surg* **51**, 417-428.

Iftinca MC & Zamponi GW (2009). Regulation of neuronal T-type calcium channels. *Trends Pharmacol Sci* **30**, 32-40.

Ihara E, Hirano K, Hirano M, Nishimura J, Nawata H, & Kanaide H (2002). Mechanism of down-regulation of L-type Ca(2+) channel in the proliferating smooth muscle cells of rat aorta. *J Cell Biochem* **87**, 242-251.

Janssen LJ (1997). T-type and L-type Ca2+ currents in canine bronchial smooth muscle: characterization and physiological roles. *Am J Physiol* **272**, C1757-C1765.

Jeon EM, Choi HC, Lee KY, Chang KC, & Kang YJ (2009). Hemin inhibits hypertensive rat vascular smooth muscle cell proliferation through regulation of cyclin D and p21. *Arch Pharm Res* **32**, 375-382.

Jiang F, Roberts SJ, Datla S, & Dusting GJ (2006). NO modulates NADPH oxidase function via heme oxygenase-1 in human endothelial cells. *Hypertension* **48**, 950-957.

Jozkowicz A, Was H, & Dulak J (2007). Heme oxygenase-1 in tumors: is it a false friend? *Antioxid Redox Signal* **9**, 2099-2117.

Kaneda H, Ohno M, Taguchi J, Togo M, Hashimoto H, Ogasawara K, Aizawa T, Ishizaka N, & Nagai R (2002). Heme oxygenase-1 gene promoter polymorphism is associated with coronary artery disease in Japanese patients with coronary risk factors. *Arterioscler Thromb Vasc Biol* **22**, 1680-1685.

Kang HW, Park JY, Jeong SW, Kim JA, Moon HJ, Perez-Reyes E, & Lee JH (2006). A molecular determinant of nickel inhibition in Cav3.2 T-type calcium channels. *J Biol Chem* **281**, 4823-4830.

Kao JP, Alderton JM, Tsien RY, & Steinhardt RA (1990). Active involvement of Ca2+ in mitotic progression of Swiss 3T3 fibroblasts. *J Cell Biol* **111**, 183-196.

Kappas A & Drummond GS (1986). Control of heme metabolism with synthetic metalloporphyrins. *J Clin Invest* **77**, 335-339.

Karmazinova M, Beyl S, Stary-Weinzinger A, Suwattanasophon C, Klugbauer N, Hering S, & Lacinova L (2010). Cysteines in the loop between IS5 and the pore helix of Ca(V)3.1 are essential for channel gating. *Pflugers Arch* **460**, 1015-1028.

Keir ST, Friedman HS, Reardon DA, Bigner DD, & Gray LA (2012). Mibefradil, a novel therapy for glioblastoma multiforme: cell cycle synchronization and interlaced therapy in a murine model. *J Neurooncol*.

Kim EJ, Kim DK, Kim SH, Lee KM, Park HS, & Kim SH (2011a). Alteration of Ryanodine-receptors in Cultured Rat Aortic Smooth Muscle Cells. *Korean J Physiol Pharmacol* **15**, 431-436.

Kim HP, Ryter SW, & Choi AM (2006). CO as a cellular signaling molecule. *Annu Rev Pharmacol Toxicol* **46**, 411-449.

Kim HP, Wang X, Galbiati F, Ryter SW, & Choi AM (2004). Caveolae compartmentalization of heme oxygenase-1 in endothelial cells. *FASEB J* **18**, 1080-1089.

Kim HP, Wang X, Nakao A, Kim SI, Murase N, Choi ME, Ryter SW, & Choi AM (2005). Caveolin-1 expression by means of p38beta mitogen-activated protein kinase mediates the antiproliferative effect of carbon monoxide. *Proc Natl Acad Sci U S A* **102**, 11319-11324.

Kim KM, Pae HO, Zheng M, Park R, Kim YM, & Chung HT (2007). Carbon monoxide induces heme oxygenase-1 via activation of protein kinase R-like endoplasmic reticulum kinase and inhibits endothelial cell apoptosis triggered by endoplasmic reticulum stress. *Circ Res* **101**, 919-927.

Kim YM, Pae HO, Park JE, Lee YC, Woo JM, Kim NH, Choi YK, Lee BS, Kim SR, & Chung HT (2011b). Heme oxygenase in the regulation of vascular biology: from molecular mechanisms to therapeutic opportunities. *Antioxid Redox Signal* **14**, 137-167.

Kimes BW & Brandt BL (1976). Characterization of two putative smooth muscle cell lines from rat thoracic aorta. *Exp Cell Res* **98**, 349-366.

Kinobe RT, Dercho RA, & Nakatsu K (2008). Inhibitors of the heme oxygenase - carbon monoxide system: on the doorstep of the clinic? *Can J Physiol Pharmacol* **86**, 577-599.

Kinobe RT, Vlahakis JZ, Vreman HJ, Stevenson DK, Brien JF, Szarek WA, & Nakatsu K (2006). Selectivity of imidazole-dioxolane compounds for in vitro inhibition of microsomal haem oxygenase isoforms. *Br J Pharmacol* **147**, 307-315.

Kocher O, Skalli O, Cerutti D, Gabbiani F, & Gabbiani G (1985). Cytoskeletal features of rat aortic cells during development. An electron microscopic, immunohistochemical, and biochemical study. *Circ Res* **56**, 829-838.

Kohler R, Wulff H, Eichler I, Kneifel M, Neumann D, Knorr A, Grgic I, Kampfe D, Si H, Wibawa J, Real R, Borner K, Brakemeier S, Orzechowski HD, Reusch HP, Paul M, Chandy KG, & Hoyer J (2003). Blockade of the intermediate-conductance calcium-activated potassium channel as a new therapeutic strategy for restenosis. *Circulation* **108**, 1119-1125.

Kronke G, Kadl A, Ikonomu E, Bluml S, Furnkranz A, Sarembock IJ, Bochkov VN, Exner M, Binder BR, & Leitinger N (2007). Expression of heme oxygenase-1 in human vascular cells is regulated by peroxisome proliferator-activated receptors. *Arterioscler Thromb Vasc Biol* **27**, 1276-1282.

Kuga T, Kobayashi S, Hirakawa Y, Kanaide H, & Takeshita A (1996). Cell cycle--dependent expression of L- and T-type Ca2+ currents in rat aortic smooth muscle cells in primary culture. *Circ Res* **79**, 14-19.

Kumar B, Dreja K, Shah SS, Cheong A, Xu SZ, Sukumar P, Naylor J, Forte A, Cipollaro M, McHugh D, Kingston PA, Heagerty AM, Munsch CM, Bergdahl A, Hultgardh-Nilsson A, Gomez MF, Porter KE, Hellstrand P, & Beech DJ (2006). Upregulated TRPC1 channel in vascular injury in vivo and its role in human neointimal hyperplasia. *Circ Res* **98**, 557-563.

Kuo IY, Wolfle SE, & Hill CE (2011). T-type calcium channels and vascular function: the new kid on the block? *J Physiol* **589**, 783-795.

La P, Fernando AP, Wang Z, Salahudeen A, Yang G, Lin Q, Wright CJ, & Dennery PA (2009). Zinc protoporphyrin regulates cyclin D1 expression independent of heme oxygenase inhibition. *J Biol Chem* **284**, 36302-36311.

Lacinova L, Kurejova M, Klugbauer N, & Hofmann F (2006). Gating of the expressed T-type Cav3.1 calcium channels is modulated by Ca2+. *Acta Physiol (Oxf)* **186**, 249-260.

Ledoux J, Werner ME, Brayden JE, & Nelson MT (2006). Calcium-activated potassium channels and the regulation of vascular tone. *Physiology (Bethesda)* **21**, 69-78.

Lee BS, Heo J, Kim YM, Shim SM, Pae HO, Kim YM, & Chung HT (2006). Carbon monoxide mediates heme oxygenase 1 induction via Nrf2 activation in hepatoma cells. *Biochem Biophys Res Commun* **343**, 965-972.

Lee CY & Yen MH (2009). Nitric oxide and carbon monoxide, collaborative and competitive regulators of hypertension. *Chang Gung Med J* **32**, 12-21.

Lee JH, Gomora JC, Cribbs LL, & Perez-Reyes E (1999). Nickel block of three cloned T-type calcium channels: low concentrations selectively block alpha1H. *Biophys J* **77**, 3034-3042.

Lee PJ, Jiang BH, Chin BY, Iyer NV, Alam J, Semenza GL, & Choi AM (1997). Hypoxia-inducible factor-1 mediates transcriptional activation of the heme oxygenase-1 gene in response to hypoxia. *J Biol Chem* **272**, 5375-5381.

Leuranguer V, Monteil A, Bourinet E, Dayanithi G, & Nargeot J (2000). T-type calcium currents in rat cardiomyocytes during postnatal development: contribution to hormone secretion. *Am J Physiol Heart Circ Physiol* **279**, H2540-H2548.

Li T, Tian H, Zhao Y, An F, Zhang L, Zhang J, Peng J, Zhang Y, & Guo Y (2011). Heme oxygenase-1 inhibits progression and destabilization of vulnerable plaques in a rabbit model of atherosclerosis. *Eur J Pharmacol* **672**, 143-152.

Li VG, Wang J, Traganos F, Kappas A, & Abraham NG (2002). Differential effect of heme oxygenase-1 in endothelial and smooth muscle cell cycle progression. *Biochem Biophys Res Commun* **296**, 1077-1082.

Li Z, Cheng H, Lederer WJ, Froehlich J, & Lakatta EG (1997). Enhanced proliferation and migration and altered cytoskeletal proteins in early passage smooth muscle cells from young and old rat aortic explants. *Exp Mol Pathol* **64**, 1-11.

Lim I, Gibbons SJ, Lyford GL, Miller SM, Strege PR, Sarr MG, Chatterjee S, Szurszewski JH, Shah VH, & Farrugia G (2005). Carbon monoxide activates human intestinal smooth muscle L-type Ca2+ channels through a nitric oxide-dependent mechanism. *Am J Physiol Gastrointest Liver Physiol* **288**, G7-14.

Lin H & McGrath JJ (1988). Vasodilating effects of carbon monoxide. *Drug Chem Toxicol* **11**, 371-385.

Lin Q, Weis S, Yang G, Weng YH, Helston R, Rish K, Smith A, Bordner J, Polte T, Gaunitz F, & Dennery PA (2007). Heme oxygenase-1 protein localizes to the nucleus and activates transcription factors important in oxidative stress. *J Biol Chem* **282**, 20621-20633.

Lipskaia L, del MF, Capiod T, Yacoubi S, Hadri L, Hours M, Hajjar RJ, & Lompre AM (2005). Sarco/endoplasmic reticulum Ca2+-ATPase gene transfer reduces vascular smooth muscle cell proliferation and neointima formation in the rat. *Circ Res* **97**, 488-495.

Lipskaia L, Hulot JS, & Lompre AM (2009). Role of sarco/endoplasmic reticulum calcium content and calcium ATPase activity in the control of cell growth and proliferation. *Pflugers Arch* **457**, 673-685.

Lipskaia L, Pourci ML, Delomenie C, Combettes L, Goudouneche D, Paul JL, Capiod T, & Lompre AM (2003). Phosphatidylinositol 3-kinase and calcium-activated transcription pathways are required for VLDL-induced smooth muscle cell proliferation. *Circ Res* **92**, 1115-1122.

Liu XM, Chapman GB, Peyton KJ, Schafer AI, & Durante W (2002a). Carbon monoxide inhibits apoptosis in vascular smooth muscle cells. *Cardiovasc Res* **55**, 396-405.

Liu XM, Chapman GB, Wang H, & Durante W (2002b). Adenovirus-mediated heme oxygenase-1 gene expression stimulates apoptosis in vascular smooth muscle cells. *Circulation* **105**, 79-84.

Liu Z, Dronadula N, & Rao GN (2004). A novel role for nuclear factor of activated T cells in receptor tyrosine kinase and G protein-coupled receptor agonist-induced vascular smooth muscle cell motility. *J Biol Chem* **279**, 41218-41226.

Liu Z, Zhang C, Dronadula N, Li Q, & Rao GN (2005). Blockade of nuclear factor of activated T cells activation signaling suppresses balloon injury-induced neointima formation in a rat carotid artery model. *J Biol Chem* **280**, 14700-14708.

Loewenstein WR (1981). Junctional intercellular communication: the cell-to-cell membrane channel. *Physiol Rev* **61**, 829-913.

Lory P, Bidaud I, & Chemin J (2006). T-type calcium channels in differentiation and proliferation. *Cell Calcium* **40**, 135-146.

Louis H, Lacolley P, Kakou A, Cattan V, Daret D, Safar M, Bonnet J, & Daniel Lamaziere JM (2006). Early activation of internal medial smooth muscle cells in the rabbit aorta after mechanical injury: relationship with intimal thickening and pharmacological applications. *Clin Exp Pharmacol Physiol* **33**, 131-138.

Lusis AJ (2000). Atherosclerosis. *Nature* **407**, 233-241.

Maines MD (1997). The heme oxygenase system: a regulator of second messenger gases. *Annu Rev Pharmacol Toxicol* **37**, 517-554.

Maines MD & Kappas A (1975). Cobalt stimulation of heme degradation in the liver. Dissociation of microsomal oxidation of heme from cytochrome P-450. *J Biol Chem* **250**, 4171-4177.

Maines MD & Trakshel GM (1992). Differential regulation of heme oxygenase isozymes by Sn- and Zn-protoporphyrins: possible relevance to suppression of hyperbilirubinemia. *Biochim Biophys Acta* **1131**, 166-174.

Mariot P, Vanoverberghe K, Lalevee N, Rossier MF, & Prevarskaya N (2002). Overexpression of an alpha 1H (Cav3.2) T-type calcium channel during neuroendocrine differentiation of human prostate cancer cells. *J Biol Chem* **277**, 10824-10833.

Martin KA, Rzucidlo EM, Merenick BL, Fingar DC, Brown DJ, Wagner RJ, & Powell RJ (2004). The mTOR/p70 S6K1 pathway regulates vascular smooth muscle cell differentiation. *Am J Physiol Cell Physiol* **286**, C507-C517.

Martin RL, Lee JH, Cribbs LL, Perez-Reyes E, & Hanck DA (2000). Mibefradil block of cloned T-type calcium channels. *J Pharmacol Exp Ther* **295**, 302-308.

Marx SO, Jayaraman T, Go LO, & Marks AR (1995). Rapamycin-FKBP inhibits cell cycle regulators of proliferation in vascular smooth muscle cells. *Circ Res* **76**, 412-417.

Matsumura T, Zerrudo Z, & Hayflick L (1979). Senescent human diploid cells in culture: survival, DNA synthesis and morphology. *J Gerontol* **34**, 328-334.

Mayr FB, Spiel A, Leitner J, Marsik C, Germann P, Ullrich R, Wagner O, & Jilma B (2005a). Effects of carbon monoxide inhalation during experimental endotoxemia in humans. *Am J Respir Crit Care Med* **171**, 354-360.

Mayr FB, Spiel A, Leitner J, Marsik C, Germann P, Ullrich R, Wagner O, & Jilma B (2005b). Effects of carbon monoxide inhalation during experimental endotoxemia in humans. *Am J Respir Crit Care Med* **171**, 354-360.

McCaffrey TA, Nicholson AC, Szabo PE, Weksler ME, & Weksler BB (1988). Aging and arteriosclerosis. The increased proliferation of arterial smooth muscle cells isolated from old rats is associated with increased platelet-derived growth factor-like activity. *J Exp Med* **167**, 163-174.

McCarter SD, Scott JR, Lee PJ, Zhang X, Choi AM, McLean CA, Badhwar A, Dungey AA, Bihari A, Harris KA, & Potter RF (2003). Cotransfection of heme oxygenase-1 prevents the acute inflammation elicited by a second adenovirus. *Gene Ther* **10**, 1629-1635.

McCarthy NJ & Bennett MR (2000). The regulation of vascular smooth muscle cell apoptosis. *Cardiovasc Res* **45**, 747-755.

McDonald TF, Pelzer S, Trautwein W, & Pelzer DJ (1994). Regulation and modulation of calcium channels in cardiac, skeletal, and smooth muscle cells. *Physiol Rev* **74**, 365-507.

Means AR (1994). Calcium, calmodulin and cell cycle regulation. *FEBS Lett* **347**, 1-4.

Mehrke G, Zong XG, Flockerzi V, & Hofmann F (1994). The Ca(++)-channel blocker Ro 40-5967 blocks differently T-type and L-type Ca++ channels. *J Pharmacol Exp Ther* **271**, 1483-1488.

Mishra SK & Hermsmeyer K (1994). Selective inhibition of T-type Ca2+ channels by Ro 40-5967. *Circ Res* **75**, 144-148.

Moon SK, Cha BY, & Kim CH (2003). In vitro cellular aging is associated with enhanced proliferative capacity, G1 cell cycle modulation, and matrix metalloproteinase-9 regulation in mouse aortic smooth muscle cells. *Arch Biochem Biophys* **418**, 39-48.

Moon SK, Thompson LJ, Madamanchi N, Ballinger S, Papaconstantinou J, Horaist C, Runge MS, & Patterson C (2001). Aging, oxidative responses, and proliferative capacity in cultured mouse aortic smooth muscle cells. *Am J Physiol Heart Circ Physiol* **280**, H2779-H2788.

Morita T & Kourembanas S (1995). Endothelial cell expression of vasoconstrictors and growth factors is regulated by smooth muscle cell-derived carbon monoxide. *J Clin Invest* **96**, 2676-2682.

Morita T, Mitsialis SA, Koike H, Liu Y, & Kourembanas S (1997). Carbon monoxide controls the proliferation of hypoxic vascular smooth muscle cells. *J Biol Chem* **272**, 32804-32809.

Morita T, Perrella MA, Lee ME, & Kourembanas S (1995). Smooth muscle cell-derived carbon monoxide is a regulator of vascular cGMP. *Proc Natl Acad Sci U S A* **92**, 1475-1479.

Motterlini R, Clark JE, Foresti R, Sarathchandra P, Mann BE, & Green CJ (2002). Carbon monoxide-releasing molecules: characterization of biochemical and vascular activities. *Circ Res* **90**, E17-E24.

Motterlini R, Foresti R, Bassi R, & Green CJ (2000). Curcumin, an antioxidant and anti-inflammatory agent, induces heme oxygenase-1 and protects endothelial cells against oxidative stress. *Free Radic Biol Med* **28**, 1303-1312.

Motterlini R, Mann BE, Johnson TR, Clark JE, Foresti R, & Green CJ (2003). Bioactivity and pharmacological actions of carbon monoxide-releasing molecules. *Curr Pharm Des* **9**, 2525-2539.

Motterlini R & Otterbein LE (2010). The therapeutic potential of carbon monoxide. *Nat Rev Drug Discov* **9**, 728-743.

Mueller CF, Laude K, McNally JS, & Harrison DG (2005). ATVB in focus: redox mechanisms in blood vessels. *Arterioscler Thromb Vasc Biol* **25**, 274-278.

Mullins ME, Horowitz BZ, Linden DH, Smith GW, Norton RL, & Stump J (1998). Life-threatening interaction of mibefradil and beta-blockers with dihydropyridine calcium channel blockers. *JAMA* **280**, 157-158.

Mulvany MJ (1993). Resistance vessel structure in hypertension: growth or remodeling? *J Cardiovasc Pharmacol* **22 Suppl 5**, S44-S47.

Munaron L, Antoniotti S, & Lovisolo D (2004). Intracellular calcium signals and control of cell proliferation: how many mechanisms? *J Cell Mol Med* **8**, 161-168.

Nakamura Y, Ono H, & Frohlich ED (1999). Differential effects of T- and L-type calcium antagonists on glomerular dynamics in spontaneously hypertensive rats. *Hypertension* **34**, 273-278.

Narayanan D, Adebiyi A, & Jaggar JH (2012). Inositol trisphosphate receptors in smooth muscle cells. *Am J Physiol Heart Circ Physiol* **302**, H2190-H2210.

Negulescu PA, Shastri N, & Cahalan MD (1994). Intracellular calcium dependence of gene expression in single T lymphocytes. *Proc Natl Acad Sci U S A* **91**, 2873-2877.

Neher E (2000). Some Quantitative Aspects of Calcium Fluorimetry. In *Imaging Neurons: A Laboratory Manual*, eds. Yuste R, Lanni R, & Konnerth A, pp. 31.1-31.11. Cold Spring Harbour Laboratory Press, New York.

Nelson MT, Joksovic PM, Perez-Reyes E, & Todorovic SM (2005). The endogenous redox agent L-cysteine induces T-type Ca2+ channel-dependent sensitization of a novel subpopulation of rat peripheral nociceptors. *J Neurosci* **25**, 8766-8775.

Nelson MT, Joksovic PM, Su P, Kang HW, Van DA, Baumgart JP, David LS, Snutch TP, Barrett PQ, Lee JH, Zorumski CF, Perez-Reyes E, & Todorovic SM (2007a). Molecular mechanisms of subtype-specific inhibition of neuronal T-type calcium channels by ascorbate. *J Neurosci* **27**, 12577-12583.

Nelson MT, Woo J, Kang HW, Vitko I, Barrett PQ, Perez-Reyes E, Lee JH, Shin HS, & Todorovic SM (2007b). Reducing agents sensitize C-type nociceptors by relieving high-affinity zinc inhibition of T-type calcium channels. *J Neurosci* **27**, 8250-8260.

Neveu D, Quignard JF, Fernandez A, Richard S, & Nargeot J (1994). Differential beta-adrenergic regulation and phenotypic modulation of voltage-gated calcium currents in rat aortic myocytes. *J Physiol* **479 (Pt 2)**, 171-182.

Neylon CB, Lang RJ, Fu Y, Bobik A, & Reinhart PH (1999). Molecular cloning and characterization of the intermediate-conductance Ca(2+)-activated K(+) channel in vascular smooth muscle: relationship between K(Ca) channel diversity and smooth muscle cell function. *Circ Res* **85**, e33-e43.

Nilius B, Owsianik G, Voets T, & Peters JA (2007). Transient receptor potential cation channels in disease. *Physiol Rev* **87**, 165-217.

Nilius B, Prenen J, Kamouchi M, Viana F, Voets T, & Droogmans G (1997). Inhibition by mibefradil, a novel calcium channel antagonist, of Ca(2+)- and volume-activated Cl- channels in macrovascular endothelial cells. *Br J Pharmacol* **121**, 547-555.

Nilius B, Talavera K, & Verkhratsky A (2006). T-type calcium channels: the never ending story. *Cell Calcium* **40**, 81-88.

Otterbein LE, Bach FH, Alam J, Soares M, Tao LH, Wysk M, Davis RJ, Flavell RA, & Choi AM (2000). Carbon monoxide has anti-inflammatory effects involving the mitogen-activated protein kinase pathway. *Nat Med* **6**, 422-428.

Otterbein LE, Soares MP, Yamashita K, & Bach FH (2003a). Heme oxygenase-1: unleashing the protective properties of heme. *Trends Immunol* **24**, 449-455.

Otterbein LE, Zuckerbraun BS, Haga M, Liu F, Song R, Usheva A, Stachulak C, Bodyak N, Smith RN, Csizmadia E, Tyagi S, Akamatsu Y, Flavell RJ, Billiar TR, Tzeng E, Bach FH, Choi AM, & Soares MP (2003b). Carbon monoxide suppresses arteriosclerotic lesions associated with chronic graft rejection and with balloon injury. *Nat Med* **9**, 183-190.

Otun H, Gillespie JI, Nicholls JA, Greenwell JR, & Dunlop W (1992). Transients in intracellular free calcium in subconfluent and confluent cultures of a rat smooth muscle cell line. *Exp Physiol* **77**, 749-756.

Owens GK (1989). Control of hypertrophic versus hyperplastic growth of vascular smooth muscle cells. *Am J Physiol* **257**, H1755-H1765.

Owens GK (1995). Regulation of differentiation of vascular smooth muscle cells. *Physiol Rev* **75**, 487-517.

Owens GK, Geisterfer AA, Yang YW, & Komoriya A (1988). Transforming growth factor-beta-induced growth inhibition and cellular hypertrophy in cultured vascular smooth muscle cells. *J Cell Biol* **107**, 771-780.

Owens GK, Kumar MS, & Wamhoff BR (2004). Molecular regulation of vascular smooth muscle cell differentiation in development and disease. *Physiol Rev* **84**, 767-801.

Owens GK, Loeb A, Gordon D, & Thompson MM (1986). Expression of smooth muscle-specific alpha-isoactin in cultured vascular smooth muscle cells: relationship between growth and cytodifferentiation. *J Cell Biol* **102**, 343-352.

Pae HO, Jeong GS, Jeong SO, Kim HS, Kim SA, Kim YC, Yoo SJ, Kim HD, & Chung HT (2007). Roles of heme oxygenase-1 in curcumin-induced growth inhibition in rat smooth muscle cells. *Exp Mol Med* **39**, 267-277.

Pae HO, Son Y, Kim NH, Jeong HJ, Chang KC, & Chung HT (2010). Role of heme oxygenase in preserving vascular bioactive NO. *Nitric Oxide* **23**, 251-257.

Panner A, Cribbs LL, Zainelli GM, Origitano TC, Singh S, & Wurster RD (2005). Variation of T-type calcium channel protein expression affects cell division of cultured tumor cells. *Cell Calcium* **37**, 105-119.

Panner A & Wurster RD (2006). T-type calcium channels and tumor proliferation. *Cell Calcium* **40**, 253-259.

Paravicini TM & Touyz RM (2006). Redox signaling in hypertension. *Cardiovasc Res* **71**, 247-258.

Paredes RM, Etzler JC, Watts LT, Zheng W, & Lechleiter JD (2008). Chemical calcium indicators. *Methods* **46**, 143-151.

Peers C (2011). Ion channels as target effectors for carbon monoxide. *Exp Physiol* **96**, 836-839.

Peers C & Steele DS (2012). Carbon monoxide: a vital signalling molecule and potent toxin in the myocardium. *J Mol Cell Cardiol* **52**, 359-365.

Peng H, Matchkov V, Ivarsen A, Aalkjaer C, & Nilsson H (2001). Hypothesis for the initiation of vasomotion. *Circ Res* **88**, 810-815.

Perez-Reyes E (1998). Molecular characterization of a novel family of low voltage-activated, T-type, calcium channels. *J Bioenerg Biomembr* **30**, 313-318.

Perez-Reyes E (2003). Molecular physiology of low-voltage-activated t-type calcium channels. *Physiol Rev* **83**, 117-161.

Perez-Reyes E (2006). Molecular characterization of T-type calcium channels. *Cell Calcium* **40**, 89-96.

Perez-Reyes E, Cribbs LL, Daud A, Lacerda AE, Barclay J, Williamson MP, Fox M, Rees M, & Lee JH (1998). Molecular characterization of a neuronal low-voltage-activated T-type calcium channel. *Nature* **391**, 896-900.

Peyton KJ, Reyna SV, Chapman GB, Ensenat D, Liu XM, Wang H, Schafer AI, & Durante W (2002). Heme oxygenase-1-derived carbon monoxide is an autocrine inhibitor of vascular smooth muscle cell growth. *Blood* **99**, 4443-4448.

Pluteanu F & Cribbs LL (2009). T-type calcium channels are regulated by hypoxia/reoxygenation in ventricular myocytes. *Am J Physiol Heart Circ Physiol* **297**, H1304-H1313.

Pluteanu F & Cribbs LL (2011). Regulation and function of Cav3.1 T-type calcium channels in IGF-I-stimulated pulmonary artery smooth muscle cells. *Am J Physiol Cell Physiol* **300**, C517-C525.

Poole JC, Cromwell SB, & Benditt EP (1971). Behavior of smooth muscle cells and formation of extracellular structures in the reaction of arterial walls to injury. *Am J Pathol* **62**, 391-414.

Poon M, Marx SO, Gallo R, Badimon JJ, Taubman MB, & Marks AR (1996). Rapamycin inhibits vascular smooth muscle cell migration. *J Clin Invest* **98**, 2277-2283.

Porter KE, Naik J, Turner NA, Dickinson T, Thompson MM, & London NJ (2002). Simvastatin inhibits human saphenous vein neointima formation via inhibition of smooth muscle cell proliferation and migration. *J Vasc Surg* **36**, 150-157.

Porter KE, Thompson MM, Loftus IM, McDermott E, Jones L, Crowther M, Bell PR, & London NJ (1999). Production and inhibition of the gelatinolytic matrix metalloproteinases in a human model of vein graft stenosis. *Eur J Vasc Endovasc Surg* **17**, 404-412.

Potier M, Gonzalez JC, Motiani RK, Abdullaev IF, Bisaillon JM, Singer HA, & Trebak M (2009). Evidence for S. *FASEB J* **23**, 2425-2437.

Powell RJ, Cronenwett JL, Fillinger MF, Wagner RJ, & Sampson LN (1996). Endothelial cell modulation of smooth muscle cell morphology and organizational growth pattern. *Ann Vasc Surg* **10**, 4-10.

Pratt PF, Bonnet S, Ludwig LM, Bonnet P, & Rusch NJ (2002). Upregulation of L-type Ca2+ channels in mesenteric and skeletal arteries of SHR. *Hypertension* **40**, 214-219.

Quignard JF, Frapier JM, Harricane MC, Albat B, Nargeot J, & Richard S (1997). Voltage-gated calcium channel currents in human coronary myocytes. Regulation by cyclic GMP and nitric oxide. *J Clin Invest* **99**, 185-193.

Rahman MN, Vlahakis JZ, Vukomanovic D, Lee W, Szarek WA, Nakatsu K, & Jia Z (2012). A novel, "double-clamp" binding mode for human heme oxygenase-1 inhibition. *PLoS One* **7**, e29514.

Raman KG, Barbato JE, Ifedigbo E, Ozanich BA, Zenati MS, Otterbein LE, & Tzeng E (2006). Inhaled carbon monoxide inhibits intimal hyperplasia and provides added benefit with nitric oxide. *J Vasc Surg* **44**, 151-158.

Ramlawi B, Scott JR, Feng J, Mieno S, Raman KG, Gallo D, Csizmadia E, Yoke CB, Bach FH, Otterbein LE, & Sellke FW (2007). Inhaled carbon monoxide prevents graft-induced intimal hyperplasia in swine. *J Surg Res* **138**, 121-127.

Rao DD, Vorhies JS, Senzer N, & Nemunaitis J (2009). siRNA vs. shRNA: similarities and differences. *Adv Drug Deliv Rev* **61**, 746-759.

Remillard CV & Yuan JX (2006). TRP channels, CCE, and the pulmonary vascular smooth muscle. *Microcirculation* **13**, 671-692.

Richard S & Nargeot J (1998). T-type Ca^{2+} currents in vascular smooth muscle cells: a role in cellular proliferation? In *Low-voltage-activated T-type calcium channels : proceedings from the International Electrophysiology Meeting, Montpellier, 21-22 October 1996*, eds. Tsien RW, Clozel JP, & Nargeot J, pp. 123-132. Adis International, Chester.

Richard S, Neveu D, Carnac G, Bodin P, Travo P, & Nargeot J (1992). Differential expression of voltage-gated Ca(2+)-currents in cultivated aortic myocytes. *Biochim Biophys Acta* **1160**, 95-104.

Rodman DM, Reese K, Harral J, Fouty B, Wu S, West J, Hoedt-Miller M, Tada Y, Li KX, Cool C, Fagan K, & Cribbs L (2005). Low-voltage-activated (T-type) calcium channels control proliferation of human pulmonary artery myocytes. *Circ Res* **96**, 864-872.

Rodriguez-Gomez JA, Levitsky KL, & Lopez-Barneo J (2012). T-type Ca2+ channels in mouse embryonic stem cells: modulation during cell cycle and contribution to self-renewal. *Am J Physiol Cell Physiol* **302**, C494-C504.

Ross R (1981). George Lyman Duff Memorial Lecture. Atherosclerosis: a problem of the biology of arterial wall cells and their interactions with blood components. *Arteriosclerosis* **1**, 293-311.

Ruiz J & Ameredes BT (2012). The Cellular Effects of Carbon Monoxide in the Airway. *Curr Mol Med*.

Ruiz-Torres A, Gimeno A, Melon J, Mendez L, Munoz FJ, & Macia M (1999). Age-related loss of proliferative activity of human vascular smooth muscle cells in culture. *Mech Ageing Dev* **110**, 49-55.

Ryter SW, Alam J, & Choi AM (2006). Heme oxygenase-1/carbon monoxide: from basic science to therapeutic applications. *Physiol Rev* **86**, 583-650.

Rzucidlo EM, Martin KA, & Powell RJ (2007). Regulation of vascular smooth muscle cell differentiation. *J Vasc Surg* **45 Suppl A**, A25-A32.

Santos MF, Seixas JD, Coelho AC, Mukhopadhyay A, Reis PM, Romao MJ, Romao CC, & Santos-Silva T (2012). New insights into the chemistry of fac-[Ru(CO)(3)](2)(+) fragments in biologically relevant conditions: the CO releasing activity of [Ru(CO)(3)Cl(2)(1,3-thiazole)], and the X-ray crystal structure of its adduct with lysozyme. *J Inorg Biochem* **117**, 285-291.

Sarbassov DD, Ali SM, & Sabatini DM (2005). Growing roles for the mTOR pathway. *Curr Opin Cell Biol* **17**, 596-603.

Schmitt R, Clozel JP, Iberg N, & Buhler FR (1995). Mibefradil prevents neointima formation after vascular injury in rats. Possible role of the blockade of the T-type voltage-operated calcium channel. *Arterioscler Thromb Vasc Biol* **15**, 1161-1165.

Schulick AH, Taylor AJ, Zuo W, Qiu CB, Dong G, Woodward RN, Agah R, Roberts AB, Virmani R, & Dichek DA (1998). Overexpression of transforming growth factor beta1 in arterial endothelium causes hyperplasia, apoptosis, and cartilaginous metaplasia. *Proc Natl Acad Sci U S A* **95**, 6983-6988.

Schwartz SM, Campbell GR, & Campbell JH (1986). Replication of smooth muscle cells in vascular disease. *Circ Res* **58**, 427-444.

Scragg JL, Dallas ML, Wilkinson JA, Varadi G, & Peers C (2008). Carbon monoxide inhibits L-type Ca2+ channels via redox modulation of key cysteine residues by mitochondrial reactive oxygen species. *J Biol Chem* **283**, 24412-24419.

Shan Y, Lambrecht RW, Donohue SE, & Bonkovsky HL (2006). Role of Bach1 and Nrf2 in up-regulation of the heme oxygenase-1 gene by cobalt protoporphyrin. *FASEB J* **20**, 2651-2653.

Shan Y, Pepe J, Lambrecht RW, & Bonkovsky HL (2002). Mapping of the chick heme oxygenase-1 proximal promoter for responsiveness to metalloporphyrins. *Arch Biochem Biophys* **399**, 159-166.

Shan Y, Pepe J, Lu TH, Elbirt KK, Lambrecht RW, & Bonkovsky HL (2000). Induction of the heme oxygenase-1 gene by metalloporphyrins. *Arch Biochem Biophys* **380**, 219-227.

Shcheglovitov A, Zhelay T, Vitko Y, Osipenko V, Perez-Reyes E, Kostyuk P, & Shuba Y (2005). Contrasting the effects of nifedipine on subtypes of endogenous and recombinant T-type Ca2+ channels. *Biochem Pharmacol* **69**, 841-854.

Sheng M, McFadden G, & Greenberg ME (1990). Membrane depolarization and calcium induce c-fos transcription via phosphorylation of transcription factor CREB. *Neuron* **4**, 571-582.

Shibahara S, Yoshida T, & Kikuchi G (1980). Intracellular site of synthesis of microsomal heme oxygenase in pig spleen. *J Biochem* **88**, 45-50.

Singh S & Evans TW (1997). Nitric oxide, the biological mediator of the decade: fact or fiction? *Eur Respir J* **10**, 699-707.

Smith PK, Krohn RI, Hermanson GT, Mallia AK, Gartner FH, Provenzano MD, Fujimoto EK, Goeke NM, Olson BJ, & Klenk DC (1985). Measurement of protein using bicinchoninic acid. *Anal Biochem* **150**, 76-85.

Song H, Bergstrasser C, Rafat N, Hoger S, Schmidt M, Endres N, Goebeler M, Hillebrands JL, Brigelius-Flohe R, Banning A, Beck G, Loesel R, & Yard BA (2009). The carbon monoxide releasing molecule (CORM-3) inhibits expression of vascular cell adhesion molecule-1 and E-selectin independently of haem oxygenase-1 expression. *Br J Pharmacol* **157**, 769-780.

Song R, Mahidhara RS, Liu F, Ning W, Otterbein LE, & Choi AM (2002). Carbon monoxide inhibits human airway smooth muscle cell proliferation via mitogen-activated protein kinase pathway. *Am J Respir Cell Mol Biol* **27**, 603-610.

Soni H, Jain M, & Mehta AA (2011). Investigation into the mechanism(s) of antithrombotic effects of carbon monoxide releasing molecule-3 (CORM-3). *Thromb Res* **127**, 551-559.

Sonoyama K, Greenstein A, Price A, Khavandi K, & Heagerty T (2007). Vascular remodeling: implications for small artery function and target organ damage. *Ther Adv Cardiovasc Dis* **1**, 129-137.

Stanford SJ, Walters MJ, Hislop AA, Haworth SG, Evans TW, Mann BE, Motterlini R, & Mitchell JA (2003). Heme oxygenase is expressed in human pulmonary artery smooth muscle where carbon monoxide has an anti-proliferative role. *Eur J Pharmacol* **473**, 135-141.

Strege PR, Bernard CE, Ou Y, Gibbons SJ, & Farrugia G (2005). Effect of mibefradil on sodium and calcium currents. *Am J Physiol Gastrointest Liver Physiol* **289**, G249-G253.

Su B, Mitra S, Gregg H, Flavahan S, Chotani MA, Clark KR, Goldschmidt-Clermont PJ, & Flavahan NA (2001). Redox regulation of vascular smooth muscle cell differentiation. *Circ Res* **89**, 39-46.

Suzuki T, Higgins PJ, & Crawford DR (2000). Control selection for RNA quantitation. *Biotechniques* **29**, 332-337.

Sylvester AM, Chen D, Krasinski K, & Andres V (1998). Role of c-fos and E2F in the induction of cyclin A transcription and vascular smooth muscle cell proliferation. *J Clin Invest* **101**, 940-948.

Taille C, Almolki A, Benhamed M, Zedda C, Megret J, Berger P, Leseche G, Fadel E, Yamaguchi T, Marthan R, Aubier M, & Boczkowski J (2003). Heme oxygenase inhibits human airway smooth muscle proliferation via a bilirubin-dependent modulation of ERK1/2 phosphorylation. *J Biol Chem* **278**, 27160-27168.

Taille C, El-Benna J, Lanone S, Boczkowski J, & Motterlini R (2005). Mitochondrial respiratory chain and NAD(P)H oxidase are targets for the antiproliferative effect of carbon monoxide in human airway smooth muscle. *J Biol Chem* **280**, 25350-25360.

Taupin P (2007). BrdU immunohistochemistry for studying adult neurogenesis: paradigms, pitfalls, limitations, and validation. *Brain Res Rev* **53**, 198-214.

Taylor JT, Zeng XB, Pottle JE, Lee K, Wang AR, Yi SG, Scruggs JA, Sikka SS, & Li M (2008). Calcium signaling and T-type calcium channels in cancer cell cycling. *World J Gastroenterol* **14**, 4984-4991.

Tenhunen R, Marver HS, & Schmid R (1969). Microsomal heme oxygenase. Characterization of the enzyme. *J Biol Chem* **244**, 6388-6394.

Togane Y, Morita T, Suematsu M, Ishimura Y, Yamazaki JI, & Katayama S (2000). Protective roles of endogenous carbon monoxide in neointimal development elicited by arterial injury. *Am J Physiol Heart Circ Physiol* **278**, H623-H632.

Toyofuku T, Yabuki M, Otsu K, Kuzuya T, Hori M, & Tada M (1998). Intercellular calcium signaling via gap junction in connexin-43-transfected cells. *J Biol Chem* **273**, 1519-1528.

Traboulsie A, Chemin J, Chevalier M, Quignard JF, Nargeot J, & Lory P (2007). Subunit-specific modulation of T-type calcium channels by zinc. *J Physiol* **578**, 159-171.

Tulis DA, Durante W, Peyton KJ, Evans AJ, & Schafer AI (2001). Heme oxygenase-1 attenuates vascular remodeling following balloon injury in rat carotid arteries. *Atherosclerosis* **155**, 113-122.

Turner NA, Ho S, Warburton P, O'Regan DJ, & Porter KE (2007). Smooth muscle cells cultured from human saphenous vein exhibit increased proliferation, invasion, and mitogen-activated protein kinase activation in vitro compared with paired internal mammary artery cells. *J Vasc Surg* **45**, 1022-1028.

Tzeng BH, Chen YH, Huang CH, Lin SS, Lee KR, & Chen CC (2012). The Cav3.1 T-type calcium channel is required for neointimal formation in response to vascular injury in mice. *Cardiovasc Res*.

Urata Y, Goto S, Kawakatsu M, Yodoi J, Eto M, Akishita M, & Kondo T (2010). DHEA attenuates PDGF-induced phenotypic proliferation of vascular smooth muscle A7r5 cells through redox regulation. *Biochem Biophys Res Commun* **396**, 489-494.

Vallot O, Combettes L, Jourdon P, Inamo J, Marty I, Claret M, & Lompre AM (2000). Intracellular Ca(2+) handling in vascular smooth muscle cells is affected by proliferation. *Arterioscler Thromb Vasc Biol* **20**, 1225-1235.

van de Wetering M, Oving I, Muncan V, Pon Fong MT, Brantjes H, van LD, Holstege FC, Brummelkamp TR, Agami R, & Clevers H (2003). Specific inhibition of gene expression using a stably integrated, inducible small-interfering-RNA vector. *EMBO Rep* **4**, 609-615.

van BC, Fameli N, & Evans AM (2013). Pan-Junctional Sarcoplasmic Reticulum in Vascular Smooth Muscle: Nanospace Ca2+ transport for Site- and Function-specific Ca2+ signalling. *J Physiol*.

Vogel RA (1997). Coronary risk factors, endothelial function, and atherosclerosis: a review. *Clin Cardiol* **20**, 426-432.

Wagner CT, Durante W, Christodoulides N, Hellums JD, & Schafer AI (1997). Hemodynamic forces induce the expression of heme oxygenase in cultured vascular smooth muscle cells. *J Clin Invest* **100**, 589-596.

Wang CY & Chau LY (2010). Heme oxygenase-1 in cardiovascular diseases: molecular mechanisms and clinical perspectives. *Chang Gung Med J* **33**, 13-24.

Wang YQ, Brooks G, Yuan WZ, Zhu CB, Li YQ, & Wu XS (2002a). [Functional analysis of the alpha1G subunit of the T-type calcium channel in cellular proliferation]. *Shi Yan Sheng Wu Xue Bao* **35**, 229-235.

Wang YQ, Brooks G, Zhu CB, Yuan WZ, Li YQ, & Wu XS (2002b). [Functional analysis of the human T-type calcium channel alpha 1H subunit gene in cellular proliferation]. *Yi Chuan Xue Bao* **29**, 659-665.

Webb RC (2003). Smooth muscle contraction and relaxation. *Adv Physiol Educ* **27**, 201-206.

Wegiel B, Gallo DJ, Raman KG, Karlsson JM, Ozanich B, Chin BY, Tzeng E, Ahmad S, Ahmed A, Baty CJ, & Otterbein LE (2010). Nitric oxide-dependent bone marrow progenitor mobilization by carbon monoxide enhances endothelial repair after vascular injury. *Circulation* **121**, 537-548.

Wei AD, Gutman GA, Aldrich R, Chandy KG, Grissmer S, & Wulff H (2005). International Union of Pharmacology. LII. Nomenclature and molecular relationships of calcium-activated potassium channels. *Pharmacol Rev* **57**, 463-472.

Wei GL, Krasinski K, Kearney M, Isner JM, Walsh K, & Andres V (1997). Temporally and spatially coordinated expression of cell cycle regulatory factors after angioplasty. *Circ Res* **80**, 418-426.

Wellman GC, Cartin L, Eckman DM, Stevenson AS, Saundry CM, Lederer WJ, & Nelson MT (2001). Membrane depolarization, elevated Ca(2+) entry, and gene expression in cerebral arteries of hypertensive rats. *Am J Physiol Heart Circ Physiol* **281**, H2559-H2567.

Widlansky ME, Gokce N, Keaney JF, Jr., & Vita JA (2003). The clinical implications of endothelial dysfunction. *J Am Coll Cardiol* **42**, 1149-1160.

Wilkinson WJ & Kemp PJ (2011). Carbon monoxide: an emerging regulator of ion channels. *J Physiol* **589**, 3055-3062.

Williams SR, Toth TI, Turner JP, Hughes SW, & Crunelli V (1997). The 'window' component of the low threshold Ca2+ current produces input signal amplification and bistability in cat and rat thalamocortical neurones. *J Physiol* **505 (Pt 3)**, 689-705.

Worth NF, Rolfe BE, Song J, & Campbell GR (2001). Vascular smooth muscle cell phenotypic modulation in culture is associated with reorganisation of contractile and cytoskeletal proteins. *Cell Motil Cytoskeleton* **49**, 130-145.

Wu L & Wang R (2005). Carbon monoxide: endogenous production, physiological functions, and pharmacological applications. *Pharmacol Rev* **57**, 585-630.

Xiang Z, Thompson AD, Brogan JT, Schulte ML, Melancon BJ, Mi D, Lewis LM, Zou B, Yang L, Morrison R, Santomango T, Byers F, Brewer K, Aldrich JS, Yu H, Dawson ES, Li M, McManus O, Jones CK, Daniels JS, Hopkins CR, Xie XS, Conn PJ, Weaver CD, & Lindsley CW (2011). The Discovery and Characterization of ML218: A Novel, Centrally Active T-Type Calcium Channel Inhibitor with Robust Effects in STN Neurons and in a Rodent Model of Parkinson's Disease. *ACS Chem Neurosci* **2**, 730-742.

Yamawaki H, Haendeler J, & Berk BC (2003). Thioredoxin: a key regulator of cardiovascular homeostasis. *Circ Res* **93**, 1029-1033.

Yang G, Nguyen X, Ou J, Rekulapelli P, Stevenson DK, & Dennery PA (2001). Unique effects of zinc protoporphyrin on HO-1 induction and apoptosis. *Blood* **97**, 1306-1313.

Yet SF, Layne MD, Liu X, Chen YH, Ith B, Sibinga NE, & Perrella MA (2003). Absence of heme oxygenase-1 exacerbates atherosclerotic lesion formation and vascular remodeling. *FASEB J* **17**, 1759-1761.

Zhang M, Zhang BH, Chen L, & An W (2002). Overexpression of heme oxygenase-1 protects smooth muscle cells against oxidative injury and inhibits cell proliferation. *Cell Res* **12**, 123-132.

Zhang Y, Zhang J, Jiang D, Zhang D, Qian Z, Liu C, & Tao J (2012). Inhibition of T-type Ca(2+) channels by endostatin attenuates human glioblastoma cell proliferation and migration. *Br J Pharmacol* **166**, 1247-1260.

Zuckerbraun BS, Chin BY, Bilban M, d'Avila JC, Rao J, Billiar TR, & Otterbein LE (2007). Carbon monoxide signals via inhibition of cytochrome c oxidase and generation of mitochondrial reactive oxygen species. *FASEB J* **21**, 1099-1106.

Zuckerbraun BS, Chin BY, Wegiel B, Billiar TR, Czsimadia E, Rao J, Shimoda L, Ifedigbo E, Kanno S, & Otterbein LE (2006). Carbon monoxide reverses established pulmonary hypertension. *J Exp Med* **203**, 2109-2119.